Structures and Properties of Multifunctional Molecular Materials: Combining Chirality and Conductivity

Jordan R. Lopez

A thesis submitted in partial fulfilment of the requirements of Nottingham Trent University

for the degree of Doctor of Philosophy.

August 2017

School of Science and Technology
Nottingham Trent University
Clifton Lane
Nottingham
NG11 8NS

Acknowledgements

First and foremost, special thanks goes to my family, friends and Alice for supporting me throughout my studies and giving me opportunities (also excuses) to relax outside of the lab.

Thanks goes to all the staff at NTU; lecturers and lab technicians for being on hand to answer questions and help with requests. Your support and willingness to help has been invaluable over the last four years.

Thanks goes to Professor Koichi Kikuchi and his research group for hosting me at Tokyo Metropolitan University for three months and helping with uniaxial and hydrostatic resistivity measurements. Your infamous lunch time 'spicy noodle' and shochu parties will always be fond memories.

Thank you to Professor Jun'ichi Yamda and Dr. Tomofumi Kadoya along with the rest of the research group, for allowing me to work in your lab at Hyogo University and helping me with low temperature resistivity measurements. Also for your support and friendship during my time in Japan.

Huge thanks goes to Professor Yasuhiro Nakazawa, Professor Hiroki Akutsu, Dr. Ryo Yoshimoto and Dr. Yamashita for allowing me to visit your lab and work within your research group. Hiroki's expertise and help in x-ray crystallography and magnetic measurements have been key to the completion of this thesis. Endless trips to my favourite Kush-katsu restaurant and Izakayas always helped ease the pain of hours trying to mount crystals for resistivity measurements.

Thanks to Laurence, Dan, Tom, Zayd, Matteo and all the other postgrad researchers for the laughs, beer and costa trips.

Special thanks goes to Professor John Wallis, for your continued academic support, friendship and seemingly endless knowledge about cricket.

Lastly, but by no means least, thanks to Dr. Lee Martin for your friendship and guidance throughout this project. Your constant support, expertise and enthusiasm in this area of research inspired me over the last few years.

Abstract

The objective of this thesis is to investigate the influence of chirality upon conducting materials through the synthesis of charge-transfer salts by diffusion or electrocrystallisation of enantiopure/racemic donor molecules and anions.

This thesis presents the characterisation of new charge-transfer salts from two new donor molecules: BHM-EDT-TTF and BHM-BEDT-TTF. BHM-EDT-TTF has produced a family of 1:1 semiconductors with tetrahedral and octahedral anions BF_4, ClO_4 and PF_6. The room temperature resistivities and activation energies are similar for all enantiopure salts but slightly different for their racemic/meso forms. The racemic donor BHM-BEDT-TTF forms a semiconducting 2:1 salt with chloride, and an insulating 1:1 salt with TCNQ which has an interesting packing arrangement in that the donors are segregated into stacks consisting of only a single enantiomer in the mode *SS:SS:RR:RR:SS:SS.*

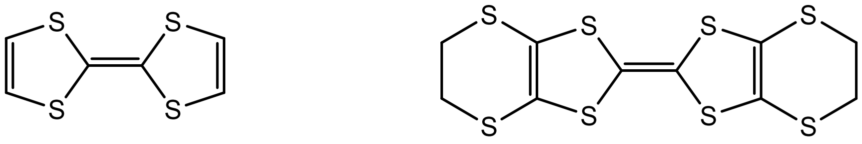

1

2

Figure A: Chemdraw representation of TTF and BEDT-TTF

The first charge-transfer salts have been synthesised and characterised from BEDT-TTF (Figure A) with racemic spiroboronate anions. Five salts of BEDT-TTF with either $B(malate)_2$, $B(mandelate)_2$, or $B(glycolate)_2$ show a variety of novel packing arrangements and conducting properties. These salts are also the first examples of preferential diastereomeric induction within the electrocrystallisation environment. Using spiroboronate anions with enantiopure ligands has also produced crystals having a macromolecular helical morphology.

The first examples of charge-transfer salts containing racemic and chiral lanthanide anions are reported including the spontaneous resolution of the racemic $[Gd(dipicolinato)_3]^{3-}$ anion in the presence of BEDT-TTF and bromobenzene to produce a chiral, paramagnetic, semiconductor. A new molecular superconductor, β”-$(BEDT\text{-}TTF)_2[(H_2O)(NH_4)_2Cr(C_2O_4)_3]$.18-crown-6, has been synthesised. This is the 2D superconductor with the widest gap between conducting layers where only a single donor packing motif is present (β”). Superconducting critical temperatures at ambient pressure observed by electrical transport and magnetic measurements are 4.0-4.9 and 2.5 K, respectively. The strong 2D nature of this system strongly suggests that the superconducting transition is a Kosterlitz-Thouless transition.

List of Publications

L. Martin,* J. D. Wallis, M. A. Guziak, J. Oxspring, J. R. Lopez, S-i. Nakatsuji, J-i. Yamada and H. Akutsu, Stereoisomeric semiconducting radical cation salts of chiral bis(2-hydroxypropylthio)ethylenedithioTTF with tetrafluoroborate anions, *CrystEngComm*, 2014, **16**, 5424-5429. **DOI:** 10.1039/c4ce00116h

M. Zecchini, J. R. Lopez, S. Allen, S. J. Coles, C. Wilson, H. Akutsu, L. Martin, J. D. Wallis,* Exo-Methylene-BEDT-TTF and Further Alkene functionalised BEDT-TTF Derivatives: Synthesis and Radical Cation Salts, *RSC Advances*, 2015, **5**, 31104-31112. DOI: 10.1039/C5RA03921E

J. Lopez, H. Akutsu and L. Martin,* Radical-cation salt with novel BEDT-TTF packing motif containing tris(oxalato)germanate(IV), *Synthetic Metals*, 2015, **209**, 188-191. DOI: 10.1016/j.synthmet.2015.07.019

J. R. Lopez, L. Martin,* J. D. Wallis, H. Akutsu, Y. Nakazawa, J-i. Yamada, T. Kadoya, S. J. Coles and C. Wilson, Enantiopure and racemic radical-cation salts of B(malate)$_2^-$ anions with BEDT-TTF, *Dalton Trans.*, 2016, **45**, 9285-9293. DOI: 10.1039/**C6DT01038E**

L. Martin,* A. L. Morritt, J. R. Lopez, H. Akutsu, Y. Nakazawa, S. Imajo and Y. Ihara, Ambient-pressure molecular superconductor with a superlattice containing layers of tris(oxalato)rhodate enantiomers and 18-crown-6, *Inorganic Chemistry*, 2017, **56** (2), 717-720. DOI: 10.1021/acs.inorgchem.6b02708

L. Martin,* A. L. Morritt, J. R. Lopez, Y. Nakazawa, H. Akutsu, S. Imajo, Y. Ihara, B. Zhang, Y. Zhang and Y. Guo, Molecular Conductors from bis(ethylenedithio)tetrathiafulvalene with tris(oxalato)rhodate, *Dalton Transactions*, 2017, **46**, 9542-9548. DOI: 10.1039/C7DT00881C

J. R. Lopez, L. Martin,* J. D. Wallis, H. Akutsu, J.-i. Yamada, S.-i. Nakatsuji, C. Wilson, J. Christensen and S. J. Coles, New semiconducting radical-cation salts of chiral bis(2-hydroxylpropylthio)ethylenedithioTTF, *CrystEngComm*, 2017, **19**, 4848-4856. DOI: 10.1039/c7ce01014a

L. Martin,* A. L. Morritt, J. R. Lopez, H. Akutsu, Y. Nakazawa and S. Imajo, Quasi-Kosterlitz-Thouless molecular superconductor β”-(BEDT-TTF)$_2$[(H$_2$O)(NH$_4$)$_2$Cr(C$_2$O$_4$)$_3$].18-crown-6, *Inorganic Chemistry,* 2017, **56(22)**, 14045-14052. DOI:10.1021/acs.inorgchem.7b02171

Abbreviations, Units and Symbols

BCS	Bardeen, Cooper and Schrieffer Theory
BHM-EDT-TTF	Bis(2-hydroxypropylthio)ethylenedithiotetrathiafulvalene
BHM-BEDT-TTF	*trans*-*vic*-bis(hydroxymethyl)ethylenedithiotetrathiafulvalene
BEDT-TTF or ET	Bis(ethylenedithio)tetrathiafulvalene
clo	4-Oxo-4H-pyran-2,6-dicarboxylic Acid
CTS 3.1	BHM-EDT-TTF.X (X = BF$_4$, ClO$_4$ and PF$_6$)
CTS 3.2	BHM-BEDT-TTF$_2$.Cl(H$_2$O)$_2$
CTS 3.3	BHM-BEDT-TTF.PF$_6$
CTS 3.4	BHM-BEDT-TTF.TCNQ
CTS 4.1	α-(BEDT-TTF)$_2$B$_{R/S}$ [(*R/S*)malate$_2$].(H$_2$O)$_{2.85}$
CTS 4.2	α-(BEDT-TTF)$_2$[B$_S$(*R*-malate)$_2$]
CTS 4.3	β-(BEDT-TTF)$_2$B$_{R/S}$[(*R/S*)mandelate]$_2$
CTS 4.4	Bis(S-mandelato)borate and BEDT-TTF
CTS 4.5	δ/δ’-(BEDT-TTF)$_2$[B$_{R/S}$(glycolate)$_2$]
CTS 5.1	α’’’-(BEDT-TTF)$_{4.5}$[La(dpa)$_3$].(EtOH)$_2$.(H$_2$O)$_n$
CTS 5.1a	α’’’-(BEDT-TTF)$_{4.5}$[Gd(dpa)$_3$].(EtOH)$_2$.(H$_2$O)$_n$
CTS 5.2	α-(BEDT-TTF)$_4$[Gd(dpa)$_3$.H$_3$O.H$_2$O
CTS 5.3	α-(BEDT-TTF)$_5$[Tb(clo)$_3$]
CTS 6.1	β”-(BEDT-TTF)$_2$[(H$_2$O)(NH$_4$)$_2$Cr(C$_2$O$_4$)$_3$].18-crown-6
CTS 6.2	β”-(BEDT-TTF)$_2$[(H$_2$O)(NH$_4$)$_2$Ir(C$_2$O$_4$)$_3$].18-crown-6
dpa	Pyridine-2,6-dicarboxylic Acid Ligand
Ea	Activation Energy
eV	Electron Volts
Hc	Superconducting Critical Field
HOMO	Highest Occupied Molecular Orbital
k	Boltzmann Constant

LUMO	Lowest Unoccupied Molecular Orbital
MS	Mass Spectrometry
NMR	Nuclear Magnetic Resonance
ox	Oxalate Ligand, C_2O_4
Q	Positive Charge on Electron Donor Molecule
SQUID	Superconducting Quantum Interference Device
Tc	Superconducting Critical Temperature
TCNQ	Tetracyanoquinodimethane
T_{MI}	Metal-Insulator Transition Temperature
TTF	Tetrathiafulvalene
TMTSF	Tetramethyltetraselenafulvalene
T_C	Curie Temperature
T_N	Neel Temperature
vdW	van der Waals

Contents List

Chapter 1: Introduction

Chapter 2: Experimental

Chapter 3: Chiral Donor Charge Transfer Salts

Chapter 4: Chiral, Racemic and Diastereomeric Spiroborate Anion Charge Transfer Salts

Chapter 5: Nine-coordinate Lanthanide Anion Charge Transfer Salts

Chapter 6: Racemic Metal Trisoxalate Charge Transfer Salts

Chapter 7: Final Conclusions and Future Work

List of Tables

List of Figures

List of Graphs

Chapter 1: Introduction

1.1 Conductivity

1.1.1 Introduction

The fundamentally important relationship between current, voltage and resistance is Ohm's Law, eqn.1 below:

$$V=IR \quad \text{eqn.1}$$

I, current, is measured in Amperes and is the equivalent of 1 coulomb of charge moving past a certain point every second. So current is the flow of charge carriers per unit of time. V, voltage, is measured in Volts and is a quantitative expression of the potential difference between two points in an electrical field, or the quantity of charge carriers that pass a fixed point per unit of time. The greater the voltage, the greater the flow of electrical current. R, resistance, has units of Ohms and is a quantity that reflects how a material reduces the electrical current flowing through it.

Electrical conduction is the flow of electrons and electron holes (charge carriers) through a materials lattice. If the material has low resistance, then the charge carriers will flow relatively unhindered through the lattice and a large current can be achieved with the same voltage. If the conductor has high resistance to the flow of charge carriers, then a larger voltage will be required to produce an equivalent current.

1.1.2 Resistance

Electrical resistance is a property held by every type of conductor apart from superconductors below their specific critical temperature (T_c), critical current (I_c) and critical field (B_c). It can be explained as the loss of an electrons momentum as it travels through a conducting material. As explained above a charge is transported through a material by the movement of charge carriers. In theory, the wave-like electrons should travel through a materials regular repetitive lattice in a perfectly straight line without any loss in momentum, as would be seen in a theoretical ‘perfect crystal’. However, in reality this is not the case, as every crystal contains defects. Any deviation from the electrons favoured path due to defects will introduce resistance into the system. The electrons are scattered along a zig-zag path due to a large number of collisions with fixed atoms within the conducting materials positive lattice and hence a loss in voltage is observed.

Resistance can be introduced into a material in two different ways. Firstly, through the presence of structural defects within the molecular lattice of the material, examples of these are shown in Figure 1.0. Structural defects are present in every crystals lattice and are unavoidable due to the presence of trace amounts of impurities in the materials synthetic process. One type of structural defect that will occur at isolated atomic positions is a point defect. This is where an atom is missing or is in an irregular place within the lattice and includes self-interstitial atoms – where an atom has forced itself into an interstitial void in the crystal structure. Self-interstitial atoms occur in low concentrations as they highly stress the tightly packed atoms within the lattice. Another point defect is the presence of interstitial impurity atoms, these are much smaller than the bulk atoms in the matrix and can fit into spaces between the atoms of the lattice. Substitutional atoms can lead to point defects and are caused by impurities within the engineering process. They are of similar size to the bulk atoms of the material and hence can fit within the lattice without forcing strain or causing instability of the molecular geometry. Lastly, vacancies within the repeating structure of a crystal can cause resistance. These are empty spaces where atoms should be. Vacancies become more common at higher temperatures as atoms are constantly moving and displacing due to thermal vibrations. All point defects other than vacancies are independent of temperature.

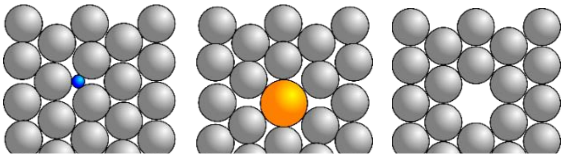

Figure 1.0. Examples of points defects in a crystal lattice. Left: Interstitial impurity. Middle: Self-interstitial. Right: Vacancy.

The second point to consider when discussing the presence of resistance in closed systems is thermal vibrations. Thermal vibrations associated with crystalline solids are based on the individual atoms possessing vibrational motion. At any temperature above absolute zero the atoms within a lattice will possess thermal energy, which is observed as vibrations away from the original equilibrium position. An atom can vibrate through three dimensions, therefore the total thermal energy for N atoms will be 3NkT, where k = Boltzmann constant and T = Absolute temperature. An electron travelling through a crystals lattice will be scattered by collisions with atoms vibrating away from their equilibrium. This scattering of the electrons hinders the path through the material and will cause a loss in the electron's momentum. At higher temperatures atoms will possess more thermal energy and will be displacing further from the equilibrium position, the further an atom moves from its original position, the more likely it is to contact a charge carrier and hence in the case of metallic conductors, electrical conductivity has an inverse temperature dependence.

1.1.3 Band Theory

Conductivity can be justified on a molecular level in solids through band theory, which explains the movement of electrons through a solids lattice via molecular orbital theory. When two atoms form a covalent bond, each of their valence orbitals overlap to form two molecular orbitals. For example, when two hydrogen atoms form a covalent bond, both the 1s orbitals will combine either in phase to give a bonding orbital or out of phase to give an anti-bonding orbital. The result is that two molecular orbitals are formed. A molecule of N atoms forms N molecular orbitals. The bonding orbital is lower in energy than the original atomic orbitals and the anti-bonding is higher in energy. Electrons are fermions and therefore have to obey the Pauli Exclusion Principle; only two electrons of opposite spins can be found in one molecular orbital. The electrons will spin pair into the lowest energy bonding orbital until full and consecutively fill the molecular orbitals of increasing energy. The bonding and anti-bonding molecular orbitals are separated by an energy gap, this prevents the electrons from entering the higher energy orbitals and in the case of a hydrogen molecule they are contained in the lower energy σ_g bonding orbitals. When looking at a molecule containing ten atoms, there will be five bonding orbitals and five anti-bonding orbitals. As more atoms are added the energy gap between the lowest energy bonding and highest energy anti-bonding orbitals increases, but the gap between each individual orbital decreases. When considering a crystal lattice one can assume an infinite number of atoms are covalently bonded, this results in the overlap of an infinite number of atomic orbitals which leads to an infinite number of molecular orbitals that are so closely spaced in energy they can be considered as a continuous band of energy levels. This produces a range of energies the electrons in those molecular orbitals are permitted to enter. Take a line of atoms that each has an available s orbital which overlaps with its neighbours, this will form an s band within a specific range of energies, if those same atoms have p orbitals available to overlap then a p band will be formed. p orbitals lie in a higher energy range than s orbitals of the same valence shell and so there will be a gap of forbidden energies (band gap) between the s and p bands. The electrons in the s band cannot enter the p band and vice versa. In the case of metallic conductors, the bands formed from different atomic orbitals are often so wide in energy they overlap and there are no band gaps. The electrons within the lattice can be thought of as delocalised across the whole lattice evenly.

The band formed from the bonding molecular orbitals acts as the valence band and the band formed from the anti-bonding molecular orbitals acts as the conduction band. When an electrical current is passed through a conducting material, electrons flow from the HOMO in the valence band to the LUMO in the conduction band. A free electron in the conduction band can now begin to move through the band into higher energy levels, carrying the charge through the material. Also, the loss of an electron from the HOMO in the valence band creates an electron ‘hole’ which can then be filled by an electron from the energy level directly below it. So the conduction of electricity can be visualised as the movement of electrons through a band into higher energy levels, or the movement of electron holes through a band into lower energy levels[1].

1.1.4 Metals

Metallic conductivity is the result of an overlap between a partially filled valence band and an empty conduction band. The bands span a wide range of energies and no band gaps are observed. The electrons are then free to move from the valence bands through the conduction bands with little resistance. A stronger interaction between atomic orbitals results in a larger overlap between conduction and valence bands, causing an increase in conducting properties. A metals conductivity will show an inverse temperature dependence due to atomic thermal motion causing resistance to the flow of charge carriers. Structural defects and temperature are the only factors that will affect a metals resistance to the flow of an electrical current[1].

1.1.5 Fermi-Level

The highest occupied molecular orbital at T=0 is termed the Fermi level. At absolute zero, electrons will half fill each available molecular orbital before spin pairing, following the Pauli and Aufbau principles. In a material containing N atoms, if each atom donates one *s* electron, at T=0, the lowest $\frac{1}{2}$N orbitals are occupied. Due to this the Fermi level is often found close to the centre of the valence band. When the valence band is partially full, electrons close to the Fermi level can be promoted to empty levels in the conduction band that are close in energy. The now mobile promoted electrons can then move relatively unhindered through the band. As the temperature is decreased towards absolute zero more electrons will begin to pack closer to the Fermi level, resulting in a large number of electron 'holes' available in lower energy levels within the conduction band. The appearance of more 'holes' allows electrons from energy levels below these to be promoted, increasing conductivity. The explanation of the Fermi level, along with thermal motion, offers a thorough conclusion as to the inverse temperature dependency seen in metallic conductors.

1.1.6 Density of states

The density of states in a conducting material is defined as the number of energy levels in an energy range, divided by the width of the range. As explained above the energy levels within a certain range are not distributed evenly and therefore the density of states is not uniform across a band. This is shown in Figure 1.1. In three dimensions the greatest density of states lie near the centre of a band and the lowest density at the edges. The

1.1.7 Semi-metals

A semi-metal is a material in which there is a very small overlap between the bottom of the conduction band and the top of the valence band at or near the Fermi level, usually due to the fact that both energy bands are very broad. These materials are not good conductors when compared with conventional metals. The band structure is similar to that of semiconductors and insulators in that there is an empty conduction band and a full valence band. Most semi-metals will show temperature independent conductivity at or above room temperature and undergo a semimetal-semiconductor transition as temperature is decreased. Due to the small overlap of valence and conduction bands a semi-metal is thought to have negligible density of states at the Fermi level.

1.1.8 Insulators

An insulating material has a very high resistance to the flow of electrons, such that the net flow of charge carriers is zero. Insulators cannot transport an electrical current due to a full valence band that is separated by a large band gap from an empty conduction band. As the band gap is too large in energy for the electrons to be promoted at normal temperaures and the result is a material in which the charge carriers are stationary. Insulating polymers are commonly used to coat conducting wires to prevent cross connections and short circuits within electrical devices.

1.1.9 Intrinsic Semiconductors

Semiconductors have the same band structure as insulators, however, in this case the band gap between the full conduction band and empty valence band is sufficiently small that the electrons can be thermally excited across it. At high temperatures, the stationary electrons within the valence band possess enough thermal energy to be promoted across the small band gap and into the empty conduction band. The promoted electron is then free to move through the conduction band into higher energy levels and the 'hole' left in the valence band can be filled by an electron from an energy level below. In semiconductors, there is a direct temperature dependency where the conductivity increases as an exponential function of temperature. Unlike metallic conductors, thermal motion of atomic centres play little to no role in the resistance within these systems, the number of mobile electrons present in the conduction band is dependent on only the size of the band gap and temperature. Semiconductors show Arrhenius-type behaviour with regards to their temperature dependent conductivity and the following equation, eqn. 2 is used to calculate the band gap of a semiconducting material:

$$\sigma_T = \sigma_0 \exp(-\Delta E/2K_BT) \quad \text{eqn. 2}$$

σ_T, is the conductivity of the material at a specific temperature. σ_0, is a material specific constant. K_B, is the Boltzmann's constant and ΔE is the band gap of the material. The thermal (activation) energy needed to promote an electron from the valence band into the conduction band is given by $\Delta E/2$. This is due to the formation of two charge carriers for every promoted electron: A mobile electron in the conduction band, and an electron 'hole' present in the valence band. The above equation can be rearranged into graphical form with a gradient equal to $\Delta E/2K_B$.

1.1.10 Extrinsic Semiconductors

Extrinsic semiconductors are achieved by the presence of a specific dopant used in order to create a tailor-made band gap of desired energy. The idea is to dope the semiconductor with elements that contain either less or more valence electrons, creating either electron rich or electron deficient bonds between the dopant and original element. Electron rich bonds will create full energy bands just below the conduction band, called the donor level. The 'donor' electrons are easily promoted into the empty conduction band and can transport the charge through the material. These are known as *n*-type semiconductors.

Electron deficient bonds produce a partially full energy band just above the valence band, known as the acceptor level. Electrons from the full valence band can easily be promoted into the acceptor level. However, the acceptor level is usually discrete due to the small amounts of dopants present in extrinsic semiconductors, therefore transport cannot occur in them. The electron 'holes' left in the valence band allow for the transport of charge. These are known as *p*-type semiconductors.

Germanium and silicon are the most commonly used elements to produce semiconducting materials within information technology. The combination of *n* and *p*-type semiconductors within electronic devices led to the ground-breaking discovery of devices such as LEDs and transistors, without which the modern age of computing could not exist today.

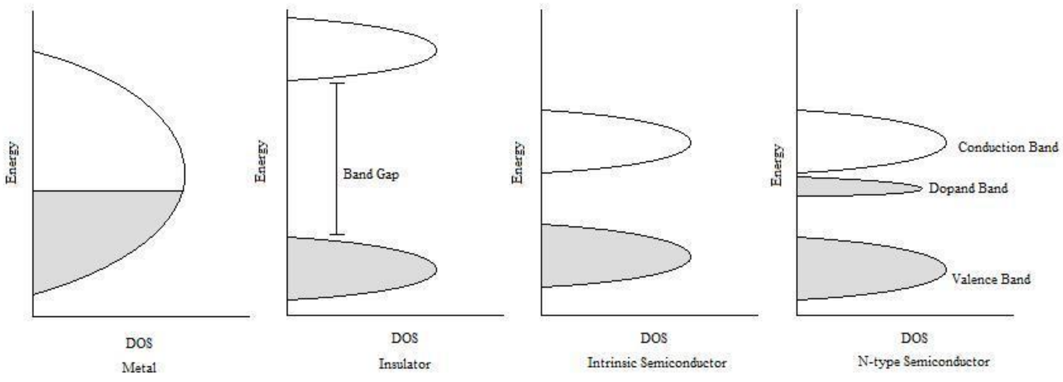

Figure 1.1 Density of states for metals, insulators, intrinsic and N-type semiconductors.

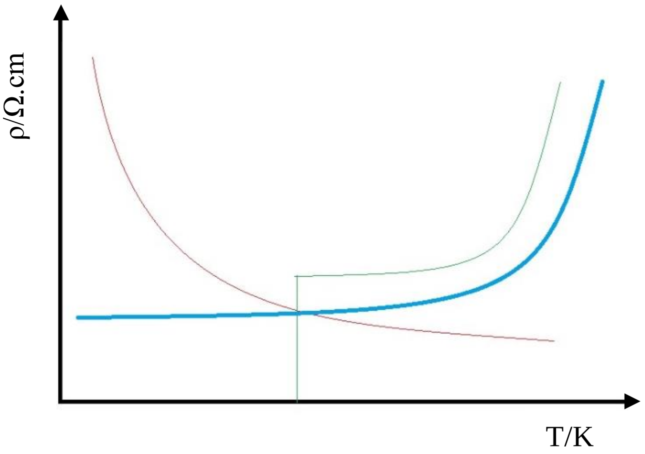

Figure 1.2. Resistivity as a function of temperature for metallic (blue), semiconducting (red) and superconducting (green) materials.

1.2 Superconductivity

1.2.1 Introduction

Superconductors exhibit two main characteristics when within the critical parameters: zero resistance and perfect diamagnetism. This allows for extremely large voltages to be produced with little to no loss in current and also the production of very strong magnetic fields. If the critical parameters, namely temperature (T_c) and external magnetic field (H_c) are not met then superconductivity will be suppressed. Above the critical temperature the material usually will behave as a conventional metal and is often an unremarkable conductor. Superconductors are grouped into two types: Type I (soft) and Type II (hard), depending on their response to an external magnetic field of increasing strength. Resistivity as a function of temperature is shown in Figure 1.2

1.2.2 History

In 1911 Hieke Kamerlingh Onnes observed the resistivity of liquid mercury dropping to an almost immeasurably low point (Figure 1.3) when cooled in liquid helium[2]. It had been predicted that metallic elements would become better conductors at low temperatures before this, however zero resistance was not previously thought possible.

This was due to Ohm's law: I = V/R, stating that if zero resistance was reached the current would tend to infinity, which was not observed by Onnes in his experiments. So it was thought that the magnetic field within a superconducting sample below its critical temperature must be ‘trapped’ within it. Walter Meissner and Robert Oschenfeld in 1933 found this not to be the case. Instead, the magnetic field is completely expelled by a material in the superconducting state[3].

Since the discovery of superconductivity in liquid mercury, initial efforts were focused around elemental and binary metal alloys and it was found that over half of the elementary compounds undergo a superconducting transition. The record T_c for this group of materials was reached in 1973 with Nb_3Ge ($T_c = 23K$)[4]. In 1986 Bednorz and Muller sparked interest when results were published claiming the observation of superconductivity at around 30K in ceramic compounds of the La-Ba-Cu-O system[5]. These results were quickly reproduced elsewhere and high T_c superconductivity rapidly became an area of huge interest. It is apparent that the Cu-O planes in the materials perovskite structure played an important role in the transition to

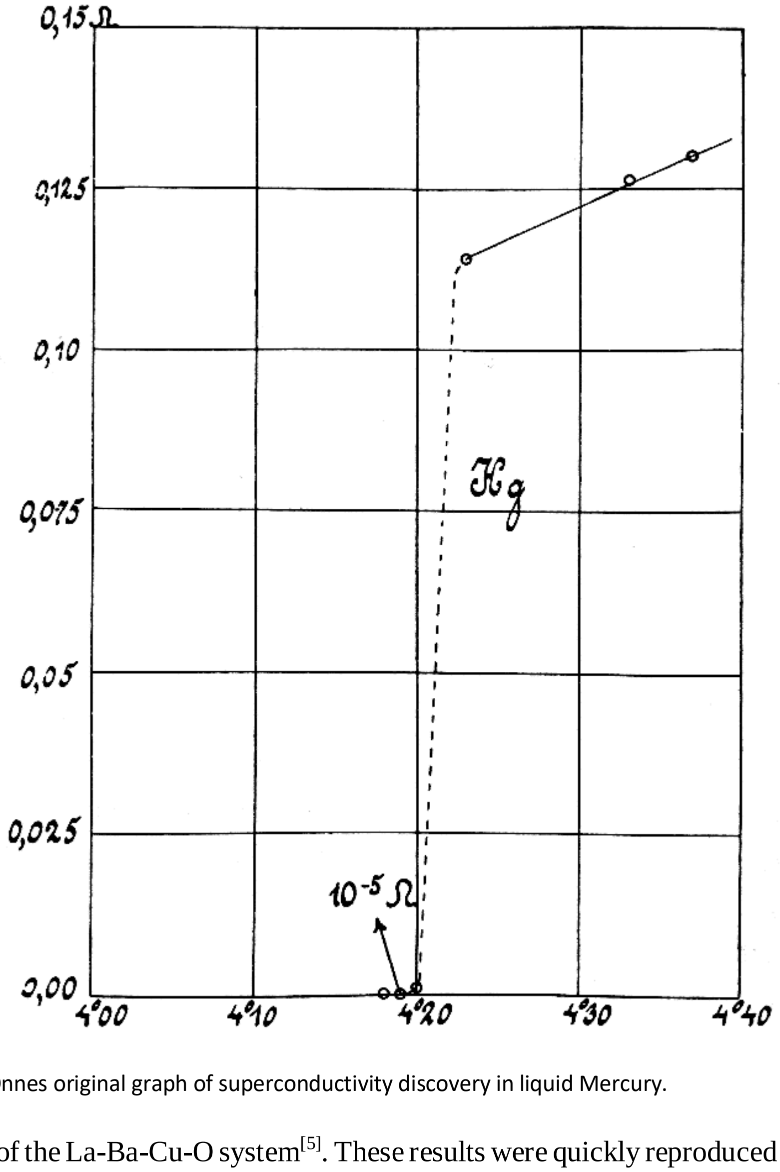

Figure 1.3. Onnes original graph of superconductivity discovery in liquid Mercury.

superconductivity and as such the research focused mainly on copper oxide materials. In 1987 a T_c of 93K was achieved in the copper oxide $YBa_2Cu_3O_{6+x}$[6], the significance of this finding was that the critical temperature could be reached by cooling with liquid nitrogen. A thallium cuprate, $Tl_2Ba_2Ca_2Cu_3O_{10}$ held the highest T_c at 125K[7]. The record T_c currently stands at 156K in the $HgBa_2Ca_2Cu_3O_{8+\delta}$ system under pressure[8] (Figure 1.4).

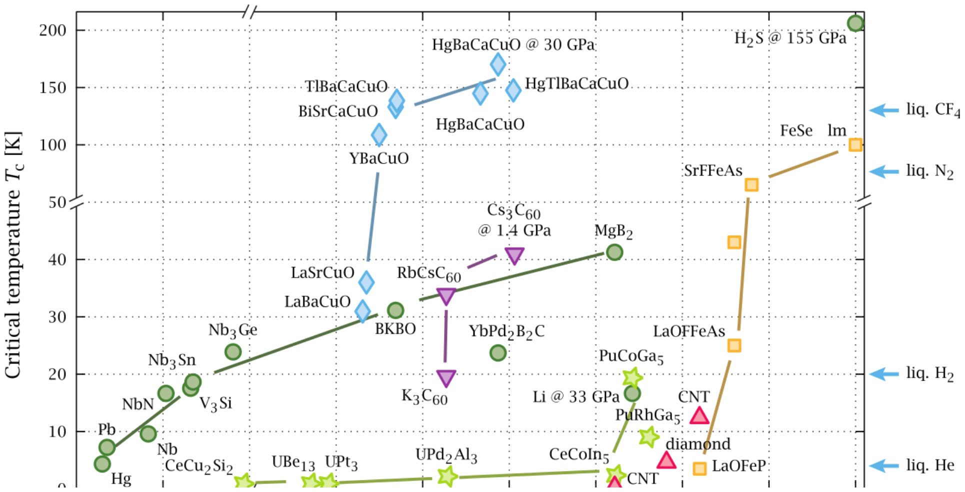

Figure 1.4. Timeline of superconductor discovery. Pia Jensen Ray. Master's Thesis Niels Bohr Institute, Faculty of Science, University of Copenhagen. Copenhagen, Denmark, November 2015. DOI:10.6084/m9.figshare.2075680.v2.

Shortly after the discovery of the production of fullerites in 1991 (quantities of fullerenes large enough to allow traditional solid-state experiments) it was found that the intercalation of certain alkali-metals in solid C_{60} (fullerides) produced materials that undergo a superconducting transition. A T_c of 33K at atmospheric pressure was observed for the $RbCs_2C_{60}$ fulleride and under pressure Cs_3C_{60} enters the superconducting state at T_c = 40K[9]. The interest in these materials is due to there being a completely new class of superconductors with a large T_c. The origin of superconductivity in these materials is not fully understood but it is believed that they are *s*-wave BCS-like (*for BCS theory see section 1.2.3*) superconductors driven by traditional electron-phonon effects although there is no conclusive evidence that this is the case.

In 2001 the discovery of superconductivity at T_c = 39K in MgB_2 renewed interest in high T_c conventional phonon-mediated superconductivity[10]. More recently in 2006 the discovery of superconductivity in the iron-pnictide, LaFePO at 4K has given birth to a large class of new superconductors[11]. Iron-pnictides have a layered structure of FeAs or FeP and it is thought the magnetic behaviour from 3*d* electrons is closely related to the superconductivity. So far the highest T_c in this class of superconductors was reached in 2008 and stands at 26K in $LaFeAsO_{1-x}F_x$[12]. Unlike the high T_c copper-oxide superconductors, the electronic and magnetic properties of iron-based superconductors are well understood and it is hoped they might provide a route to explaining the origin of unconventional Type II superconductivity. It had been stated previously by Bill Little that the superconducting state in polymeric organic conductors could theoretically support critical temperatures approaching and surpassing room temperature[13]. In 1980, Klaus Bechgaard and Denis Jerome synthesised the first organic superconductor in the form of a charge transfer salt with the formula $(TMTSF)_2PF_6$ with a T_c of 0.9K at 12kbar[14], (TMTSF = Tetramethyltetraselenafulvalene). This sparked a major interest in the synthesis of molecular radical cation salts. The first ambient pressure organic superconductor was synthesised soon after, $(TMTSF)_2ClO_4$ with a T_c of 1.3K[15]. Since then, many charge transfer salts have been prepared in the search for the superconducting ground state, however a large number of interesting and unexpected properties have since been discovered in these systems, including the first paramagnetic superconductor[16].

Very recently in 2015 it was discovered that hydrogen sulphide (H_2S) undergoes a superconducting transition when under high pressure[17]. The major significance of this finding was that the recorded T_c was 203K, only 70 degrees below room temperature. Under conventional BCS superconducting theory, it is thought that lighter elements can oscillate at a higher frequency, therefore giving rise to electron-phonon interactions at higher temperatures. Since superconductivity in elemental hydrogen has eluded scientists so far, efforts in this specific area are now focused around hydrogen rich materials.

1.2.3 BCS Theory

John Bardeen, Leon Cooper and Robert Schieffer earned a Nobel prize in physics in 1972 for their research into the electronic behaviour of superconductors below the critical temperature[18]. BCS theory offers a reasonable explanation for the macroscopic quantum phenomena of superconductivity through the existence of coupled electrons (Cooper pairs) travelling through a materials positive lattice. The idea of coupled electrons being prevalent in producing superconductivity was first proposed by Frohlich in 1950[19].

An electron travelling through a cationic lattice will experience a slight attraction to a positive ion which in turn distorts the lattice around it, creating an area of increased positive charge density. A second electron at the same distance from the positive ion in the lattice is attracted to the charge distortion (phonon). This creates an electron-phonon-electron interaction overcoming electron-electron repulsion and the two electrons are indirectly attracted to one another and condense to form a Cooper pair. As the Cooper pair moves through the lattice, the leading electron causes an increase in positive charge around itself and the trailing electron is attracted by this. If the energy required to condense the electrons into Cooper pairs is less than the energy of thermal vibrations of the lattice, then the electrons will stay bound and the material will enter the superconducting state.

Cooper pairs are more stable than a single electron and so experience less scattering from lattice vibrations. BCS theory also states that all Cooper pairs in a lattice are correlated which constitutes a system that functions as a single entity. This suggests that for one pair of Cooper electrons to be scattered, they would all have to be.

Experimental evidence to support BCS theory in Type I superconductors was shown through the isotope effect[20], in which the critical temperature, T_c, of a superconductor is proportional to the reciprocal of the square root of the elements mass number, M.

$$T_c \propto \frac{1}{\sqrt{M}}$$

eqn. 3

Eqn. 3 suggests that the transition to superconductivity is not purely electronic and involves a rearrangement of the lattice. However, when changing from O^{18} to O^{16} in the Type II superconducting ceramic cuprates mentioned above, there was no apparent isotope effect observed. It is thought that phonons may play a part in the electrical behaviour of Type II superconductors however, no credible theory that explains all the experimental data has yet emerged.

A material that shows good electrical conductivity at room temperature proves that its electrons experience minimal interactions with the positive lattice. Hence these materials will not form superconductors as the formation of electron-phonon interactions are much less favourable. Materials with high resistance at room temperature exhibit this property because the electrons experience a strong interaction with the cationic lattice, this suggests that at low temperatures it is more favourable for Cooper pairs to form and superconductivity to be observed.

1.2.4 Meissner Effect

Walter Meissner and Robert Oschenfeld measured the magnetic flux distributions of tin and lead while cooling to below their T_c in an external magnetic field. They found that at the transition from metal to superconductor the materials spontaneously became perfectly diamagnetic[3]. They completely expelled the external field cancelling all magnetic flux inside the material. In the metallic ground state the magnetic field will pass through the material, however when the critical temperature is reached a magnetic field of negative and equal flux density to the applied field is produced and results in the complete expulsion of the magnetic field from the material. This property is known as the ‘Meissner Effect’ and can be demonstrated experimentally as the act of levitating a superconducting sample above a magnet (Figure 1.4).

Figure 1.4. Example of Meissner effect.

1.2.5 Magnetic Properties of Superconductors

Another way to suppress superconductivity in a material below its Tc is through the application of an external magnetic field. It was stated previously that a superconducting sample will spontaneously become a perfect diamagnet due to the condensation of free electrons into Cooper pairs. However, when an external critical field, H_c is reached, the internal magnetic field of a superconductor will behave in two different ways. Below H_c the perfect diamagnet will express an internal field of negative flux density equal to the applied field (Figure 1.6). Above H_c superconductivity is lost and the material returns to the normal state, regardless of temperature.

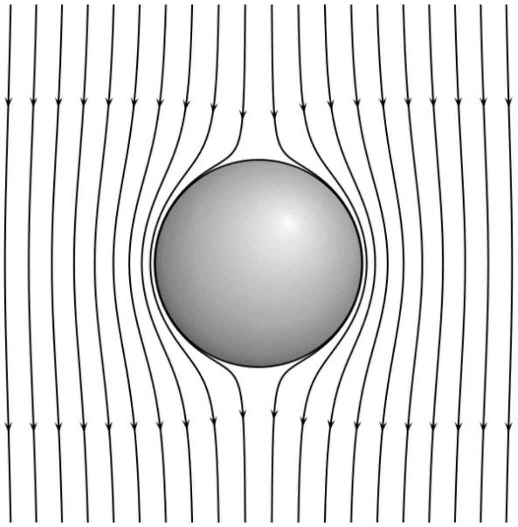

Figure 1.6. Magnetic fields around a material in the superconducting state. © 2010 Geek3 / GNU-FDL, commons.wikimedia.org/wiki

1.2.6 Type I Superconductors

Type I superconductors will completely expel an external magnetic field up to a critical field, H_c. As the external field strength is increased the internal field of the superconductor remains diamagnetic and $-M = H$, where M is magnetisation of the sample and H is the external field. When the critical field is reached, M falls suddenly to zero as the external field enters the sample and superconductivity is lost. Elemental superconductors, such as Lead, Mercury and Tin are type I superconductors.

1.2.7 Type II Superconductors

As in Type I superconductors, -M = H up to a critical field, H_{c1}. It is at this critical field the behaviour differs to Type I superconductivity. At H_{c1}, the magnetic flux of the applied field will begin to enter the sample however, not uniformly. The flux enters the material in the form of vortices which concentrate the external field into localised areas and shield the bulk of the sample from the external field. The material is in the mixed ‘vortex’ or ‘Abrikosov’ state and superconductivity is not suppressed. As the external field is increased a second critical field, H_{c2} is reached. Between H_{c1} and H_{c2} the amount of magnetic flux entering the material increases until the magnetisation of the sample reaches zero and superconductivity is lost (Figure 1.7). All organic and high T_c superconductors are type II. By doping lead with 3% indium it is possible to achieve the change from type I to type II superconductivity.

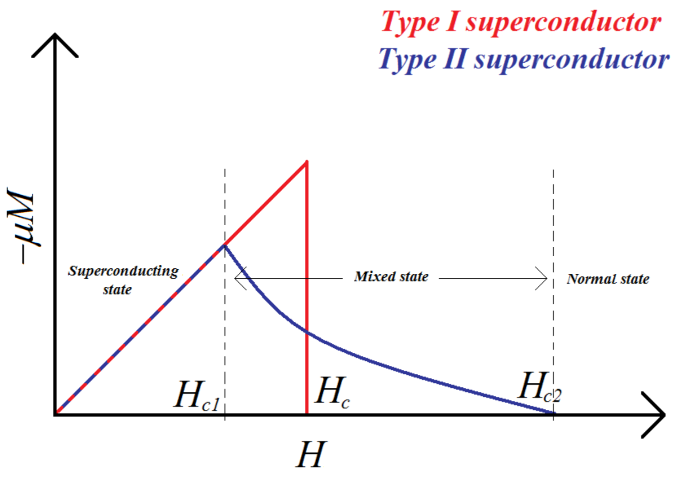

Figure 1.7. Magnetic behaviour of Type I and Type II superconductors[21]

1.2.8 Applications

A superconducting wire can transport huge currents over long distances, provided the wire is constantly cooled to below its critical temperature. However, it is the consequential magnetic field that is produced by the large density of charge carriers moving through a superconducting coil that provides the largest applications in commercial, medical and private industries.

Some of the strongest electromagnets known are produced by superconducting wires and although they must be constantly cooled to below the critical temperature to produce the magnetic fields, which can be expensive, there is very little loss of thermal energy through dissipation. So oftentimes they are cheaper to run than conventional room temperature electromagnets. Superconducting magnets are found in MRI machines, NMR spectrometers, mass spectrometers and particle accelerators.

Japans high speed MagLev (magnetic levitation) trains utilise the Meissner effect in order to suspend a train carriage slightly above a track, allowing for no friction between guideway and vehicle[22]. High speeds can be reached and as there is no conventional fossil fuel burning engine present, it is a much more cost effective and environment friendly way to travel long distances.

1.3 Magnetism

1.3.1 Introduction

A compelling property of highly ordered solid state materials is that the characteristics of individual atoms or molecules can interact cooperatively throughout the lattice when an external force is applied. Cooperative effects can occur for the response of a crystal to mechanical stress, electrical or magnetic fields. Such properties have been widely manipulated to produce a range of materials with huge commercial and industrial importance.

A magnetic field produces lines of force that will penetrate a material that is placed within it, the density of the lines produced from the magnetic field is known as the magnetic flux density, H and is related to magnetic field, B and the permeability of free space, μ_0 by the following equation, eqn. 4:

$$B = \mu_0 H \quad \text{eqn. 4}$$

A magnetic material will repel (diamagnetic) or increase (paramagnetic) the flux density of the magnetic field as it flows through it. The magnetic field flowing through the material while within the external field is termed its *magnetisation,* M and the magnetic flux density can now be expressed in eqn. 5 as:

$$B = \mu_0 (H+M) \quad \text{eqn. 5}$$

Magnetisation is more commonly expressed as magnetic susceptibility, χ, where $\chi = M/H$

1.3.2 Diamagnetism

A certain amount of diamagnetism is associated with every material as it is a property expressed through the existence of paired electrons. Diamagnetism is fundamentally a very weak property and is difficult to observe if other effects are present, however a perfect diamagnet will completely repel an external magnetic field, reducing the magnetic flux density of the applied field to zero within the sample. Atoms or molecules with closed electronic shells at lower energy than the Fermi Level are diamagnetic.

1.3.3 Paramagnetism

The presence of unpaired electrons within a material gives rise to paramagnetism. A simple paramagnet will have randomly orientated dipoles at different centres within the material, the application of an external magnetic field will cause the magnetic moments on each centre to begin to align with the field and consequently with each other. As the moments begin to align the magnet will be attracted to the applied field. The thermal energy possessed by the paramagnet however, prevents the magnetic moments from aligning perfectly. In the absence of an applied magnetic field this thermal randomization causes the dipoles on different centres to align randomly and hence no long-range magnetisation is retained by the material. This inverse temperature dependence is expressed by the Curie-Weiss law:

$$\chi_m = \frac{C}{T - \theta}$$

eqn. 6

Where χ_m is the molar susceptibility [(χ/specific gravity) x M_r], C is the curie constant, T is temperature in Kelvin and θ is the Weiss constant. A plot of $1/\chi$ against temperature will give a straight line of gradient 1/C and a value of θ in units of Kelvin at the X intersect. A simple paramagnet will have a Weiss constant of zero and will have independent magnetic behaviour at high temperatures. In respect to metal complexes, the isolated metal centre and its associated dipole acts as a small magnet producing its own magnetic field. If the material contains the same metal complex then each magnet will produce a magnetic field of equal magnitude, with thermal motion causing the orientation of each independent field to be random.

The Curie constant, C, is related to the number of unpaired spins per mole and to the spin-only magnetic moment. Orbital angular momentum can be neglected when calculating the magnetic moments for first row transition elements due to the lifting of the fivefold degeneracy of the 3*d* orbitals. Leaving the equation below.

$$\mu_s = g\sqrt{S(S+1)} \quad \text{eqn. 7}$$

S, the spin quantum number describes the angular momentum of an electron, g is a constant which for a free electron has the value 2.00023 and μ_s, the spin only magnetic moment is in Bohr magnetons (B.M). For heavier metal ions contributions from the orbital angular momenta are greater and may need to be considered. When calculating magnetic moments for the lanthanide series the total angular momentum of the electrons, J, is used in equation 9.

$$J = L + S \quad \text{eqn. 8}$$

$$\mu = g\sqrt{J(J+1)} \quad \text{eqn. 9}$$

Where L is the orbital angular momentum, S is the spin angular momentum and J, total angular momenta is the vector sum of L and S. This can lead to large magnetic moments for *f* shells that are more than half full.

1.3.4 Ferromagnetism

Ferromagnetic materials exhibit a long-range ordering phenomenon which causes the dipoles on each atomic centre to align parallel with each other in a region termed a domain. The short-range exchange interactions present in a ferromagnet stem from electron-electron repulsions and initially keep neighbouring moments aligned parallel with respect to one another, however, long range magnetic-dipole interactions also occur, and these tend to align the spins anti-parallel. This results in localised domains of equivalent spin alignment within the lattice. However, each domain is aligned randomly with respect to the next. This results in a net cancellation of the individual magnetic moments and at temperatures high above the Curie temperature the material acts as a simple paramagnet. It is only at or approaching the Curie temperature that the thermal randomisation slows enough to allow the domains to align parallel and the moments add up constructively to exhibit a net magnetic moment. In order to quantify this behaviour, see again the Curie-Weiss law, eqn. 6.

The sign of θ will give an indication of the short-range exchange interactions present in the material above its specific long range ordering temperature. A positive value suggests ferromagnetic coupling. A ferromagnet at high temperature will have domains randomly aligned, like a simple paramagnet. However, when the sample is cooled the adjacent domains throughout the lattice align themselves parallel with respect to one another. Plotting susceptibility against temperature will show a sharp rise in susceptibility at the ordering temperature, the Curie temperature (T_C), as the material becomes strongly magnetized. The molar susceptibility of a ferromagnet at temperatures far above the Curie temperature follows the Curie-Weiss law with a positive Weiss constant.

A particularly interesting and useful property of ferromagnets is an asymmetry in the magnetisation as a function of field that leads to the ability to retain magnetisation (information) when the external field is removed. This is known as hysteresis and is explained as a ferromagnets magnetisation as a function of external field strength. When the ferromagnet is placed in an external field of zero, H_0, the domains are aligned randomly due to thermal energy. As the external field is increased the materials magnetisation follows a non-linear path to reach its magnetic saturation, M_s, due to the alignment of all domains. If the external field is then reduced back to zero the material does not follow the initial curve as some magnetisation is retained by the material, this value of M_r is known as the remnant magnetisation. In order to drive the magnetisation of the ferromagnet back to zero the external field must be decreased to a value, H_c, known as the coercive field. This is the point at which the domains align themselves randomly again and the magnetic memory retained by the material is lost. Ferromagnets can have varied values for H_c and M_r, those with high values for both are termed hard magnets and those with lower values termed soft magnets.

1.3.5 Applications of Ferromagnets

Many applications have been found for ferromagnets, mostly due to the hysteretic behaviour explained above, but also because they are a form of permanent magnet. Hard magnets are used due to their ability to retain information with large values of coercivity and remnantisation, such as magnetic tape in audio cassettes, hard disks or drives, credit cards and permanent magnets. Soft magnets are used as electromagnets, in the core of transformers and in motors or electrical generators. This is due to their low coercivity which reduces the energy loss associated with hysteresis.

1.3.6 Antiferromagnetism

Antiferromagnetism is a property associated with materials whose unpaired electrons will spontaneously align anti-parallel with one another below a specific temperature, the Neél Temperature, T_N. Above this temperature the material will act as a simple paramagnet with a negative Weiss constant. The independent spins will tend to align with an external magnetic field, however if the temperature is increased far enough thermal randomisation dominates and no magnetic moment is observed. When the temperature is decreased to below T_N the spins will align themselves antiparallel to their neighbour, gradually cancelling the magnetisation in the material. However, in reality antiferromagnets always contain impurities and therefore the net magnetisation will never reach zero.

1.3.7 Ferrimagnetism

Ferrimagnetism is closely linked to antiferromagnetism, with an internal force tending to align spins anti-parallel with one another in the presence of an applied magnetic field. However, in this case the neighbouring spins are of different magnitude, i.e a different number of electrons. The effect can be interpreted as two competing ferromagnetic sublattices and the magnetic behaviour is characterised in the same way as ferromagnets. In order to distinguish ferromagnetic behaviour from ferrimagnetic it is important to look at magnetic data over a large range of temperatures. Figure 1.8 shows the orientation of magnetic moments in different magnetic materials.

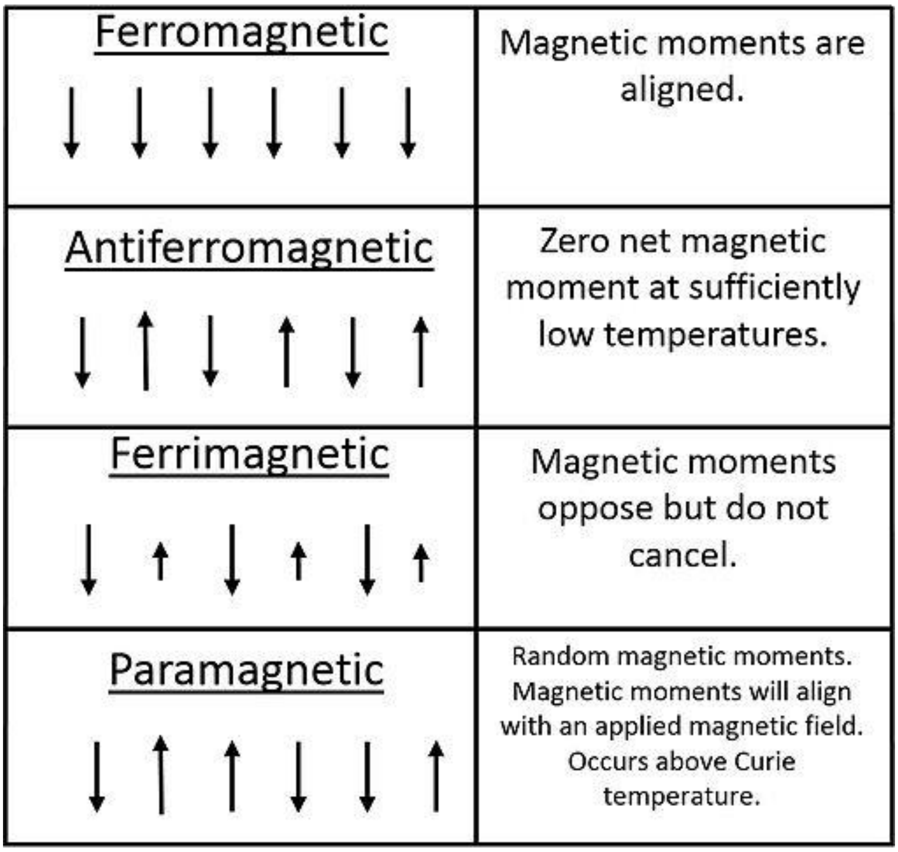

Ferromagnetic ↓ ↓ ↓ ↓ ↓ ↓	Magnetic moments are aligned.
Antiferromagnetic ↓ ↑ ↓ ↑ ↓ ↑	Zero net magnetic moment at sufficiently low temperatures.
Ferrimagnetic ↓ ↑ ↓ ↑ ↓ ↑	Magnetic moments oppose but do not cancel.
Paramagnetic ↓ ↑ ↑ ↓ ↓ ↑	Random magnetic moments. Magnetic moments will align with an applied magnetic field. Occurs above Curie temperature.

Figure 1.8. Orientation of magnetic moments in magnetic materials.

1.4 Charge Transfer Salts

1.4.1 Introduction

Charge transfer salts have been used widely to produce multifunctional molecular conducting materials. Particularly, organic-inorganic hybrids have attracted attention from solid-state chemists and physicists as a route to study the origins and behaviour of organic superconductivity. The two moieties crystallise in separate stacks and the stack segregation throughout the lattice produces materials in which the properties of each component can be expressed as separate characteristics, allowing for the production of multifunctional materials. The majority of conducting molecular charge transfer salts contain the TMTSF, TTF (Figure 1.9) or BEDT-TTF chalcogenides as the organic electroactive unit, however organic conductors have also been derived from several different organic electron donor molecules, including DMET, MDT-TTF, BEDO-TTF and metal-organic acceptor complexes $[M(dmit)_2]^{2-}$. These donors can adopt a range of packing motifs and the lattice formation is heavily controlled by non-covalent interactions and charge compensation between donor and anion. Therefore, a large number of anions of differing size, shape and charge can be co-crystallised with organic donors to produce a huge number of new materials with a wide range of properties. The largest and most interesting group of organic conductors and superconductors has arisen from the BEDT-TTF (Figure A) donor molecule due to its ability to adopt an extended range of packing modes and the expression of distinguished electronic properties including superconductivity.

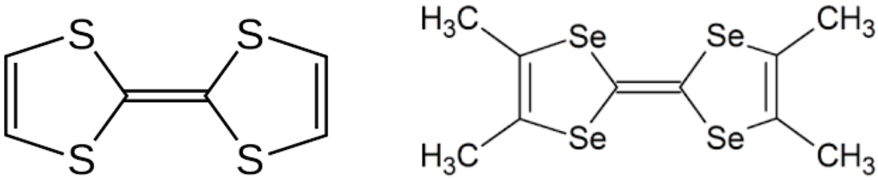

Figure 1.9. Right: TTF, tetrathiafulvalene and Left: TMTSF, (tetramethyl)tetraselenafulvalene organic donor molecules.

1.4.2 History

The synthesis of the electron acceptor tetracyano-p-quinodimethane (TCNQ) in 1960[23], the electron donor tetrathiafulvalene (TTF) in 1970[24] and their subsequent combination in 1972 led to the discovery of the π-molecular donor-acceptor complex TTF-TCNQ[25]. The material conducts along the stacking axis and the conductivity increases with decreasing temperature to 10^4 Ω.cm^{-1} at around 60 K, below which a metal-insulator transition occurs due to lattice distortions and localisation of the conducting electrons. The discovery and characterisation of this material kick-started a serious investigation into the synthesis of synthetic metals.

In 1976 the first organic superconductor was synthesised by Bechgaard *et al.*, $(TMTSF)_2PF_6$ (Figure 1.10). The material shows metallic behaviour at ambient pressure (<10^5 Ω.cm^{-1}) and a sharp metal- insulator antiferromagnetic ordering transition occurs at 15 K, forming a Mott-Hubbard insulator. A temperature drop to 0.9 K and a hydrostatic pressure of 12 kbar suppresses the antiferromagnetic change and leads to a superconducting transition[14]. The Bechgaard salts of formula $(TMTSF)_2X$ (X = e.g PF_6^-, SbF_6^-, ClO_4^-) afforded the first isostructural families of metallic and superconducting charge transfer salts.

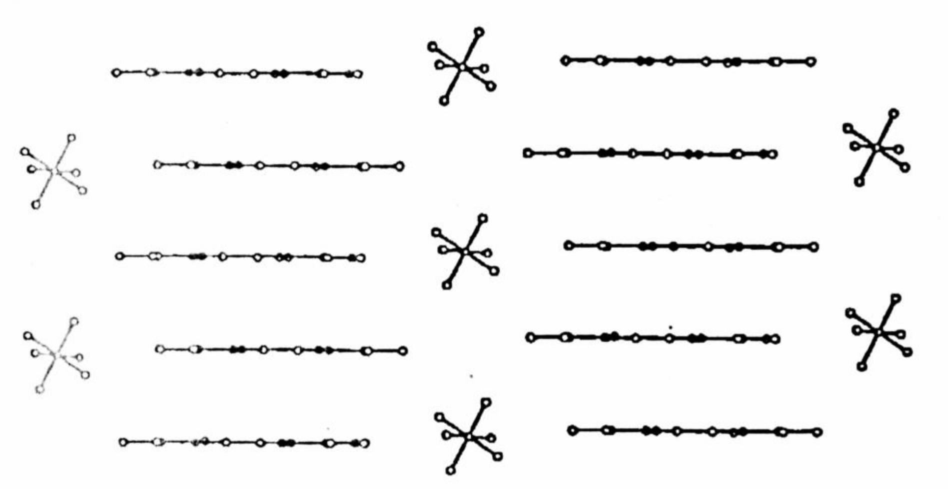

Figure 1.10. TMTSF.PF_6 crystal structure showing BEDT-TTF stacks[26].

Since then a number of organic superconductors have been synthesised and are summarised in Table 1.0 below[27]. T_c values have increased to around 14 K.

Organic Superconductor	**Tc / K**
$\text{(TMTTF)}_2\text{ClO}_4$	1.4
$\theta\text{-(ET)}_2\text{I}_3$	3.6
$\alpha\text{-(ET)}_2\text{KHg(SCN)}_4$	0.3 (1.2 at 1.2 kbar)
$\beta''\text{-(ET)}_2\text{SF}_5\text{CH}_2\text{CF}_2\text{SO}_3$	5.3
$\kappa\text{-(ET)}_2\text{Cu[N(CN)}_2\text{]Cl}$	12.8 (at 0.3 kbar)
$\kappa\text{-(ET)}_2\text{Cu[N(CN)}_2\text{]Cl}$ deuterated	13.1 (at 0.3 kbar)
$\kappa\text{-(ET)}_2\text{Cu[N(CN)}_2\text{]Br}$ deuterated	11.2
$\kappa\text{-(ET)}_2\text{Cu(NCS)}_2$	10.4
$\kappa_H\text{-(ET)}_2\text{Cu(CF}_3)_4\cdot\text{TCE}$	9.2
$\kappa_H\text{-(ET)}_2\text{Ag(CF}_3)_4\cdot\text{TCE}$	11.1

Table 1.0. Summary of organic superconductors

Charge transfer salts are an appealing route to multifunctional materials and in 2010 the first example of ferromagnetism and metallic conductivity in the same material was achieved[28]. This salt contained the BEDT-TTF molecule co-crystallised with the bimetallic oxalato complex $[Mn^{II}Cr^{III}(C_2O_4)_3]^-$. Throughout the material the anion forms polymeric sheets in which the metal centres can cooperatively interact to produce a ferromagnetic material.

Anionic coordination complexes are an obvious direction in which to focus when attempting to prepare bi-functional materials through the synthesis of charge transfer salts. The metal complexes can be carefully designed through the choice of different metal centres or ligands, to produce compounds displaying a variety of electronic properties. The oxalato metallates $\{[M(C_2O_4)_3]^{n-}\}$ have afforded a large family of charge transfer salts. Included in this group are a number of superconducting materials[29] and importantly the first example of a paramagnetic superconductor[16]. Subtle changes in anion size or shape can produce large changes in the properties observed[30]. The metal trisoxalate molecule contains a chiral axis; these salts and other charge transfer salts containing chiral anions will be discussed in further detail in section 1.5.3.2.

1.4.3 *Bis(ethylenedithio)tetrathiafulvalene – BEDT-TTF*

Tetrathiafulvalenes in general are chemically stable and can be synthesised at close to standard conditions (room temperature and pressure). BEDT-TTF was synthesised by Mizuno *et al.* in 1982[31], the structure is shown below in Figure 1.11. The symmetrical central TTF unit is flanked either side by 1,3-dithiol six- membered rings which provides more scope for potential π orbital overlap of sulphur atoms and leads to advanced conducting properties when compared with tetrathiafulvalene (TTF). The terminal ethylene groups adopt non-planar geometry while the central unit remains relatively flat. Neutral BEDT-TTF^0 is slightly bent with respect to the central portion and the molecule will flatten on oxidation. The central C=C is extremely sensitive to charge transfer and the bond length increases on oxidation. This allows for an estimation of the molecular charge by calculating the difference in bond lengths of the central TTF unit using the following equation[32], where δ is the average bond length and Q is the charge estimation.

$$\delta = (b + c) - (a + d)$$

$$Q = 6.347 - 7.463\delta \quad \text{eqn. 10}$$

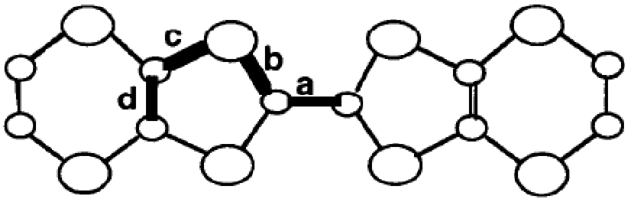

Figure 1.11. BEDT-TTF with Central TTF bonds labelled for charge estimations[32].

It is noted that the radical cation can adopt a wide variety of packing modes owing to the flexibility of the terminal ethylene groups, while the central TTF portion remains relatively planar. The 'twist' confirmation is observed when both ethylene groups are displaced either side of the plane of the molecule defined by the co-planar sulphur and inner carbon atoms of the six-membered ring, however one group is always displaced to a lesser degree. When both sides of the molecule show twist confirmations, two forms can exist. The 'eclipsed' form, where the ethylene carbon atoms on either side of the molecule are displaced to the same side of the plane and hence eclipse each other when viewed along the long axis of the molecule, and the ‘staggered’ confirmation where the ethylene groups have opposed orientations with respect to the central TTF plane. A boat confirmation can also exist where both ethylene groups are displaced to the same side of the plane of the molecule. Neutral BEDT-TTF has one side in a twist confirmation and one side in a boat confirmation.

1.4.4 BEDT-TTF Packing Motifs

The wide variety of electronic ground states and the consequential number of properties assigned to charge transfer salts of the BEDT-TTF donor molecule is due to the array of packing motifs that have been observed. Each results in different intramolecular interactions and characteristic networks of S…S contacts. The band structure formed throughout donor stacks within each motif give rise to markedly different conducting properties, superconducting transition temperatures and magnetic behaviour of the mobile π electrons. The most commonly observed phases are discussed here along with the characteristic conducting properties.

The alpha, α, phase adopts a herringbone arrangement with the donors weakly dimerised. Adjacent layers are orientated orthoganol to each other. This phase usually produces a semi-metallic band structure indicating a small overlap of valence and conduction bands (Figure 1.12).

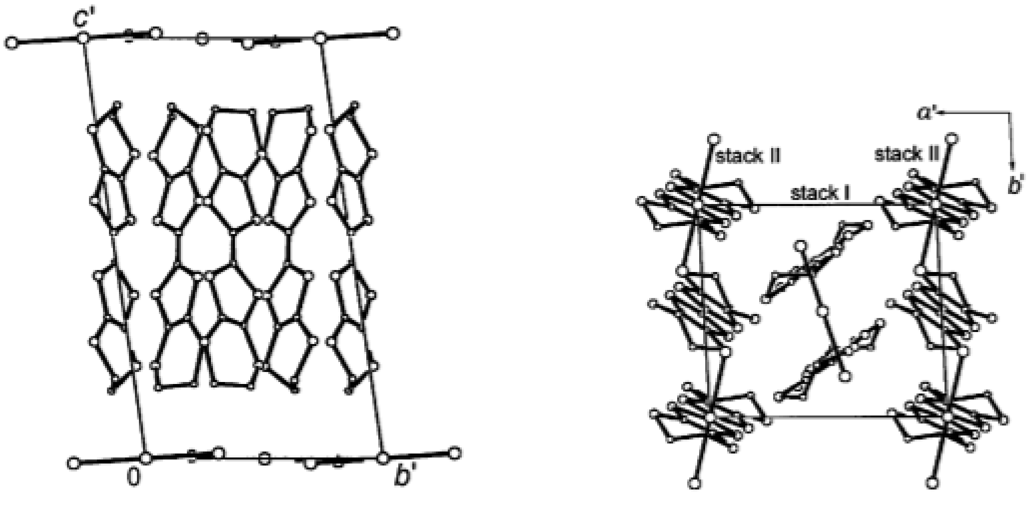

Figure 1.12: Crystal structure of α-(ET)$_2$I$_3$ along the *a* (left) and *c* (right) axes[28].

The delta, δ, phase consists of mixed stacks of the donor and anion layers, parallel to the *ab* plane. This phase usually exhibits metallic behaviour with a metal-insulator transition on cooling (Figure 1.13).

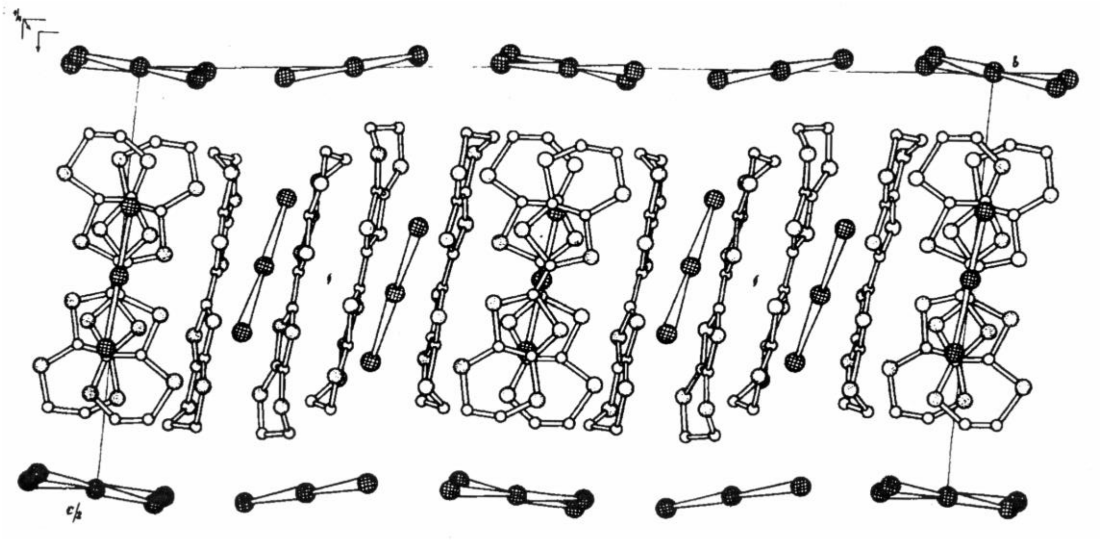

Figure 1.13. Crystal structure of δ-(ET)I_3 viewed along the *a* axis[26].

In the beta, β, phase, within stacks the molecules are strongly dimerised and closest S…S contacts are between stacks (Figure 1.14). This phase tends to produce 2-D electrical properties. A modified beta phase has been observed with linear anions (I_3, AuI_2, IBr_2) producing quasi 1-D conductors with pairs of ET (ET = BEDT-TTF) molecules more strongly dimerised[33]. This phase has produced ambient pressure superconductors and applying hydrostatic pressure reduces the Tc of superconductors.

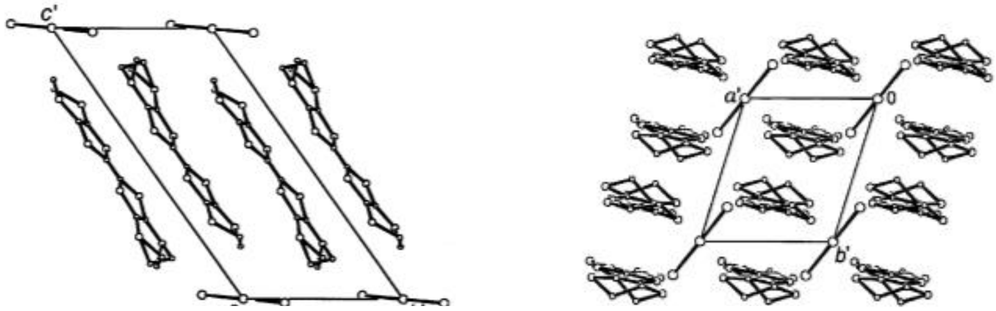

Figure 1.14. Crystal structure of β-$(ET)_2I_3$ along the *c′* (left) and *a′* (right) axes[34].

The beta'', β'', phase is similar however the dimers carry effectively half-filled flat bands producing Mott insulators. The beta'' phase results in quasi 2-D metals with layers of adjacent stacks almost coplanar and at low temperatures this can give rise to superconducting properties (Figure 1.15).

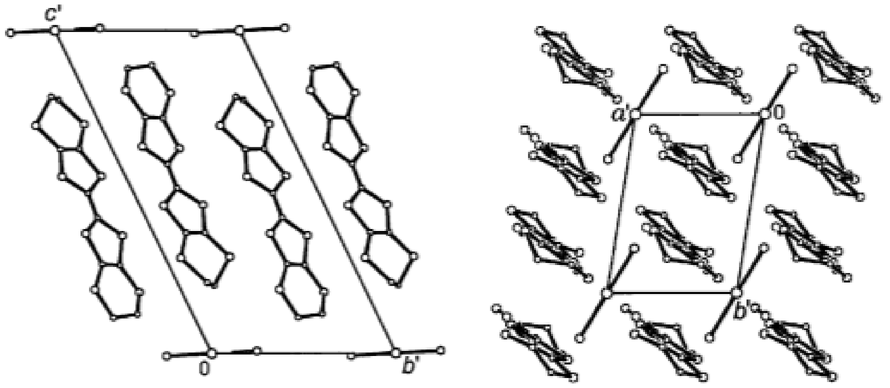

Figure 1.15. Crystal structure of β''-$(ET)_2ICl_2$ along the *c′* (left) and *a′* (right) axes[34].

In the kappa, k, phase the molecules form dimer pairs arranged orthogonally to each other. In superconducting kappa phase the C=C of one ET lies above 5-membered ring of the other ET in the dimer pair (Figure 1.16). In the non-superconducting phase the C=C lies directly above the C=C of the other molecule in the dimer pair which produces longer S…S contacts.

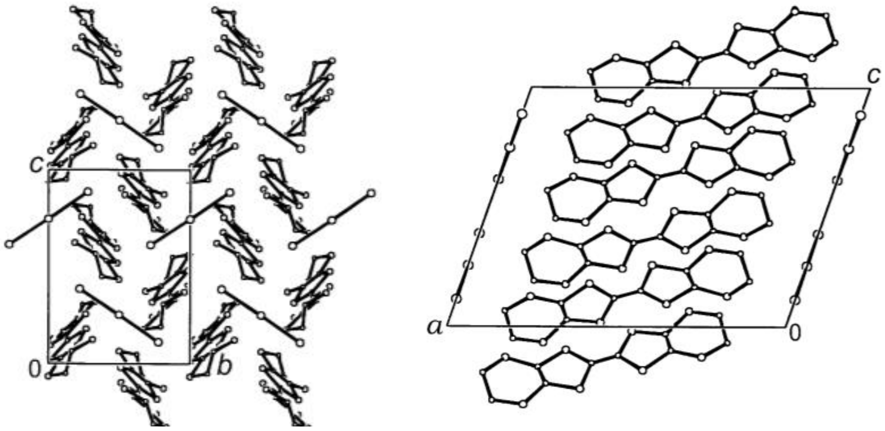

Figure 1.16. Crystal structure of κ-$(ET)_2I_3$ viewed along the *a* (left) and *b* (right) axes[34].

1.5 Chirality

1.5.1 Introduction

Chirality is a property expressed by molecules or materials that can exist as two non-superimposable mirror images. The materials can be characterised by the optical rotation of linearly polarised light. The left-handed enantiomer will rotate the incident light anti-clockwise (levorotary – *L*) and the right-handed enantiomer clockwise (dextrorotary – *D*). A common example is shown below in Figure 1.17 as a tetrahedral carbon atom bonded to four different groups, this is known as atomic chirality where the handedness is confined to a configurationally stable atomic centre. The two enantiomers can have drastically different properties even though the atom-atom bonding is identical.

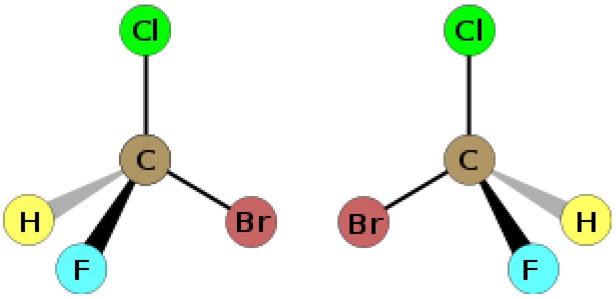

Figure 1.17. Stereogenic carbon atom bonded to four R groups

Axial chirality is possessed by molecules or materials that are devoid of a stereogenic centre, but instead hold an axis of chirality about which substituents are arranged such that their mirror images are non-superimposable. When synthesising axially chiral molecules the choice of ligand is important in creating the axes about which the chirality is defined, homoligatily is essential.

The preparation of multifunctional materials using molecular building blocks possessing chirality as one function has long been an area of interest for chemists and physicists alike as it is hoped the handedness will modulate or synergise with the other integrated properties[35]. Families of materials prepared from enantiopure or racemic reagents can be synthesised and the subtle differences in properties can be studied intensively. It follows that efforts have been made to produce molecular materials where one or more of the primary building blocks contain a form of chirality. Chiral conducting lattices are of particular interest due to the observation of electrical magnetotransport anisotropy phenomena such as circular dichroism and Electrical Magneto Chiral Anisotropy (eMChA)[36].

1.5.2 Magnetotransport Anisotropy

A conducting material can be chiral due to many reasons, it can crystallise in a chiral space group, can be made up of chiral subunits or it can adopt a chiral shape even if the individual units are achiral *e.g.* a helix. Therefore, a chiral conductor can exist in two forms where each is the mirror image of the other. Chiral materials show optical activity depending on the enantiomer, Rikken *et al.* showed that an analogous effect exists for electrical magnetotransport in chiral conductors[36]. The Electrical Magneto Chiral Anisotropy Effect argues that 'the electrical resistance of any chiral conductor should depend linearly both on the external magnetic field and the current through the conductor as well as the materials handedness'. As charge carriers moving within a magnetic field acquire some angular motion due to their cyclic motion, so charge carriers moving parallel to the magnetic field fulfil this condition and form a chiral system. Due to a longitudinal external magnetic field causing the charged particles to adopt a chiral motion while travelling through the helical lattice.

Major interest was sparked in 2001 after the discovery of the Magneto Chiral Anisotropy Effect in conducting chiral bismuth helices and chiral carbon nanotubes, where the resistivity within an external magnetic field perpendicular to the direction of current was dependent on the enantiomer[36]. This phenomenon arises not due to the structural integrity, as both enantiomers are identical, but due to the Lorentz effect.

In 2017 the first observation of the effect of chirality upon superconductivity was reported in an individual nanotube of tungsten disulphide[37]. In an achiral material, the current flows equally in both directions, but in tungsten disulphide nanotubes the superconductivity has been shown to reflect the chiral structure where the forward and backward current flows are not equivalent in an applied magnetic field[38]. This antisymmetric superconducting transport may be useful for applications in circuits as 'superconducting diodes'.

1.5.3 Chiral Charge Transfer Salts

The synthesis of chiral charge transfer salts in order to study the eMChA effect is an attractive avenue. The introduction of an enantiopure molecule within these salts, which display molecular stacking motifs, could cause the stacks to form helical twists or screw axes throughout the material. This chiral twist is analogous to the helical morphology seen in the carbon nanotubes mentioned above and the conducting electrons would follow this path, possibly producing an advanced expression of the MChA effect. Also, as already mentioned, charge transfer salts offer the possibility of introducing multifunctionality into charge transfer salrs, with cooperative magnetic effects existing in tandem with conducting properties. Investigating the interplay between phenomena such as MChA and ferromagnetism in the same material would be highly interesting and it is hoped that novel and exciting electrical or magnetic properties could be discovered.

It is known that the production of a chiral entity must take place within a chiral environment and due to this there are three routes to achieve chiral lattices within hybrid radical cation salts, through either of the two molecular building blocks, or the crystallisation environment.

1.5.3.1 Chiral Donors

A straight forward strategy to introduce chirality within charge transfer salts is through the radical cation. It is well known that structural disorder can affect the conducting properties of a material so inclusion of enantiopure donors within charge transfer salts is hoped to produce cleaner and more distinguished electronic properties. Given that the synthesis of families of enantiopure and racemic donor molecules also allows for the creation of families of radical cation salts, it is also an effective way to investigate eMChA between enantiomers and racemates. Wallis *et al*. provided the first route to an enantiopure TTF derivative in the form of a tetramethyl substituted BEDT-TTF molecule[39]. Numerous chiral TTF derivatives have been synthesised since, including TTF-oxazolines[40], EDT-TTF derivatives[41], hydroxyalkyl-BEDT-TTFs[42] and pyrrolo-TTFs[43]. Substitution at any of the four methylene carbons of the BEDT- TTF molecule produces a chiral molecule. It is therefore relatively easy to design donors with chiral sidechains of differing properties. Another route to chiral TTF derivatives is the selective transformation of one of the central sulphur atoms to a sulfoxide. This has the effect of placing the chiral information directly onto the core of the potentially mobile π electrons. However, the high oxidation potential of these donors means that radical salts can only be synthesised through solvent evaporation with suitably oxidising acceptor molecules, like TCNQ-F4[44].

Electro Chiral Magneto Anisotropy has been observed previously in chiral perchlorate salts of DM-EDT-TTF[39] and also in chiral TTF-oxazolines[40], where there is a small difference in resistivity observed between enantiomers. The only reported charge-transfer salts to combine chirality with conductivity was κ-(*S*,*S*)-DM-BEDT-TTF)$_2$ClO$_4$[45], but other groups have since synthesised this salt and not been able to observe any superconductivity.

1.5.3.2 Chiral and Racemic Anions

The charge-transfer salts from the donor molecule BEDT-TTF have produced the majority of superconductors and so have been the focus for electrocrystallisation with a variety of racemic and chiral anions of different sizes, shapes and charges. The most well known, and also the largest family of BEDT-TTF salts, are those with racemic tris(oxalate)metallate anions (a racemic pair is shown in Figure 1.18). Since the first discovery of superconductor β”-(BEDT-TTF)$_4$[(H$_3$O)Fe(C$_2$O$_4$)$_3$].benzonitrile in 1995[46] a multitude of semiconducting, metallic and superconducting salts have been prepared through making small changes to the formula by changing the metal centre[47] and the solvent molecule[48]. Efforts to produce a chiral superconductor from tris(oxalate)metallate were unsuccessful owing to the racemisation of Cr(oxalate)$_3$ in the time taken for crystals to grow[49]. Several other racemic and chiral anions have been used to produce radical-cation salts with BEDT-TTF including Fe(croconate)$_3$[50], Cr(2,2’-bipy)(oxalate)$_2$[51], Sb$_2$(L-tartrate)$_2$[52], TRISPHAT[53] and Fe(C$_6$O$_4$Cl$_2$)$_3$. Fe(C$_6$O$_4$Cl$_2$)$_3$ has also been combined with tetramethyl-BEDT-TTF where a chiral donor and chiral anion have been combined, although the anion crystallised as a racemic mixture[54,55].

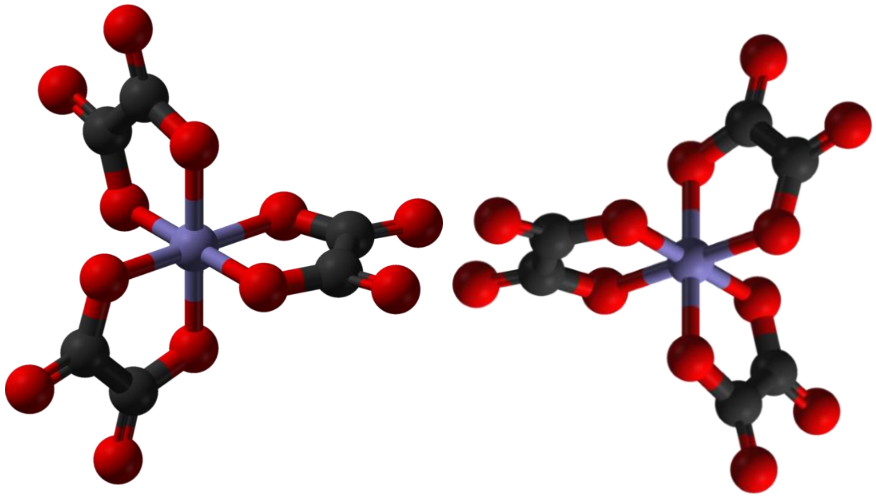

Figure 1.18. Enantiomers of the metal tris(oxalate) molecule.

1.5.3.3 Chiral Solvents

The inclusion of a guest solvent molecule of crystallisation is a relatively common occurrence in charge-transfer salts grown via electrocrystallisation and hence the use of chiral solvents is an attractive avenue. It has been shown that chiral solvents can affect charge transfer salts in two different ways. Through chiral inclusion, where the solvent molecule is included in the insulating layer of the lattice[56] and chiral induction, where in situ resolution of racemic reagents is possible[57].

The aforementioned family of BEDT-TTF salts with tris(oxalate)metallate anions contain a cavity within their inorganic layer trisoxalate framework. The hexagonal shape is ideally suited to the templating effect of a solvent molecule having the size of a benzene ring with a small side group (benzonitrile, bromobenzene, chlorobenzene, nitrobenzene). Martin *et al.*[56] used *sec*-phenethyl alcohol as the medium for electrocrystallisation and found that enantiopure *sec*-phenethyl alcohol molecules could be incorporated into the lattice (Figure 1.19). When repeating the synthesis from racemic *sec*-phenethyl alcohol the guest solvent molecule was disordered in the hexagonal cavity within the trisoxalate layer which had the effect of increasing the metal-insulator transition in the salt β"-(BEDT-TTF)$_4$[(H$_3$O)Fe(C$_2$O$_4$)$_3$].sec-phenethyl alcohol. Repeating the synthesis using the larger chiral molecule (*R*)-carvone gave a different charge-transfer salt, possibly due to the solvent molecule being too large to fit within the hexagonal cavity in the trisoxalate layer. Instead, a chiral induction was observed and the presence of (*R*)-carvone led to chiral induction giving the first charge-transfer salts containing only a single enantiomer of $Cr(C_2O_4)_3$ or $Al(C_2O_4)_3$ despite the electrocrystallisation being performed with the racemic starting tris(oxalate)metallate[58].

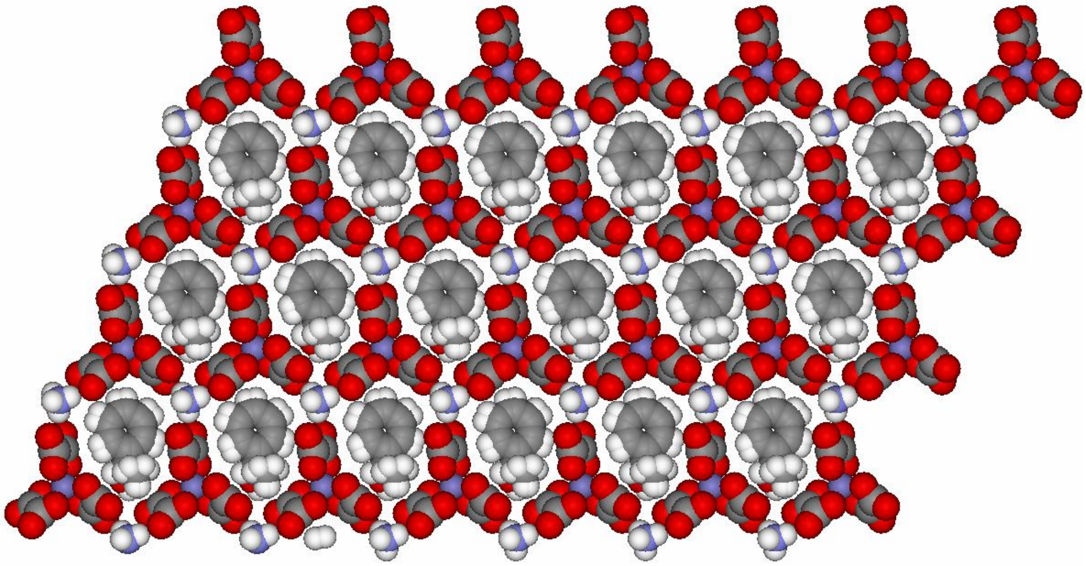

Figure 1.19. Anion layer of β''-$(BEDT\text{-}TTF)_4[(H_3O)Fe(C_2O_4)_3]$.sec-phenethyl alcohol[56].

1.6 Aims

1.6.1 Introduction

Building multifunctionality into materials is an area of great interest in modern materials science. The production of molecular materials that can demonstrate two or more properties desirable to the information technology sector offers the prospect of designing future devices in which the efficiency is greatly increased. Bespoke molecular building blocks can be used to manipulate and tweak desired properties so that materials can be tailor made for particular applications. Conventional continuous lattice solids pose a much harder route to achieve this aim. Through the use of molecular materials, devices can be produced where the useful physical properties are contained within a much smaller area, allowing for the miniaturisation of future technologies that perform tasks equal and above that of today's macromolecular electronics[31].

In this respect, anion/cation salts are an attractive avenue as each molecular network can furnish distinct properties to the material and even novel properties can arise due to the co-existence of the two. It was long thought that superconductivity and magnetism were inimical however, charge transfer salts in which the superconducting and localized magnetic networks are expressed in tandem have shown this not to be the case[45,46]. Although long range magnetic ordering such as ferromagnetism is yet to be achieved in a superconducting charge transfer salt and it is suggested that unless the Curie temperature is much lower than the critical temperature the former suppresses the latter.

The question of whether chirality has an effect on the electrical properties of a material (Electrical Magnetochiral Anisotropy = eMChA) has only recently been experimentally observed owing to a lack of suitable enantiopure materials[40]. The mechanism is not known and the aim of this project is to investigate routes to provide enantiopure materials to help formulate a model for eMChA. Research conducted for this thesis is centred around the production of multifunctional molecular materials combining chirality and conductivity via the synthesis and characterisation of charge-transfer salts made from racemic and chiral donor and anion molecules.

1.6.2 Racemic and Chiral Donor Molecules

One part of the project will produce families of chiral charge-transfer from both racemic and chiral donor molecules. This allows for a meaningful investigation into the effect that chirality plays on the physical properties when the handedness is associated to the conducting phase. Chiral derivatives of the conducting TTF molecule are synthesised by Professor John Wallis at NTU with chiral side-chains which may induce expression of a chiral crystal packing on the molecular material, e.g. chiral hydroxylalkyl-BEDT-TTF derivatives with the aim of transmitting the chirality between anion and conducting donor layers through hydrogen-bonding interactions. Other chiral TTF molecules with large side-chains have the potential for forming helical crystal packing arrangements, which, like spiral staircases, can be left- or right-handed. The helix provides a natural axis along which to measure the conductivity as a function of magnetic field to investigate eMChA.

Slow diffusion techniques will be employed at first using TCNQ as acceptor, and then electrocrystallisation will be performed using newly synthesised chiral and racemic organic donor molecules to prepare conducting materials with simple anions such as PF_6^-, Cl^-, Br^- and I_3^- at first, and if successful future work can employ more complex chiral/racemic anions. Some donors can be synthesised in both the *R*,*R* or *S*,*S* or racemic forms to provide an analogous series on which to study the effects of chirality change upon the magnetic and electrical properties.

1.6.3 Racemic and Chiral Anions

The other part of the project will produce families of chiral charge-transfer salts from racemic and chiral anions. There are a variety of chiral anions having axial, helical or propeller stereogenic elements and this project will focus on those with boron or lanthanide centres.

The synthesis of bis-chelated spiroborate anions offers the prospect of creating complexes with more than one stereogenic centre. In the case of $B(malate)_2^-$ the chirality of the bidentate chelated malate ligand is retained but diastereoisomers are produced through two possible stereochemical configurations at the boron centre which is labile in solution. There are a multitude of bidentate ligands of different sizes and shapes suitable for preparing bis-chelated spiroborate anions.

Using dianionic tridentate ligands, a variety of racemic nine-coordinate lanthanide anions varying in size, shape and hydrogen-bonding ability will be synthesised. As well as being racemic, these lanthanide anions also offer the opportunity to introduce luminescent properties to the material. The presence of highly magnetic lanthanide of f-block metal centres in an odd-parity environment (chiral) also offers the prospect of the observation of anomalous Hall effects or electric current induced magnetisation orginating from the f-pi electron interactions.

The family of salts of BEDT-TTF with tris(oxalate)metallate anions has produced a large number of racemic superconductors, metals, semiconductors and insulators, and also chiral semiconductors. New salts in this family will be sought out, in particular those from the tris(oxalate)iridate anions which has the potential to remain as a single enantiomer in solution for the duration of electrocrystallisation, unlike tris(oxalate)chromate.

1.6.4 Magnetic, Chiral/Racemic Conducting/Superconducting Charge Transfer Salts

To further investigate the synergy and co-existence between chirality, conductivity and magnetism through the production of multi-functional hybrid charge transfer salts. By synthesising a wide range of magnetic, non-magnetic, chiral and racemic coordination complexes and co-crystallising with BEDT-TTF it will be possible to gain a further understanding of how these properties interact.

1.7 References

1 John Singleton (2001). *Band Theory and Electronic Properties of Solids,* Oxford Master Series in Condensed Matter Physics. ISBN 0-19-850644-9.

2 N. Bohr, Trans. Of PhD Thesis, 1911, 291.

3 W. Meissner and R. Oschenfeld, *Naturwiss*, 1933, **21**, 787.

4 J.R. Gavaler, M.A. Janocko and C. Jones, *J. Appl. Phys*., 1974, **45**, 3009.

5 J. G Bednorz and K. A. Muller, *Physik B, Condensed Matt*., 1986, **64**, 189.

6 M. Wu, J. Ashburn, C. J. Torng, P. H. Hor, R. L. Meng, L. Gao, Z. J. Huang, Y. Q. Wang and C. W. Chu, *Phys. Rev. Lett.*, 1987, **58**. 908.

7 A. Maignan, C. Martin, V. Hardy, Ch Simon, M. Hervieu and B. Raveau, *Physica C: Superconductivity*, 1994, **219**, 3.

8 H. Ihara, M. Hirobayashi, H. Tanino, K. Tokiwa, H. Ozawa, Y. Akahana and H. Kawamura, *J. App. Physics*, 1993, **32**, 1732.

9 S. Margadonna and K. Prassides, *J. Solid State Chem*., 2002, **168**, 639.

10 Y. Takano, H. Takeya, H. Fujii, H. Kumakura, T. Hatano and K. Togano, *Appl. Phys. Lett*., 2001, **78**, 2914.

11 Y. Kamihara, H. Hiramatsu, M. Hirano, R. Kawamura, H. Yanagi, T. Kamiya and H. Hosono, *J. Am. Chem. Soc.*, 2006, **128**, 10012.

12 Y. Kamihara, T. Watanabe, M. Hirano and H. Hosono, *J. Am. Chem. Soc*., 2008, **130**, 3296.

13 W. A. Little, *Phys. Rev*., 1964, **134A**, 1416.

14 K. Bechgaard, P. Jerome, A. Mazaud and M. Ribaut, *J. Phys. Lett*., 1980, **41**, 95.

15 R. Brusetti, P. Garoche and K. Bechgaard, *J. Phys. C. Solid State Phys*., 1983, **16**, 3535.

16 M. Kurmoo. A. Graham, P. Day, S. Coles, M. Hursthouse, J. Caulfield, J. Singleton, F. Pratt, W. Hayes, L. Ducasse, and P. Guionneau, *J. Am. Chem. Soc*., 1995, **117**(49), 11209.

17 A. P. Drozdov, M. I. Eremets, I. A. Troyan and V. Ksenofontov, *Nature*, 2015, **525**, 73.

18 J. Bardeen, L. Cooper and R. Schieffer, *Phys. Rev*., 1957, **108**(5), 1175.

19 H. Frohlich, *Proc. Phys. Soc*., 1950, **63**, 778.

20 C. Reynolds, B. Suin and L. Nesbitt, *Phys. Rev.*, 1951, **84**(4), 691.

21 https://commons.wikimedia.org/wiki/File:Magnetisation_and_superconductors.png

22 D. S. Acker, R. J. Harder, W. R. Hertler, W. Mahler, L. R. Melby, R. E. Benson and W. E. Mochel, *J. Am. Chem. Soc*., 1960, **82**(24), 6408.

23 F. Wudl, G. M. Smith and E. J. Hufnagel, *J. Chem. Soc. Chem. Commun*., 1970, 1453.

24 J. Ferraris, D. O. Cowan, V. Walatka and J. H. Perlstein, *J. Am. Chem. Soc*., 1973, **95**(3), 948.

25 J. M. Williams, J. R. Ferraro, R. J. Thorn, K. D. Carlson, U. Geiser, H. H. Wang, A. M. Kini and M.-H. Whangbo, *Organic Superconductors (Including Fullerenes) Synthesis, Structure, Properties and Theory*: Prentice Hall. pp.270-275. (1992).

26 K. Bechgaard, C. S. Jacbosen, K. Mortenson, H. J. Pederson and N. Thorup, *Solid State Comm.*, 1980, **33**, 1119.

27 A. K. Klehe, V. Lauhkin, P. A. Goddard, J. A. Symington, J. Aghassi, J. Singleton, E. Coronado, J. R. Galan-Mascaros, C. J. Gomez-Garcia and C. Gimenez-Saiz, *Synth. Met*., 2008, **134**, 549.

28 E. Coronado and J. R. Galan-Mascaros, *J. Mater. Chem*., 2005, **15**, 66.

29 M. Mizuno, A. F. Garito and M. P. Cava, *J. Chem. Soc., Chem. Commun.* 1978, 18.

30 F. Pop, P. Auban-Senzier, E. Canadell and N. Avarvari, *Chem. Commun.,* 2016, **52**, 12438.

31 G. Rikken, K. Kan, M. Burghard, S. Roth and V. Krstic, *J. Chem. Phys.*, 2002, **117**(24), 1131.

32 J. R. Brandt, F. Salerno and M. J. Fuchter, *Nat. Rev. Chem.*, 2017, **1**, Article number 0045.

33 I. Hennig, K. Bender, D. Schwitzer, K. Dietz, H. Endres, H. J. Keller, A. Gleitz and H. W. Helberg, *Mol, Cryst. Liq. Cryst.*, 1985, **119**(1), 337.

34 R. P. Shibaeva and E. B. Yagubskii, *Chem. Rev.*, 2004, **104**, 5347.

35 G. L. J. A. Rikken and E. Raupach, Nature, 1997, **390**, 493.

36 V. Krstic, S. Roth, M. Burghard, K. Kern and G. L. J. A. Rikken, *J. Chem. Phys*., 2002, **117**, 11315.

37 V. Krstic and G. L. J. A. Rikken, *Chem. Phys. Lett*., 2002, **364**, 51; G. L. J. A. Rikken, J. Fölling and P. Wyder, *Phys. Rev. Lett*., 2001, **87**, art. no. 236602.

38 F. Qin, W. Shi, T. Ideue, M. Yoshida, A. Zak, R. Tenne, T. Kikitsu, D. Inoue, D. Hashizume and Y. Iwasa, *Nat. Commun.*, 2017, 8, 14465.

39 J. D. Wallis, A. Karrer and J. D. Dunitz, *Helv. Chim. Acta*, 1986, **69**, 69.

40 F. Riobé and N Avarvari, *Chem. Commun.*, 2009, 3753.

41 F. Pop, P. Auban-Senzier, E. Canadell, G. L. J. A. Rikken and N. Avarvari, *Nature Commun.*, 2014, **5**, 3757.

42 I. Awheda, S. Krivickas, S. Yang, L. Martin, M. A. Guziak, A. C. Brooks, F. Pelletier, M. Le Kerneau, P. Day, P. Horton, H. Akutsu and J. D. Wallis, *Tetrahedron*, 2013, **69**, 8738; S. J. Krivickas, C. Hashimoto, J. Yoshida, A. Ueda, K. Takahashi, J. D. Wallis and H. Mori, *Beilstein J. Org. Chem*, 2015, **11**, 1561.

43 S. Yang, A. C. Brooks, L. Martin, P. Day, H. Li, P. Horton, L. Male and J. D. Wallis, *CrystEngComm*, 2009, **11**, 993.

44 M. Chas, M. Lemarié, M. Gulea and N. Avarvari, *Chem. Commun.*, 2008, 220; M. Chas, F. Riobé, R. Sancho, C. Minguıllón and N. Avarvari, *Chirality*, 2009, **21**, 818.

45 J. S. Zambounis, C. W. Mayer, K. Hauenstein, B. Hilti, W. Hofherr, J. Pfeiffer, M. Bürkle and G. Rihs, *Adv. Mater*., 1992, **4**, 33.

46 M. Kurmoo, A. W. Graham, P. Day, S. J. Coles, M. B. Hursthouse, J. L. Caulfield, J. Singleton, F. L. Pratt, W. Hayes, L. Ducasse and P. Guionneau, *J. Am. Chem. Soc*., 1995, **117**, 12209.

47 L. Martin, S. S. Turner, P. Day, F. E. Mabbs and E. J. L. McInnes, *J. Chem. Soc., Chem. Commun*., 1997, 1367.

48 S. S. Turner, P. Day, D. E. Hibbs, K. M. A. Malik, M. B. Hursthouse, S. J. Teat, E. J. MacLean, L. Martin and S. A. French, *Inorg. Chem.*, 1999, **38**, 3543.

49 L. Martin, S. S. Turner, P. Day, K. M. A. Malik, S. J. Coles and M. B. Hursthouse, *Chem. Commun*., 1999, 513.

50 C. J. Gómez-García, E. Coronado, S. Curreli, C. Giménez-Saiz, P. Deplano, M. L. Mercuri, L. Pilia, A. Serpe, C. Faulmann and E. Canadell, *Chem. Commun.*, 2006, 4931.

51 A. M. Madalan, E. Canadell, P. Auban-Senzier, D. Brânzea, N. Avarvari and M. Andruh, *New J. Chem.*, 2008, **32**, 333.

52 E. Coronado, J. R. Galán-Mascarós, C. J. Gómez-García, A. Murcia-Martinez and E. Canadell, *Inorg. Chem*., 2004, **43**, 8072.

53 M. Clemente-León, E. Coronado, C. J. Gómez-García, A. Soriano-Portillo, S. Constant, R. Frantz and J. Lacour, *Inorg. Chim. Acta*, 2007, **360**, 955.

54 S. Benmansour, E. Coronado, C. Giménez-Saiz, C. J. Gómez-García and C. Rößer, *Eur. J. Inorg. Chem.*, 2014, **24**, 3949; M. Atzori, F. Pop, P. Auban-Senzier, C. J. Gómez-García, E. Canadell, F. Artizzu, A. Serpe, P. Deplano, N. Avarvari and M. L. Mercuri, *Inorg. Chem.*, **2014**, ***53***, 7028.

55 M. Atzori, F. Pop, P. Auban-Senzier, R. Clérac, E. Canadell, M. L. Mercuri, and N. Avarvari, *Inorg. Chem*. 2015, **54**, 3643.

56 L. Martin, P. Day, H. Akutsu, J-i. Yamada, S-i. Nakatsuji, W. Clegg, R. W. Harrington, P. N. Horton, M. B. Hursthouse, P. McMillan and S. Firth, *CrystEngComm*, 2007, **10**, 865.

57 L. Martin, P. Day, S.-i. Nakatsuji, J.-i. Yamada, H. Akutsu and P. Horton, *CrystEngComm*, 2010, **12**, 1369.

58 L. Martin, S.-i. Nakatsuji, J.-i. Yamada, H. Akutsu and P. Day, *J. Mater. Chem*., 2010, **20**, 2738.

Chapter 2 – Experimental

2.1 Purchase and Purification of Chemicals

Bis(ethylenedithio)tetrathiafulvalene (BEDT-TTF) was purchased from Sigma-Aldrich and recrystallised from chloroform. BEDT-TTF can also be synthesised by the methods of Larsen and Lenoir (1988)[1] and Mizuno *et al*. (1986)[2]. Alternatively the synthesis of chiral donors results in the side production of BEDT-TTF that can be recrystallised from chloroform and used. Solvents were purchased from TCI and Sigma-Aldrich and distilled prior to use. 18-crown-6 was obtained from Sigma-Aldrich and dried over acetonitrile. Chiral donors received from Wallis *et al*. were recrystallised[3]. All other chemicals were used as received unless otherwise stated.

2.2 Experimental Techniques

2.2.1 X-ray Crystallography

Several structures presented in this thesis were solved at room and low temperatures at NTU, Osaka University in Japan and the National Crystallographic Service (NCS) in Southampton. Data was collected in Osaka by Professor Hiroki Akutsu on a Rigaku R-AXIS VII imaging plate system with FR-E SuperBright High-Brilliance Rotating Anode Generator with confocal mono-chromated MoKα radiation, using Rapid Auto software for control and processing. Structures were solved via programs from the SHELX family by direct methods and refined on F^2 full-matrix least squares using all unique data.

Data was collected by Claire Wilson at the NCS on a Rigaku AFC12 diffractometer with Mo rotating anode, using standard control and processg software. Structures were solved via programs from the SHELX family by direct methods and refined on F^2 full-matrix least squares using all unique data.

Data was collected at NTU on a Agilent Excalibur System equipped with a Sapphire detector at 120 K, or at room temperature. Structures were solved via programs from the SHELX family by direct methods and refined on F^2 full matrix least squares using all unique data.

2.2.2 Raman Spectroscopy

Raman spectra were recorded at University College London at room temperature with a Renishaw InVia Raman microscope equipped with a diode laser (785 nm) and a 1200 l/mm grating using a laser power of *ca*. 1mW. Scans were performed from 1200 to 1650 cm^{-1} to observe the BEDT-TTF v_3 and v_4 bands which shift depending on the charge upon the BEDT-TTF molecule[4].

2.2.3 Nuclear Magnetic Resonance Spectroscopy

NMR spectroscopy was used to deduce the nature of the diastereomeric borate anions synthesised in chapter 2 and discussed in chapter 4.1, It is a useful technique for attaining the ratio of diastereomers present in solution. ^{1}H, and ^{13}C spectra were recorded on a JEOL ECX 400 instrument – 400 MHz for ^{1}H NMR and 100.6 MHz for ^{13}C NMR. All chemical shifts (δ) are quoted in ppm and coupling constants (J) measured in Hertz. Residual signals from the solvents were used as an internal reference.

2.2.4 Infra-red Spectroscopy

Infra-red spectra were recorded on a Perkin-Elmer Spectrum 100 FT-IR spectrophotometer, with only the characteristic peaks reported in cm^{-1}

2.2.5 SQUID Magnetometry

SQUID magnetometers work by arranging two Josephson junctions, connected in parallel on a superconducting loop and is operated in the voltage state with a current bias. When the flux in the loop is increased, the voltage oscillates. By detecting small changes in voltage, one is able to detect a change in flux in a magnetic sample at a very low level.

Magnetic susceptibility measurements were performed with a Quantum Design MPSM2 SQUID magnetometer using randomly orientated polycrystalline material encased in aluminium foil and placed in a diamagnetic straw. Magnetization was recorded from 2 to 300K either cooling or warming within a range of external magnetic fields depending on the behaviour of the sample being analysed. Data was collected by Professor Hiroki Akutsu at Osaka University.

2.2.6 Transport Measurements

Two and four probe electrical transport measurements were performed. For semi-conducting samples with high resistance, the two-probe technique can be used as contact resistance was assumed to be negligible. Four probes were used on samples with low resistance to eliminate crystal-electrode contact resistances, with the current being passed through the outer probes and the voltage drop measured across the two inner probes. DC transport measurements were made on crystals using a HUSO HECS 994 multi-channel conductometer. Gold wire electrodes (15 μm diameter) were attached to the crystal using conducting carbon cement or gold paste and the wires were connected via silver paint or gold paste to an integrated eight-pin circuit plug.

2.2.7 Band Structure and Fermi Surface Calculations

Electronic band structure diagrams are plots of energy versus the three-dimensional wavevector, *k*. Band diagrams are drawn along various lines from point to point. Points and lines inside the Brillouin zone are given Greek letters, whilst points on the surface of the Brillouin zone are given Roman letters. The Γ point denotes k = 0 and lines through the Brilloiun zone connect special symmetry points (M, V, X, Y, U). Fermi energy, E_F, is also shown on these diagrams.

Electronic band structures are calculated through the Huckel tight binding approximation which uses atomic orbitals as individual wave functions in order to build up a picture of the energy level of separate bands located within the material. Similar to the linear combination of atomic orbitals which is used to describe band theory in solids. The approximation starts from the wave functions of free atoms and is relatively good for the description of the inner electronic shells of atoms and relatively localised bands. However, it is not so effective for the explanation of conduction electrons, this is due to the fact that the origin of the free electrons is different to the nature of the localised atomic states. Tight binding band calculations were performed by Professor Hiroki Akutsu of Osaka University using the software of Prof Takehiko Mori of TITECH.

2.2.8 Crystallisation Techniques

2.2.8.1 H-cells

The H-cells had two platinum electrodes separated by a porous glass frit to prevent contamination between the anodic and cathodic solutions. Electrodes were cleaned by applying a small current (10-100μA) whilst submerged in 1M H_2SO_4 resulting in the evolution of H_2 and O_2. The direction of current was then swapped and repeated for 1 minute. They were then washed with distilled water, ethanol and dried thoroughly. The H-cells were cleaned by passing conc. HNO_3, acetone and distilled water (separately, in that order) through the glass frit. Then washed with distilled water, then acetone and thoroughly dried in the oven at 60°C. A solution of electrolyte (50-100 mg), solvent (20ml) and crown ether (sodium, potassium and ammonium salts only) (200-320 mg) was stirred until dissolution and added to the cathode side of the H-shaped cell. Donor (10mg) was added to the anode side along with solvent (20ml). Alternatively, the solution containing the source of the anion can be filtered directly into the cathode side of the H-cell and the solution allowed to equilibrate through the porous glass frit into the anode side containing the neutral donor. For crystal phases that were produced during this research the crystal habit and structural integrity could be improved depending which of the two techniques was used, however, it is impossible to say which is more effective as it depends on the thermodynamics and affinity of the individual phase during nucleation, that is to say it is crystal specific.

All joints present on electrodes and H-cells were sealed tightly with paraffin film. The cells were fixed in black-out boxes on a vibration free table and kept at a constant temperature of 293K. A constant current of 0.1-0.5 μA was passed through the platinum electrodes for up to two months. In any cells that showed no activity after 3 weeks the current was increased daily up to 5.0 μA to induce nucleation. Cells that showed crystal growth were detached from current source and crystals harvested. The electrode was carefully removed and rinsed with acetone to remove single crystals onto filter paper. Any crystals still present on the electrode were removed very carefully with a scalpel after evaporation of the acetone. Crystals that remained in the H- cell after removal of the electrode can be retrieved by filtering the H-cell solution and washing with acetone. Crystal integrity can be improved remarkably by recycling the H-cell solution. After harvesting single crystals from the H-cell the remaining solution was filtered into a freshly cleaned and dried H-cell containing donor (5mg) in the anode side, the electrodes replaced, sealed with paraffin film and the H-cell replaced at the same previous constant current. As the new batch of donor added dissolves and the radical species is formed it is thought that a higher concentration of cation will cause a more uniform nucleation and single crystals of superior quality than the previous batch can be grown. This method can be employed up to three times, after which the eventual lowered concentration of electrolyte causes a decrease in crystal quality.

2.2.8.2 Electrocrystallisation

Electric-field induced phase transformation is a technique used to create the deposition of molecules on an electrode from a solution through the application of a sufficiently high electric field. Electrocrystallisation involves the *in situ* anodic oxidation of the neutral donor molecule in an electrolytic solution which contains the anion to be incorporated into the charge transfer salt. It is a very sensitive technique and crystal habit can be changed subtly or dramatically by varying any of the external variables slightly, i.e. electrolyte, current, temperature, concentration of starting material and purity of chemicals used. Several phases can grow on the anode at the same time and under the same conditions if both are thermodynamically stable. The transition from liquid to crystal involves the rearrangement of molecules into a spatially ordered lattice. The molecules will pack in the lowest energy geometry which heightens interactions between the dipoles of neighbouring molecules. Non-covalent interactions are key in deciding the phase and motifs adopted by the anion and in turn the donor molecule during nucleation.

2.2.8.3 Chiral Donors

The use of chiral donors to express handedness throughout hybrid radical cation salts offers a different route than that of chiral anions. Firstly, the chiral information will be contained within a closer environment to the potentially mobile π electrons and hence could influence the charge transport more radically than chiral anions. Secondly, a higher potential for observing helical twists throughout donor stacks exists as enantiopure side chains could adopt a helical geometry when stacking. The resolution of axially chiral coordination complexes becomes more difficult due to thermal influences affecting the lability of metal centres. Chiral donor molecules can be synthesised using enantiopure or racemic starting reagents, or resolved post-synthetically and hence families of enantiopure and racemic charge transfer salts are more easily achieved. A chiral side-chain will provide a decrease in packing motifs of derivatised TTF, EDT-TTF and BEDT-TTF donors and therefore crystal engineering is first attempted with mononuclear and linear anions or highly oxidising acceptors such as iodide, bromide, chloride and TCNQ (and its fluorinated analogues). Electrocrystallisation experiments can then be attempted using small mono-valent anions in the form of Tetrabutylammonium salts. Small tetrahedral or octahedral molecules allow for a wide number of donor orientations throughout crystal nucleation. The use of highly oxidising acceptors allows for the removal of an electric current in order to create the radical cation species, this provides more scope for a variety of crystallisation techniques.

2.2.8.4 Hot Diffusion

A hot solution of donor (5mg) in solvent (3ml) was added to a hot stirred solution of acceptor (10mg) in solvent (6ml). The reaction mixture was heated to reflux for 5 hours, during which time the solution turned opaque black indicating successful oxidation of donor molecule and charge transfer. The solution was cooled to room temperature and slow evaporation of the solvent afforded black shiny crystals which were harvested, washed with acetone and dried thoroughly. Crystal integrity can be changed by allowing the solvent to evaporate at different rates.

For donors with lower oxidation potential, this technique can be applied but with the removal of heat. Simply, the two solutions are mixed together and allowed to stand in a sealed flask for up to 5 hours before slow evaporation of the solvent.

2.2.8.5 Test Tube Diffusion

Donor (5mg) was placed in the bottom of a test tube. Solvent A (3ml) was added slowly. A 50:50 mixture of solvent A and B (2ml total volume) was then added carefully down the side of the tube to ensure not to break the surface of the bottom solvent layer. A 0.1M solution of solvent B (3ml) and acceptor was then added slowly to the top of the middle solvent layer. The test tube was sealed and placed in a dark and vibrationless environment. Slow diffusion across the solvent boundaries allows for a highly controlled rate of nucleation as the length (total volume) of the middle layer can be adjusted. Over a period of 2-4 weeks black crystals will begin to grow on the side of the tube. These were harvested, washed with acetone and dried thoroughly.

2.2.8.6 Vapour Diffusion

A 10ml sample vial containing donor (5mg) and solvent (5ml) was placed upright in a large beaker containing iodine pellets (*ca*. 20mg). The beaker was sealed with paraffin film and over time iodine vapour diffused into the donor solution and the solution turned black. The solvent was allowed to evaporate slowly at room temperature to afford black single crystals. By changing the concentration of donor solution one can control the rate of charge transfer. Alternatively, the size of beaker or amount of iodine can determine the rate of diffusion into the donor solution.

2.3 Synthesis of Tetrahedral Spiroborate Complexes

Synthesising coordination complexes using a central atom of small atomic radius like boron creates smaller anions and allows us to look into the effect of decreased size and charge on the structure of layered hybrid charge transfer salts. A variety of ligands with differing size, shape and functionality can be used. The low charge and decreased geometric radii of the tetrahedral borate complexes should prove to produce charge transfer salts with a higher anion packing density, increasing the potential for non-covalent interactions between conducting and insulating layers. The coordination of a stereogenic ligand to the boron centre allows for the production of enantiopure complexes for use in crystal engineering with BEDT-TTF.

Boron in its trivalent state can form 4-coordinate anions. The reaction of electrophilic boric acid ($B(OH)_3$) with two equivalents of conjugate ligand in a basic aqueous solution can produce a tetrahedral borate complex carrying a formal negative charge. $B(OH)_3$ is capable of cleaving protons from water to form a monoprotic acid in aqueous solution. However, $B(OH)_3$ can also dissociate and form two complexes in aqueous solution[5], $BL(OH)^{2-}$ and BL^{2-}. A slight excess of ligand is therefore required to force the equilibrium towards the formation of a tetrahedral BL_2 anion. The borate anions in this thesis were synthesised using modified procedures from the methods of Zviedre *et al.*[6], Arndtsen *et al.*[7] and Leitner *et al.*[8].

$$B(OH)_3 + MOH + 2\ LH_2 \rightarrow M[B(L)_2] + 4\ H_2O \quad \text{eqn. 11}$$

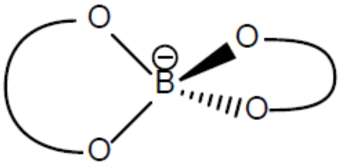

Figure 2.0. Chemdraw representation of the $B(L)_2^-$ complex.

The coordination of two identical chiral ligands to the central boron atom will produce a chiral complex, holding a stereogenic centre on each ligand. Also, the coordination of two identical asymmetric ligands produces an axially chiral complex, showing a clockwise or anti-clockwise 'spirane' like twist at the boron centre. The synthesis of bis-chelated borate anions therefore offers the prospect of creating complexes with more than one stereogenic centre, where the chirality of the chelated ligand is retained but diastereomers are produced through two possible stereochemical configurations at the boron centre which is labile in solution. α- Hydroxyl acid derivatives can be used as dioxo bidentate ligands to create a large family of chiral diastereomeric anions as the R group alpha to the stereogenic centre can easily be substituted.

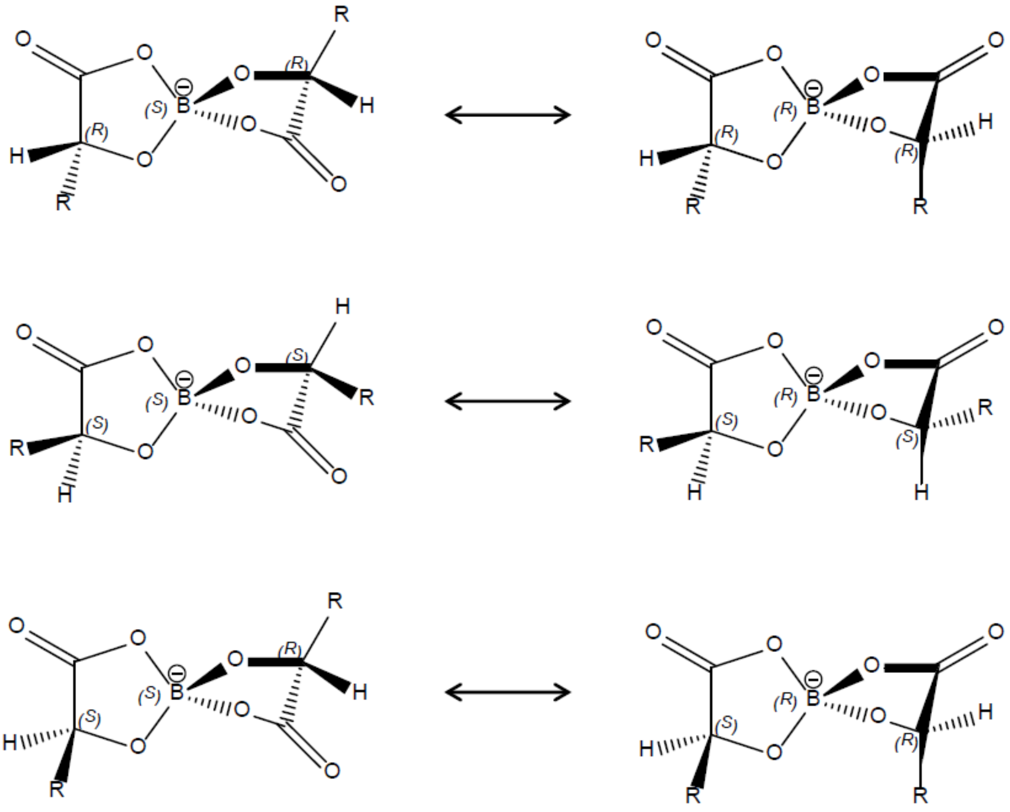

Figure 2.1: Six possible diastereomeric configurations of the $B(L)_2^-$ complex when using a racemic α-hydroxy acid derivative as a ligand

Figure 2.1 shows the six possible diastereoisomers that can be produced when using a racemic α-hydroxy acid derivative as a ligand (R= H, Ph, COOH, CH_2COOH, CH_2OCOOH). If using an enantiopure ligand diastereomers 1-4 will be produced depending on the chirality of the ligand. In the case of glycolic acid (R=H) diastereomers are not produced as the ligand does not have a chiral centre, but enantiomers still exist due to the molecular dissymmetry at the boron centre. Tartronic acid (R=COOH) does not possess a chiral centre as the neutral acid. However, the deprotonated ligand in the presented coordination geometry now becomes chiral due to the absence of two carboxylate groups. Previously charge transfer salts have been engineered to contain racemic or chiral anions, but the inclusion of chiral and diastereomeric anions within the same radical salt has not been seen before. It is hoped that the presence of three separate stereogenic centres within the anion will lead to new and exciting electronic properties.

2.3.1 K[B(R/S-$C_4H_4O_5$)$_2$].H_2O - Potassium bis(R/S-malato)boratehydrate

$B(OH)_3 + 2\ C_4O_5H_6 + KOH \rightarrow K[B(C_4O_5H_4)_2].H_2O + 4\ H_2O$

Boric acid (2.47g, 40mmol) was added to a rapidly stirred solution of *R/S*-malic acid (10.73g, 80mmol) in H_2O (20ml). Aqueous potassium hydroxide (2.08g, 40mmol) in H_2O (20ml) was added dropwise and the reaction mixture was stirred in an open flask at 95ºC for 3 hours. After evaporation of the water the crude borate salt was isolated as a white powder. The product was dissolved in a minimum of hot H_2O and excess cold ethanol added to precipitate the white crystalline powder which was collected via vacuum filtration and washed with ice cold ethanol. Yield = 10.47g (79%). Calculated for $K[B(C_4O_5H_4)_2].H_2O$, C 28.95%, H 3.01%; found: C 28.94%, H 3.04%. δ_H (400 MHz, CD_3CN): four diastereomers, 4.44–4.51 (2H, m) (2× OCH), 2.65–2.74 (2H, m) (2 × $Ch_{\alpha}H_{\beta}CO_2H$), 2.46–2.55 (2H, m) (2 × $Ch_{\alpha}H_{\beta}CO_2H$); δ_C (100 MHz, CD_3CN): 178.3 & 178.4 (2 × CO_2B), 171.8(2 × CO_2H), 72.2 & 72.4 (2 × OCH), 38.87, 38.91, 39.11 & 39.14 (2 × CH_2CO_2H).

2.3.2 K[B(R-$C_4H_4O_5$)$_2$] – Potassium bis(R-malato)borate

$B(OH)_3 + 2\ C_4O_5H_6 + KOH \rightarrow K[B(C_4O_5H_4)_2] + 4\ H_2O$

Boric acid (2.47g, 40mmol) was added to a rapidly stirred solution of *R*-malic acid (10.73g, 80mmol) in H_2O (20ml). Aqueous potassium hydroxide (2.08g, 40mmol) in H_2O (20ml) was added dropwise and the reaction mixture was stirred in an open flask at 95ºC for 3 hours. After evaporation of the water the crude borate salt was isolated as a white powder and recrystallized twice from minimum hot H_2O. Yield = 10.34g (82%). Calculated for $K[B(C_4O_5H_4)_2]$, C 30.6%, H 2.57%; found: C 30.32%, H 2.72%. δ_H (400 MHz, CD_3CN): two diastereomers in ratio 2 : 1, 4.47 (2H, dd, J = 7.9, 4.3 Hz, major) & 4.49 (2H, dd, J = 8.6, 4.2 Hz, minor) (2 × OCH), 2.67 (2H, dd, J = 15.6, 4.2 Hz, minor) & 2.71 (2H, dd, J = 15.8, 4.3 Hz, major) (2 × $Ch_{\alpha}H_{\beta}CO_2H$), 2.49 (2H, dd, J = 15.6, 8.6 Hz, minor) & 2.52 (2H, dd, J = 15.8, 7.9 Hz, major) (2 × $CH_{\alpha}H_{\beta}CO_2H$); δ_C (100 MHz, CD_3CN): 178.2 & 178.3 (2 × CO_2B), 171.8 (2 × CO_2H), 72.1 & 72.3 (2 × OCH), 38.8 & 39.0 (2 × CH_2CO_2H).

2.3.3 $K[B(S\text{-}C_4H_4O_5)_2]$ – Potassium bis(S-malato)borate

$B(OH)_3 + 2\ C_4O_5H_6 + KOH \rightarrow K[B(C_4O_5H_4)_2] + 4\ H_2O$

Boric acid (2.47g, 40mmol) was added to a rapidly stirred solution of *S*-malic acid (10.73g, 80mmol) in H_2O (20ml). Aqueous potassium hydroxide (2.08g, 40mmol) in H_2O (20ml) was added dropwise and the reaction mixture was stirred in an open flask at 95ºC for 3 hours. After evaporation of the water the crude borate salt was isolated as a white powder and recrystallised twice from minimum hot H_2O. Yield = 10.41g (83%).

2.3.4 $K[B(R/S\text{-}C_8H_6O_3)_2]$ – Potassium bis(R/S-mandelato)borate

$B(OH)_3 + 2\ C_8O_3H_8 + KOH \rightarrow K[B(C_8H_6O_3)_2] + 4\ H_2O$

Boric acid (0.62g, 10mmol) and *R/S*-mandelic acid (3.04g, 20mmol) were dissolved in H_2O (30ml). Potassium hydroxide (0.56g, 10mmol) in H_2O (10ml) was added dropwise to the stirred solution. The reaction mixture was heated to reflux for 8 hours. The solvent was removed in vacuo and the white powder was recrystallised twice from hot H_2O and once from hot EtOH. The final product was dissolved in minimum hot H_2O and left to crystallise over 3 days to leave off white powder. Yield = 2.94g (85%).

2.3.5 $K[B(S\text{-}C_8H_6O_3)_2]$ – Potassium bis(S-mandelato)borate

$B(OH)_3 + 2\ C_8H_8O_3 + KOH \rightarrow K[B(C_8H_6O_3)_2] + 4\ H_2O$

Boric acid (0.62g, 10mmol) and *S*-mandelic acid (3.04g, 20mmol) were dissolved in H_2O (30ml). Potassium hydroxide (0.56g, 10mmol) in H_2O (10ml) was added dropwise to the stirred solution. The reaction mixture was heated to reflux for 8 hours. The solvent was removed in vacuo and the white product recrystallised twice from minimum hot H_2O and once form hot EtOH. The final product was dissolved in minimum H_2O and left to crystallise over 3 days to leave off white powder. Yield = 3.40g (98%).

2.3.6 K[B(R-$C_8H_6O_3$)$_2$] – Potassium bis(R-mandelato)borate

$B(OH)_3 + 2\ C_8H_8O_3 + KOH \rightarrow K[B(C_8H_6O_3)_2] + 4\ H_2O$

Boric acid (0.62g, 10mmol) and *R*-mandelic acid (3.04g, 20mmol) were dissolved in H_2O (30ml). Potassium hydroxide (0.56g, 10mmol) in H_2O (10ml) was added dropwise to the stirred solution. The reaction mixture was heated to reflux for 8 hours. The solvent was removed in vacuo and the white product recrystallised twice from minimum hot H_2O and once form hot EtOH. The final product was dissolved in minimum H_2O and left to crystallise over 3 days to leave off white powder. Yield = 3.01g (87%).

2.3.7 K[B($C_2H_2O_3$)$_2$] – Potassium bis(glycolate)*borate*

$B(OH)_3 + 2\ C_2H_4O_3 + KOH \rightarrow K[B(C_2H_2O_3)_2] + 4\ H_2O$

Potassium hydroxide (0.56g, 10mmol) in H_2O (10ml) was added dropwise to a stirred solution of boric acid (0.62g, 10mmol) and glycolic acid (1.25g, 20mmol) in H_2O (20ml). The reaction mixture was heated to reflux for 7 hours. The solvent was removed in vacuo to leave colourless oil which was dissolved in minimum EtOH. The flask was stoppered and left to stand for five days during which time colourless crystals formed from solution and were recrystallised from minimum hot ethanol. Yield = 1.26g (64%).

2.4 Synthesis of Racemic Nine-coordinate Lanthanide Complexes

The synthesis of racemic nine-coordinate lanthanoid complexes for inclusion into hybrid charge transfer salts poses compelling questions as to how the increased size of the inorganic species will affect the packing motifs of the organic conducting layer. The potential of long-range magnetic ordering of delocalised lanthanoid electrons or paramagnetic metal centres alongside the mobile conducting electrons of the organic layer is an area that can be investigated in the charge transfer salts synthesised in this chapter.

Rare earth metal complexes and associated materials have been used widely in cathodoluminescent displays, lasers and lamps due to their photoluminescent properties and their ability to exhibit high quantum efficiencies and very sharp spectral bands. Lanthanide aromatic carboxylates in particular have good luminescence properties and adsorption characteristics in the near UV region. The strong electron attraction of complexed lanthanides leads to metal-ligand bonds that are mostly ionic in nature and hence the coordination sphere is controlled by a subtle interplay between metal-ligand interactions and interligand steric constraints.

The production of highly ordered coordination environments rely largely on the geometrical preferences of the metal ion but also on the choice of appropriate ligands. The lanthanide series however doesn't show the same geometrical preferences as most of the transition metal series and therefore the careful selection of ligands is important in order to influence some control over the coordination sphere.

The H_2dpa ligand is known to form a number of stable chelates with simple metal ions and oxometal cations as it can display a variety of coordination geometries. As a tridentate ligand, it has been shown to form chiral tris-chelated complexes with most of the lanthanide series[9], all in nine-coordinate geometry. Due to the high coordination number of these complexes they have much higher labilities (relative to d-block complexes) and hence optical resolution is via a chiral crystallisation environment is preferred.

The tris-chelate non-flexible dpa^{2-} and clo^{2-} ligands (Figure 2.2) create rigid nine- coordinate complexes with heteroatoms outside the coordination sphere well placed to form non-covalent bonds with neighbouring complexes, providing a scope for building metal-based supramolecular architectures and the potential for self-assembly of molecular devices and nanostructures[10]. In fact, dpa^{2-} lanthanoids have shown the ability to form infinite single-strand helicates[11]. The ability of heteroatoms outside the coordination sphere to take part in non-covalent interactions shows good potential for crystal engineering of these complexes with BEDT-TTF.

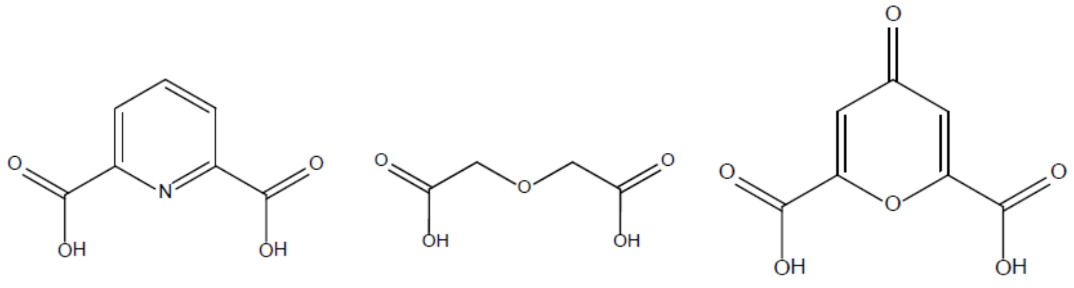

H_2dpa = pyridine-2,6-dicarboxylic acid H_2oda = oxydiacetic acid H_2clo = chelidonic acid

Figure 2.2. H_2dpa, H_2oda and H_2clo tridentate ligands

Flexible aliphatic ligands such as H_2oda, which holds donor atoms in the same orientation as the above dpa^{2-} ligand, have formed mononuclear tris(oxydiacetate) lanthanates(III) in which the ligand is fully deprotonated[12]. The mononuclear $[Ln(oda)_3]^{3-}$ anion (Ln = Ce, Nd, Sm, Eu, Gd, Yb) again shows potential for crystallisation with BEDT-TTF due to the presence of heteroatoms outside the coordination sphere. Other lanthanoids formed from oda^{2-} were shown to be polynuclear and/or bridged. Spontaneous resolution of some of these complexes (Dy, Er, Pr) in the presence of $NaBF_4$ has been possible without the use of chiral auxiliaries or solvents[13].

2.4.1 Synthesis of Racemic Nine-Coordinate Lanthanide Complexes of the dpa Ligand

2.4.1.1 $Na_3[La(C_7O_4H_3N)_3].xH_2O$ (Method 1[9]) – Sodium tris(dipicolinato)lanthanate hydrate[9]

$LaCl_3.6H_2O + 3\ C_7O_4H_5N + 6\ NaOH \rightarrow Na_3[La(C_7O_4H_3N)_3] + 6\ H_2O + 3\ NaCl$

Dipicolinic acid (1.50g, 9mmol) was suspended in H_2O (30ml). Aqueous sodium hydroxide (0.72g, 18mmol) in H_2O (10ml) was added dropwise and the solution stirred for five minutes. Lanthanum (III) chloride hexahydrate (0.75g, 3mmol) was added and the reaction mixture heated to reflux for 5 hours before cooling to room temperature. The solution was condensed to 10ml and cooled to 0°C to precipitate large white block crystals which were collected via vacuum filtration and washed with ice cold water. The product was recrystallised three times from minimum hot H_2O and crystallinity increased remarkably. The identity of the product was confirmed by a unit cell of 10.4Å, 11.0Å, 17.4Å, 74.1°, 77.6°, 72.6°. Yield = 0.94g (45%).

2.4.1.2 $Na_3[La(C_7O_4H_3N)].xH_2O$ (Method 2) – Sodium tris(dipicolinato)lanthanate hydrate

$LaCl_3.6H_2O + 3\ NaOH \rightarrow La(OH)_3 + 3\ NaCl$

Lanthanum (III) chloride hexahydrate (5.00g, 20mmol) was dissolved in H_2O (20ml). Aqueous sodium hydroxide (2.40g, 60mmol) in H_2O (10ml) was added dropwise and a white precipitate formed instantly. The mixture was stirred for 5 minutes and the gelatinous white precipitate collected via vacuum filtration and dried over the pump for ten minutes. The gummy product was suspended in water and stirred for half an hour before isolation via vacuum filtration. The washing procedure was repeated three times. Yield = 2.36g (62%).

$La(OH)_3 + 3\ C_7O_4H_5N + 3\ NaOH \rightarrow Na_3[La(C_7O_4H_3N)_3] + 6\ H_2O$

Lanthanum (III) hydroxide (0.57g, 3mmol) and dipicolinic acid (1.50g, 9mmol) were suspended in H_2O (30ml). Aqueous sodium hydroxide (0.72g, 18mmol) in H_2O (10ml) was added dropwise until pH 7 was reached. The clear solution was heated to reflux for 5 hours, condensed to 10ml and cooled to 0ºC to precipitate white powder. The product was collected via vacuum filtration, washed with ice cold water and recrystallised twice from minimum hot H_2O. The identity of the product was confirmed by a unit cell of 10.4Å, 11.0Å, 17.4Å, 74.1º, 77.6º, 72.6º. Yield = 1.08g (51%).

2.4.1.3$Na_3[Gd(C_7O_4H_3N)_3].xH_2O$ (Method 1[9]) – Sodium tris(dipicolinato)gadolinate

$GdCl_3.6H_2O + 3\ C_7O_4H_5N + 6\ NaOH \rightarrow Na_3[Gd(C_7O_4H_3N)_3] + 6\ H_2O + 3\ NaCl$

Dipicolinic acid (1.50g, 9mmol) was suspended in H_2O (30ml). Aqueous sodium hydroxide (0.72g, 18mmol) in H_2O (10ml) was added dropwise and the solution stirred for five minutes. Gadolinium (III) chloride hexahydrate (0.79g, 3mmol) was added and the reaction mixture heated to reflux for 5 hours before cooling to room temperature. The solution was condensed to 10ml and cooled to 0ºC to precipitate large white block crystals which were collected via vacuum filtration and washed with ice cold water. The product was recrystallised three times from minimum hot H_2O and crystallinity increased remarkably. The identity of the product was confirmed by a unit cell of 10.4Å, 11.0Å, 17.4Å, 74.1º, 77.6º, 72.6º. Yield = 1.35g (62%).

2.4.1.4 $Na_3[Gd(C_7O_4H_3N)].xH_2O$ (Method 2) – Sodium tris(dipicolinato)gadolinate

$GdCl_3.6H_2O + 3\ NaOH \rightarrow Gd(OH)_3 + 3\ NaCl$

Gadolinium (III) chloride hexahydrate (5.26g, 20mmol) was dissolved in H_2O (20ml). Aqueous sodium hydroxide (2.40g, 60mmol) in H_2O (10ml) was added dropwise and a white precipitate formed instantly. The mixture was stirred for 5 minutes and the gummy white precipitate collected via vacuum filtration and dried over the pump for ten minutes. The gummy product was suspended in water and stirred for half an hour before isolation via vacuum filtration. The washing procedure was repeated three times. Yield = 3.34g (80%).

$Gd(OH)_3 + 3\ C_7O_4H_5N + 3\ NaOH \rightarrow Na_3[Gd(C_7O_4H_3N)_3] + 6\ H_2O$

Gadolinium (III) hydroxide (0.62g, 3mmol) and dipicolinic acid (1.50g, 9mmol) were suspended in H_2O (30ml). Aqueous sodium hydroxide (0.72g, 18mmol) in H_2O (10ml) was added dropwise until pH 7 was reached. The clear solution was heated to reflux for 5 hours, condensed to 10ml and cooled to 0ºC to precipitate white powder. The product was collectedvia vacuum filtration, washed with ice cold water and recrystallised twice from minimum hot H_2O. The identity of the product was confirmed by a unit cell of 10.4Å, 11.0Å, 17.4Å, 74.1º, 77.6º, 72.6º. Yield = 1.26g (58%).

2.4.2 Synthesis of Racemic Nine-Coordinate Lanthanide Complexes of the clo Ligand

2.4.2.1 $Na_3[Tb(C_7H_2O_6)_3]$ – Sodium tris(chelidonato)terbate

$C_7H_4O_6 + 2\ NaOH \rightarrow 2Na^+(C_7H_2O_6)^{2-} + 2\ H_2O\ 3[2Na^+(C_7H_2O_6)^{2-}] + TbCl_3.6H_2O \rightarrow Na_3[Tb(C_7H_2O_6)_3] + 3\ NaCl$

Sodium hydroxide (0.24g, 6mmol) in H_2O (20ml) was added dropwise to a stirred solution of chelidonic acid (0.52g, 3mmol) in H_2O (20ml). The pink suspension dissolved and a yellow solution was formed. Terbium (III) chloride hexahydrate (0.26g, 1mmol) dissolved in H_2O (5ml) was added and the reaction mixture stirred at room temperature for 15 hours. During which time a yellow precipitate formed and was removed via vacuum filtration. Excess cold ethanol was added to the filtrate to precipitate light yellow powder which was recrystallised from hot H_2O:EtOH. Yield = 0.58g (69%).

2.5 Synthesis of Metal Trisoxalates

The use of d-block coordination complexes for inclusion into hybrid charge transfer salts allows for the potential of including central metal atoms with unpaired 3 or 4 *d* electrons, leading to cooperative or independent magnetic behaviour. By changing the size and shape of the ligand used to produce these complexes it should be possible to produce charge transfer salts where the coordination sphere of the inorganic anion is the right size to encourage cooperative magnetic effects. Long range magnetic ordering such as ferromagnetism alongside a conductive pathway made possible from the presence of BEDT-TTF within the same material is very interesting and has been shown previously[14,15]. The coordination of a central metal to three identical bidentate ligands will produce an enantiomeric complex with left or right-handed propeller like twists creating a chiral axis through the complex. The racemic metal trisoxalates have afforded the largest family to date of hybrid charge transfer salts and multifunctional materials have been produced, such as paramagnetic superconductors or ferromagnetic metals[16,17]. This is due to the ease of substitution of the central metal, making the synthesis of a family of complexes of differing size and properties relatively easy. The use of central metals of relatively low lability also allows for the chiral resolution of some of these complexes and the potential production of the first chiral superconductor.

2.5.1 $(NH_4)_3[Ir(C_2O_4)_3]$ – Ammonium tris(oxalato)Iridate (III)

Ammonium hexachloroiridate(IV) monohydrate (2.00g, 4.20mmol) and ammonium oxalate monohydrate (17.91g, 12.6mmol) were dissolved in H_2O (40ml) and refluxed for five days. The solution was cooled to room temperature and slowly stirred into 600ml ethanol. The precipitated oxalates were separated via vacuum filtration, washed with ethanol, redissolved in H_2O (ca. 500ml), reduced to 40ml and refluxed for five further days. The ethanol precipitate procedure was repeated. Tetrabutylammonium sulphate (4.20g, 12.6mmol) was added to the aqueous solution and the product was extracted with nitromethane (6 x 25ml). The combined extracts were dried in vacuo and the gummy product was dissolved in ca. 60ml dichloromethane, filtered to remove a small amount of white impurity and evaporated to dryness. The final product was then dissolved in 100ml ethanol and precipitated with ammonium acetate (1.94g, 25.20mmol) in ethanol (100ml), collected via vacuum filtration and washed with ethanol. The product was dissolved in minimum H_2O and stored over ethanol to produce gold needles[18]. The identity of the product was confirmed by a unit cell of 12.6Å, 11.5Å, 21.2Å, 90º, 95.9º, 90º. Yield = 1.07g (50%).

2.5.2 $(NH_4)_3[Cr(C_2O_4)_3]$ – Ammonium tris(oxalato)chromate(III)

This was prepared previously by Dr Lee Martin and used as received.

2.6 References

1. J. Larsen and C. Lenoir, Synthesis, 1988, **2** ,134.
2. M. Mizuno, A. F. Garito and M. P. Cava, *J. Chem. Soc. Chem. Commun.*, 18, 1978.
3. J. D. Wallis and J.-P. Griffiths, *J. Mater. Chem.*, 2005, **15**, 347; N. Avarvari and J. D. Wallis, *J. Mater. Chem*, 2009, **24**, 4061.
4. H. H. Wang, J. R. Ferraro, J. M. Williams, U. Geiser and J. A. Schlueter, *J. Chem. Soc., Chem. Commun*., 1994, 1893.
5. V. Kochkodan, N. B. Darwish and N. Hilal, *The Chemistry of Boron in Water, in Boron Separation Processes*, Publisher: Elsevier, Editors: Nalan Kabay, Nidal Hilal, Marek Bryak, pp.35-62
6. I. I. Zviedre and S. V. Belyakov, *Russ. J. Inorg. Chem.*, 2007, **52(5)**, 686.
7. D. B. Llewellyn and B. A. Arndtsen, *Tetrahedron: Asymmetry*, 2005, **16**, 1789.
8. R. Gausepohl, P. Buskens, J. Kleinen, A. Bruckmann, C. W. Lehmann, J. Klankermayer and W. Leitner, *Angew. Chem. Int. Ed*., 2006, **45**, 3689.
9. C. Reinhard and H. U. Guidel, *Inorg. Chem.*, 2002, **41(5)**, 1048.

10. P. P. Lima and O. L. Malta e Severino Alves Júnior, *Quim. Nova,* 2005, **28(5)**, 805.

11. S. K. Ghosh and P. K. Bharadwaj, *Inorg. Chem,*. 2004, **43**, 2293.

12. J-G. Kang, T-J. Kim, H-J. Kang and S. K. Kang, *J. Photochem. Photobiol. A: Chem.*, 2005, **174**, 28.

13. A. Lennartson and M. Håkansson, *CrystEngComm,* 2009, **11**, 1979.

14. E. Coronado, J. R. Galán-Mascarós, C. J. Gómez-García, V. Laukhin, Nature, 408 (2000) 447.

15. A. Alberola, E. Coronado, J. R. Galán-Mascarós, C. Giménez-Saiz and C. J. Gómez-García, *J. Am. Chem. Soc.,* 2003, **125**, 10774.

16. A. W. Graham, M. Kurmoo and P. Day, *J. Chem. Soc. Chem. Commun*., 1995, 2061.

17. L. Martin, S. S. Turner, P. Day, P. Guionneau, J. A. K. Howard, D. E. Hibbs, M. E. Light, M. B. Hursthouse, M. Uruichi and K. Yakushi, *Inorg. Chem*., 2001, **40**, 1363.

18. H. G. Kruszyna, I. Bodek, L. K. Libby and R. M. Milburn, *Inorg. Chem.,* 1974, **13(2)**, 435.

Chapter 3: Chiral Donor Charge Transfer Salts

Chiral donor charge transfer salts have proved a fruitful area in which to design multifunctional materials[1,2] and also to study eMChA in radical cation salts[3,4]. The synthetic research group of Professor John Wallis at NTU are one of very few groups to produce novel chiral donors for the sole purpose of the production of multifunctional conducting materials[5-7]. As such, there is a large variety of chiral donors available for crystal engineering. In this chapter is discussed three new groups of chiral and racemic radical cation salts.

The first group to be investigated are two new families of isostructural 1:1 radical salts of the EDT-TTF derivative bis(2-hydroxypropylthio)ethylenedithiotetrathiafulvalene, BHP-EDT-TTF. This group of novel materials are semiconductors with modest activation energies and the long sidechain containing a chiral carbon centre on the donor molecule appears to play an important role in the formation of the lattice during crystal growth. The results of physical and structural characterisation are discussed and a comparison is made between the three families. These salts are some of very few enantiopure charge transfer salts to have been synthesised and it follows that a deeper understanding of how chirality stemming from the radical cation can affect the conducting properties of a material has been gained.

The second family of salts to be investigated is a large family of non-isostructural radical salts containing the BEDT-TTF derivative bis(2-hydroxymethyl)ethylenedithiotetrathiafulvalene (BHM-BEDT-TTF). This new family of salts are semiconductors, with large difference in stoichiometry between salts. Some of the less common donor packing motifs have been observed. The physical and structural characterisation offers a deep insight into the properties of the donor and a new route to producing novel multifunctional conducting materials.

3.1 Bis(hydroxypropylthio)ethylenedithiotetrathiafulvalene BHP-EDT-TTF

The TTF based donor molecule bis(2-hydroxypropylthio)ethylenedithiotetrathiafulvalene (Figure 3.1) can be synthesised from *R*, *S* or *racemic* methyl oxirane (propylene oxide) as starting material. Synthesis of the racemic analogue actually produces an inseparable statistical mixture of compounds, the *meso* form (1:1:2, *R,R*:*S,S*:*R,S*). During the discussion in this section (3.1) the term *meso* and *racemic* will be considered interchangeable.

Hydroxyl groups are positioned on the extremities of chiral sidechains with the intent of increasing non-covalent interactions between the radical cation and anion throughout crystal engineering. The donor has the potential to form hydrogen bonds through its chiral 2-hydroxypropylthio sidechains and the flexible sidechains can adopt a number of different orientations throughout the lattice. Electrocrystallisation of BHM-EDT-TTF has previously produced a family of tri-iodides[8] in which the isostructural enantiomers display semiconducting behaviour and the racemates display completely different lattices and are insulators. In this section is discussed three isostructural semiconducting families of chiral and racemic salts, produced from the monovalent BF_4^-, ClO_4^- and PF_6^- anions respectively. The structural and physical characteristics have been investigated and a possible explanation for the observed properties through chiral influence is suggested.

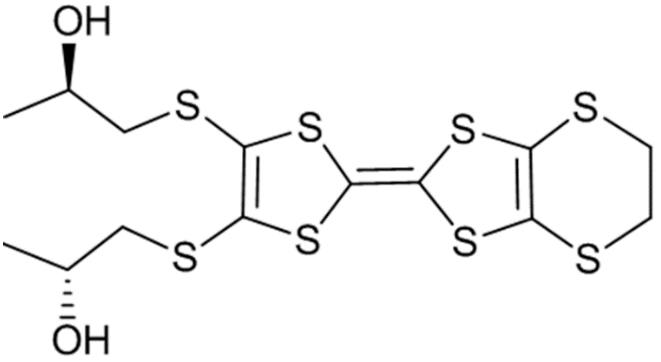

Figure 3.1. Chemdraw representation of BHP-EDT-TTF.

3.1.1 BHP-EDT-TTF salts with BF_4^-, PF_6^-, or ClO_4^-

Three salts of the title compound are discussed. *S,S*-BHP-EDT-TTF.X and *R,R*-BHP-EDT-TTF.X are isostructural while the disordered *meso*-BHP-EDT-TTF.X forms an almost isostructural lattice (X = BF_4, ClO_4 and PF_6). The results for the salts were published[9,10]. Synthetic procedures, structural and physical property characterisation are presented below.

3.1.2 Electrocrystallisation Table

Donor	**Counterion**	**Electrolyte**	**Solvent**	**Current /µA**	**Crystal Growth**	**Observation**
S,*S*-BHM-EDT-TTF	TBA^+	$BF_4^-/ClO_4^-/PF_6^-$	PhCl	0.1	YES – Collected after three weeks.	Large quantity of black needles were collected from the electrode.
R,*R*-BHM-EDT-TTF	TBA^+	$BF_4^-/ClO_4^-/PF_6^-$	PhCl	0.1	YES – Collected after three weeks	Large quantity of black needles were collected from the electrode.
meso-BHM-EDT-TTF	TBA^+	$BF_4^-/ClO_4^-/PF_6^-$	PhCl	0.1	YES – collected after three weeks.	Large quantity of black needles were collected from the electrode.
S,*S*:*R*,*R*-BHM-EDT-TTF (50:50)	TBA^+	$BF_4^-/ClO_4^-/PF_6^-$	PhCl	0.5-1.1	NO	Black amorphous solid was collected from the electrode.

Table 3.1.1. Electrocrystallisation table for synthesis of enantiopure and racemic salts of CTS 3.1.

In all cases presented in table 3.1.1 above, chlorobenzene produced crystals of superior quality when compared with other organic solvents. Crystal engineering of an analogue containing a true racemic mixture of the *S*,*S* and *R*,*R* enantiomers was attempted, however it is clear that to obtain an exact mixture of both enantiomers through a measurement by mass method is almost impossible and no crystal growth was observed. The long needle shaped crystals of the *S*,*S*, *R*,*R* and *rac/meso* analogues were extremely thin, with dimension typically in the range (0.001 - 0.005) x (0.001 – 0.005) x (0.005 – 0.01 mm).

3.1.3 Crystal Structures

S,S*-BHP-EDT-TTF.*X			
	BF_4^-	***ClO_4^-***	***PF_6^-***
Formula	$C_{14}H_{18}O_2S_8F_4B$	$C_{14}H_{18}O_6S_8Cl$	$C_{14}H_{18}O_2S_8F_6P$
M_r/g mol^{-1}	561.58	574.28	619.74
Temp / K	293.1	296.1	298.0
Radiation	Mo Kα	Mo Kα	Mo Kα
Wavelength	0.7107	0.7107	0.7107
Crystal System	Orthorhombic	Orthorhombic	Orthorhombic
Space group	$C222_1$	$C222_1$	$C222_1$
a / Å	7.8100(13)	7.8561(6)	7.937(7)
b / Å	21.238(4)	21.2753(16)	21.4936(16)
c / Å	26.989(5)	27.155(2)	27.622(3)
α / °	90	90	90
β / °	90	90	90
γ / °	90	90	90
V/Å^3	4476.6(13)	4538.6(6)	4712.3(7)
Z	8	8	8
ρ/g cm^{-1}	1.666	1.681	1.747
μ/cm^{-1}	8.416	9.338	8.844
Absorption Applied	Yes	Yes	Yes
Abs. Type	Numerical	Numerical	Numerical
Abs. Range	0.786 – 0.968	0.860 – 0.966	0.893 – 0.966
Total Reflections	17369	15558	24711
Unique Reflections	5151	5099	5293
R [all data]	0.0761	0.0811	0.0557
R_1 [$I > 2\sigma(I)$]	0.0647	0.0589	0.0517
wR [all data]	0.2003	0.1424	0.1618
Goodness of fit	1.299	1.052	1.199
Refinement Program	SHELX	SHELX	SHELX
Refinement Mode	F^2	Single	Single
Flack Parameter	-0.01(17)	-0.09(15)	0.07(12)

Table 3.1.2. X-ray data for *S,S* enantiomers CTS 3.1.

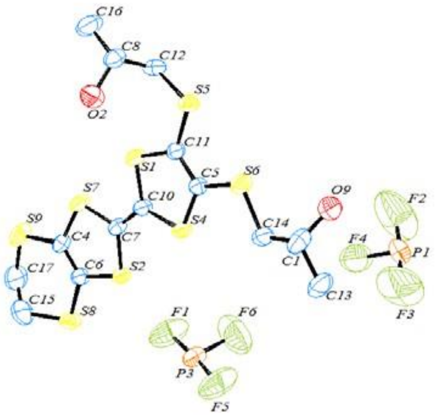

Figure 3.1.1. ORTEP diagram of asymmetric unit of enantiopure *S,S* CTS 3.1, PF_6 analogue. Displacement ellipsoids are drawn at the 50% level. Hydrogens are omitted for clarity.

R*,*R*-BHP-EDT-TTF.*X			
	BF_4^-	ClO_4^-	PF_6^-
Formula	$C_{14}H_{18}O_2S_8F_4B$	$C_{14}H_{18}O_6S_8Cl$	$C_{14}H_{18}O_2S_8F_6P$
M_r/g mol^{-1}	561.58	572.21	619.73
Temp / K	293.1	293.0	100.2
Radiation	Mo Kα	Mo Kα	Mo Kα
Wavelength	0.7107	0.7107	0.7107
Crystal System	Orthorhombic	Orthorhombic	Orthorhombic
Space group	$C222_1$	$C222_1$	$C222_1$
a / Å	7.8172(13)	7.707(16)	7.8564(18)
b / Å	21.232(4)	21.04(4)	21.389(5)
c / Å	26.987(5)	26.59(5)	27.036(6)
α / °	90	90	90
β / °	90	90	90
γ / °	90	90	90
V/Å^3	4479.1(13)	4312(15)	4543.1(18)
Z	8	8	8
ρ/g cm^{-1}	1.665	1.769	1.812
μ/cm^{-1}	8.401	0.906	0.9.18
Absorption Applied	Yes	Yes	No
Abs. Type	Numerical	Semi-empirical	n/a
Abs. Range	0.808 – 0.958	0.237 – 1.000	n/a
Total Reflections	17569	9727	11781
Unique Reflections	5132	3893	4938
R [all data]	0.0919	0.2257	0.0700
R_1 [$I > 2\sigma(I)$]	0.0678	0.1393	0.0678
wR [all data]	0.1812	0.3991	0.1550
Goodness of fit	1.029	1.031	1.205
Refinement Program	SHELX	SHELX	SHELX
Refinement Mode	F^2	F^2	F^2
Flack Parameter	-0.03(19)	-0.2(5)	0.08(7)

Table 3.1.3. X-ray data for *R,R* enantiomers of CTS 3.1.

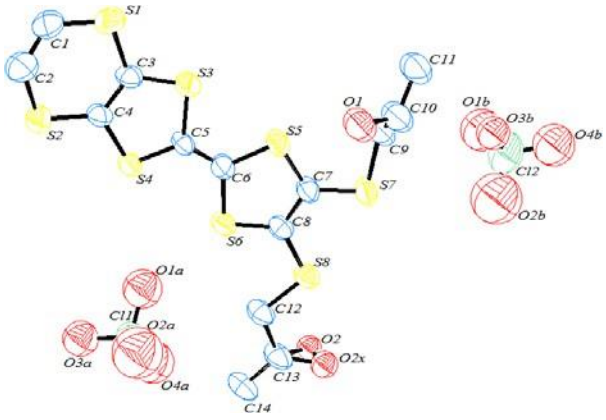

Figure 3.1.2. ORTEP diagram of asymmetric unit of enantiopure *R,R* CTS 3.1, PF_6 analogue. Displacement ellipsoids are drawn at the 50% level. Hydrogens are omitted for clarity.

rac/meso*-BHP-EDT-TTF.*X			
	BF_4^-	***ClO_4^-***	***PF_6^-***
Formula	$C_{14}H_{18}O_2S_8F_4B$	$C_{14}H_{18}O_6S_8Cl$	$C_{14}H_{18}O_2S_8F_6P$
M_r/g mol^{-1}	561.58	571.19	619.73
Temp / K	300.1	100.0(2)	298.0
Radiation	Mo Kα	Mo Kα	Mo Kα
Wavelength	0.7107	0.7107	0.7107
Crystal System	Monoclinic	Monoclinic	Monoclinic
Space group	C2/$_c$	C2/*c*	C2/*c*
a / Å	7.807(3)	7.6787(3)	7.958(14)
b / Å	21.223(6)	21.1403(8)	21.560(4)
c / Å	26.992(7)	26.7794(10)	26.950(5)
α / °	90	90	90
β / °	91.394(7)	91.782(4)	93.670(2)
γ / °	90	90	90
V/Å^3	4471.0(3)	4345.0(3)	4614(15)
Z	8	8	8
ρ/g cm^{-1}	1.669	1.749	1.784
μ/cm^{-1}	8.416	0.976	0.833
Absorption Applied	Yes	Yes	Yes
Abs. Type	Numerical	Multi-scan	Multi-scan
Abs. Range	0.849 – 0.981	0.666 – 1.000	0.312 – 1.000
Total Reflections	17283	4444	14353
Unique Reflections	4994	3360	6683
R [all data]	0.1770	0.1332	0.2707
R_1 [$I > 2\sigma(I)$]	0.1062	0.1053	0.1796
wR [all data]	0.3351	0.2478	0.4803
Goodness of fit	1.419	1.161	1.050
Refinement Program	SHELX	SHELX	SHELX
Refinement Mode	F^2	F^2	F^2
Flack Parameter	n/a	n/a	n/a

Table 3.1.4. X-ray Data for racemic CTS 3.1.

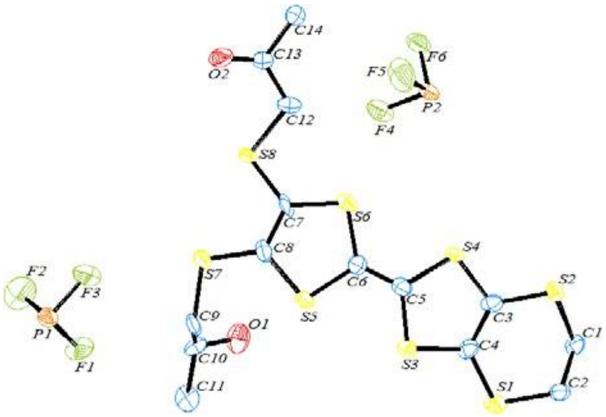

Figure 3.1.3. ORTEP diagram of asymmetric unit of enantiopure *S,S* CTS 3.1, PF_6 analogue.

Displacement ellipsoids are drawn at the 50% level. Hydrogens are omitted for clarity.

Both *S*,*S*-BHP-EDT-TTF.X and *R*,*R*-BHP-EDT-TTF.X (X = PF_6^-, ClO_4^-, BF_4^-) crystallise in the orthorhombic crystal system in the chiral space group $C222_1$, whilst *meso*-BHP-EDT-TTF.X crystallises in monoclinic C2/*c* (Tables 3.1.2-3.1.4). The asymmetric unit of all three salts have one donor molecule and two crystallographically independent anions. Both anions lie on symmetry elements, a 2-fold axis for the enantiomers and a centre of symmetry for the meso/racemate. The chiral $C222_1$ unit cell for *S,S*-BHP-EDT-TTF.PF_6 is shown below in Figure 3.1.4.

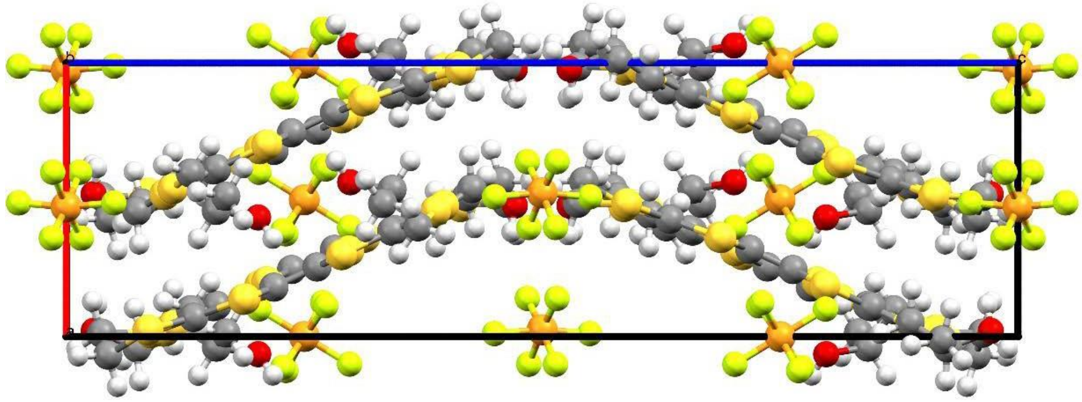

Figure 3.1.4. Unit cell of CTS 3.1, *S,S*-BHP-EDT-TTF.PF_6

For the BF_4^- family of salts the non-hydrogen atoms were refined with anisotropic displacement parameters apart from BF_4^- anions of the *meso/rac* salt, which were refined isotropically. In all the enantiopure salts the anions appear disordered with F and O atoms modelled over two partially occupied sites, apart from the *S,S*-BHP-EDT-TTF.PF_6 salt where the anions are not disordered. There is disorder present in one OH group of *R,R*-BHP-EDT-TTF.ClO_4 with the oxygen modelled over two partially occupied sites (0.75/0.25 occupancy). The anions in *Rac/meso*-BHP-EDT-TTF.ClO_4 are both disordered with oxygen atoms modelled over two partially occupied sites and occupancy competitively refined. Static disorder is also present on both OH groups with two possible positions for the oxygen depending on the chirality of the molecule.

In all nine salts the donor molecules form stacks in the *a* direction (Figure 3.1.5) with neighbouring stacks segregated in the *b* direction by anions. In the enantiopure salts, the best planes of donor cations lie at ca. 68° to the stacking axis, this causes an ABAB stacking through the *c* direction. In the racemic salts each plane of donors lies at the same angle to the stacking axis, causing an AAA stacking through the c direction (Figure 3.1.6). Pairs of donors, related by a 2-fold axis, are dimerised face-to-face with short S…S contacts between the four central TTF sulfur atoms as shown in Figure 3.1.8. S…S contacts are similar in both enantiopure and rac/meso salts (Table 3.1.5). Donors within each dimer are orientated such that the terminal ethylene groups are lying above the stereogenic centre of the donor below. The top donor of each dimer lies level with the bottom donor in adjacent pairs. The plane–plane distance between donors in all three salts are similar: ca. 3.37 Å within a pair, and ca. 3.77 Å between pairs, despite the different crystal systems. Adjacent pairs are slipped by ca. 2.3 Å, while within a pair the slip distance is ca. 0.9 Å. The ethylene groups on each donor molecule hold a twist confirmation and each anion occupies the cavity between the outlying 2-hydroxypropylthio side chains.

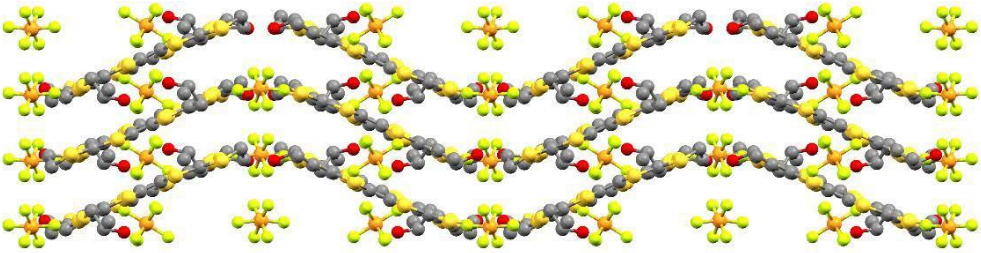

Figure 3.1.5. Lattice packing of enantiopure CTS 3.1 viewed along the *b* axis. The salt shown here is *S,S*-BHP-EDT-TTF.PF_6.

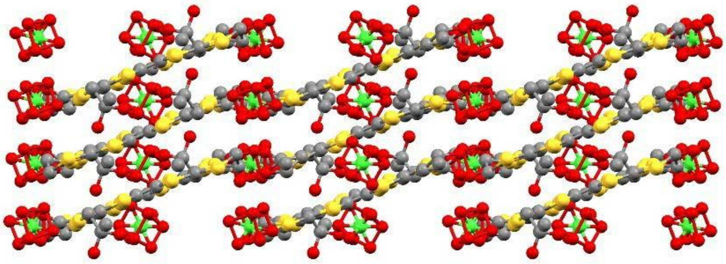

Figure 3.1.6. Lattice packing of racemic CTS 3.1 viewed along the *b* axis. Salt shown here is *rac/meso*-BHP-EDT-TTF.ClO_4

There are no S…S contacts observed between stacks, creating a charge localisation between dimers. The space group of the chiral salts indicates a 2_1 screw in the c axis, however the direction of charge transport does not lie on these symmetry elements neither does it follow the same direction.

The central C=C bond lengths in all cases are close to the value expected for a TTF donor charge of 1^+ (Table 3.1.6). For the enantiopure salts the two hydroxylated side chains adopt different conformations, one lies in the donor plane and directed out from the donor towards an anion, while the other bends down under the donor. Dimer pairs are likely to be connected by hydrogen bonding, since two symmetry related oxygen atoms from the latter type of side chains lie ca. 2.8 Å apart in both enantiomers. There is a long O···H–C contact from the other side chain to the ethylene bridge of a donor molecule (2.57 Å *R*,*R*-isomer).

For the *rac/meso* salt, the overall conformation of the donors is very similar to that in the enantiomeric salts (Figure 3.1.6), but there are two positions for each hydroxyl oxygen atom. For the side chain directed out from the donor, both O positions are directed towards anions. For the other side chain, one oxygen position corresponds to those involved in a hydrogen bond between donor pairs, while the other is directed towards an anion.

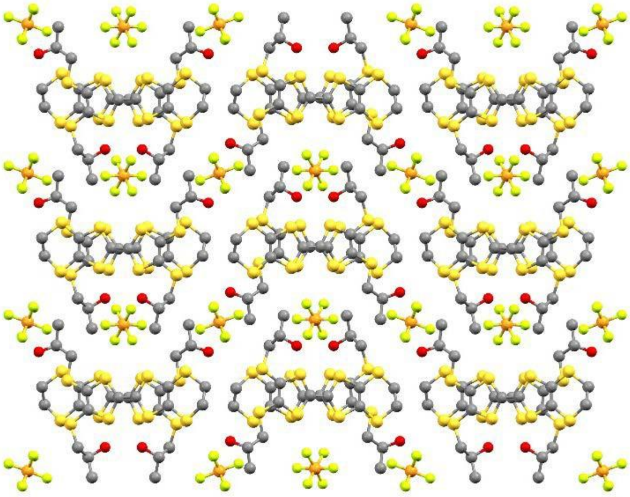

Figure 3.1.7. Lattice packing of enantiopure CTS 3.1 viewed along the *a* axis. The salt shown here is *S,S*-BHP-EDT-TTF.PF_6

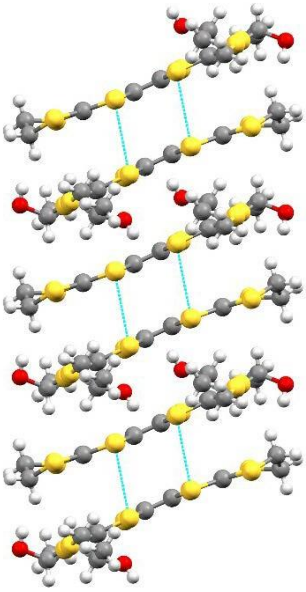

Figure 3.1.8. Single donor stack in CTS 3.1. S...S contacts within dimers are shown in light blue. The salt shown here is *S,S*-BHP-EDT-TTF.PF_6

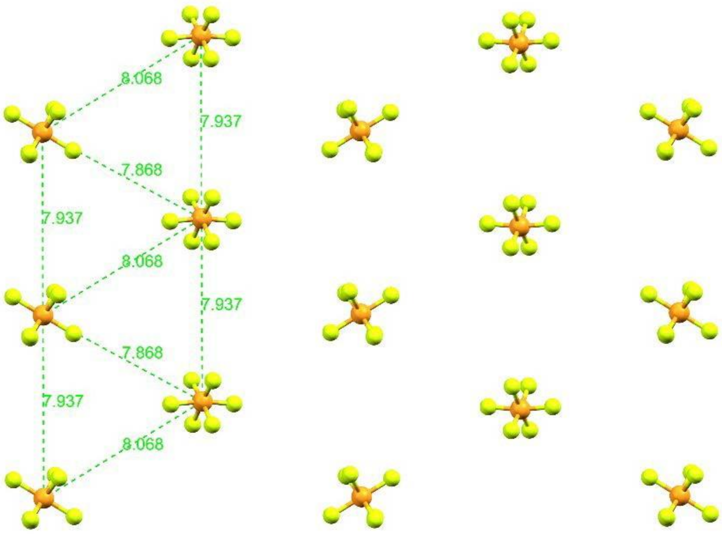

Figure 3.1.9. PF_6^- layer in enantiopure CTS 3.1. Long P...P contacts are shown in green dotted lines and P...P distances are shown in angstroms. Viewed along the *c* direction.

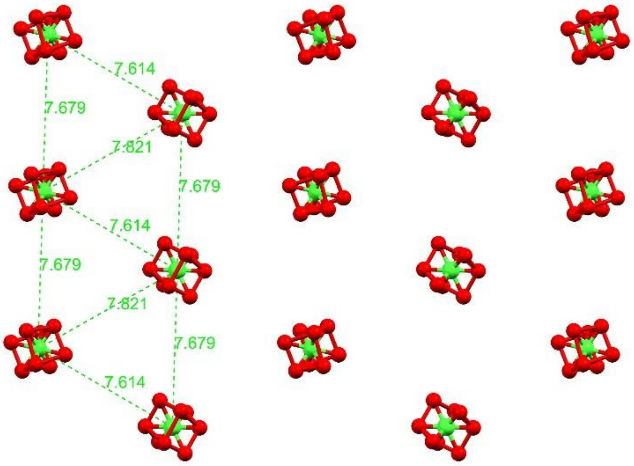

Figure 3.1.10. ClO_4^- layer in racemic CTS 3.1. Oxygens are modelled as two partially occupied sites (50:50). Long Cl...Cl contacts are shown in green dotted lines and Cl...Cl distances are shown in angstroms. Viewed along the *c* direction

Figure 3.1.9 and 3.1.10 displays the packing arrangement of the anions for the enantiopure PF_6^- salt and the racemic ClO_4^- salt. The packing and inter atomic distances (green dotted lines, numbers are distance in angstroms) are similar. P-F bonds range from 1.450(1) – 1.579(1) Å and Cl-O bonds range from 1.330(1) – 1.500(1) Å.

Two short contacts exist between sulphur atoms and outlying hydroxyl groups. Each central sulphur of the crystallographically independent donor molecule makes a S…O contact with the chiral side-chain that is directed under the donor, one with the oxygen on the same molecule (S1...O2, 2.970 Å) and one with the oxygen on the donor from a neighbouring dimer (S7...O2, 3.275 Å). One O…O contact exists between these two sidechains (O2...O2, 2.863 Å).

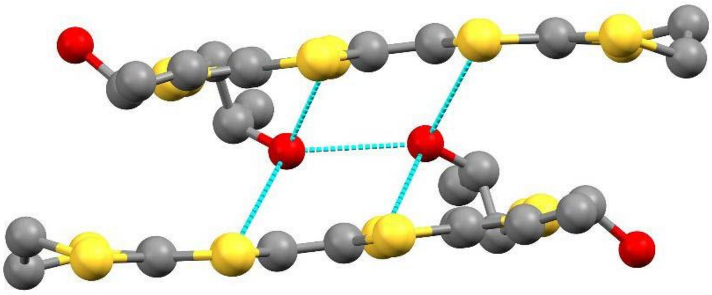

Figure 3.1.11. Orientation of short contacts between donors of separate dimer pairs in CTS 3.1 are shown in light blue.

3.1.4 S...S Contacts

	BF$_4$	***ClO$_4$***	***PF$_6$***
S,S			
S3…S5 / Å	3.557(2)	3.565(1)	3.613(1)
S4…S6 / Å	3.466(2)	3.475(1)	3.524(1)
R,R			
S3...S5 / Å	3.562(2)	3.586(1)	3.527(1)
S4...S6 / Å	3.468(2)	3.502(1)	3.450(1)
rac/meso			
S3...S5 / Å	3.560(4)	3.586(1)	3.527(1)
S4...S6 / Å	3.476(4)	3.502(1)	3.450(1)

Table 3.1.5. Short sulphur interactions below the sum of the vdW radii (3.6 Å) are shown for both the racemic and enantiopure salts for all three families. Figure 3.1.3 shows atom numbering scheme.

The short sulphur interactions below the sum of the vdW radii (3.6 Å) are shown above in Table 3.1.5. Each dimer makes four short face-to-face contacts through the four central sulfurs of each donor. The BF_4^- salts show very little difference between the enantiopure and racemic salts. The S...S contacts in the ClO_4^- salts are the same for the R,R enantiomer and the racemate, and slightly shorter for the S,S enantiomer. *S,S*-BHP-EDT-TTF.PF_6 salt has significantly longer contacts. The value observed for the S3...S5 contact is above that needed for efficient pi orbital overlap (3.60 Å) while the *R,R* enantiomer and racemate have the same values for both contacts. It is noted that structural data for the *R,R* enantiomer was collected at low temperature while data for the racemate was collected at room temperature. However, the high R factor for the racemic PF_6^- crystal structure makes the values unreliable.

3.1.5 C=C Bond Length, Charge Calculations and Raman

	BF$_4$	***ClO$_4$***	***PF$_6$***
S,S			
C=C Bond Length / Å	1.400(5)	1.402(7)	1.379(1)
R,R			
C=C Bond Length / Å	1.398(6)	1.400(4)	1.381(1)
rac/meso			
C=C Bond Length / Å	1.389(10)	1.361(1)	1.364(1)

Table 3.1.6. CTS 3.1: Central C=C bond lengths for both the racemic and enantiopure salts of all three families.

The central TTF C=C bond lengths for the enantiopure and racemic salts are consistent with that expected of a TTF donor of charge 1^+. The central bond lengths of the racemic salts are slightly shorter than the enantiomers within each family.

	S,S*-BHP-EDT-TTF.*ClO$_4$	***R,R*-BHP-EDT-TTF.*ClO$_4$***	***meso*-BHP-EDT-TTF.*ClO$_4$***
a / Å	1.402	1.404	1.361
b / Å	1.721	1.73	1.730
c / Å	1.736	1.745	1.732
d / Å	1.365	1.382	1.368
δ	0.69	0.689	0.733
Q	**1.198 (1^+)**	**1.205 (1^+)**	**0.877 (1^+)**

Table 3.1.7. Donor charge calculations for racemic and enantiopure ClO_4^- salts[11] estimated as 1^+.

	***S,S*-BHP-EDT-TTF.PF$_6$**	***R,R*-BHP-EDT-TTF.PF$_6$**	***Meso*-BHP-EDT-TTF.PF$_6$**
***a* / Å**	1.379	1.381	1.364
***b* / Å**	1.726	1.729	1.744
***c* / Å**	1.737	1.740	1.721
***d* / Å**	1.368	1.360	1.434
δ	0.716	0.728	0.667
Q	**1.003 (1^+)**	**0.914 (1^+)**	**1.369 (1^+)**

Table 3.1.8. Donor charge calculations for racemic and enantiopure PF_6^- salts[11].

The original method for estimating the donor charge was designed only for BEDT-TTF radical cation salts[11]. Therefore the presence of the chiral side chain on the BHP-EDT-TTF donor molecule will have an effect on the results. However, the values of charge for all the salts are consistent with a donor charge of 1^+. The donor charge in the racemic ClO_4^- salt is skewed negatively with respect to the enantiopure salts, however it is still consistent with a donor charge of $^+1$ given the inaccuracy of the calculation due to the presence of the chiral sidechains. The donor charge in the racemic PF_6^- salt is much higher than expected however, this result is likely to be unreliable due to the high error in the crystal structure.

Wang *et al.*[11] previously found that an approximately linear dependence exists between the degree of charge transfer and the Raman active C=C stretching frequencies in conducting salts of the BEDT-TTF donor molecule. Correlation of the υ_4 and υ_3 symmetric C=C vibration frequencies with oxidation states of the BEDT-TTF donor in 1:1 radical cation salts, showed that the Raman shift for the υ_4 and υ_3 vibration frequencies exist between 1400-1420 and 1450-1470 cm^{-1} respectively.

Consequently, the donor under investigation in this section isn't BEDT-TTF, rather an EDT-TTF derivative and therefore it can be concluded that the values presented by Wang *et al.*[11] will not be entirely accurate, due to the presence of the side-chains and the different molecular structure. However, there are still two totally symmetrical C=C bonds that correspond to the υ_4 and υ_3 vibration frequencies.

Reproducible room temperature Raman scattering experiments were performed on several crystals of the (*S*,*S*) and (*R*,*R*) enantiomers for both the ClO_4^- and PF_6^- salts. High intensity peaks (>150) are observed at shifts of 1375-1376 and 1472-1474 cm^{-1} in each of the four salts. These peaks almost certainly correspond to the υ_4 and υ_3 totally symmetrical C=C vibration frequencies for a donor cation of $^{+}1$ charge. The smaller peak observed in between these two values may be due to some other Raman active stretching frequency present in the donor molecule but is impossible to assign to a specific bond. The results are therefore in good agreement with experimental data collected on 1:1 BEDT-TTF salts.

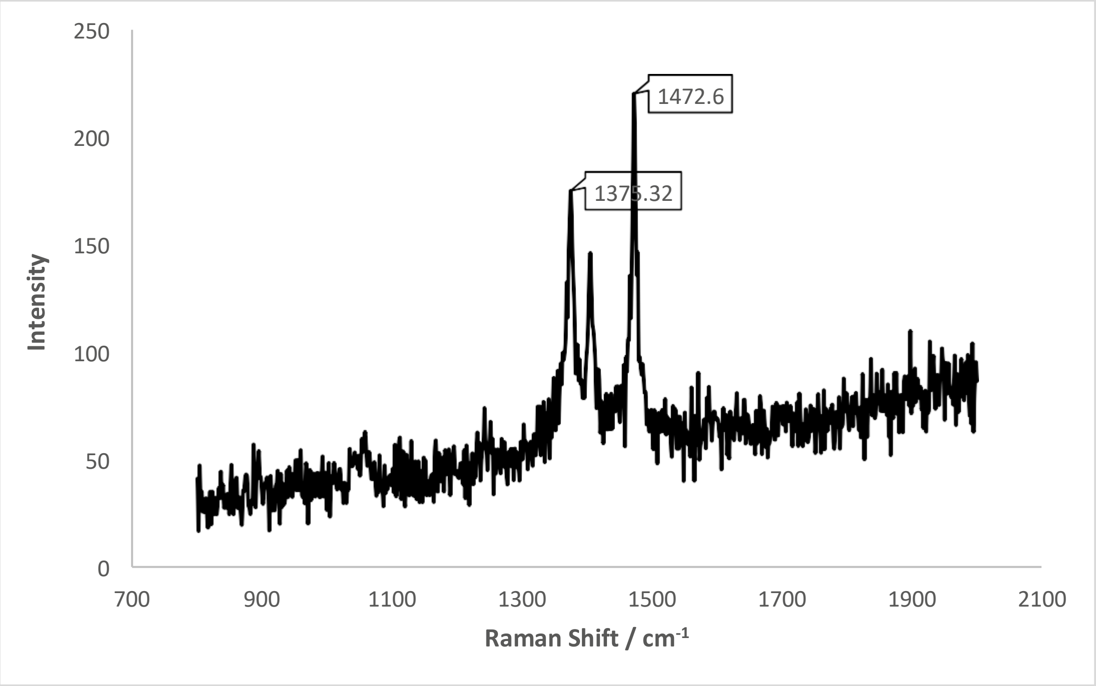

Graph 3.1.1. Relative intensity of Raman shifts for *S,S*-BHP-EDT-TTF.ClO_4. The high intensity Raman shifts are labelled.

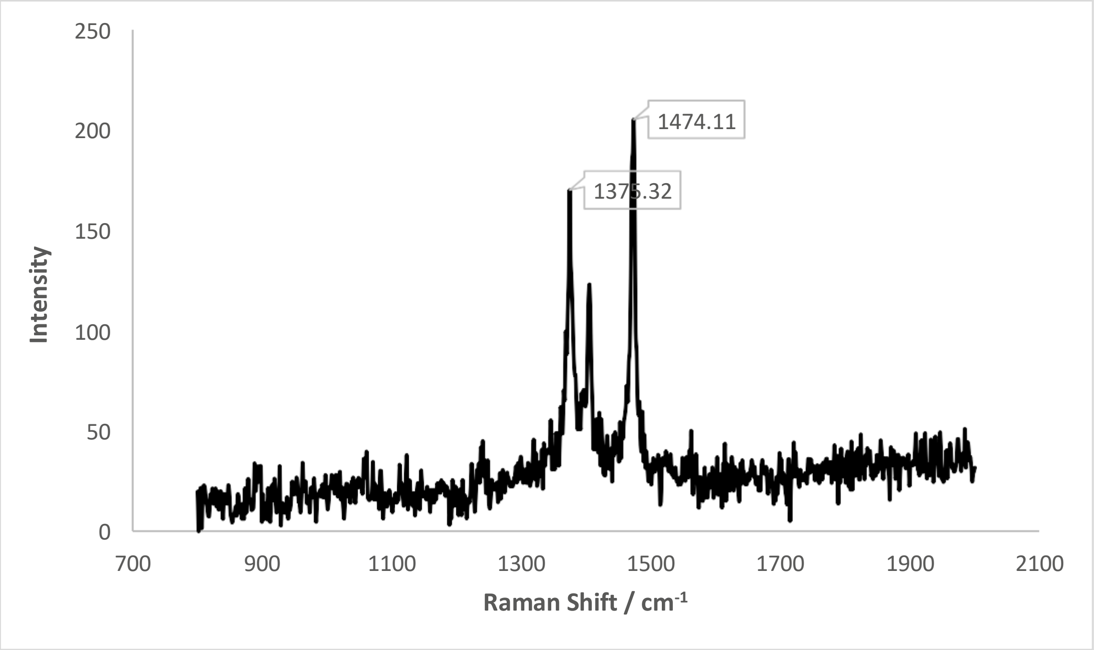

Graph 3.1.2. Relative intensity of Raman shifts for *R*,*R*-BHP-EDT-TTF.ClO_4. The high intensity Raman shifts are labelled.

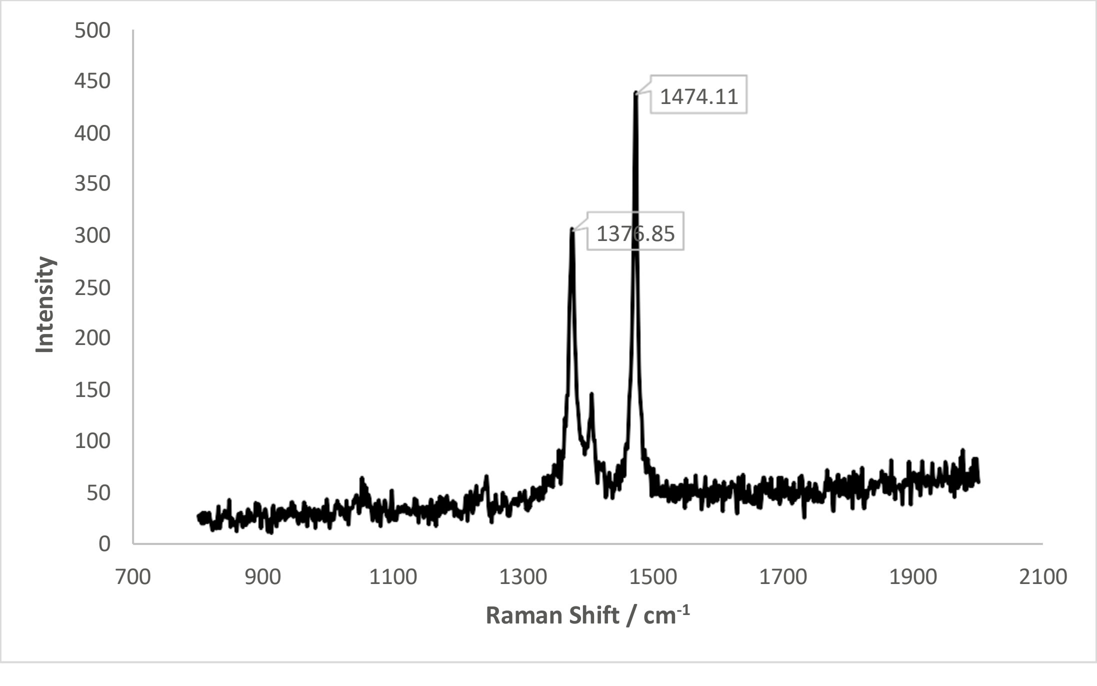

Graph 3.1.3. Relative intensity of Raman shifts for *S*,*S*-BHP-EDT-TTF.PF_6. The high intensity Raman shifts are labelled.

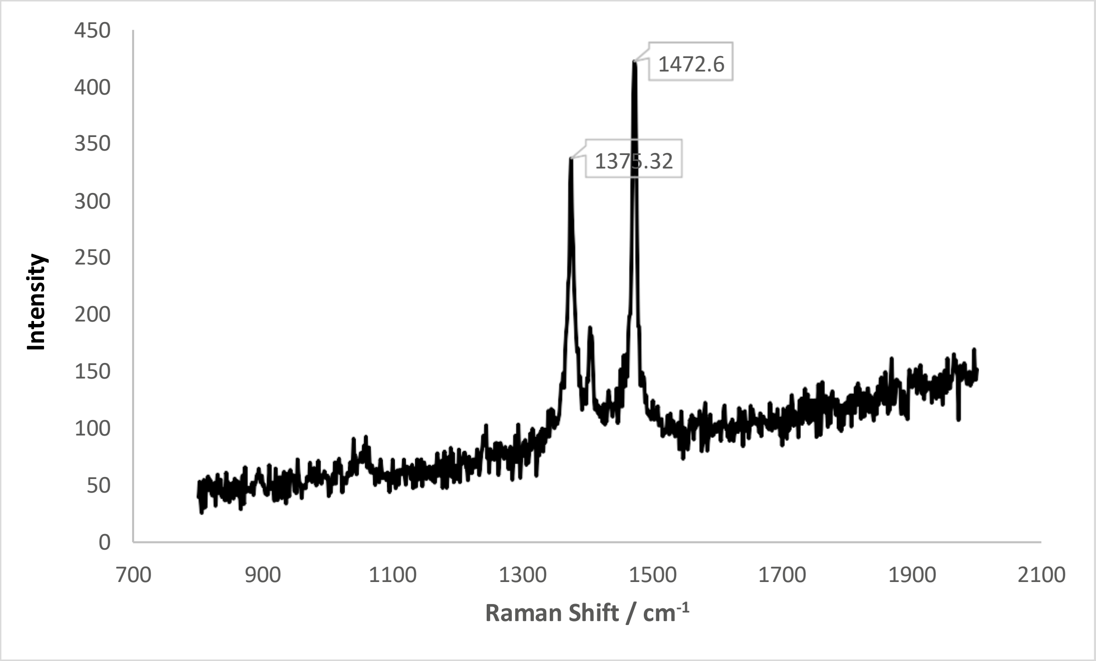

Graph 3.1.4. Relative intensity of Raman shifts for *R*,*R*-BHP-EDT-TTF.PF_6. High intensity Raman shifts are labelled.

3.1.6 Resistivity Data

	***S,S*-BHP-EDT-TTF.BF_4**	***R,R*-BHP-EDT-TTF.BF_4**	***Meso*-BHP-EDT-TTF.BF_4**
E_a (A)	0.218 eV	0.244 eV	0.156 eV
ρRT (A)	1.3 x 10^3 Ohm.cm	2.9 x 10^4 Ohm.cm	1.6 x 10^3 Ohm.cm
E_a (B)	0.205 eV	0.202 eV	0.167 eV
ρRT (B)	2.0 x 10^3 Ohm.cm	1.1 x 10^3 Ohm.cm	8.6 x 10^2 Ohm.cm

Table 3.1.9. Activation energy and room temperature resistivity for two different samples (A and B) of racemic and enantiopure BF_4^- salts.

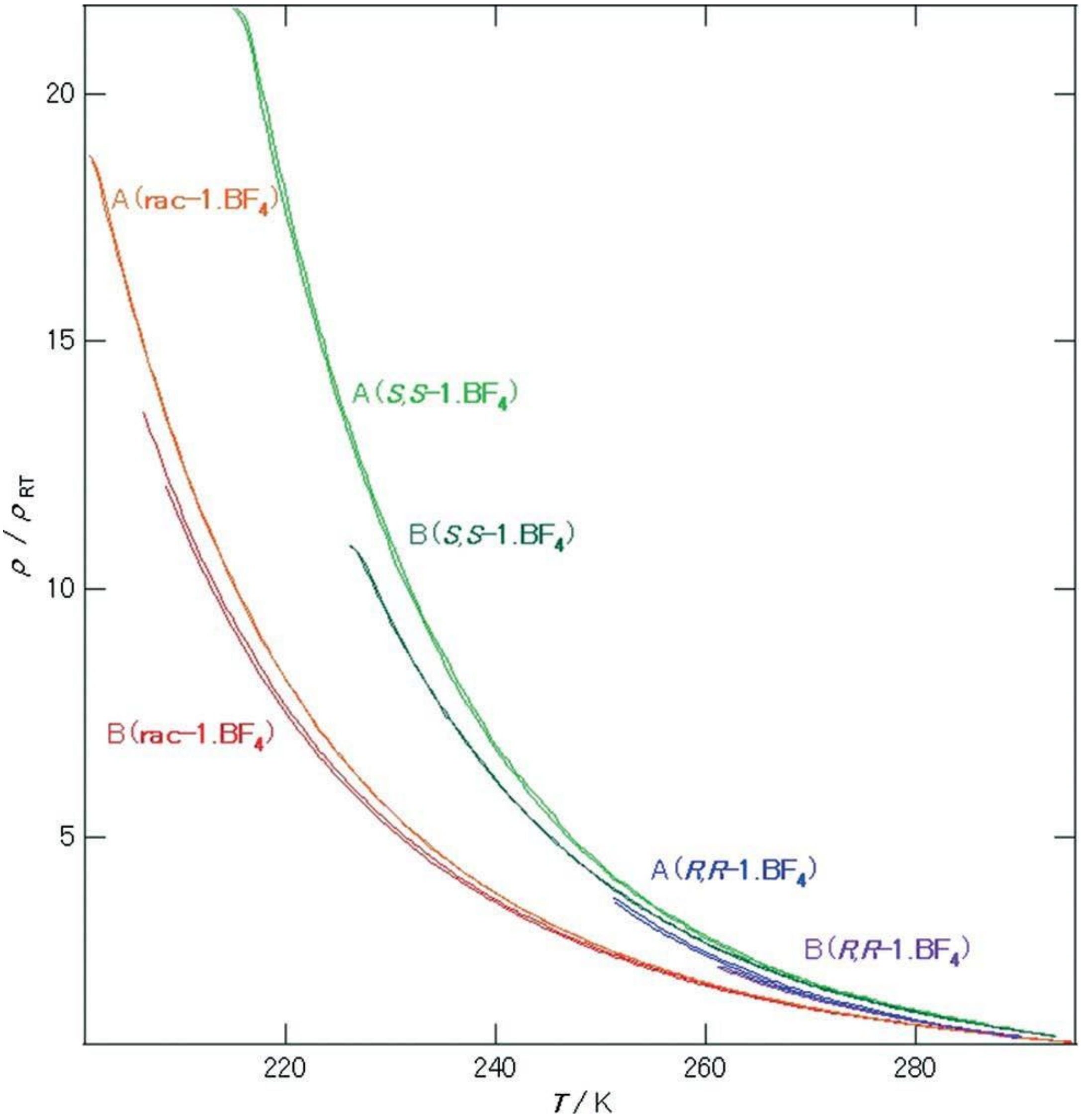

Graph 3.1.5. Temperature dependent resistivity for racemic and enantiopure BF_4^- salts.

	***S,S*-BHP-EDT-TTF.ClO$_4$**	***R,R*-BHP-EDT-TTF.ClO$_4$**
***E$_a$* (A)**	0.079 eV	0.094 eV (cooling) 0.088 eV (heating)
***ρRT* (A)**	3.4 x 10^3 Ohm.cm	3.2 x 10^3 Ohm.cm (cooling) 2.5 x 10^3 Ohm.cm (heating)
***E$_a$* (B)**	0.084 eV	0.083 eV
***ρRT* (B)**	9.05 x 10^2 Ohm.cm	7.1 x 10^3 Ohm.cm

Table 3.1.10. Activation energy and room temperature resistivity for two different samples (A and B) of enantiopure ClO_4^- salts.

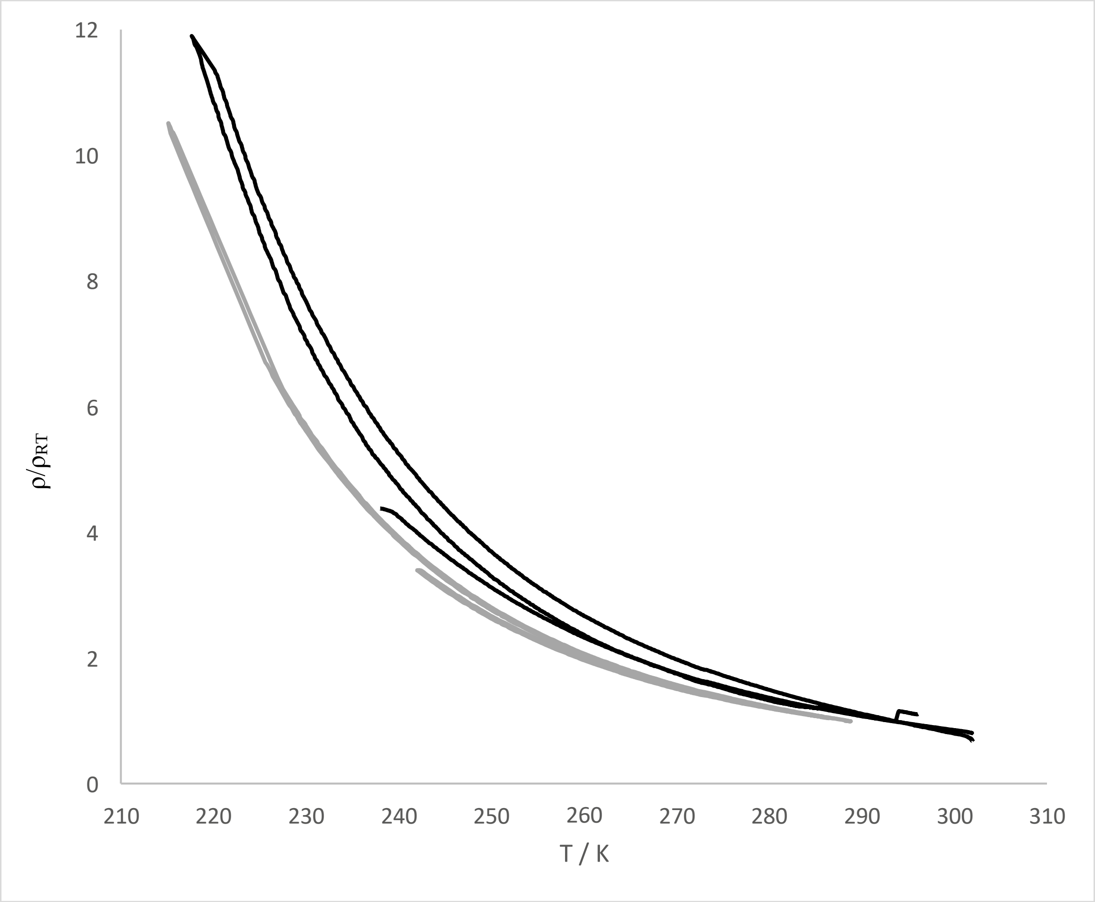

Graph 3.1.6. Temperature dependent resistivity of enantiopure ClO$_4^-$ salts. Black lines are sample A and grey lines are sample B.

	_S,S_-BHP-EDT-TTF._PF_$_6$	**_R,R_-BHP-EDT-TTF._PF_$_6$**
_E_a (A)_ **_(A1)_**	0.083 eV 0.083 eV	0.128 eV
ρRT (A) **_(A1)_**	x 10^2 Ohm.cm x 10^2 Ohm.cm	5.2 x 10^3 Ohm.cm
_E_a (B)_ **_(B1)_**	0.082 eV 0.082 eV	0.085 eV
ρRT (B) **_(B1)_**	x 10^2 Ohm.cm x 10^2 Ohm.cm	5.2 x 10^3 Ohm.cm

Table 3.1.11. Activation energy and room temperature resistivity for two different samples (A and B) of enantiopure PF$_6^-$ salts.

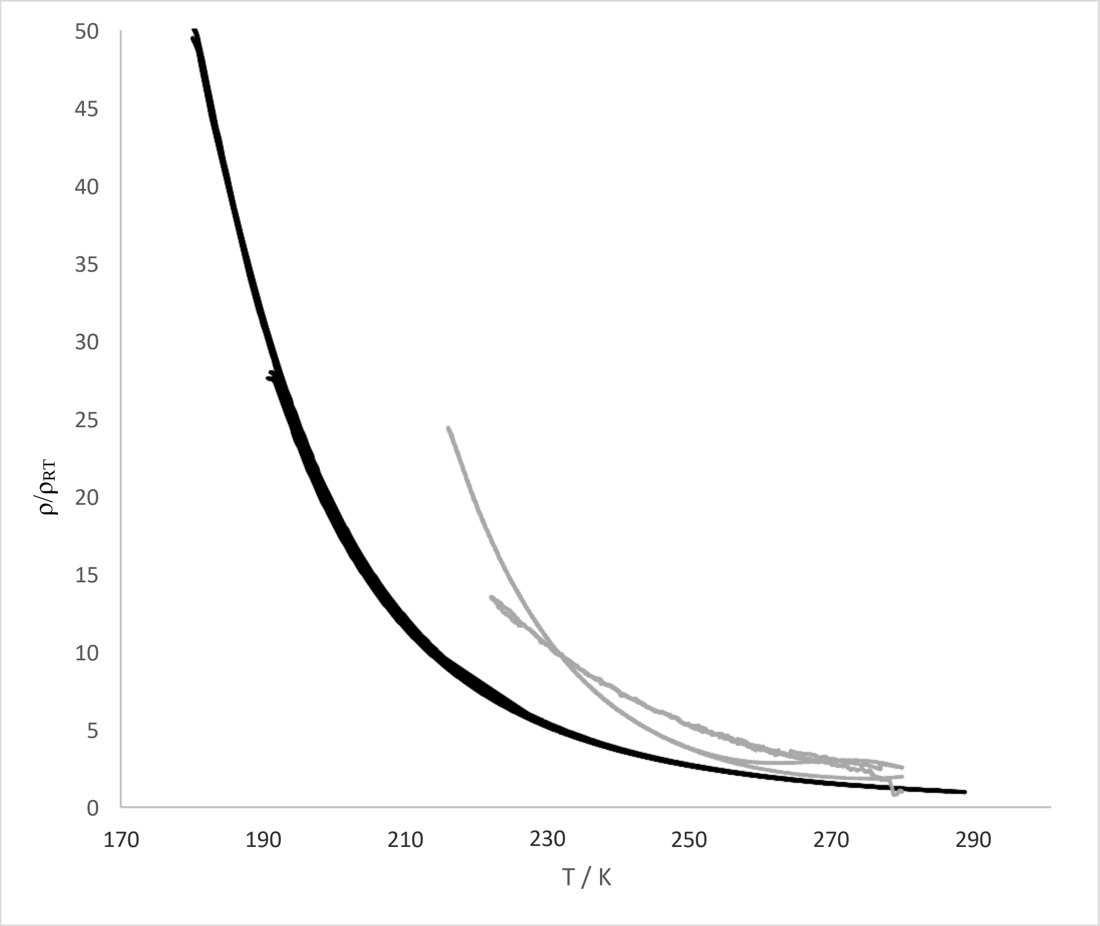

Graph 3.1.7. Temperature dependent resistivity for enantiopure PF_6^- salts. Grey lines are samples A and black lines are samples B.

Reproducible four-probe transport measurements show that *S*,*S*-BHP-EDT-TTF.BF_4, *R*,*R*-BHP-EDT-TTF.BF_4 and *meso*-BHP-EDT-TTF.BF_4 are all semiconducting (Table 3.1.9). The room temperature resistivities are similar but the activation energy for the racemate is significantly smaller than either the *S*,*S* or *R*,*R* enantiomers. This result differs from the previous examples of chiral and racemic conductors, where the disordered racemate is usually found to have a larger activation energy than its chiral counterparts.

Four-probe transport measurements on crystals of both *S*,*S* and *R*,*R* enantiopure ClO_4^- salts (Table 3.1.10) show the salts to be semi-conducting with activation energies and room temperature resistivities similar between the two enantiomers. There is a small hysteresis observed in sample A of the *R*,*R* enantiomer between cooling and heating runs. However, the change in E_a and ρRT is negligible and the hysteresis is likely to be due to defects in the structural integrity of the thin needle crystals.

Four-probe transport measurements were made on several crystals of *S*,*S*-BHP-EDT-TTF.PF_6 and *R*,*R*-BHP-EDT-TTF.PF_6. The samples show semiconducting behaviour (Table 3.1.11). At around 220 K the resistivity of the *R*,*R* enantiomer reaches a peak, therefore the exponential curve is only displayed from 280 – 220 K. The *R*,*R* enantiomer has a higher room temperature resistivity compared with the *S*,*S* enantiomer. The activation energy is significantly different between sample A and sample B of the *R*,*R* enantiomer and as can be observed from Graph 3.1.7, sample B does not produce a smooth curve. Due to the extremely small size of crystals of the *R*,*R* enantiomer it was not possible to mount more than two samples. The oscillation from the mean resistivity value seen in sample B of the *R*,*R* enantiomer may be due to gold contacts not being attached efficiently during the mounting process.

All transport measurements were made parallel to the long axis of the needle-shaped crystals.

	S*,*S	***R*,*R***
BHP-EDT-TTF.BF_4		
E_a / eV	0.212	0.223
BHP-EDT-TTF.ClO_4		
E_a / eV	0.162	0.266
BHP-EDT-TTF.PF_6		
E_a / eV	0.165	0.214

Table 3.1.12. Average activation energies in eV for the six enantiopure salts of BHM-BEDT-TTF.

The table above shows the average activation energies for the enantiopure salts of each family discussed in this section. The results are significantly lower for the ClO_4^- and PF_6^- salts and there is a noticeable difference between the *S*,*S* and *R*,*R* enantiomers for these two salts, both average activation energies being lower for the *S*,*S* enantiomer. *S*,*S*-BHP-EDT-TTF.BF_4 also has a lower average activation energy than its chiral counterpart, however the difference is negligible and cannot be deemed significant. The room temperature resistivities of all chiral salts are similar.

The cause of this difference in conducting properties between enantiomers could be due to electromagnetochiral anisotropy, however in the absence of magnetic field dependent resistivity data it is not possible to calculate the eMChA voltage and to prove if this effect is due to chiral anisotropy.

3.2 trans-vic-Bis(hydroxymethyl)bis(ethylenedithio)tetrathiafulvalene, BHM-EDT-TTF

The chiral *trans*-*vic*-bis(hydroxymethyl)ethylenedithiotetrathiafulvalene donor molecule, BHM-EDT-TTF, is a di-substituted BEDT-TTF derivative. The donor is produced as a racemic mixture of the *trans* (*S*,*S*) and (*R*,*R*) analogues, with two hydroxymethyl groups of the same chiral configuration on each methylene carbon of one side of the BEDT-TTF unit. Mori *et al.* previously synthesised the enantiopure version of the donor by using chiral HPLC after the initial Diels-Alder addition to remove the (*R*,*R*) enantiomer of the thione[12].

The outlying hydroxyl groups on the donor are well placed for participation in non-covalent interactions during crystal engineering, and the stereogenic centre is positioned directly on the BEDT-TTF unit which places the chiral information closer to the potentially mobile π electrons. Previously an enantiopure semiconducting radical cation salt of donor BHM-EDT-TTF and the perchlorate anion was reported along with a racemic analogue of the same anion[12].

The new donor has proved to be successful in producing a number of charge transfer salts for investigation. In this section is discussed four separate radical cation salts containing the title molecule and the anions Cl^-, ClO_4^-, PF_6^-, TCNQ. Rotation at the CH_2-OH bond can allow for a number of different geometries to be adopted in the solid-state and the radical cation shows different packing motifs in each of the salts. Structural, physical and magnetic properties of the salts are discussed and compared.

Figure 3.2 below shows a chemdraw representation of chiral donor BHM-BEDT-TTF.

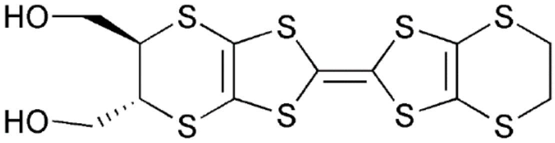

Figure 3.2. Chemdraw representation of BHM-BEDT-TTF.

3.2.1 BHM-EDT-TTF$_2$Cl(H$_2$O)$_2$

A charge transfer salt of the title compound has been produced through constant current electrocrystallisation experiments with BHM-BEDT-TTF and tetrabutylammonium chloride. The crystal size and habit obtained was suitable for structural, magnetic and physical characterisation. The synthesis, structure and physical properties of the semiconducting charge transfer salt are discussed in detail below.

3.2.1.1 Electrocrystallisation Table

Donor	**Counterion**	**Electrolyte**	**Solvent**	**Current /μA**	**Crystal Growth**	**Observation**
BHM-BEDT-TTF	TBA^+	Cl^-	PhCl	0.1	YES – Collected after 4 weeks.	Large quantity of thick black rhombi were collected form the electrode.

Table 3.3.1. Electrocrystallisation table for synthesis of CTS 3.2

Chlorobenzene produced crystals of superior quality compared with the other solvent systems that were used i.e PhBr, PhCl:EtOH of differing ratios. The crystal size was roughly 0.5x0.4x0.03(mm). Due to the crystal thickness and apparent twinning, the sample was sent to the National Crystallographic Service in Southampton for final data collection.

3.2.1.2 Crystal Structure

BHM-BEDT-TTF₂.Cl(H₂O)₂	
Formula	$C_{24}S_{16}O_6H_{28}Cl$
M_r/g mol^{-1}	960.97
Temp / K	150
Radiation	Mo Kα
Wavelength	0.7103
Crystal System	Monoclinic
Space group	$P2_1$
a / Å	7.4627(4)
b / Å	13.1892(5)
c / Å	18.1041(9)
α / °	90
β / °	93.961(5)
γ / °	90
V/Å^3	1778.23(14)
Z	2
ρ/g cm^{-1}	n/a
μ/cm^{-1}	n/a
Absorption Applied	No
Abs. Type	n/a
Abs. Range	n/a
Total Reflections	25258
Unique Reflections	11474
R [all data]	0.104
R_1 [$I > 2\sigma(I)$]	0.104
wR [all data]	n/a
Goodness of fit	n/a
Refinement Program	SHELX
Refinement Mode	F^2
Flack Parameter	n/a

Table 3.3.2. X-ray data for $BHM-BEDT-TTF_2.Cl(H_2O)_2$

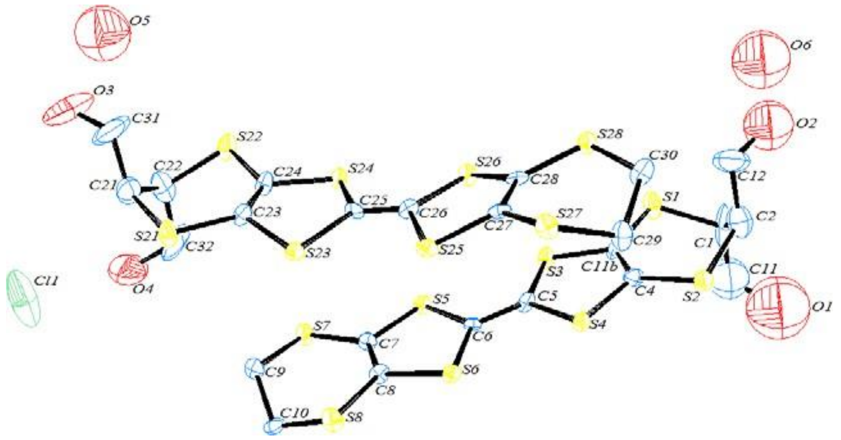

Figure 3.3.1. ORTEP diagram of the asymmetric unit of BHM-BEDT-TTF$_2$.Cl(H$_2$O)$_2$. Displacement ellipsoids are drawn at the 50% probability level. Hydrogens are omitted for clarity.

CTS 3.2 crystallises in the monoclinic crystal system in centrosymmetric space group P 2_1. The crystal is twinned with the two components existing in a 4:1 ratio. The asymmetric unit contains two crystallographically independent BHM-BEDT-TTF molecules one chloride ion and two independent water molecules. The ORTEP diagram with numbering scheme is shown in Figure 3.3.1. Below shows the independent unit cell (Figure 3.3.2). The donor is synthesised as the trans racemic analogue and the two symmetry inequivalent donors adopt either the *R*,*R* (Donor A) or the *S*,*S* (Donor B) chiral configuration. The donors form stacks in the ab plane with neighbouring stacks separated in the *c* direction by the insulating chloride layer.

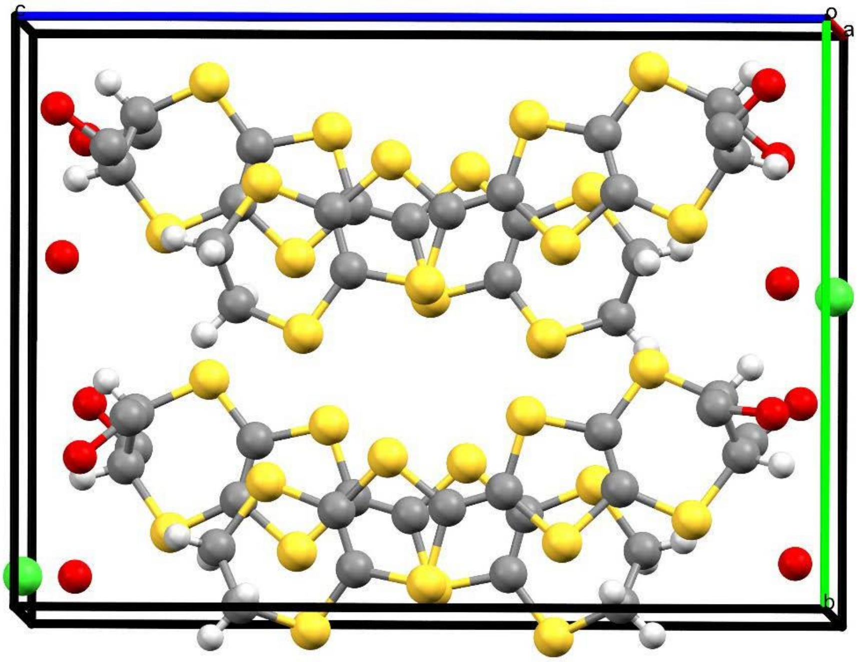

Figure 3.3.2. Unit cell of CTS 3.2.

Each BHM-BEDT-TTF molecule is twisted by about 25° with respect to the donor below and above it in the *a* direction with each row of donors along the *b* axis in the same orientation but of alternating chirality. The lattice packing as viewed along the *b* axis is shown in Figure 3.3.3. The donors form head-to-tail stacks in which the crystallographically independent donors alternate through the *a* axis. This alternates the direction in which the chiral side chain protrudes into the insulating layer. The neighbouring donor stacks are positioned either ‘tail-to-tail’ or ‘head-to-head’ along the *c* direction with the ‘head-to-head’ ends packing next to the opposite enantiomer and creating the cavity in which the chloride ions sit. The crystal packing as viewed along the *a* axis is also shown in Figure 3.3.4, the chloride ions occupy the cavity created by the outlying chiral side chains of the donor molecules and the ca. 25° twist through each donor stack.

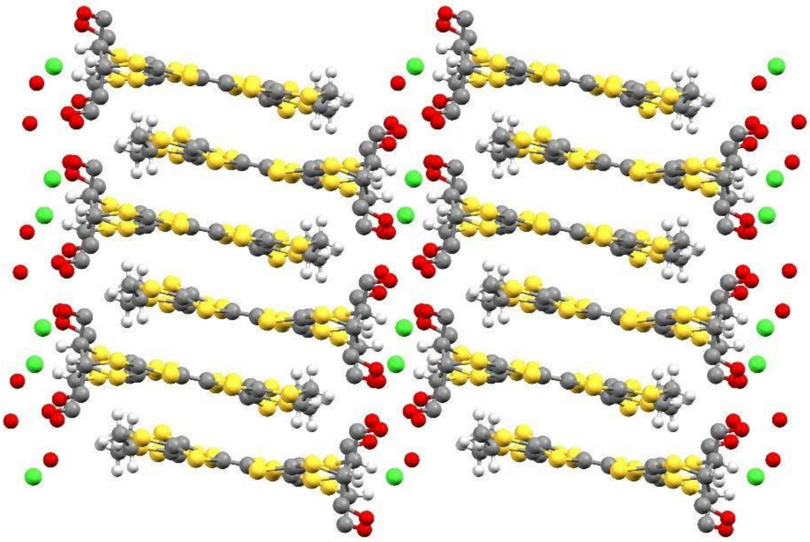

Figure 3.3.3. Lattice packing of CTS 3.2, viewed along the *b* axis.

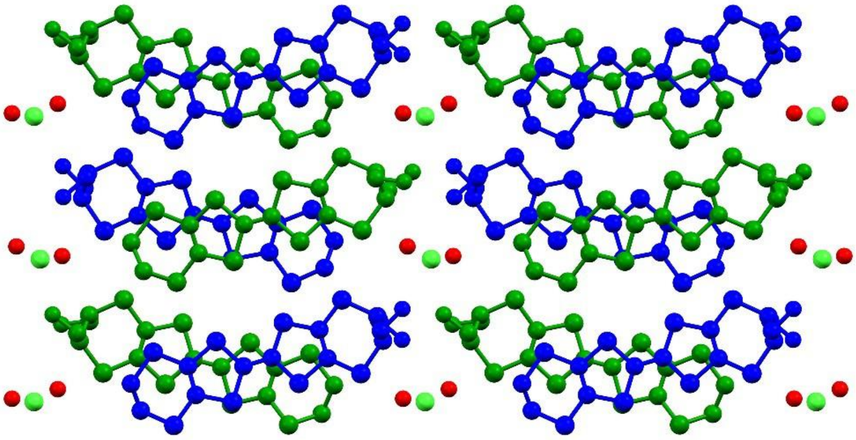

Figure 3.3.4. Lattice packing of CTS 3.2, viewed along the *a* axis. Donors are coloured according to symmetry.

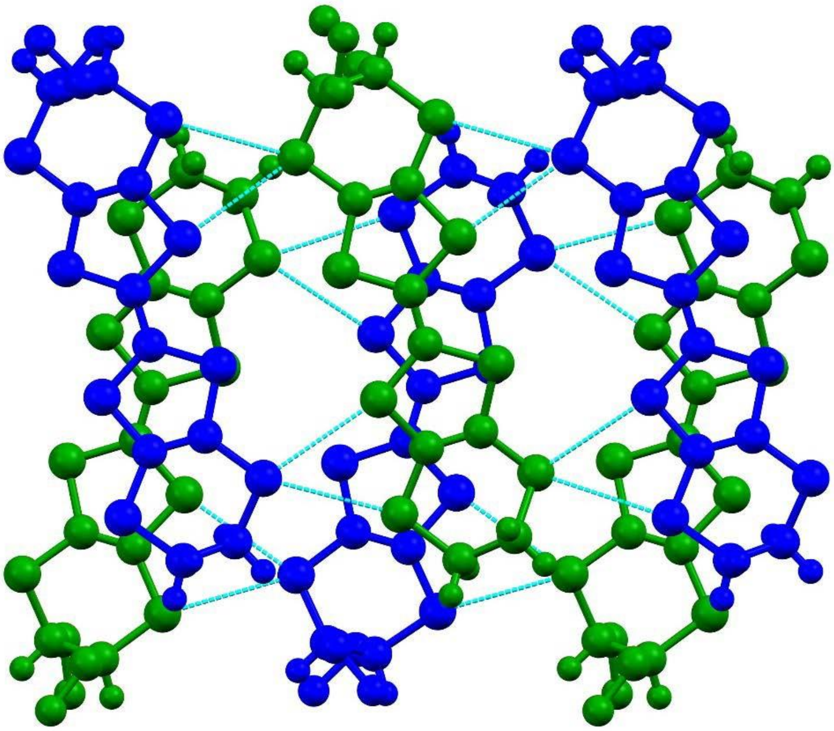

Figure 3.3.5. Single stack of donors in CTS 3.2, viewed along the *a* axis. S...S contacts are shown in light blue. Donors A and B are coloured green and blue respectively.

Figure 3.3.5 above shows the donor packing arrangement viewed along the *a* axis, with short sulphur interactions below the sum of the vdW radii (<3.6 Å) shown in blue. Only side-to-side contacts are observed between rows of donors with each donor making a total of eight S...S contacts. The half-chair confirmation of the substituted dithiin rings places the two -CH_2OH groups in pseudo axial positions for both donors. Due to the alternating chirality of the donors through both the *a* and *b* directions this causes a very slight staggering of the chloride ions, such that they do not lie parallel throughout the insulating layer. The hydrated insulating layer as viewed along the *c* direction is shown in Figure 3.3.6.

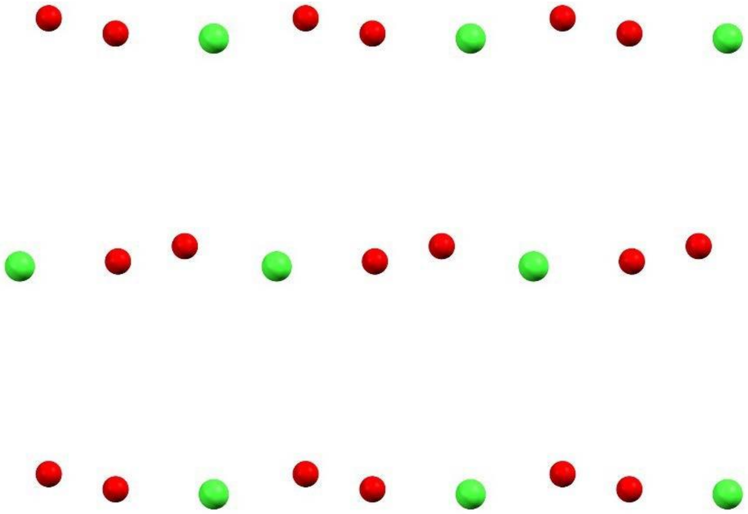

Figure 3.3.6. Insulating hydrated chloride layer of CTS 3.2 viewed along the *c* axis.

Figure 3.3.7 pictures donor A, shown above in green. Short sulphur interactions below the sum of the vdW radii (<3.6 Å) are shown in dotted red lines, contact length and central TTF bond lengths are shown in green. The donor makes a total of eight 'in plane' side-to-side contacts with neighbouring donor B molecules. Donor A has a twisted confirmation at the ethoxy groups, with both ethoxy carbons displaced from the central axis of the molecule by the same distance. The opposite end of the molecule has a sofa confirmation with one of the methylene groups displaced by a much larger degree than the other. Figure 3.3.8 shows the side on profile of the donor, the shape is heavily bent from the central C=C bond and both hydroxyl bonds adopt similar geometries pointing along the *c* direction. The hydroxyl bonds are directed almost diagonally between the *bc* plane. Donor A is calculated to have a neutral charge. Throughout the crystal lattice donor A adopts exclusively the *R*,*R* chiral configuration at the hydroxymethyl side-chains.

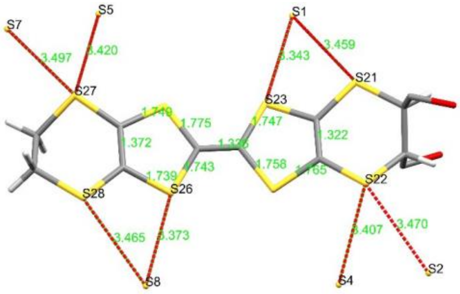

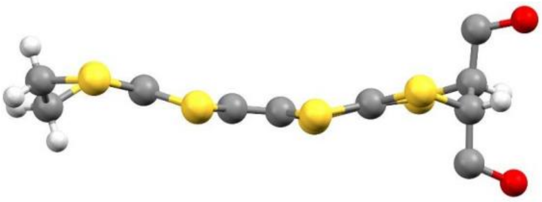

Figure 3.3.7 (left). CTS 3.2: Capped stick diagram of donor A. S...S contacts are shown in dotted red lines and contacts atoms are labelled in black. Contact length and central TTF bond lengths are shown in green. Figure 3.3.8 (right). Side profile view of donor A.

Figure 3.3.9 shows donor B, pictured above in blue. Short sulphur interactions below the sum of the vdW radii (<3.6 Å) are shown in dotted red lines, contact length and central TTF bond lengths are shown in green. The donor makes a total of eight 'in plane' side-to-side S...S contacts with neighbouring donor A molecules. The chiral side-chains have a twisted confirmations at the ethoxy carbons with both carbons displaced by equal amounts from the central axis of the molecule. The other end is also in the twisted confirmation with the four terminal groups staggered as viewed down the long axis of the molecule. The side on profile pictured in Figure 3.3.10 shows the central portion of the donor is relatively planar until the terminal ethylene and ethoxy carbons. Both the CH-CH_2OH bonds are directed away from the central axis of the molecule but the hydroxyl bonds are slightly different. One bond is directed almost diagonally between the *ac* plane and the other is more parallel with the *c* axis.

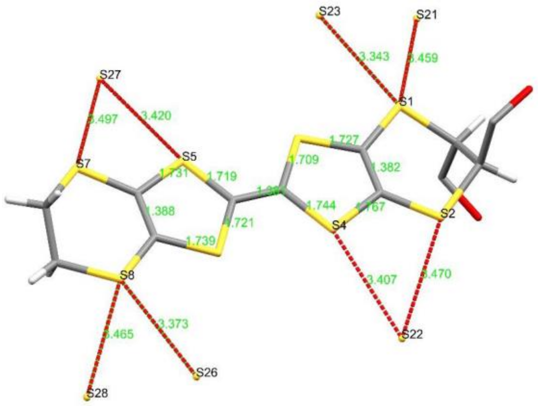

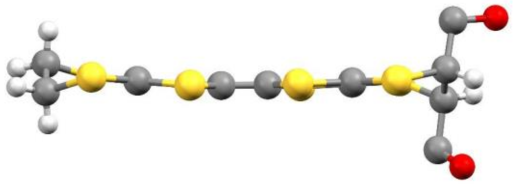

Figure 3.3.9 (left). CTS 3.2: Capped stick diagram of donor A. S...S contacts are shown in dotted red lines and contacts atoms are labelled in black. Contact length and central TTF bond lengths are shown in green. Figure 3.3.10 (right). Side profile view of donor A.

There is likely to be a network of hydrogen bonding interactions between the two hydroxyl groups, the chloride ion and the two water molecules. A summary of the possible hydrogen bonding is shown below in Figure 3.3.11. However, there is disorder present in the two hydroxyl groups with a possible minor confirmation for each disubstituted dithiin ring. Due to the inherent disorder it was not possible to locate with any certainty the hydrogens for the two hydroxyl groups and the two water molecules. The present structure refined to an R-value of 10% however no completely convincing model has been obtained to date.

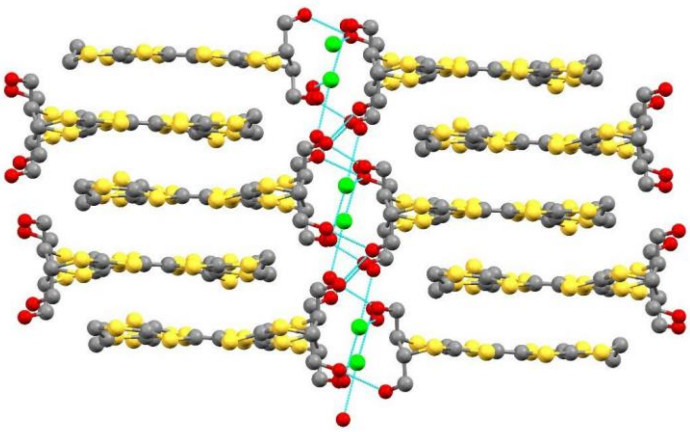

Figure 3.3.11. Possible geometry of hydrogen bonding between donor stacks, chloride ions and water molecules. It was not possible to locate the hydrogens on the hydroxyl groups or the water molecules due to a possible minor confirmation for the chiral side-chain.

3.2.1.3 S…S Contacts

BHM-BEDT-TTF$_2$.Cl(H$_2$O)$_2$	
Atom...Atom	***Length / Å***
S1...S15	3.387
S12...S15	3.492
S13...S2	3.465
S13...S10	3.550
S6...S16	3.418
S11...S16	3.537
S14...S3	3.426
S14...S9	3.497

Table 3.3.3. S...S contacts for CTS 3.2

Table 3.3.3 shows the sulphur-sulphur interactions below the sum of the vdW radii (3.6 Å). There are eight 'in plane' side-to-side contacts observed between neighbouring donors within each stack. No face-to-face contacts are present.

3.2.1.4 C=C Bond Length, Charge Calculations and Raman

	A – Green	***B - Blue***
C=C Bond Length / Å	1.349	1.364

Table 3.3.4. Central C=C bond lengths for CTS 3.2.

The central C=C bond lengths for A and B in table 3.3.4 indicate that the two donors carry different charges and the values are consistent with the presence of one neutral donor and one donor cation.

	A - Green	***B - Blue***
a / Å	1.349	1.364
b / Å	1.749	1.724
c / Å	1.755	1.741
d / Å	1.337	1.341
δ	0.818	0.760
Q	**0.182**	**0.675**

Table 3.3.5. Charge calculations for independent donor molecules in CTS 3.2.

BHM-EDT-TTF consists of a complete BEDT-TTF core and it follows that the charge estimations using Kepert *et al*.[10] average TTF bond length calculations should not be skewed considerably in the presence of the chiral side-chain.

Considering the salts 2:1 stoichiometry it would be expected that both donors carry a charge of $^{+}0.5$. However, the results in Table 3.3.5 along with the central C=C bond lengths above suggest that the majority of the charge is localised to donor A.

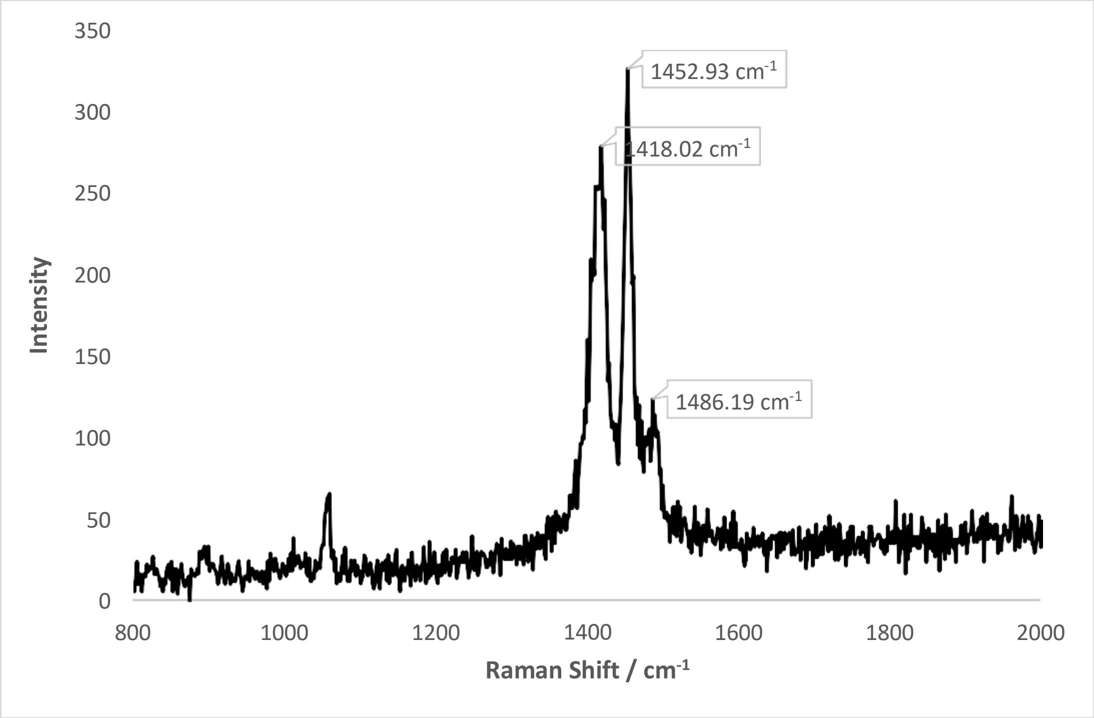

Graph 3.3.1. Relative intensity against Raman shift a single crystal for CTS 3.5. Raman shifts for the high intensity peaks are labelled.

Reproducible room temperature Raman measurements were made on several single crystals of CTS 3.5. The stretching frequencies expected for a neutral BEDT-TTF donor are 1486 – 1494cm^{-1} and 1546 – 1554cm^{-1} for the υ_4 and υ_3 modes respectively. Here one observes only a peak at 1486cm^{-1}, which could correspond to the υ_4 stretching mode of a neutral BEDT-TTF type donor. The stretching frequencies expected for a 1:1 BEDT-TTF radical cation salt are 1406 – 1416 cm^{-1} and 1448 – 1465cm^{-1} for the υ_4 and υ_3 modes respectively. In the spectra above one can observe both peaks (1418 and 1452cm^{-1}) expected for a $^{+}1$ radical cation.

However, it is noted that the peak at 1452cm^{-1} is at a higher intensity than the 1418cm^{-1}. This is in contrast to previous studies where the υ_4 mode is always observed at a higher intensity than the υ_3 mode. It is possible that the neutral υ_4 and the cationic υ_3 stretching modes are occurring at the same frequencies and hence overlap to produce a peak of higher intensity.

3.2.1.5 Magnetic Data

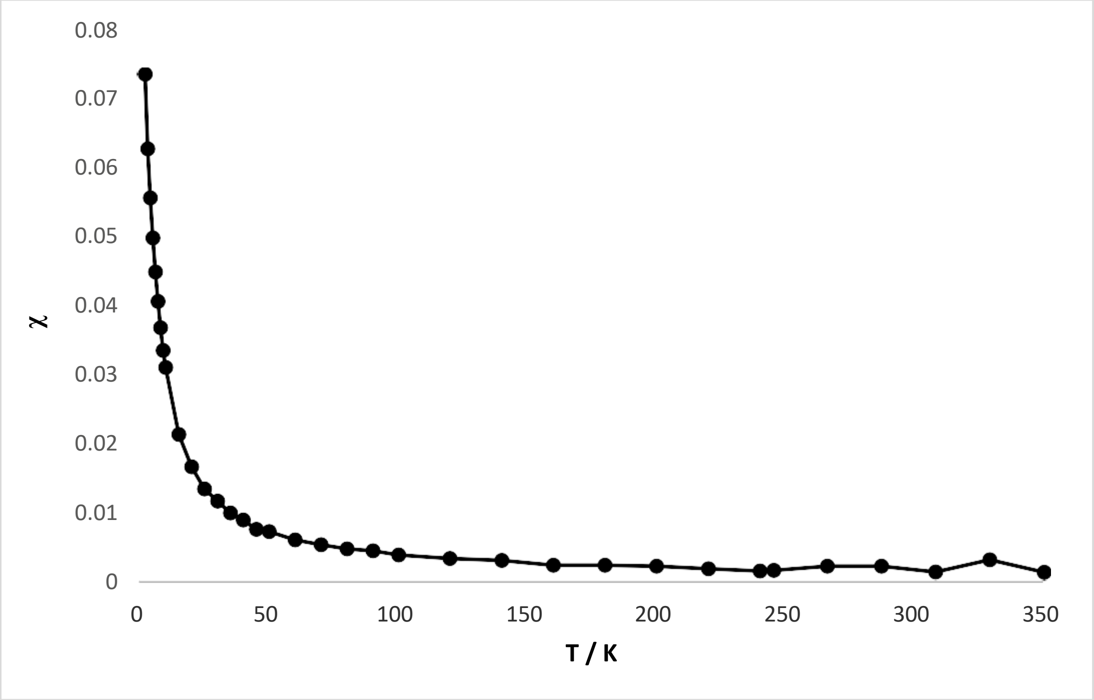

Graph 3.3.2. Temperature dependant magnetic susceptibility for CTS 3.2.

Temperature dependent magnetic susceptibility measurements were performed on 0.3488 mg of randomly orientated crystalline sample. Above 250 K the data becomes incoherent and noisy, perhaps due to such small sample size. This data has been fitted to the Curie-Weiss law for a simple paramagnet by Prof. H. Akutsu of Osaka University and he proposes that there is a charge localisation with one spin on donor B and donor A in a neutral state.

3.2.1.6 Resistivity Data

	BHM-BEDT-$TTF_2.Cl(H_2O)_2$
E_a **Cooling**	0.0787 eV
E_a **Heating**	0.0743 eV
ρRT	6.615 Ohm.cm

Table 3.3.6. Activation energy and room temperature resistivity of cooling and heating runs for CTS 3.2.

Four-probe resistivity measurements were performed on two single crystals of CTS 3.2. The temperature dependant resistivity profile from 300 – 110 K is shown in Graph 3.3.3. The salt shows perfect Arrhenius semiconducting behaviour below 200K with a room temperature resistivity of 6.615 Ω.cm. The resistivity reaches a minimum at around 117 K. There is a hysteresis observed between cooling and heating runs which is defined by a small decrease in activation energy. Inset shows the logarithmic resistivity against 1/T for both the cooling and heating runs. Above 200K the salt deviates from Arrhenius semiconducting behaviour as is seen from the deviation from the straight line in the graph inset, the material is still a semiconductor with a positive temperature dependency however it no longer follows an exponential trend. The activation energy for both the cooling and heating runs was calculated from fitting the straight lines below 1/T = 0.005 = 200 K (Graph 3.3.5 and 3.3.6). The activation energies and room temperature resistivity are given in Table 3.3.6.

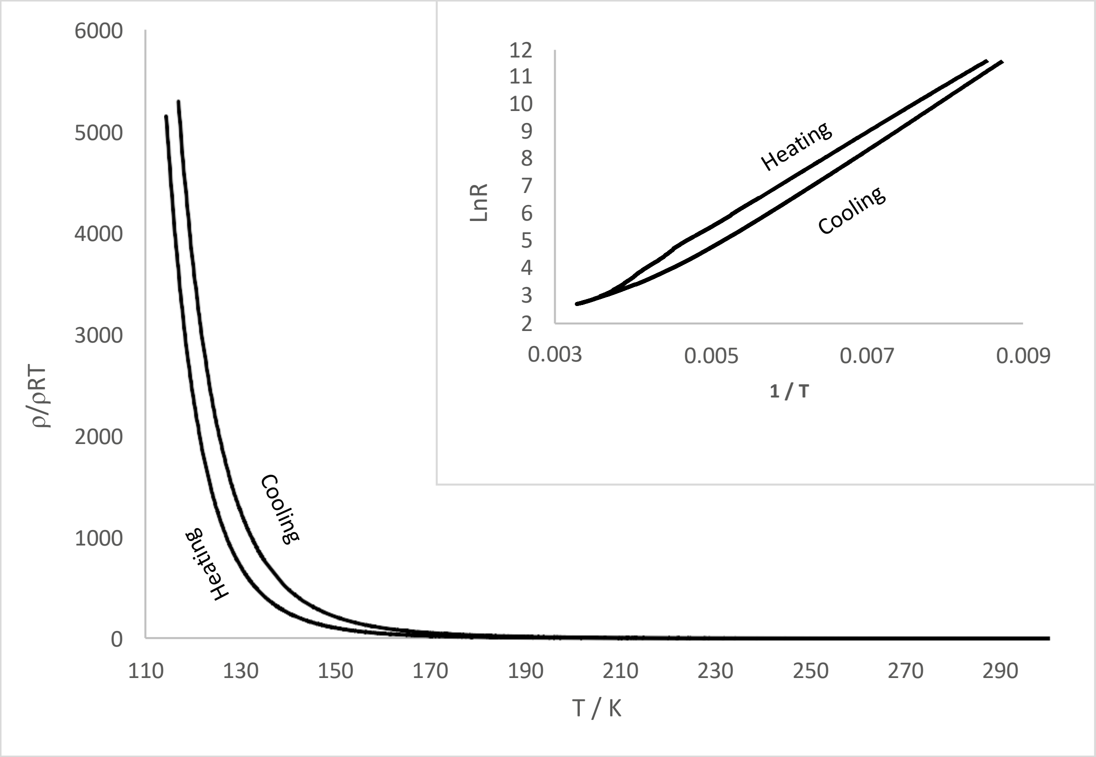

Graph 3.3.3. Temperature dependent resistivity for CTS X. *Inset*: Graph 3.3.4. Logarithmic resistivity against 1/T for CTS 3.2.

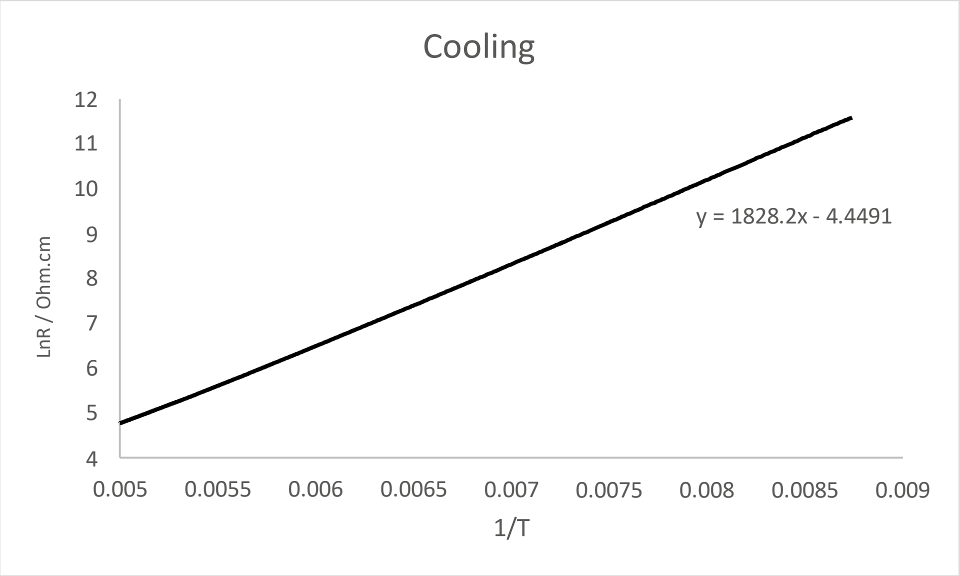

Graph 3.3.5. Logarithmic resistivity against 1/T for Arrhenius temperature range of cooling run for CTS 3.2.

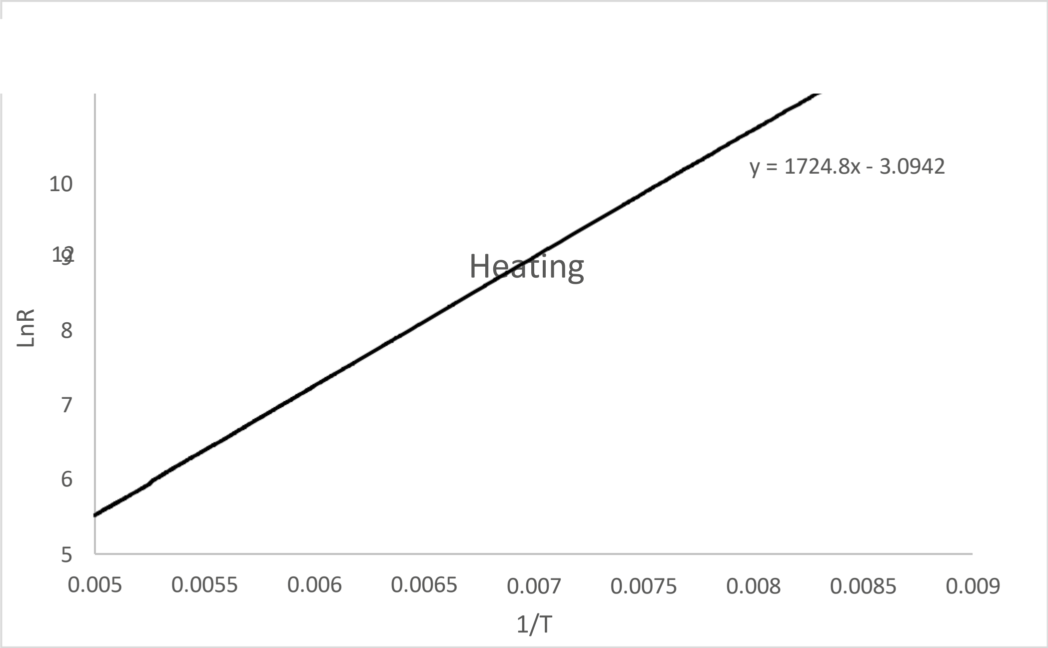

Graph 3.3.6. Logarithmic resistivity against 1/T for Arrhenius temperature range of heating run for CTS 3.2.

3.2.2 BHM-BEDT-TTF.PF_6

A charge transfer salt of the title compound has been produced through constant current electrocrystallisation experiments with BHM-BEDT-TTF and tetrabutylammonium hexafluorophosphate. It was not possible to complete charge transport measurements due to the extremely small size of the crystals. However, structural, magnetic and Raman measurements were performed.

3.2.2.1 Electrocrystallisation Table

Donor	**Counterion**	**Electrolyte**	**Solvent**	**Current /μA**	**Crystal Growth**	**Observation**
BHM-BEDT-TTF	TBA^+	PF_6^-	1,1,2-TCE	0.2	Yes	Large quantity of small black plates were collected from the electrode after 1 week.
BHM-BEDT-TTF	TBA^+	PF_6^-	DCM	0.2	Yes	Large quantity of tiny black plates were collected from the electrode after 2 weeks.

Table 3.3.7. Electrocrystallisation table for synthesis of CTS 3.3.

Both 1,1,2-trichloroethane and dichloromethane produced crystals of similar quality. X-ray diffraction experiments elucidated that the crystals are twinned with many reflections overlapping, however they are not perfect merohedral twins but instead may be called pseudo-merohedral twin.

3.2.2.2 *Crystal Structure*

δ-BHM-BEDT-TTF.PF_6	
Formula	$C_{24}S_{16}O_4H_{24}PF_6$
M_r/g mol^{-1}	1034.36
Temp / K	290
Radiation	Mo Kα
Wavelength	0.7105
Crystal System	Monoclinic
Space group	P2/*c*
a / Å	16.1236(12)
b / Å	6.7918(5)
c / Å	17.1860(14)
α / °	90
β / °	98.783(7)
γ / °	90
V/Å^3	1859.94
Z	2
ρ/g cm^{-1}	1.847
μ/cm^{-1}	1.038
Absorption Applied	Yes
Abs. Type	Multi-scan
Abs. Range	0.198 – 0.990
Total Reflections	4257
Unique Reflections	3059
R [all data]	0.1332
R_1 [$I > 2\sigma(I)$]	0.1169
wR [all data]	0.0856
Goodness of fit	0.9614
Refinement Program	SHELX
Refinement Mode	F^2
Flack Parameter	n/a

Table 3.3.8. X-ray data for CTS 3.3.

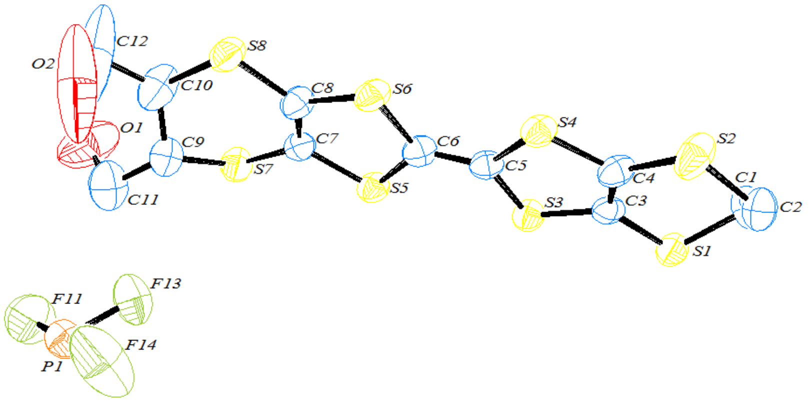

Figure 3.3.12. ORTEP diagram of the asymmetric unit of CTS 3.3. Displacement ellipsoids are drawn at the 50% probability level. Hydrogens are omitted for clarity.

CTS 3.3 crystallises in the monoclinic crystal system in the centrosymmetric space group P 2/*c*. The asymmetric unit contains one crystallographically independent BHM-BEDT-TTF molecule and half a PF_6 anion. The anion lies on a 2-fold axis of symmetry. Figure 3.3.12 above shows the ORTEP diagram of the asymmetric unit with numbering scheme. The donors form AAA stacks in the *c* direction with neighbouring stacks separated in the *a* direction by the insulating layer, this packing is known as the δ motif. Figure 3.3.13 shows the independent unit cell for CTS 3.3 as viewed along the *b* axis. The donor is calculated to have a charge of +0.5 and the positive charge is satisfied by the monovalent PF_6 anion in a 2:1 stoichiometry. The crystal exists as a pseudo-merohedral twin and the current model was refined to an R factor of 11.3%.

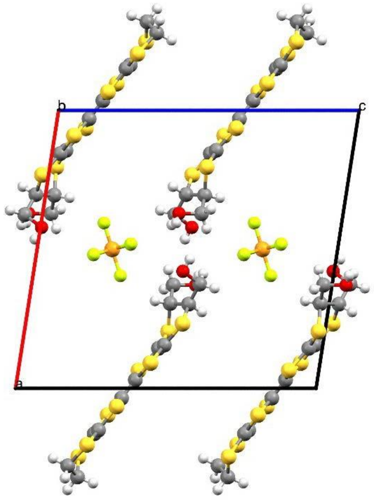

Figure 3.3.13. Unit cell of CTS 3.3.

The donors form stacks in the *bc* plane with the chiral (bis)hydroxymethyl group alternating through the *c* axis. BHM-BEDT-TTF packs head-to-tail within stacks and the donor packing is arranged such that molecules of neighbouring stacks are either positioned 'tail-to-tail' or 'head-to-head' and the PF_6^- anions occupy the cavity left by the 'ethylene-to-ethylene' packed donors. The lattice packing is shown below in Figure 3.3.14 viewed along the b axis.

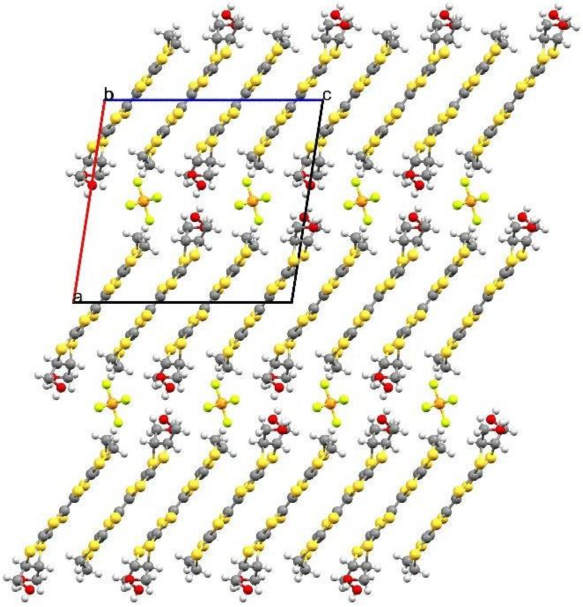

Figure 3.3.14. Lattice packing of CTS 3.3 viewed along the *b* axis.

Throughout each stack the donors are ordered (RR).(RR).(SS).(SS). This means that the side-chain pointing into the insulating layer alternates between enantiomers within a stack. The 'head-to-head' arrangement of donors through neighbouring stacks line up with the opposite enantiomer. It is of note that in the previous chloride salt discussed in this chapter the donor molecules packed in a similar AAA fashion however the smaller chloride anion occupied the cavity formed by the outlying hydroxyl group. In this example the PF_6^- anion which is of considerably larger size cannot fit inside the space between the hydroxyl groups and instead packs between the two ethylene groups of neighbouring donors. This causes the donors to adopt a less staggered arrangement along each stack through the *c* axis.

The donor packing viewed along the *a* axis is shown in Figure 3.3.15, five layers of donors are shown along the *b* axis and each row of donors is coloured only to ease the viewing of each separate molecule. Short sulphur interactions below the sum of the vdW radii (<3.6 Å) are shown in blue. The donors lie parallel along the *a* axis but are shifted at about 45° between rows of donors along the *c* axis. Only 'in plane' side-to-side contacts are observed between neighbouring donors along the crystallographic *b* direction. Figure 3.3.16 shows the donor layer viewed down the long axis of the green and purple molecules, the figure demonstrates the 45° twist seen between rows of donors in each layer.

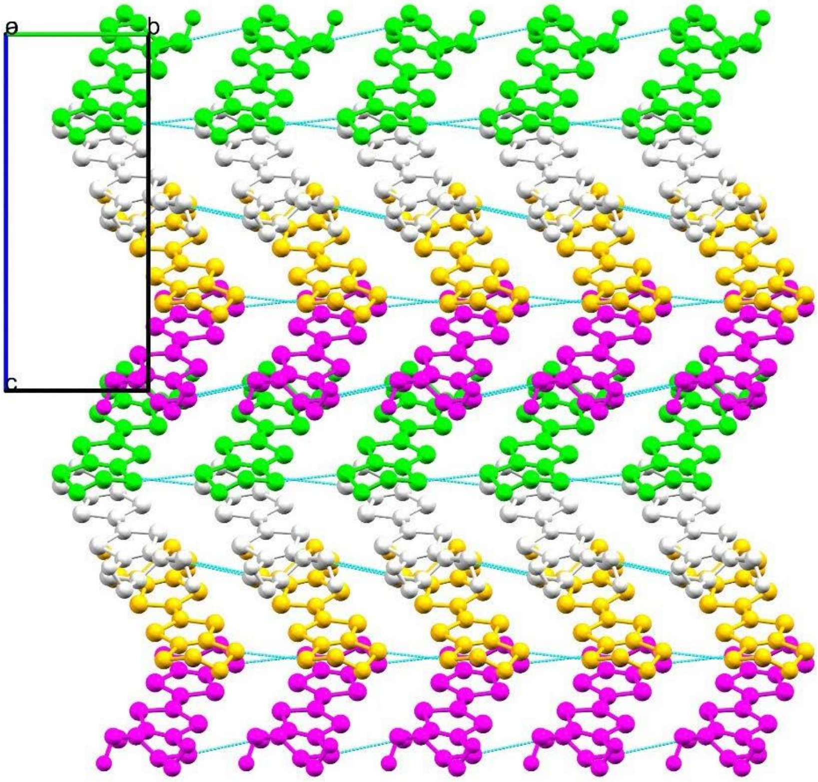

Figure 3.3.15. Donor packing of CTS 3.3 viewed along the *a* axis. Donor molecules are coloured separately for ease of viewing single molecules. S...S contacts are shown in light blue. Hydrogens and omitted for clarity.

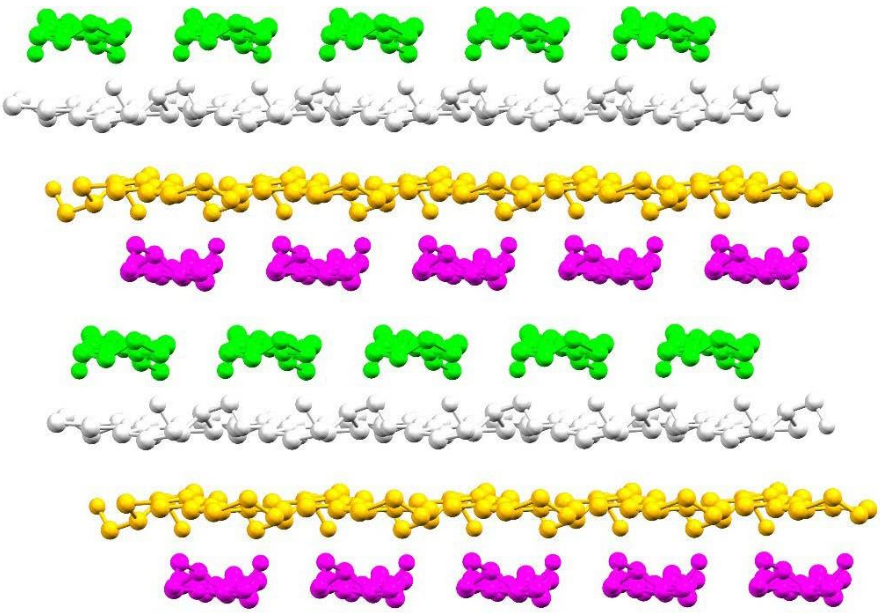

Figure 3.3.16. Donor stack in CTS 3.3 viewed along the long axis of the green and purple molecules to show twist throughout donor stack. Hydrogens are omitted for clarity.

The lattice packing as viewed along the *c* axis is shown in Figure 3.3.17, note the double layer of anions throughout the insulating layer. This can be seen more clearly below in Figure 3.3.18 which shows a single insulating layer viewed along the *a* axis. The PF_6^- molecules can only occupy the space left by the ethylene groups of tail-to-tail donors and as such this creates a staggered effect throughout the PF_6^- layer along the *c* direction due to the 45° twist seen throughout the conducting layer. Two fluorine atoms of each PF_6^- protrude into the conducting layer while the other four flourines are pointing into the *b* axis.

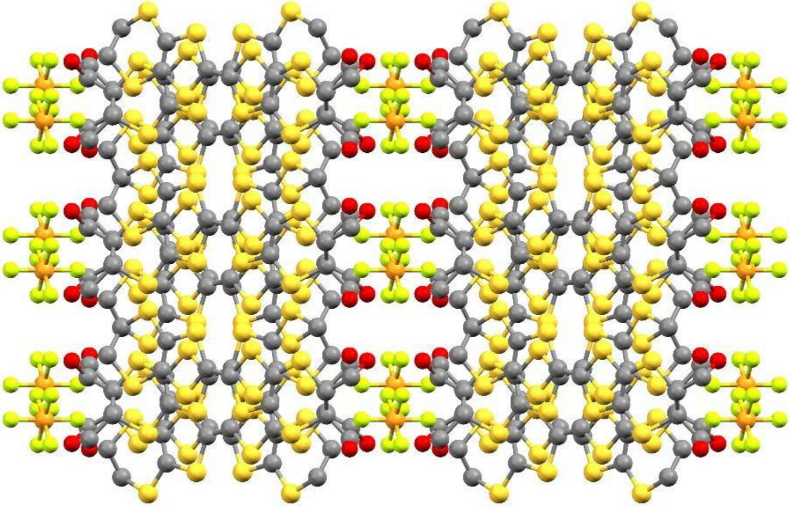

Figure 3.3.17. Lattice packing of CTS 3.3 viewed along the *c* axis. Hydrogens are omitted for clarity.

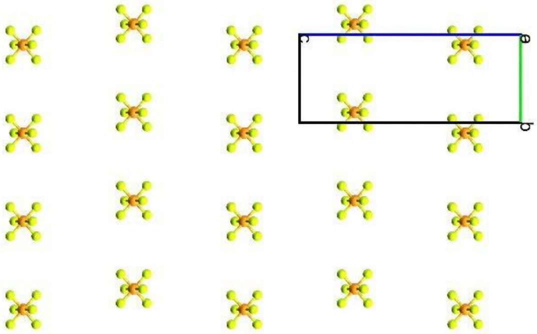

Figure 3.3.18. PF_6^- layer in CTS 3.3 viewed along the *a* axis.

The PF_6^- anion is shown below in Figure 3.3.19. Atoms and P-F bond lengths are labelled. The 2-fold axis running through the centre of the molecule is also present. P-F bonds range from 1.571(1) – 1.584(1) Å.

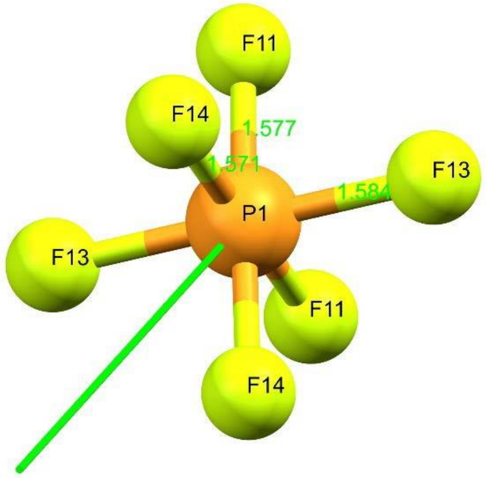

Figure 3.3.19. Independent PF_6^- anion in CTS 3.3 with atoms labelled in black. The green numbers represent P-F bond lengths in angstroms, Å. The green line represents the 2-fold axis running through the centre of the molecule.

Figure 3.3.20 shows the independent donor present in CTS 3.3. Short sulphur interactions below the sum of the vdW radii (<3.6 Å) are shown in dotted red lines, contact length and central TTF bond lengths are shown in green. The donor makes a total of two 'in plane' side-to-side S...S contacts with neighbouring donor molecules along the crystallographic b direction, no face-to-face S...S contacts are observed. The terminal ethylene and ethoxy groups are in the eclipsed sofa confirmation with one carbon displaced from the central axis of the molecule and the other in plane. The ethoxy carbon is displaced from the BEDT-TTF plane by a larger degree than the methylene carbon. The chiral hydroxyl groups adopt a different orientation to that seen in the chloride salt above where the C-O bond was pointed away and to the centre of the central BEDT-TTF axis. Here the C-O bond points away from the central axis, one group above and one below. However, the bond is directed towards the edge of BEDT-TTF molecule rather than towards the centre. The central TTF portion of the donor is planar until the terminal groups which is shown in the side on profile view in Figure 3.3.21.

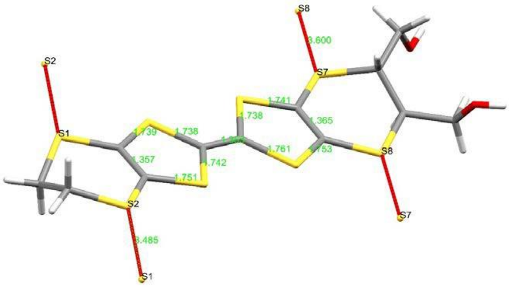

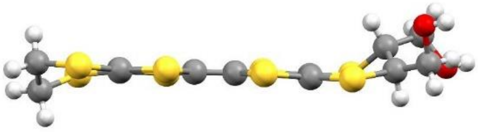

Figure 3.3.20 (left). CTS 3.3: Capped stick diagram of independent donor. S...S contacts are shown in dotted red lines and contacts atoms are labelled in black. Contact length and central TTF bond lengths are shown in green. Figure 3.3.21 (right). Side profile view of independent donor in CTS 3.3.

There is a large network of hydrogen bonding and short contacts between insulating and conducting layers, the short contacts from PF_6^- to donor are shown in Figure 3.3.22. Each independent fluorine atom makes a short contact with at least one donor molecule creating a total of five F...H contacts per half anion. The shortest contacts are between F13 and outlying hydrogens of either the terminal ethylene group or the chiral side-chain of donor molecules in the same stack (F13...H22, 2.359 and F13...H91, 2.528 Å). F14 makes one short contact (F14...H121, 2.663(1) Å) and F11 makes two short contacts with neighbouring donor molecules (F11...H112, 2.668(1) and F11...H122, 2.611(1) Å). There is one hydrogen bond between donor molecules along the b direction (O2…H123, 2.391 Å) (Figure 3.3.23).

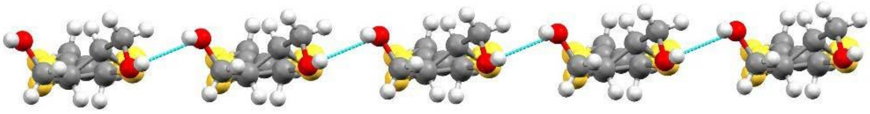

Figure 3.3.22. Hydrogen bonding interactions between rows of donors in the conducting stack are shown in light blue lines for CTS 3.3.

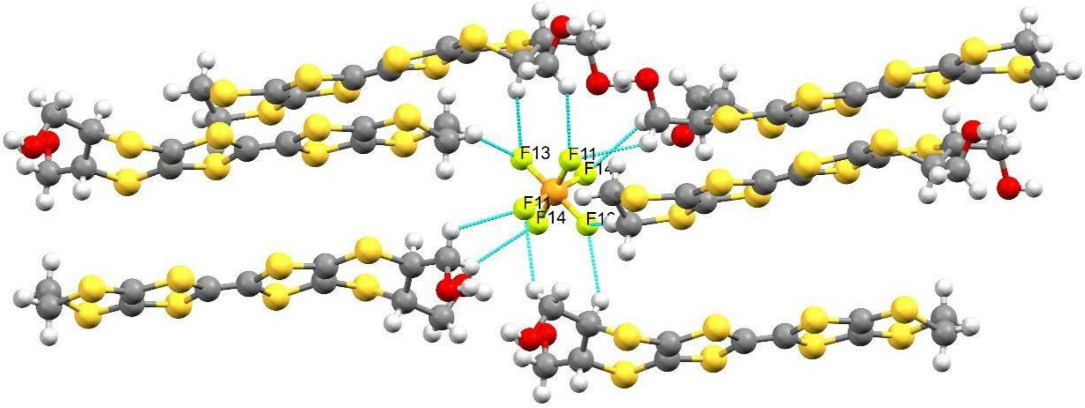

Figure 3.3.23. Hydrogen bonding interactions between PF$_6^-$ anion and donor molecules are shown in light blue lines for CTS 3.3. Fluorine atoms are labelled in black.

3.2.2.3 S…S Contacts

Contact	***Length / Å***
S2...S1 / Å	3.485(1)
S8…S7 / Å	3.600(1)

Table 3.3.9. S...S contacts for CTS 3.3.

Short sulphur interactions below the sum of the vdW radii (3.6 Å) are presented in table 3.3.9. There are only two S...S contacts present.

3.2.2.4 C=C Bond Length and Charge Calculations

C=C Bond Length / Å	
C5...C6	1.353(9)

Table 3.3.10. Central C=C bond lengths for CTS 3.3.

The central BEDT-TTF C=C bond length is consistent with a donor charge of $^{+}$0.5.

a / Å	1.353
b / Å	1.745
c / Å	1.746
d / Å	1.361
δ	0.777
Q	**0.548**

Table 3.3.11. Charge calculations for independent donor in CTS 3.3

Charge estimations using the Kepert *et al*.[10] average TTF bond length calculations agree with the proposed $^+0.5$ valency for the independent donor present in CTS 3.3.

3.2.2.5 Magnetic Data

Temperature dependent magnetic susceptibility measurements could were fitted to the Curie-Weiss equation by Prof. H. Akutsu of Osaka University from 2-20 K and a Curie spin of 3.3% of $S = ½$ - the origin of which would seem to be impurities in the crystal lattice (Graph 3.3.7). The Curie tail can be subtracted from χ to give χ_{int}. Graph 3.3.8 shows a broad peak around 170 K and the data can be fitted to a 2D Heisenberg model, which indicates that the electron holes in the delta' layer are localised and therefore the material should show semiconducting behaviour.

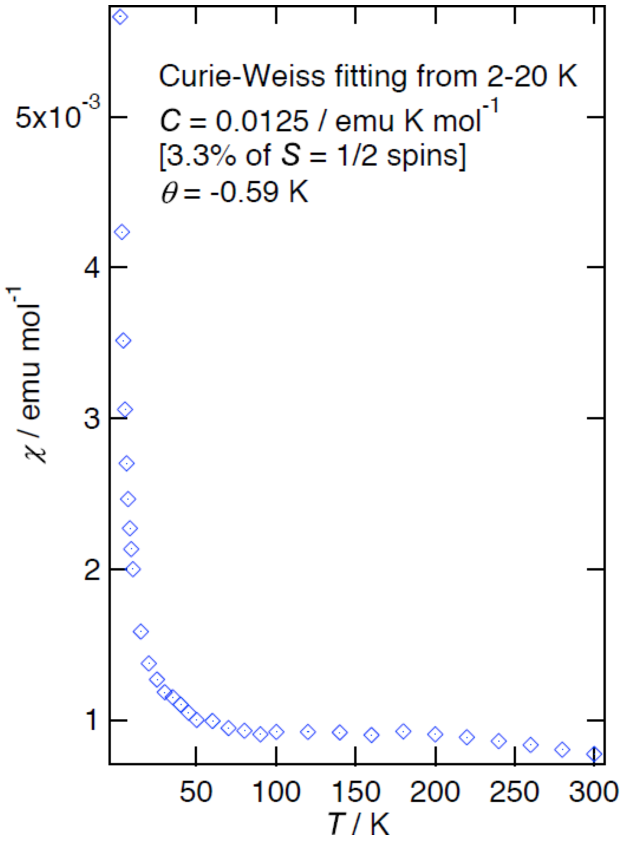

Graph 3.3.7. Temperature dependent magnetic susceptibility for CTS 3.3

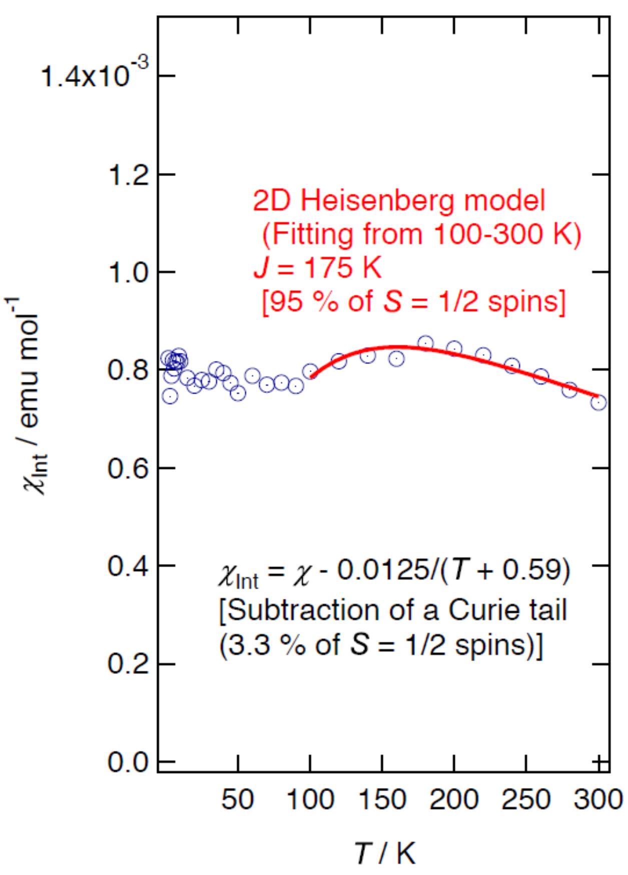

Graph 3.3.8. Integrated magnetic susceptibility (after subtraction of Curie tail) against temperature for CTS 3.3.

3.2.3 BHM-BEDT-TTF.TCNQ

A charge transfer salt of the title compound has been produced through room temperature test tube diffusion experiments with BHM-BEDT-TTF and tetracyanodimethanequinone. The salt is insulating with a checkerboard packing of alternating donor and acceptor molecules with the chiral donor packing in enantiopure stacks throughout. Structural and Raman data are presented and discussed.

3.2.3.1 Electrocrystallisation Table

Donor	**Acceptor**	**Solvent A**	**Solvent B**	**Crystal Growth**	**Observation**
BHM-BEDT-TTF	TCNQ	MeCN	DCM	Yes	Large quantity of black diamonds collected from electrode.

Table 3.3.12. Test Tube Diffusion table for synthesis of CTS 3.4.

Evaporation of the solvent left large black plates of CTS 3.4. The crystals were large enough for structural and physical characterisation. Two probe resistivity measurements on the material showed a resistance of over 1 Mohm suggesting insulating behaviour.

3.2.3.2 Crystal Structure

BHM-BEDT-TTF.TCNQ	
Formula	$C_{24}H_{16}O_2S_8N_4$
M_r/g mol^{-1}	648.94
Temp / K	293
Radiation	Mo Kα
Wavelength	0.7103
Crystal System	Orthorhombic
Space group	Ac2a
a / Å	50.6068(18)
b / Å	12.5452(5)
c / Å	8.5422(3)
α / °	90
β / °	90
γ / °	90
V/Å^3	5423.2(3)
Z	8
ρ/g cm^{-1}	1.589
μ/cm^{-1}	0.691
Absorption Applied	Yes
Abs. Type	Analytical
Abs. Range	0.810 – 0.985
Total Reflections	9189
Unique Reflections	3960
R [all data]	0.0683
R_1 [$I > 2\sigma(I)$]	0.0670
wR [all data]	0.1359
Goodness of fit	1.176
Refinement Program	SHELX
Refinement Mode	F^2
Flack Parameter	n/a

Table 3.3.13. X-ray data for CTS 3.4

.

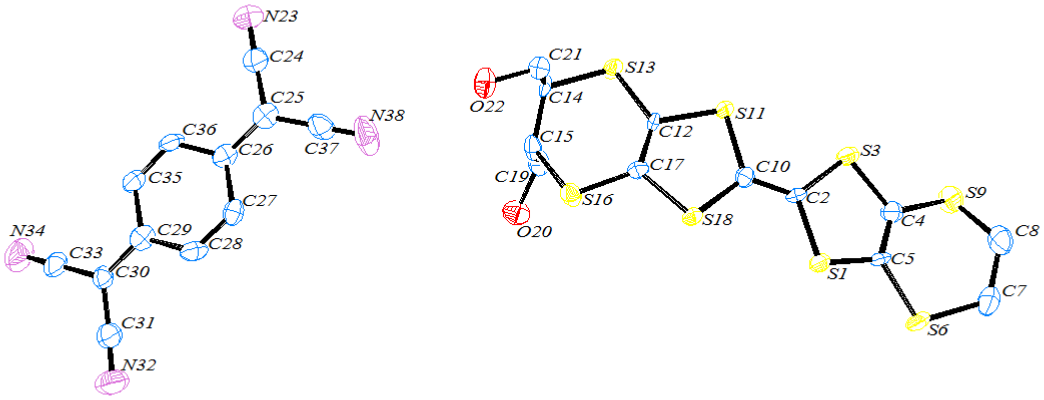

Figure 3.3.24. ORTEP diagram of the asymmetric unit of CTS 3.4. Displacement ellipsoids are drawn at the 50% probability level. Hydrogens are omitted for clarity.

CTS 3.4 crystallises in the orthorhombic crystal system in the achiral space group Ac2a. The asymmetric unit contains one crystallographically independent donor molecule and one TCNQ acceptor. There are eight formula units in the independent cell, pictured below in Figure 3.3.25, with the crystallographic *a* axis significantly larger than the other two vectors. There is no disorder present in CTS 3.4 and as such it was possible to locate all hydrogen atoms. Interestingly, the donors and acceptors alternate throughout stacks in the *bc* plane with neighbouring stacks packing at an angle of ~90° through the *a* direction. There are no discrete conducting and insulating layers. It is of note that each stack contains only a single enantiomer, producing enantiopure stacks. The four stacks shown below in the unit cell alternate SS.SS.RR.RR.

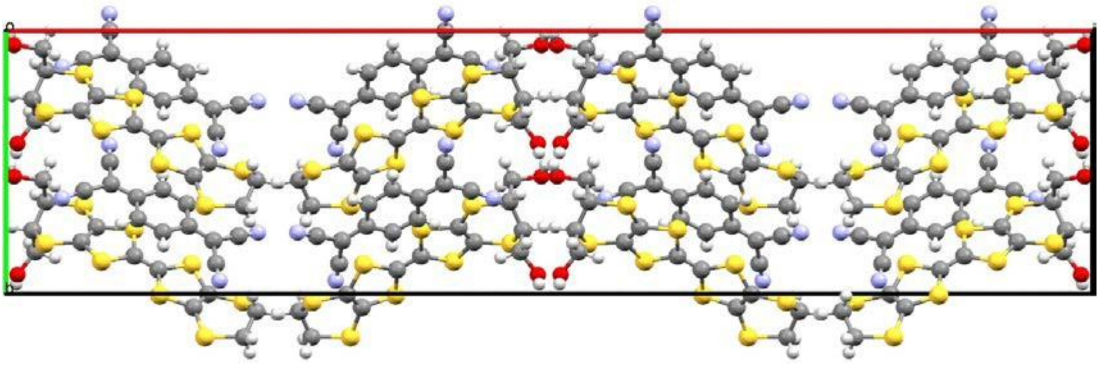

Figure 3.3.25. Unit cell of CTS 3.

Figure 3.3.26 shows the lattice packing of CTS 3.4 viewed between the *a* and *b* axes. Along the *a* axis the stacks alternate at an angle of about 90deg. However, as seen below along the b axis the stacks are orientated in an XYYX… fashion with the derivatised end of the BEDT-TTF molecule pointing towards the centre of the stacking pair. Also of importance is that each stacking pair is racemic i.e. is made up of two enantiopure stacks of opposing chirality.

The salt is expected to have a non-stoichiometric charge transfer. The Flandrois *et al*.[13] method using the TCNQ bond length differences was employed for charge calculation of the acceptor, attempts to calculate TCNQ charge using either the Coppens *et al*.[14] method or the Kistenmacher[15] equation produced unrealistic results.

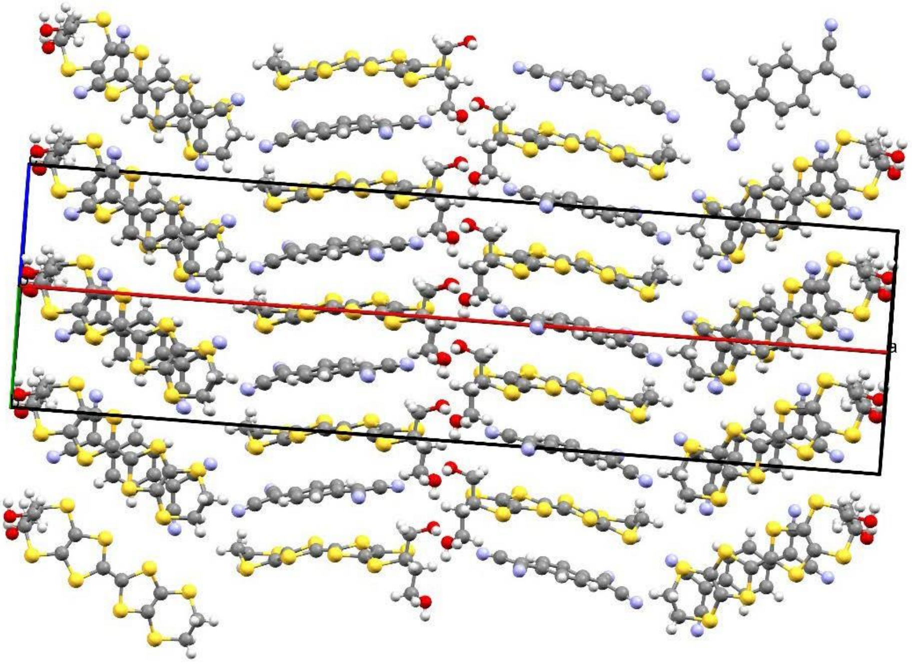

Figure 3.3.26. Lattice packing of CTS 3.4 viewed between the *a* and *b* axes.

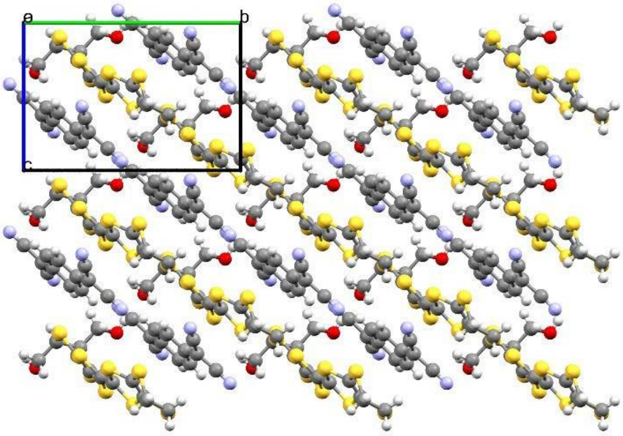

Figure 3.3.27. Single stack of donors and acceptors in CTS 3.4 viewed along the *c* axis.

The single stack packing viewed along the *c* axis is shown in Figure 3.3.27 above. The chiral hydroxymethyl sidechains of the donor are all positioned in the same orientation and are all the same chiral configuration. Side-to-side S...S contacts are observed between rows of donors and no face-to-face contacts are present due to the alternating arrangement of donor and acceptor molecules. Figure 3.3.28 shows the packing arrangement of a single stack as viewed along the long axis of the donor molecule. Short sulphur interactions below the sum of the vdW radii (3.6 Å) are shown in blue and hanging contacts are shown in red. Both CH_2-CH_2OH bonds on each molecule are almost perpendicular to the central BEDT-TTF axis, however one CH_2-OH bond is positioned parallel with the central axis and the other protrudes into the TCNQ layer.

Figure 3.3.29 displays the conduction pathway via S...S contacts for a single layer of donor molecules. Complete S...S contacts are shown in blue and hanging contacts in red. Only one contact per donor below the sum of vdW radii (3.6 Å) is present.

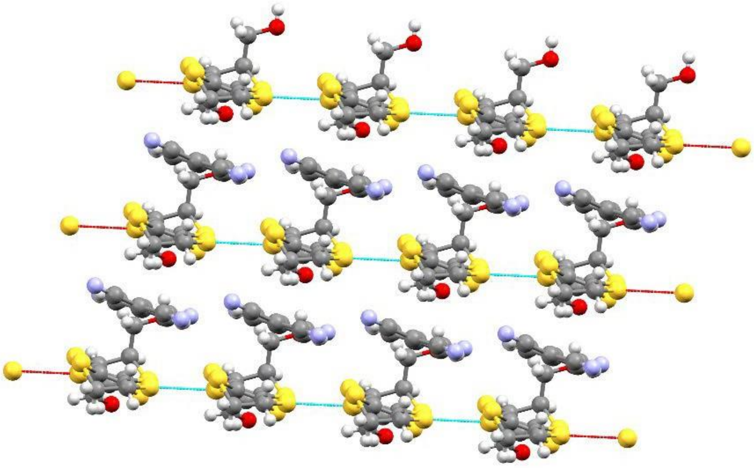

Figure 3.3.28. Single stack of donors and acceptors in CTS 3.4 viewed along the long axis of the donor molecule. S...S contacts are shown in light blue and red (hanging contacts).

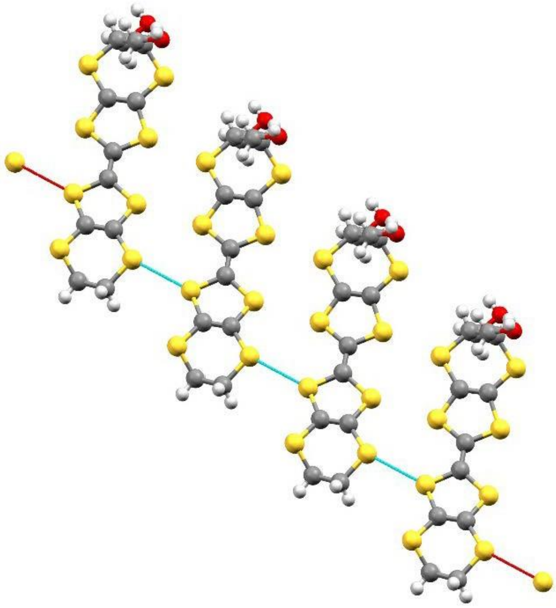

Figure 3.3.29. S...S contacts within rows of donors in CTS 3.4 are shown in light blue and red (hanging contacts).

As discussed at the top of this section, BHM-BEDT-TTF is synthesised as the trans analogue and produced as a racemic mixture of enantiopure molecules. However, in contrast to the other salts in this series, which all consist of racemic stacks throughout the crystal structures; the lattice is made up of enantiopure stacks. Figure 3.3.30 shows the alternating arrangement of enantiomers along the *a* direction TCNQ molecules are removed for clarity. The central two stacks become one stacking pair as described above. The chiral side-chains of each molecule are positioned towards the centre of the respective stacking pair and each stacking pair is made up of opposing enantiomers. Therefore, the donors line up ‘*R*-end-to-*S*-end’ as a pose to ‘*R*-end-to-*R*-end’ or ‘*S*-end-to-*S*- end’. By packing in racemic stacking pairs the overall symmetry of the crystal remains centrosymmetric but the configuration of the lattice during crystal growth is heavily reliant on the difference in chirality between the two enantiopure donor molecules.

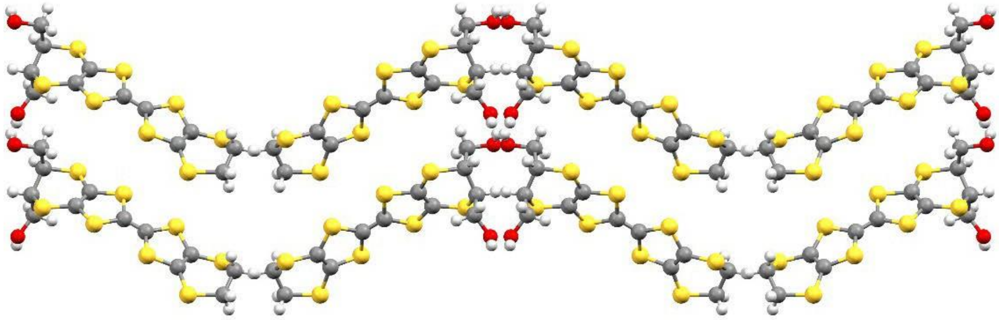

Figure 3.3.30. Donor packing in CTS 3.4 viewed along the *b* axis. TCNQ molecules have been removed for clarity.

Below in Figure 3.3.31 is pictured the independent donor in CTS 3.4. Short sulphur interactions below the sum of the vdW radii (3.6 Å) are shown in dotted red lines, contact length and central TTF bond lengths are shown in green. The donor makes only one side-to-side S...S contact with neighbouring donor molecules. There are no donor stacks throughout the lattice and therefore no face-to-face contacts are observed. The ethylene group on the donor adopts the sofa confirmation while the chiral hydroxyethyl groups adopt the half-chair. Figure 3.3.32 below shows both the side and end on profile view of the donor molecule. It is clear to see that the central TTF portion of the donor is heavily bent and the hydroxymethyl groups both adopt different positions. One hydroxyl is positioned away from the central plane and the other is bent parallel with the plane of the donor.

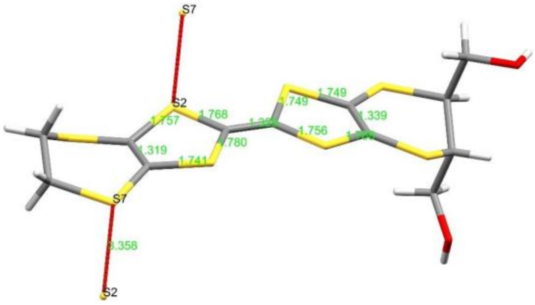

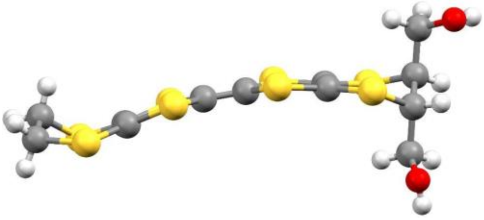

Figure 3.3.31 (left). Capped stick diagram of independent donor in CTS 3.4. S...S contacts are shown in red dotted lines and contacts atoms are shown in black. Contacts lengths and central TTF bond lengths are shown in green.

Figure 3.3.32 (right). Side on profile view of the independent donor in CTS 3.4.

Short O...H contacts between outlying chiral side-chains within a stacking pair are displayed in Figure 3.3.33. The gap between donors is occupied by TCNQ molecules, which have been removed for clarity. Each donor makes two hydrogen bonds with neighbouring donor molecules, one between donors in the same stack (O9...H101, 1.924(1) Å) and one between stacks within the stacking pair (H91...O10, 1.919(1) Å). The short contacts create a network of hydrogen bonds running through the racemic channel within stacking pairs.

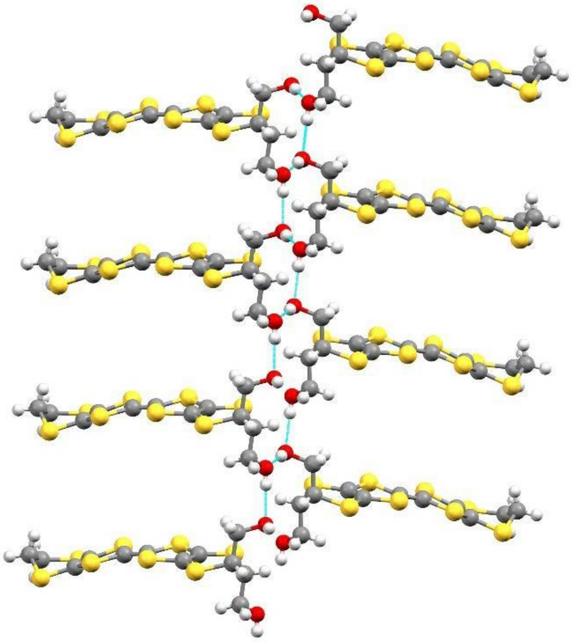

Figure 3.3.33. Hydrogen bonding interactions in CTS 3.4 between donor molecules are shown in light blue. TCNQ molecules have been removed for clarity.

The acceptor also makes a number of short contacts throughout the lattice. Each peripheral nitrogen makes at least one short contact with neighbouring acceptor or donor molecules. However, no contacts are observed between TCNQ molecules of different stacks. Figure 3.3.34 shows, in blue, the contacts for the central labelled TCNQ molecule. There are four inter acceptor contacts between TCNQs in the same stack (N36...H201, 2.708(1)Å) and (H291...N22, 2.663(1) Å), one between donor and acceptor in the same stack (N38...S6, 3.272(1) Å) and two contacts between acceptor and donor in neighbouring stacks (the neighbouring stack is not within a stacking pair) (N37...H251, 2.736(1) and N37...H322, 2.663(1) Å). Interestingly three out of the four contacts between cyclic TCNQ carbons and central TTF sulphurs are below the sum of vdW radii (3.6 Å) with the fourth just above (3.68(1) Å).

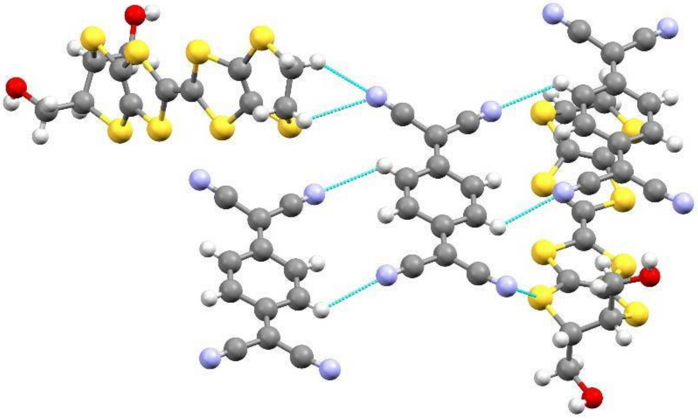

Figure 3.3.34. Hydrogen bonding interactions in CTS 3.4 between acceptor and donor molecules are shown in light blue.

3.2.3.3 S…S Contacts

Contact	***Length / Å***
S2…S7	3.358(1)

Table 3.3.14. S...S contacts for independent donor in CTS 3.4.

Only one side-to-side short sulphur interaction below the sum of the vdW radii (3.6 Å) is observed due to the lack of a discrete donor layer.

3.2.3.4 C=C Bond Length, Charge Calculations and Raman

Donor A	
C=C Bond Length / Å	1.329

Table 3.3.15. Central C=C bond lengths for independent donor in CTS 3.4.

The central BEDT-TTF C=C bond length for the independent donor in CTS 3.4 seems to be much lower than expected for BEDT-TTF type radical cation. The length is consistent with a charge somewhere between 1/3 and zero.

	Donor A
a / Å	1.329
b / Å	1.764
c / Å	1.756
d / Å	1.324
δ	0.875
Q	**-0.183** (± 0.1)

Table 3.3.16. Charge calculations for independent donor in CTS 3.4.

Charge calculations for the independent donor in CTS 3.4 are unrealistic. Given the low R factor associated with the crystal structure the donor bond lengths are expected to be accurate.

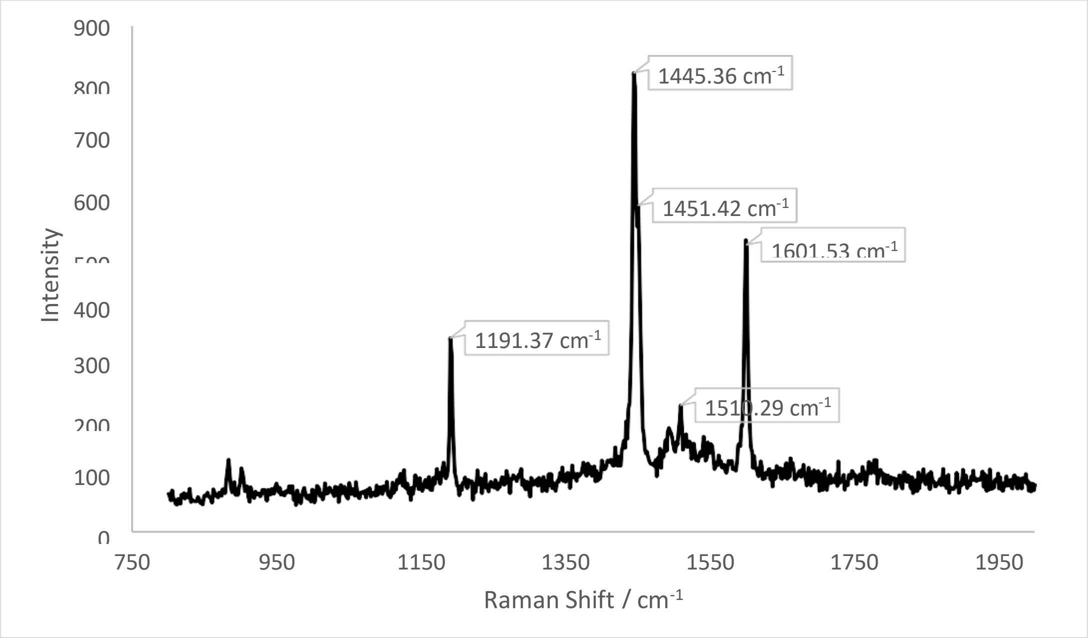

Graph 3.3.9. Relative intensity against Raman shift for a single crystal of CTS 3.4.

Reproducible room temperature Raman measurements were made on several single crystals of CTS 3.4. Due to the raman active symmetrical vibration frequencies present in TCNQ it is more complex to deduce the charge of the donor molecule from the Raman spectra. TCNQ is known to form non-stoichiometric salts with TTF and BEDT-TTF[16] and this is likely to be the case in CTS 3.4.

The ring C=C stretching mode for TCNQ is observed at a shift of 1451 cm^{-1}. The two remaining symmetrical stretching modes C=C and C≡N are observed at shifts of 1191 and 1601 cm^{-1}. The remaining high intensity peak at 1445 cm^{-1} is consistent with the υ_4 stretching mode of a BEDT- $TTF^{+0.5}$ type donor.

3.3 Chapter Conclusions

We report the crystal structures and resistivities of a series of new 1:1 salts of the enantiopure donor bis(2-hydroxylpropylthio)ethylenedithiotetrathiafulvalene, BHP-EDT-TTF, with tetrafluoroborate, perchlorate or hexafluorophosphate anions[10]. Also reported are crystal structures of the corresponding racemic salts. The crystal structures, room temperature resistivities and activation energies are similar for all four enantiopure salts from perchlorate and hexafluorophosphate salts, and are comparable to those from the isostructural tetrafluoroborate salts which were reported previously[9].

The crystal structures of the previously reported hydrated chloride salt are quite different. The flexibility and hydrogen-bonding ability of the side-chains of the donor molecule are responsible for producing the variety in packing motifs, and the hydroxyl groups are involved in interactions with the anions in the cases reported here. In contrast for the salts with polyiodide ions, the hydrogen bonding almost exclusively involves interactions between side chains[9]. The resistivities of some of the chiral radical-cation salts reported here are lower than might have been expected for $(donor)_2^{2+}$ dimers having inter-dimer S---S contacts >3.7 Å. This donor has now produced a family of semiconductors and a single metallic radical-cation salt with triiodide.

A new family of non-isostructural salts has been synthesised from donor BHM-BEDT-TTF. The di-substituted BEDT-TTF derivative shows a propensity to form a number of stoichiometries depending on the anion and crystallisation environment owing to the hydroxyl groups on the side-chains.

The donor forms a semiconducting hydrated 2 : 1 salt in the presence of a solvent and chloride ions. The crystals are twinned with a possible minor confirmation of the donors. It is clear however that the interactions between hydroxyl groups and the insulating layer is key to producing the packing motif of the donor. The two independent donors are in a charge ordered $^{+}1$ and 0 ground state, leading to semiconducting characteristics and Curie-Weiss magnetic behaviour.

3.4 References

1. J.D. Wallis and J-P. Griffiths, *J. Mater. Chem.*, 2005,**15**, 347.
2. N. Avarvari and J. D. Wallis, *J. Mater. Chem.*, 2009, **19**, 4061
3. F. Pop, P. Auban-Senzier, E. Canadell, G. L. J. A. Rikken and N. Avarvari, *Nat. Commun.*,5:3757 DOI: 10.1038/ncomms4757 (2014).
4. F. Pop, P. Auban-Senzier, A. Frackowiak, K. Ptaszyński, I. Olejniczak, J. D. Wallis, E. Canadell and N. Avarvari, *J. Am. Chem. Soc., 2013*, **135**, 17176
5. J. D. Wallis, A. Karrer and J. D. Dunitz, *Helv. Chim. Acta.*, 1986, **69**, 69-70.
6. F. Pop, S. Laroussi, T. Cauchy, C. J. Gomez-Garcia, J. D. Wallis and N. Avarvari, *Chirality*, 2013, **25**, 466.
7. S. Yang, F. Pop, C. Melan, A. C. Brooks, L. Martin, P. Horton, P. Auban-Senzier, G. L. J. A. Rikken, N. Avarvari and J. D. Wallis, *CrystEngComm*., 2014, **16**, 3906.
8. L. Martin, J. D.Wallis, M. Guziak, P. Maksymiw, F. Konalian-Kempf, A. Christian, S.-i. Nakatsuji, J.-i. Yamada and H. Akutsu, *Dalton Trans.*, 2017, **46**, 4225.
9. L. Martin, J. D. Wallis, M. A. Guziak, J. Oxspring, J. R. Lopez, S-i. Nakatsuji, J-i. Yamada and H. Akutsu, *CrystEngComm*, 2014, **16**, 5424.
10. J. R. Lopez, L. Martin, J. D. Wallis, H. Akutsu, J.-i. Yamada, S.-i. Nakatsuji, C. Wilson, J. Christensen and S. J. Coles, *CrystEngComm*, 2017, **19**, 4848.
11. P. Guionneau, C. J. Kepert, D. Chasseau, M. R. Truter and P. Day, *Synth. Met*., 1997, **86**, 1973.
12. S. J. Krivickas, C. Hashimoto, J. Yoshida, A. Ueda, K. Takahashi, J. D. Wallis and H. Mori, *Beilstein J. Org. Chem*., 2015, **11**, 1561.
13. P. S. Flandrois, *Acta Cryst*., 1977, **B33**, 2744.
14. T. C. Urnland, S. Allie, T. Kuhlmann, and P. Coppens, *J. Phys. Chem.* 1988, **92**, 6456.
15. T. J. Kistenmacher, T. J. Emge, A. N. Bloch and D. O. Cowan, *Acta Crystallogr., Sect. B: Struct. Crystallogr. Cryst. Chem*., 1982, **38**, 1193.
16. M. Fujiki and H. Tabei, *Synth. Met*., 1987, **18**, 815.
17. G. Saito and T. Murata, *Phil. Trans. R. Soc A.*, 2008, **366**, 139.

Chapter 4: Chiral, Racemic and Diastereomeric Spiroborate Anion Charge Transfer Salts

In this chapter is discussed BEDT-TTF charge transfer salts derived from diastereomeric and chiral borate anions. The synthesis of the borate anions is discussed in Chapter 2. The presence of a configurationally stable stereogenic carbon centre on the ligand as well as the axially chiral molecule that can be formed by the ‘spirane’ like twist through the boron centre produces anionic compounds which hold two separate origins of chirality.

Thus, the introduction of borate anions within charge transfer salts of BEDT-TTF should increase the handedness throughout the material and lead to electro-chiral properties, where the chirality affects the conducting properties of the material.

Presented here are two families of chiral and diastereomeric charge transfer salts produced using the $B(malate)_2^-$ and $B(mandelate)_2^-$ anions respectively. The former produces charge transfer salts in which the conducting properties and structural motifs are noticeably different depending on whether the racemic or chiral malate ligand is used during synthesis of the anion. The latter family consists of two charge transfer salts, produced using either the racemic or chiral forms of mandelic acid during synthesis of the anions. The chiral form produced crystals of helical morphology, the bent nature of these crystals meant that X-ray structure determination is impossible. However, conducting and magnetic data shows that there is a noticeable difference between the racemic and chiral forms. These two families of salts show the first examples of diastereomeric induction within the electrocrystallisation environment[1].

Also presented is a racemic charge transfer salt of BEDT-TTF and the $B(glycolate)_2^-$ anion. The glycolate ligand is devoid of a chiral centre and the only point of chirality is that from the ‘spirane’ twist through the labile boron centre.

4.1 *Bis*(malate)*borate*

The first examples of radical-cation salts of BEDT-TTF with chiral borate anions are discussed in this section, the results are published in the RSC journal Dalton Transactions[1].

$[\mathrm{B(malate)_2}]^-$ was prepared using either enantiopure or racemic bidentate malate ligands and in the former case only one of two diastereoisomers of the borate anion is incorporated, while in the racemic salt one racemic pair of borate anions containing a *R* and a *S* malate ligand is incorporated. The synthesis of such bis-chelated borate anions offers the prospect of creating complexes with more than one stereogenic centre. In the case of the B(malate) $^-$ reported here the chirality of the bidentate chelated malate ligand is retained but diastereoisomers are produced through two possible stereochemical configurations at the boron centre which is labile in solution. Therefore, when using enantiopure *R*-malic acid (*(R)*-hydroxybutanedioic acid), a mixture of diastereoisomeric anions will be produced in solution : $\mathrm{B}_{S}RR$ with an *S* boron centre and two *R* malate ligands, and $\mathrm{B}_{R}RR$ which differs only in having an *R* boron centre. ^{1}H NMR in deuterio-acetonitrile shows the anions exist in a 2 : 1 ratio with very similar NMR spectra. When using racemic *DL*-malic acid, four further diastereoisomers will be produced: $\mathrm{B}_{S}SS$ and $\mathrm{B}_{R}SS$ (the mirror images of the anion described above) and $\mathrm{B}_{S}RS$ and $\mathrm{B}_{R}RS$. ^{1}H NMR in deuterio-acetonitrile is complex but consistent with the presence of these diastereomers. Reported in this section is a chiral radical-cation salt of BEDT-TTF, synthesised in the presence of chiral $\mathrm{B}_{S}RR$ and $\mathrm{B}_{R}RR$, in which just the $\mathrm{B}_{S}RR$ anion is incorporated into the structure. When repeating the synthesis using a mixture of the six possible diastereomeric borate anions the two racemic pairs are not incorporated, instead only the $\mathrm{B}_{S}RS$ and $\mathrm{B}_{R}RS$ are present.

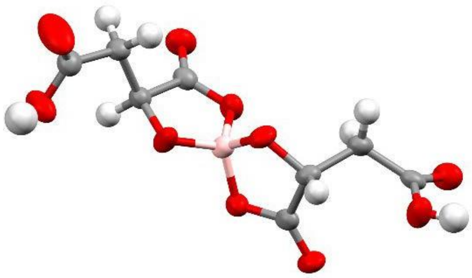

Figure 4.1. Representation of the chiral $\mathrm{B}_{S}RR$ malato anion. Ellipsoids are drawn at the 50% probability level.

4.1.1 α-(BEDT-TTF)$_2$B$_{R/S}$ [(R/S)malate$_2$].(H$_2$O)$_{2.85}$

Structural, conducting and magnetic data for the title compound is discussed. The salt crystallises in the centrosymmetric space group P-*1* with only two of the possible six diastereoisomers present throughout the lattice. The two independent BEDT-TTF molecules pack in the alpha motif and semiconducting behaviour is observed down to 150 K.

4.1.1.1 Electrocrystallisation Table

Donor	Counterion	Electrolyte	Solvent	Current /μA	Crystal Growth	Observation
ET	K^+	B*R/S*[(*R/S*)malate]$_2^-$	1,1,2-TCE	0.2	YES	Large quantity of black hexagonal crystals collected from the electrode after 21 days.

Table 4.1. Electrocrystallisation table for the synthesis of CTS 4.1.

1,1,2-Trichloroethane as solvent during electrocrystallisation produced high quality crystals of CTS 4.1. Electrocrystallisation experiments using other organic solvents (PhCl, PhBr) produced only amorphous materials with no crystallinity.

4.1.1.2 *Crystal Structure*

α-(BEDT-TTF)$_2$B$_{R/S}$ [(*R/S*)malate$_2$].(H$_2$O)$_{2.85}$	
Formula	$C_{28}H_{29.71}O_{12.85}S_{16}B$
M_r/g mol^{-1}	1095.61
Temp / K	200
Radiation	Mo
Wavelength	0.7105
Crystal System	Triclinic
Space group	P-*1*
a / Å	8.69808(16)
b / Å	11.9375(2)
c / Å	21.7391(4)
α / °	76.897(5)
β / °	84.153(6)
γ / °	70.370(5)
V/Å^3	2069.79(1)
Z	2
ρ/g cm^{-1}	1.758
μ/cm^{-1}	8.959
Absorption Applied	Yes
Abs. Type	Multi-scan
Abs. Range	0.814-1.000
Total Reflections	21987
Unique Reflections	9478
R [all data]	0.0557
R_1 [$I > 2\sigma(I)$]	0.0378
wR [all data]	0.1059
Goodness of fit	1.034
Refinement Program	SHELX
Refinement Mode	Single
Flack Parameter	n/a

Table 4.2. X-ray data for CTS 4.1

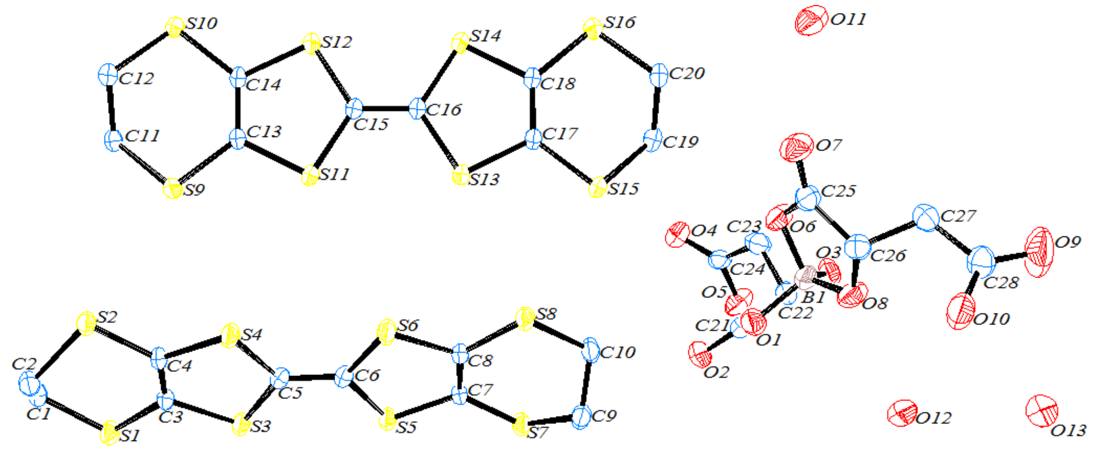

Figure 4.2. ORTEP diagram of asymmetric unit of CTS 4.1. Displacement ellipsoids are drawn at the 50% probability level. Hydrogens are omitted for clarity.

CTS 4.1 crystallises in the triclinic crystal system in the centrosymmetric space group P-*1*. The asymmetric unit contains two crystallographically independent BEDT-TTF molecules, one racemic borate anion and 2.85 water molecules with the formula (BEDT-TTF)$_2$B$_{R/S}$[(*R/S*)-malate)]$_2$.(H$_2$O)$_{2.85}$. Only two of the six possible diastereoisomers are present in the lattice, B$_R$*RS* and *B$_S$RS*. Each borate anion contains both an *R*- and an *S*- malate ligand and they differ only in the configuration at the boron centre with each anion of the racemic pair present in the unit cell (Figure 4.1). This is the first example of spontaneous diastereomeric induction within the electrocrystallisation environment. Figure 4.2 above shows the ORTEP diagram of the asymmetric unit with numbering scheme.

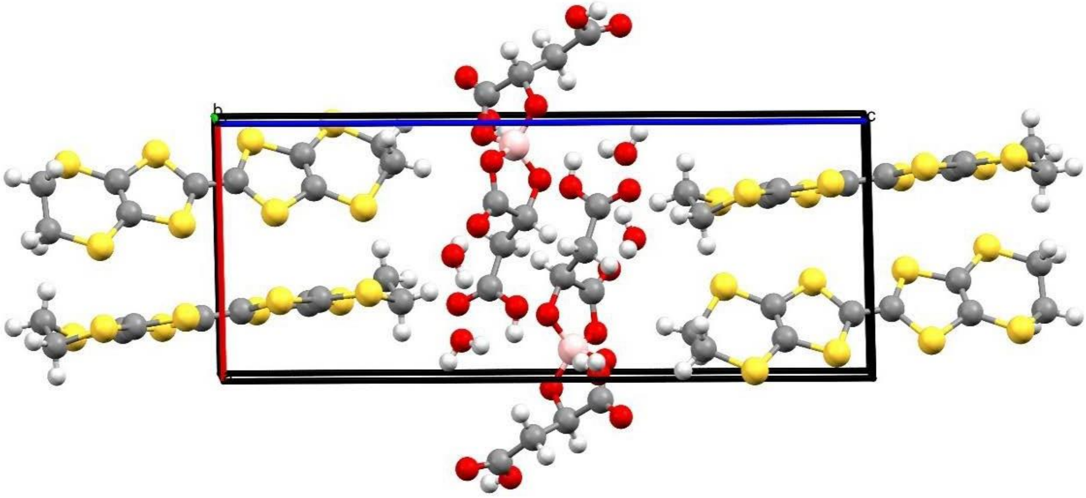

Figure 4.3. Unit cell of CTS 4.1 viewed along the *b* axis.

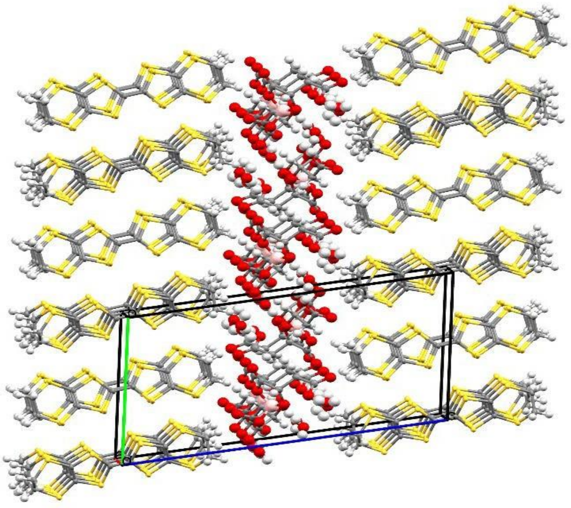

Figure 4.4. Layered structure of CTS 4.1 viewed along the *a* axis.

Figure 4.4 above shows the layered structure of CTS 4.1 viewed along the *a* axis. The water molecules occupy the space left by the outlying CH_2COOH side-chains. The anions alternate between B*R**RS* and B*S**RS* through the *ab* plane. The crystallographically independent donors pack separately in each stack along the *a* axis with stacks alternating along the *b* axis.

Each independent donor forms separate stacks along the *a* axis and the stacks lie side by side in the *b* direction. This corresponds to the alpha-type packing motif with the two planes of donors arranged at an angle of 70.64°. Donor layers are separated in the *c* direction by the hydrated insulating layer, containing the borate anions and hydrogen bonded water molecules. Each donor has thirteen side-to-side S...S contacts below the sum of the vdW radii (3.6 Å).

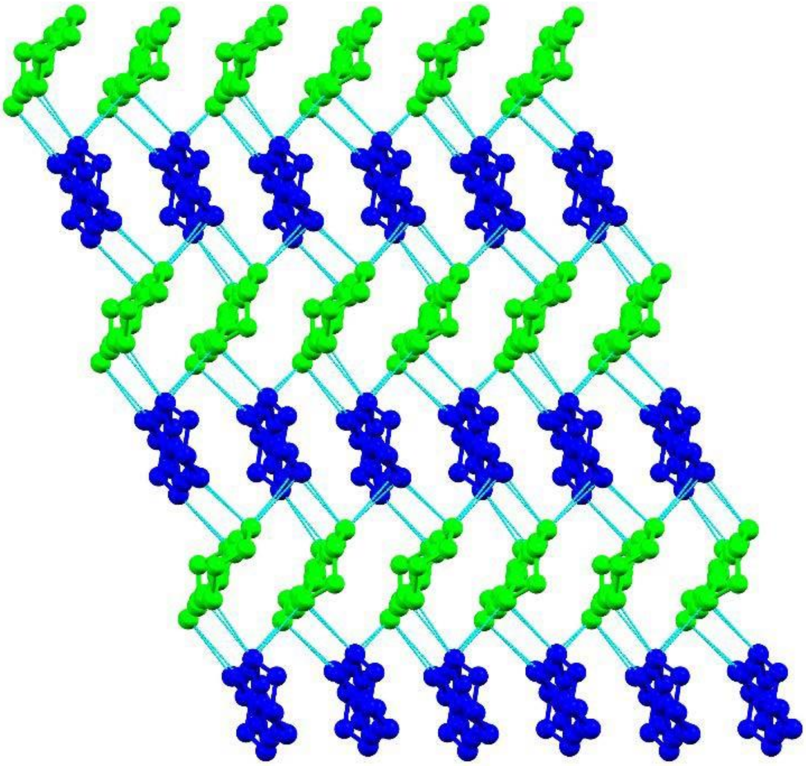

Figure 4.5. Donor packing of CTS 4.1 viewed along the *c* axis. Donor A is coloured green and donor B coloured dark blue. S...S contacts are shown in light blue lines.

Figure 4.6 shows donor A, pictured above in green. Short sulphur interactions below the sum of the vdW radii (3.6 Å) are shown in red dotted lines. Contacts atoms are shown in black, contact length and central TTF bond lengths are shown in green. The donor makes a total of thirteen 'in plane' and 'out of plane' side-to-side S...S contacts. Due to the segregated stacking between donors A and B all contacts are with the other independent donor B. The terminal ethylene groups both show the half chair confirmation with each sp^3 carbon displaced equidistant from the plane of the central TTF unit, the displaced carbons do not eclipse one another when viewed along the long axis of the BEDT-TTF molecule. Estimation of charge per Kepert *et al*. method of averaging the central TTF bond lengths agree with a donor charge of $^+$0.5. The side on profile view Figure 4.7, shows that the central TTF portion of the donor remains relatively planar except for the terminal sp^3 carbons which are considered to have sp^3 hybridised valence orbitals.

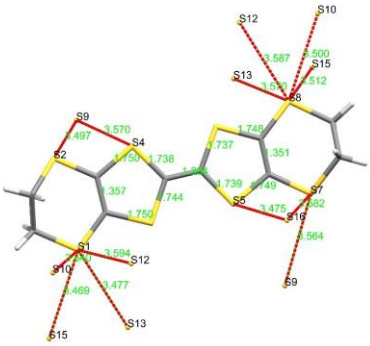

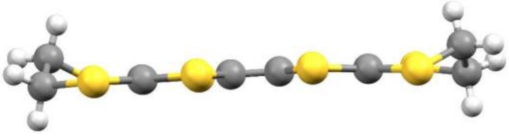

Figure 4.6 (left). CTS 4.1: Donor A with S...S contacts drawn in red and contact atoms labelled in black. Contact length and central TTF bond lengths are labelled in green. Figure 4.7 (right). CTS 4.1: Side on profile view of donor A.

Figure 4.8 shows donor B, pictured above in blue. Short sulphur interactions below the sum of the vdW radii (3.6 Å) are shown in red dotted lines. Contacts atoms are shown in black, contact length and central TTF bond lengths are shown in green. The donor makes a total of thirteen ‘in plane’ and ‘out of plane’ side-to-side S...S contacts with donor A. The terminal ethylene groups both show the same confirmation as donor A; the uneclipsed half-chair, with each sp^3 carbon displaced equidistant from the plane of the central TTF unit. Estimation of charge per Kepert *et al*. method of averaging the central TTF bond lengths calculate that donor B also carries a charge of $^+$0.5. This is in good agreement with the formula stated above and both donors satisfy the monovalency of the racemic borate anion. The side on profile view,

Figure 4.9, shows the central TTF unit to be relatively planar until the terminal ethylene groups.

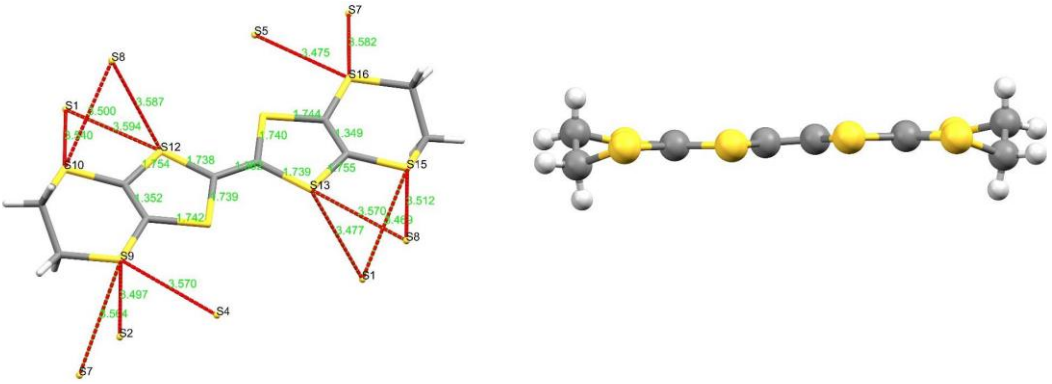

Figure 4.8 (left). CTS 4.1: Donor A with S...S contacts drawn in red and contact atoms labelled in black. Contact length and central TTF bond lengths are shown in green. Figure 4.9 (right). CTS 4.1: Side on profile view of donor A.

The insulating layer packs in the *ab* plane with each layer containing an equal number of each anions in the racemic pair. The anion layer contains 2.85 water molecules per borate anion and these are hydrogen bonded throughout to create a network of hydrogen bonding interactions between the water molecules and $B_{R/S}[(R/S)\text{mal})_2]^-$ anions.

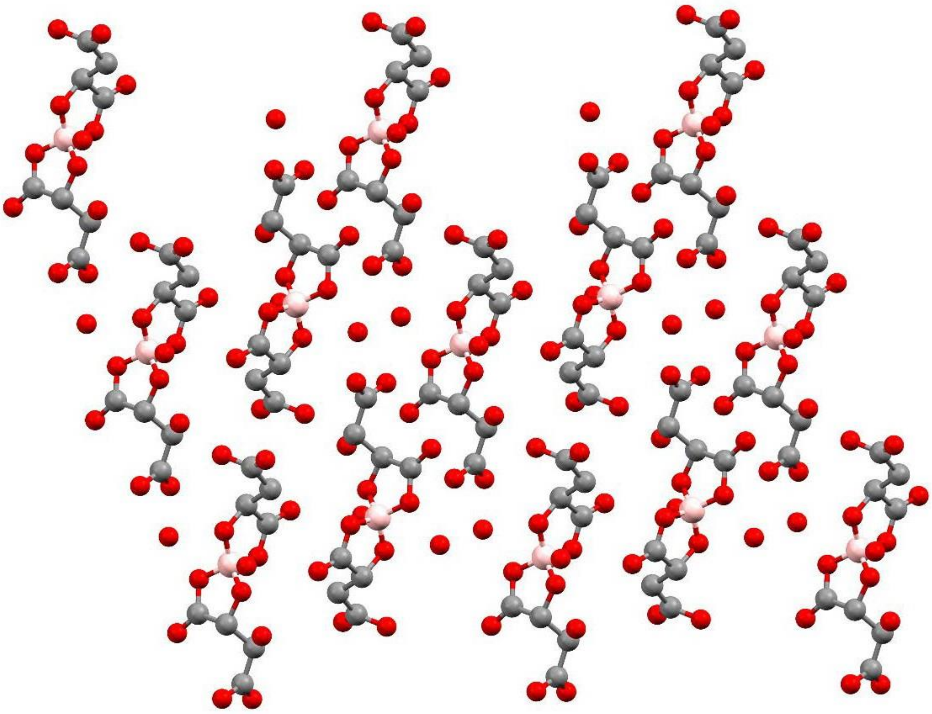

Figure 4.10. Hydrated anionic layer of CTS 4.1 as viewed along the *c* axis.

The two carboxylic hydrogen atoms are each hydrogen bonded to water molecules (1.78-1.85 Å), one of the waters is also hydrogen bonded to two borate ring O atoms (2.05 and 2.15 Å), while the other water is hydrogen bonded to a ring carbonyl oxygen (2.20 Å) and to a third water molecule (1.99 Å). This third water molecule makes a second hydrogen bond to a ring carbonyl O atom (1.93 Å). Donor A makes two short contacts with two of the water molecules (S7-O13, 3.28(5) Å and S2-O11, 3.142 Å) and donor B has one short contact with a borate anion (S10...O4, 3.14(5) Å).

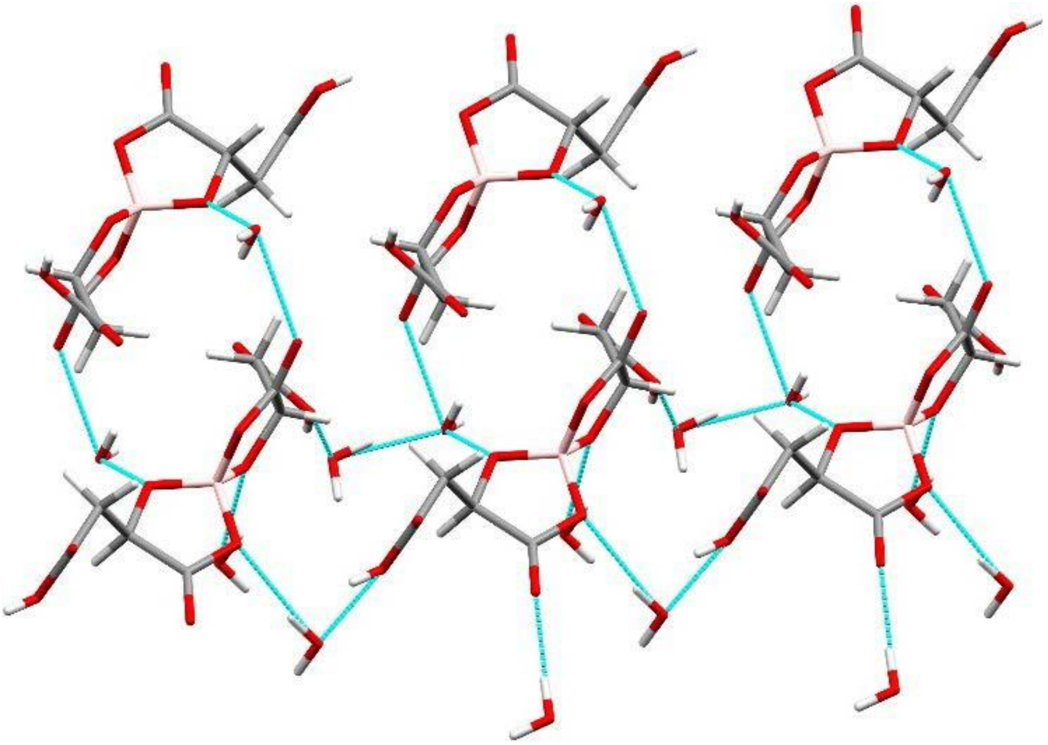

Figure 4.11. Capped stick diagram of the anionic layer in CTS 4.1 with hydrogen bonding interactions shown in light blue.

4.1.1.3 S…S Contacts

Contact	***Atom***	***Atom***	***Length / Å***
1	S1	S10	3.539(12)
2	S1	S12	3.594(18)
3	S5	S16	3.475(18)
4	S7	S16	3.582(11)
5	S2	S9	3.497(10)
6	S4	S9	3.569(18)
7	S8	S13	3.569(18)
8	S8	S15	3.512(10)
9	S8	S10	3.499(8)
10	S8	S12	3.587(9)
11	S1	S13	3.477(3)
12	S1	S15	3.469(8)
13	S7	S9	3.563(8)

Table 4.3. Short sulphur interactions in CTS 4.1 below the sum of the vdW radii (3.6 Å).

There is a total of thirteen short sulphur interactions below the sum of the vdW radii (3.6 Å). The shortest of these is between donor A and donor B (S1...S15, 3.469(2) Å).

4.1.1.4 C=C Bond Length, Charge Calculations and Raman

	A - Green	***B - Blue***
C=C Bond Length / Å	1.364(3)	1.362(4)

Table 4.4. Central C=C bond lengths for donors A and B in CTS 4.1.

The central C=C bond lengths for the two independent donors present in CTS 4.1 are presented above in Table 4.4. The two values are very similar and it can be deduced that both donors therefore carry the same charge.

	A – Green	***B – Blue***
a / Å	1.364	1.362
b / Å	1.740	1.739
c / Å	1.749	1.749
d / Å	1.354	1.352
δ	0.771	0.774
Q	**0.593** (± 0.1)	**0.571** (± 0.1)

Table 4.5. Charge estimations according to Kepert *et al.*[2] average TTF bond length calculations for CTS 4.1.

Charge estimation for the two independent BEDT-TTF molecules in CTS 4.1 suggest that the two donors both carry equal charges of $^{+}$0.5. This is in good agreement with the central C=C bond lengths.

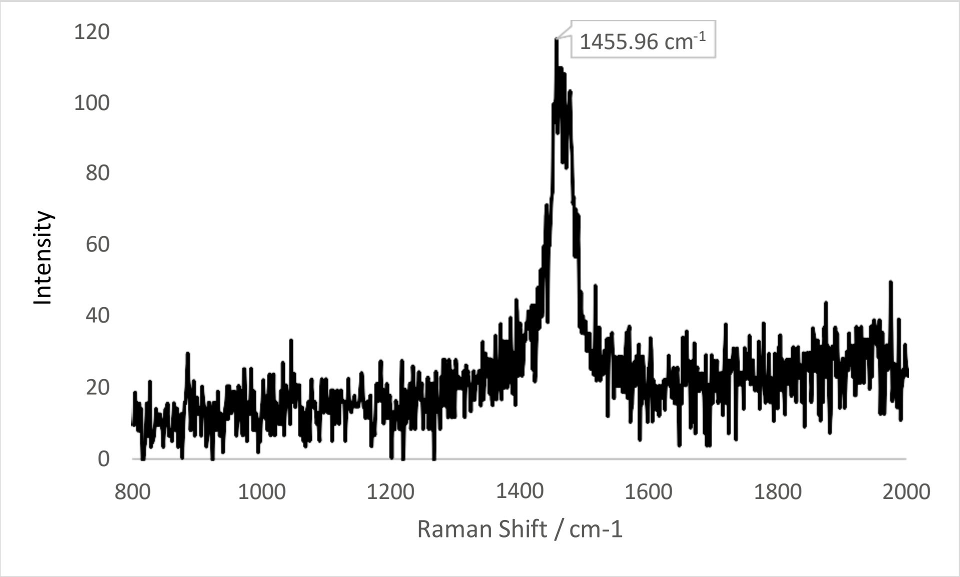

Graph 4.1. Relative intensity against the Raman shift for a single crystal of CTS 4.1

Reproducible room temperature Raman measurements were made on several crystals of CTS 4.1. The stretching frequencies expected for a 2:1 BEDT-TTF radical cation salt are 1457-1471 cm^{-1} and 1488-1498 cm^{-1} for the υ_4 and υ_3 modes respectively.

Although the spectrum above is noisy, the observation of high intensity peaks between 1450 and 1480 cm^{-1} are consistent with the presence of two $^{+}$0.5 radical cations. The highest intensity peak is labelled for reference. Along with central C=C bond lengths and charge estimations it can be concluded that CTS 4.1 is a 2:1 radical cation salt.

4.1.1.5 Magnetic Data

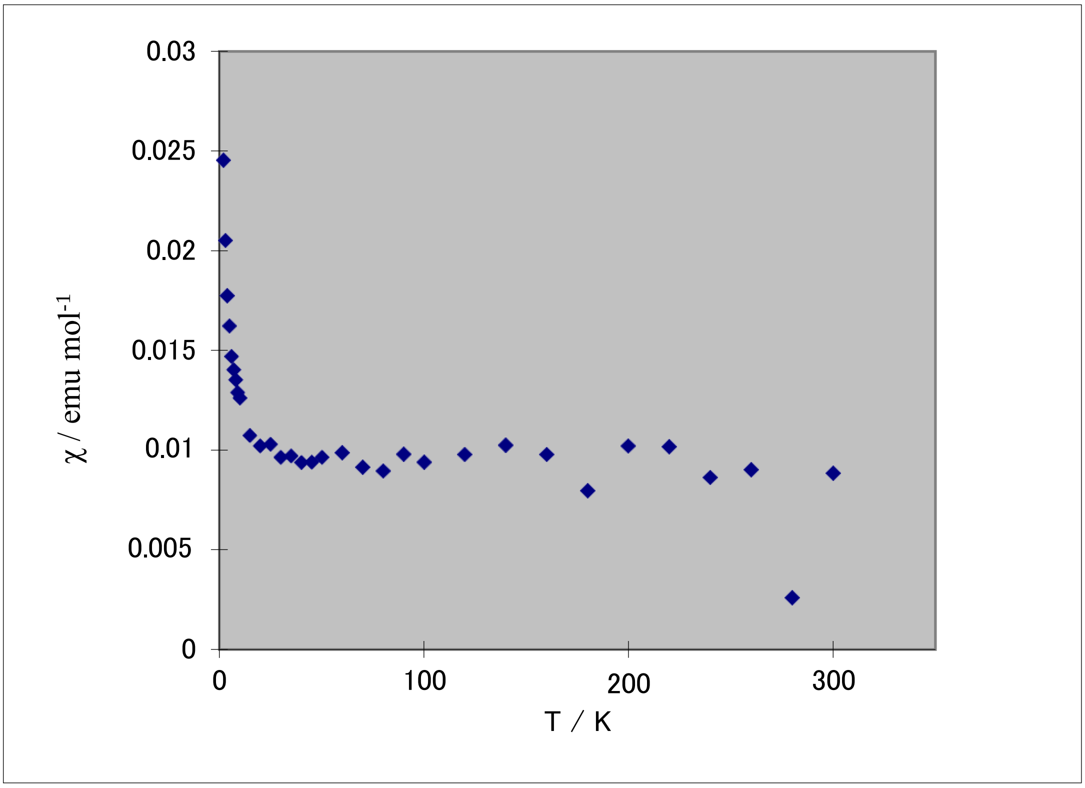

Graph 4.2. Temperature dependent magnetic susceptibility for CTS 4.1.

Magnetic susceptibility measurements were performed using only 0.38 mg of randomly orientated polycrystalline sample. The data has been fitted to the Curie-Weiss law by Prof. H. Akutus of Osaka University. No magnetic transition is observed from 300 – 2 K which suggests that the ground state of the salt is non-magnetic as is expected from the BEDT-TTF molecular charge calculations showing that the salt is not in the paramagnetic charge disproportionation state at least down to 150 K.

4.1.1.6 Band Structure Calculations

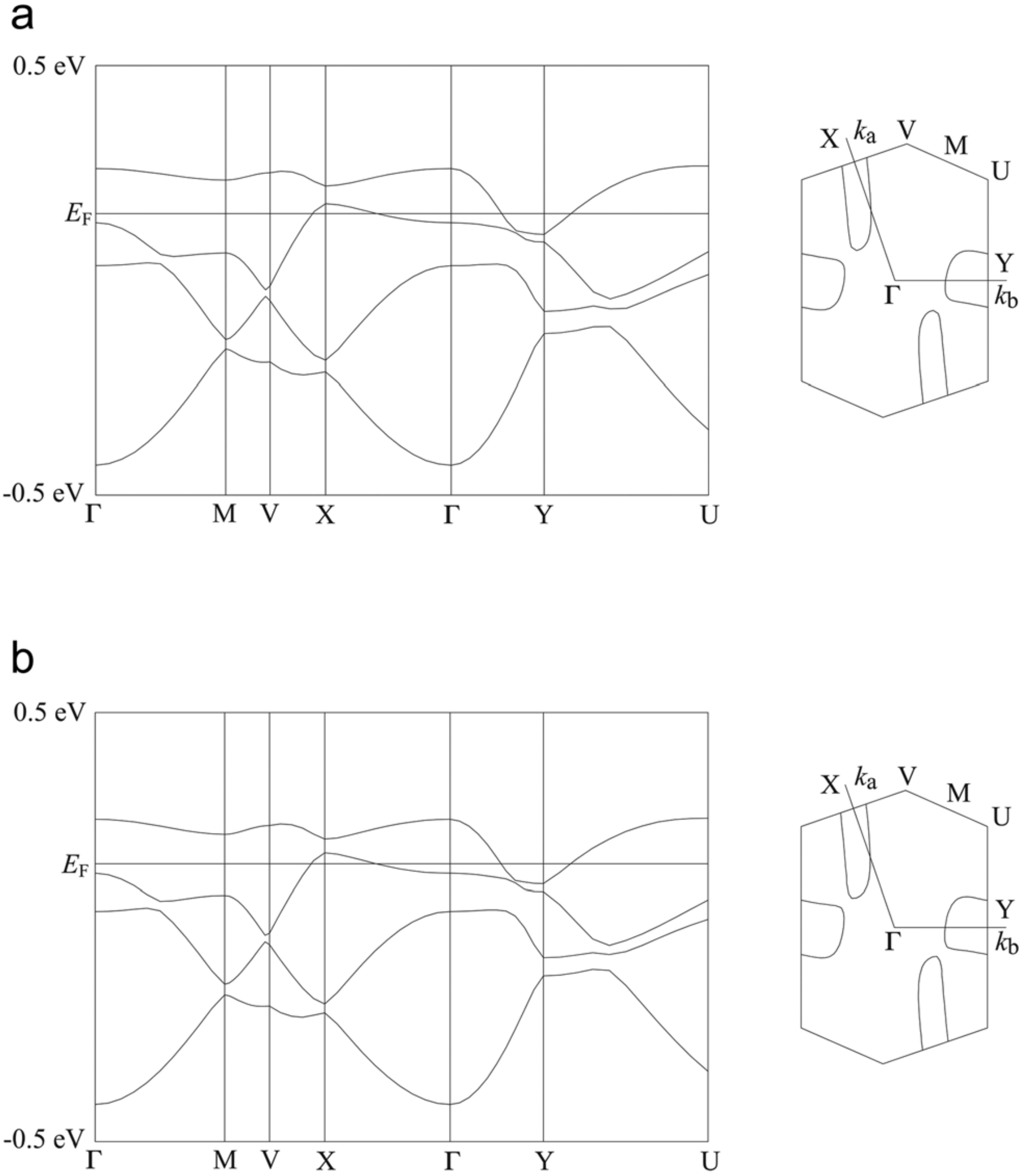

Graph 4.3. Band dispersions and Fermis surfaces for CTS 4.1 at 150 K (a) and 250 K (b).

Hückel tight binding band calculations were performed for CTS 4.1 at 150 and 250 K. The band dispersions and Fermi surfaces are shown in Graph 4.3a and 4.3b respectively. There is no significant difference between the results at either temperature. CTS 4.1 has an electron and a hole pocket which suggests that the salt is semi-metallic.

4.1.1.7 Resistivity Data

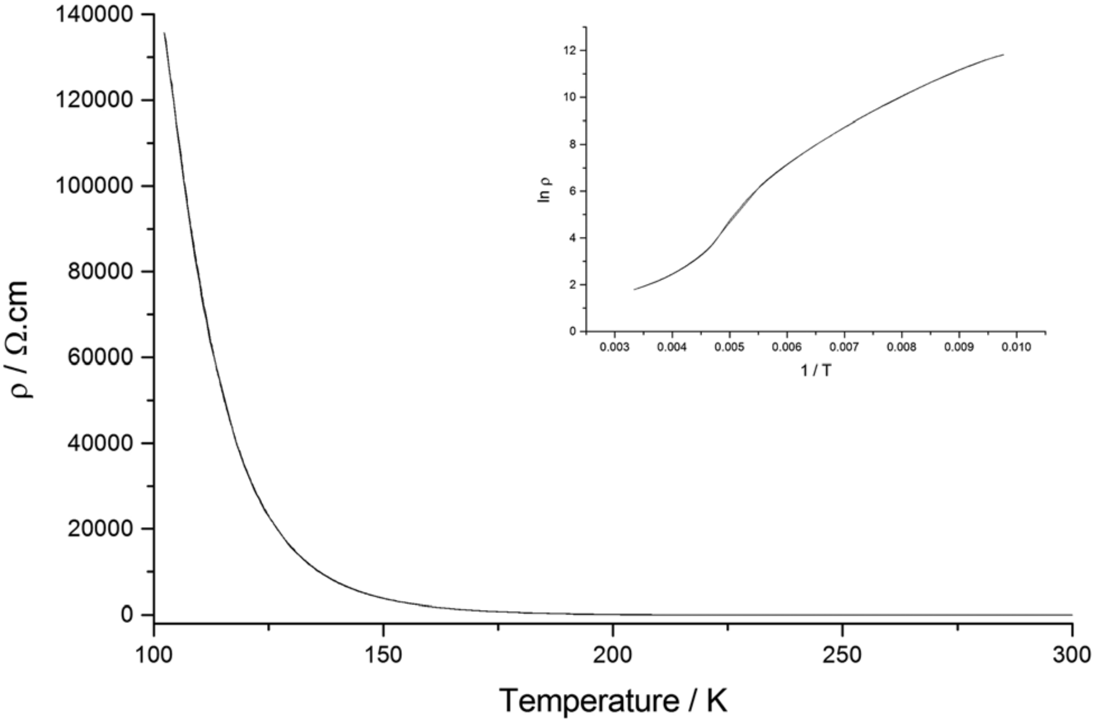

Graph 4.4. Temperature dependent resistivity for CTS 4.1. Inset: Logarithmic resistivity against 1/T for CTS 4.1.

CTS 4.1 exhibits metallic properties at room temperature ($\rho_{RT} = 0.00163$ Ω.cm). However, on cooling the resistivity increases with decreasing temperature. This behaviour indicates that the salt becomes a semi-conductor in the low temperature region. In fact, exponential temperature dependence of the resistivity is only observed below 250 K with a calculated activation energy of 0.100 eV. Band structure calculations and magnetic susceptibility measurements suggest that CTS 4.1 is in the non-magnetic semi-metallic ground state at room temperature and the semimetal-to-semiconductor transition can be attributed to band nesting in the low temperature region.

4.1.2 α-*(BEDT-TTF)$_2$[B$_s$(R-malate)$_2$]*

Electrocrystallisation of BEDT-TTF in the presence of the borate anion synthesised from chiral *d*+ malic acid afforded a non-isostructural charge transfer salt. In which only the anion of B$_S$*RR* stereochemistry is present in the lattice and no water is included. Structural, magnetic and conducting properties are discussed.

4.1.2.1 Electrocrystallisation Table

Donor	**Counterion**	**Electrolyte**	**Solvent**	**Current /µA**	**Crystal Growth**	**Observation**
ET	K^+	B*R/S*[(*R*)malato]$_2^-$	1,1,2-TCE	0.2	YES	Large quantity of black plates collected from the electrode after 21 days.

Table 4.6. Electrocrystallisation table for the synthesis of CTS 4.2.

As above in the racemic example of CTS 4.1, 1,1,2-Trichlorethane produced chiral crystals of high quality for full physical and structural characterisation.

4.1.2.2 *Crystal Structure*

α-(BEDT-TTF)$_2$[B$_S$(*R*-malate)$_2$]	
Formula	$C_{28}H_{24}O_{10}S_{16}B$
M_r/g mol^{-1}	1044.24
Temp / K	100
Radiation	Mo Kα
Wavelength	0.7105
Crystal System	Orthorhombic
Space group	$P2_12_12_1$
a / Å	9.1696(8)
b / Å	10.2343(9)
c / Å	41.196(4)
α / °	90
β / °	90
γ / °	90
V/Å^3	3866.0(6)
Z	4
ρ/g cm^{-1}	1.794
μ/cm^{-1}	0.0950
Absorption Applied	Yes
Abs. Type	Analytical
Abs. Range	0.224-1.000
Total Reflections	44369
Unique Reflections	8836
R [all data]	0.0825
R_1 [$I > 2\sigma(I)$]	0.0760
wR [all data]	0.1980
Goodness of fit	1.064
Refinement Program	SHELX
Refinement Mode	F^2
Flack Parameter	0.04(9)

Table 4.7. X-ray data for CTS 4.2

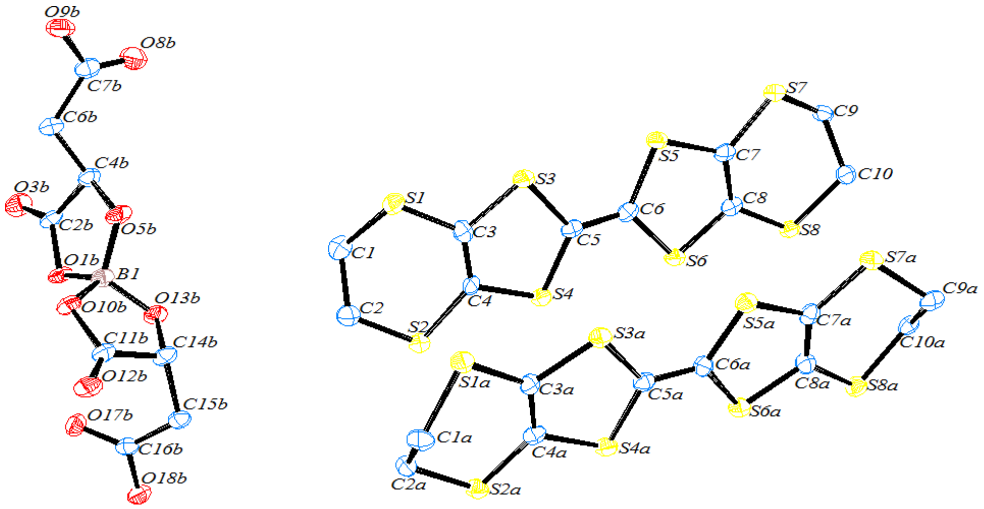

Figure 4.12. ORTEP diagram of the asymmetric unit of CTS 4.2. Displacement ellipsoids are drawn at the 50% probability level.

CTS 4.2 crystallises in the orthorhombic crystal system in the non-centrosymmetric space group $P2_12_12_1$. Two crystallographically independent BEDT-TTF molecules and one borate anion are present in the asymmetric unit. The formula is (BEDT-TTF)$_2$[B$_S$(*R*-malate)$_2$] and only one borate anion with stereochemistry B$_S$*RR* is present throughout the lattice. The unit cell as viewed along the *b* axis is shown in Figure 4.13.

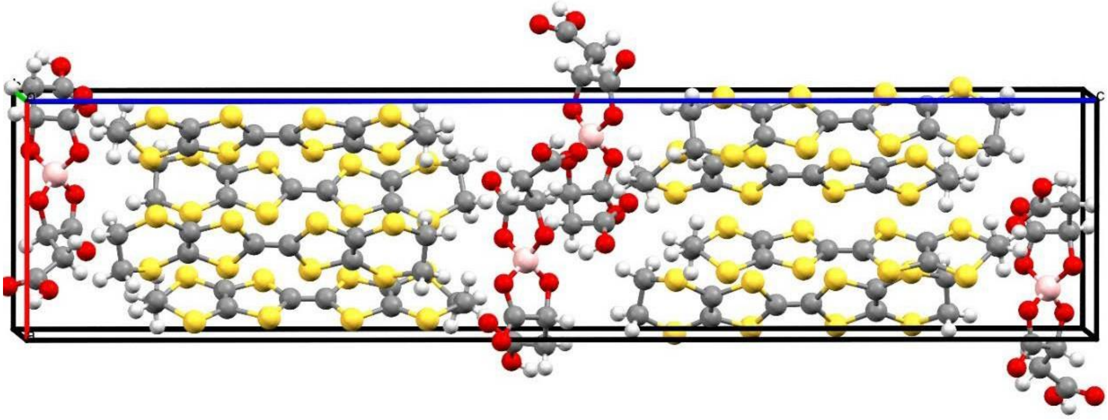

Figure 4.13. Unit cell of CTS 4.2 viewed along the *b* axis.

The donors are organised in an ABAB arrangement in stacks along the a axis. The stacks are in the alpha packing motif and propagate along the crystallographic *b* axis with neighbouring layers separated by the insulating layer in the *c* direction. Side-to-side S...S contacts between donors in neighbouring stacks are observed. Unlike the hydrated racemic salt, donors A and B in CTS 4.2 alternate throughout stacks. The layered structure of CTS 4.2 viewed along the *a* axis is shown overleaf in Figure 4.15.

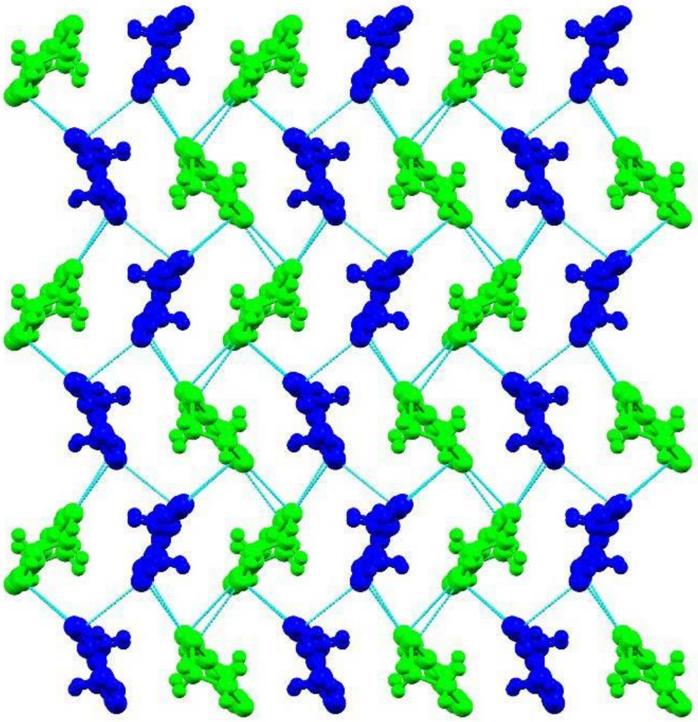

Figure 4.14. Donor packing of CTS 4.2 viewed along the *c* direction. S...S contacts are shown in light blue lines. Donors are coloured according to symmetry.

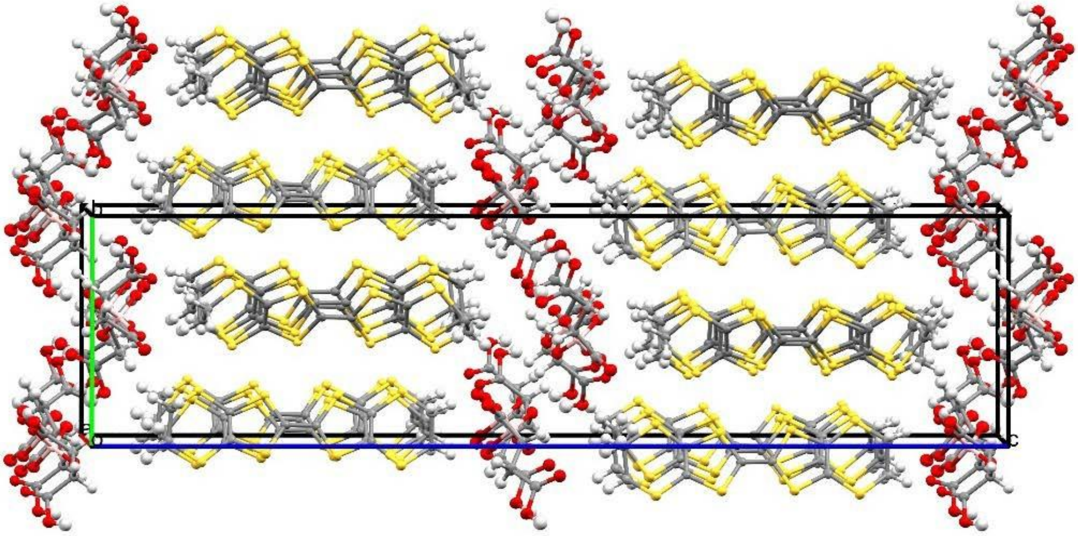

Figure 4.15. Layered structure of CTS 4.2. Viewed along the *b* axis. Ellipsoids are drawn at the 50% probability level.

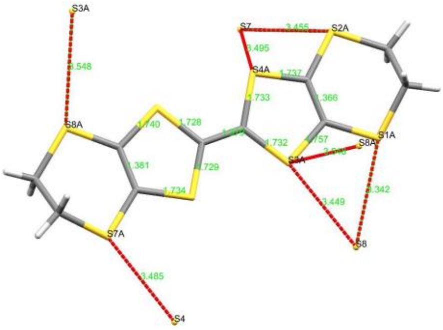

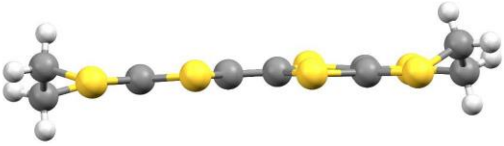

Figure 4.16 (left). CTS 4.2: Donor A with S...S contacts drawn in red and contact atoms labelled in black. Contact length and central TTF bond lengths are shown in green. Figure 4.17 (right). CTS 4.2: Side on profile view of donor A.

Figure 4.16 shows donor A, pictured above in green. Short sulphur interactions below the sum of the vdW radii (3.6 Å) are shown in dotted red lines and contact atoms are labelled in black. Contact length and central TTF bond length are shown in green. The donor makes a total of seven 'in plane' and 'out of plane' S...S contacts. Both terminal ethylene groups are in the half chair confirmation with each methylene carbon displaced equidistant from the long axis of the molecule. The central TTF core is planar which can be seen in the side on profile view in Figure 4.17. The donor is calculated to carry a neutral charge.

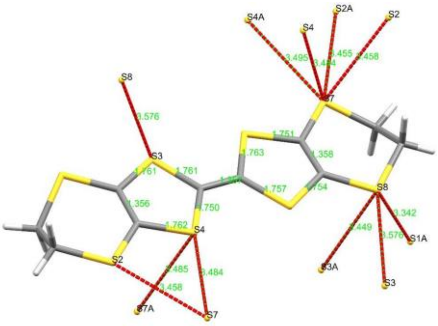

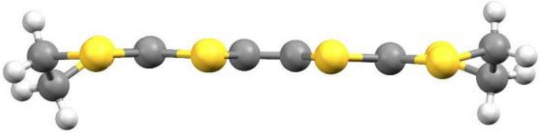

Figure 4.18 (left). CTS 4.2: Donor B with S...S contacts drawn in red and contact atoms labelled in black. Contact length and central TTF bond lengths are shown in green. Figure 4.19 (right). CTS 4.2: Side on profile view of donor B.

Figure 4.18 above shows donor B, pictured above in blue. Short sulphur interactions below the sum of the vdW radii (3.6 Å) are shown in dotted red lines and contacts atoms are labelled in black. Contact lengths and central TTF bond lengths are shown in green. The donor makes a total of eleven 'in plane' and 'out of plane' S...S contacts. The terminal ethylene groups are in the half chair confirmation with each methylene carbon displaced equidistant from the long axis of the molecule. The TTF core is planar as can be viewed from the side on profile view in Figure 4.19. The donor is calculated to carry a charge of $^{+}1$ which is in good agreement with the formula $(\mathrm{BEDT\text{-}TTF})_2\mathrm{B}_S[(R)\mathrm{mal}]_2$ where donor A is neutral, donor B is cationic and $\mathrm{B}_S[(R)\mathrm{mal}]_2^{-}$ is a monovalent anion.

The chiral borate anion stacks in the *ab* plane with neighbouring stacks separated by alpha packed BEDT-TTF molecules along the *c* direction. The insulating layer is stabilised through hydrogen bonding between the carboxylic acid groups and borate ring O atoms. The two side-chains adopt different confirmations, one is orientated away from the centre of the borate while the other is folded back on itself so the acid's carbonyl oxygen makes a short contact with adjacent ring carbonyl carbon (O...C, 2.738 Å). There is also a short intermolecular contact between a methylene hydrogen belong to the extended side chain and a ring carbonyl carbon (H...C, 2.37 Å). A short contact is observed between donor B and a borate anion (S2A...O17B, 3.04(3) Å).

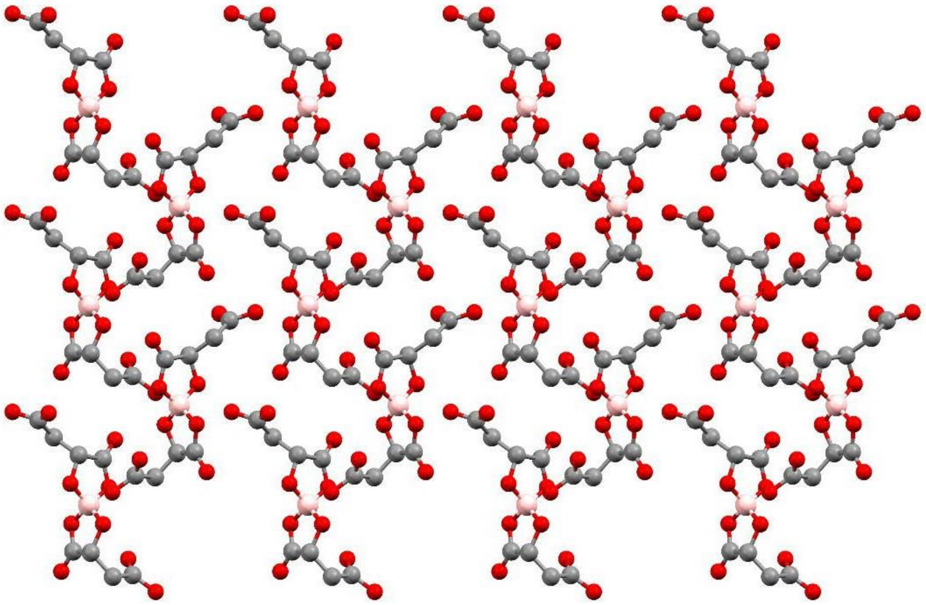

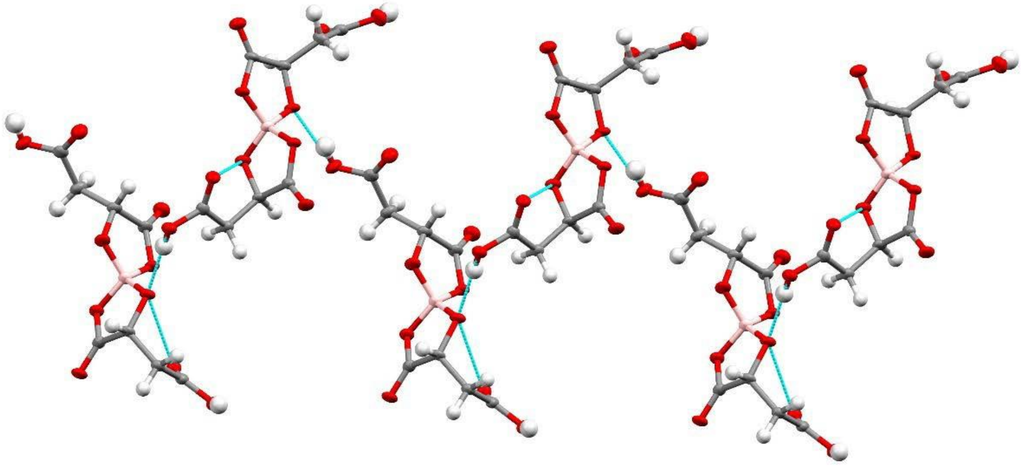

Figure 4.20 (Top). Anionic layer of CTS 4.2 as viewed along the *c* axis. Figure 4.21 (bottom). Hydrogen bonding interactions between B_S*RR* anions in CTS 4.2.

4.1.2.3 S…S Contacts

Contact	***Atom***	***Atom***	***Length / Å***
1	S2	S7	3.458(18)
2	S4	S7	3.485(2)
3	S8	S3	3.576(2)
4	S4	S7A	3.485(19)
5	S8	S1A	3.342(18)
6	S8	S3A	3.449(19)
7	S7	S2A	3.455(19)
8	S7	S4A	3.495(2)
9	S8A	S3A	3.548(2)

Table 4.8. Short sulphur interactions below the sum of the vdW radii (3.6 Å) for CTS 4.2.

Short sulphur interactions below the sum of the vdW radii are presented in Table 4.8 above. The shortest S...S contacts (S8...S1A, 3.342(18) Å) is between donor A and B. The S...S contacts are on average shorter than those observed in the hydrated racemic salt above.

4.1.2.4 C=C Bond Length, Charge Calculations and Raman

	A - Green	***B - Blue***
C=C Bond Length / Å	1.357(13)	1.379(13)

Table 4.9. Central C=C bond lengths for the two independent BEDT-TTF molecules present in CTS 4.2.

The central C=C bond lengths of the donors are noticeably different and one would expect both to donors to carry different charges.

	A – Green	***B – Blue***
a / Å	1.357	1.379
b / Å	1.758	1.731
c / Å	1.757	1.742
d / Å	1.357	1.374
δ	0.801	0.720
Q	**0.369** (± 0.1)	**0.974** (± 0.1)

Table 4.10. BEDT-TTF charge estimations according to Kepert *et al.*[2] average TTF bond length calculations for CTS 4.2.

The assumption that both donors carry different charges from the length of the central C=C bonds is supported by the charge estimations displayed in Table 4.10. The calculations indicate that there is a charge localisation between the two independent donors and that one BEDT-TTF is neutral while the other carries a charge of $^{+}1$.

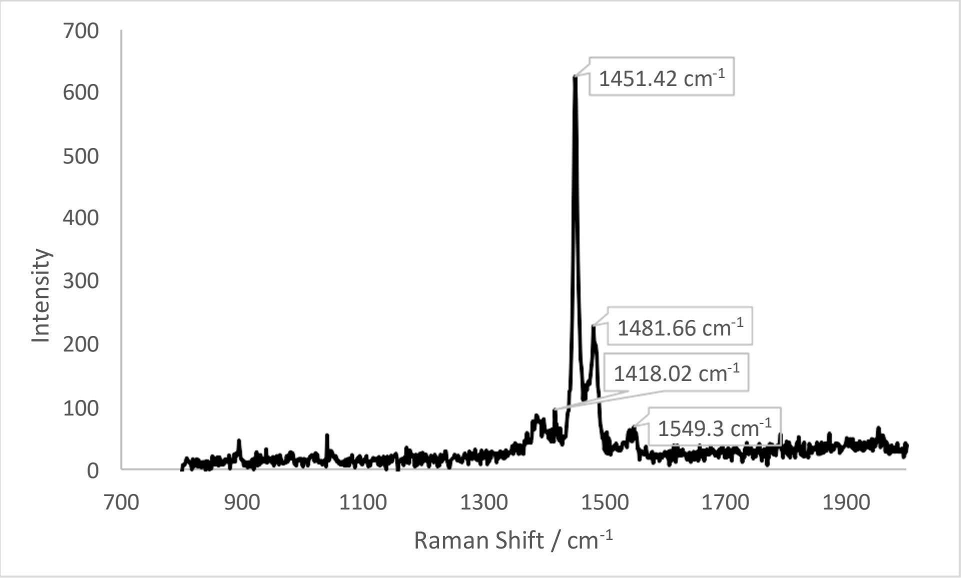

Graph 4.5. Relative intensity against Raman shift for a single crystal of CTS 4.2.

Reproducible room temperature Raman measurements were made on several crystals of CTS 4.2. The spectrum above adds evidence to the proposal that there is one neutral and one cationic BEDT-TTF molecule present in the salt. Although the relative intensity of the peaks is lower than expected (this is probably due to structural defects present in the crystal); the four highest intensity peaks labelled in Graph 4.5 above are at the stretching frequencies expected for both neutral and cationic BEDT-TTF molecules. BEDT-TTF^{+1} shows stretching frequencies at values between 1406-1416 cm^{-1} (υ_4) and 1448-1465 cm^{-1} (υ_3), while BEDT-TTF^{0} shows stretching frequencies at values between 1489-1494 cm^{-1} (υ_4) and 1546-1554 cm^{-1} (υ_3). The results presented are therefore in good agreement with the presence of both BEDT-TTF^{+} and BEDT-TTF^{0}.

4.1.2.5 *Magnetic Data*

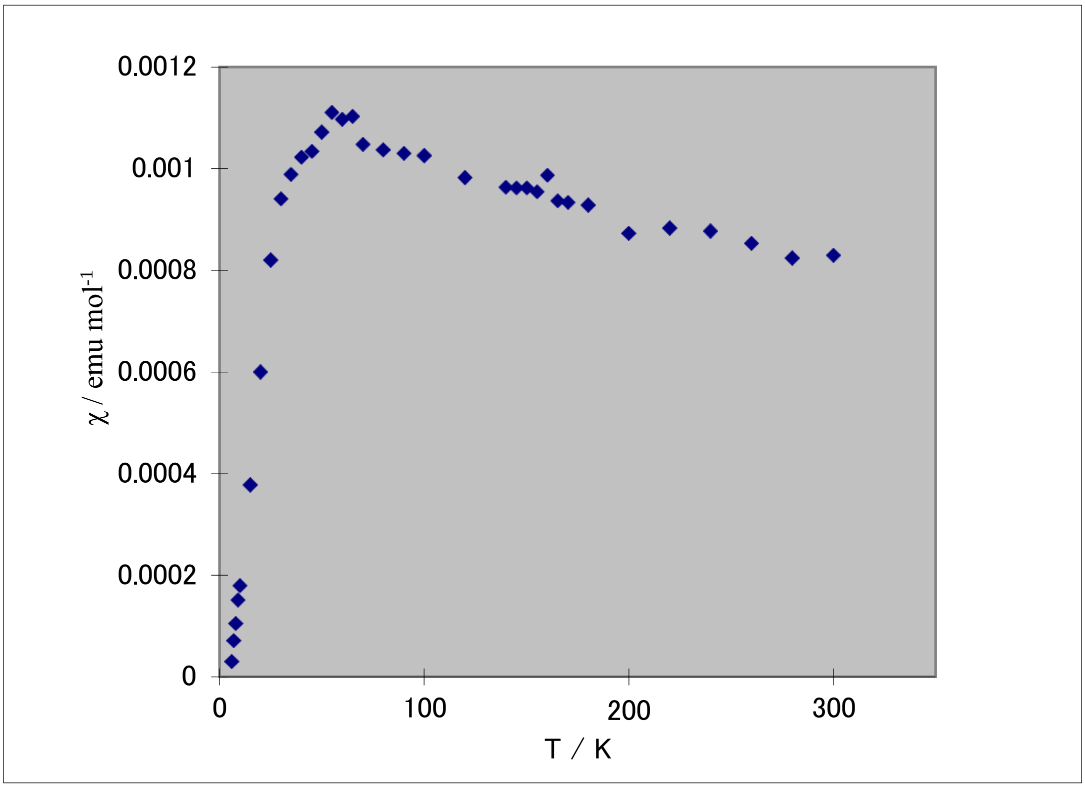

Graph 4.6. Temperature dependent magnetic susceptibility for CTS 4.2.

Magnetic susceptibility measurements using 2.70 mg of randomly orientated polycrystalline sample of CTS 4.2 indicate that the curve obeys a 2D Heisenberg model where *J* = -71.1 K and the salt has a spin concentration of 25%. 5.7 x 10^{-4} emu mol^{-1} was observed as the residual temperature independent magnetic susceptibility.

4.1.2.6 *Band Structure Calculations*

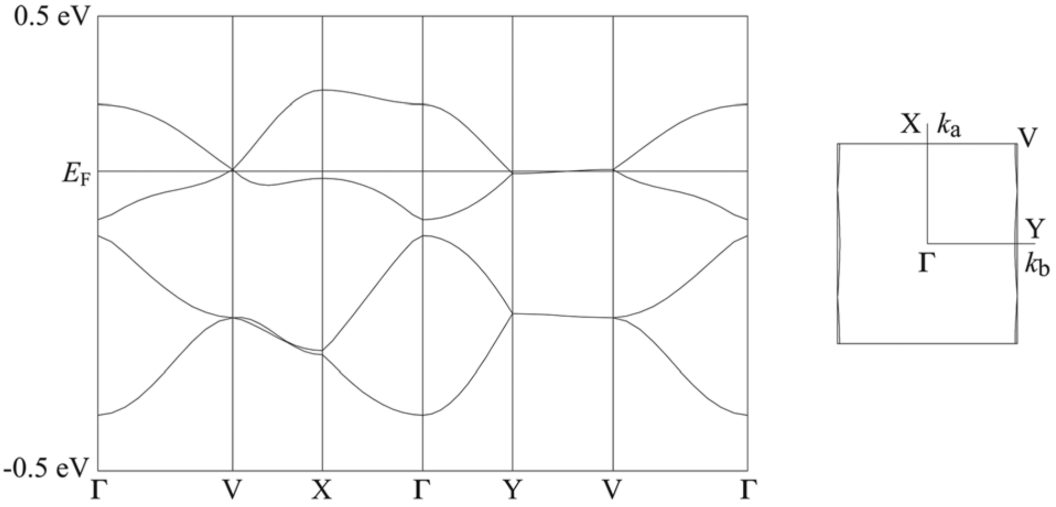

Graph 4.7. Band dispersions and Fermi surfaces for CTS 4.2

Hückel tight binding band calculations were performed for CTS 4.2 the band dispersions and Fermi surfaces are shown above in Graph 4.7. Even though CTS 4.1 and 4.2 both adopt the α-packing motif, the band structures are very different. CTS 4.2 has a Mott gap at the centre of the band dispersion, indicating that the band is effectively half-filled and the salt can become a Mott insulator. Instead the BEDT-TTF molecules select a charge ordered state where one BEDT-TTF is neutral and the other cationic.

As shown above an effectively half-filled flat band is observed from Y to V at which the Fermi surface is located which results in Fermi surfaces that are 1D in nature. This is unique to α-type BEDT-TTF salts where the band structure usually consists of quasi-1D and 2D Fermi surfaces.

4.1.2.7 *Resistivity Data*

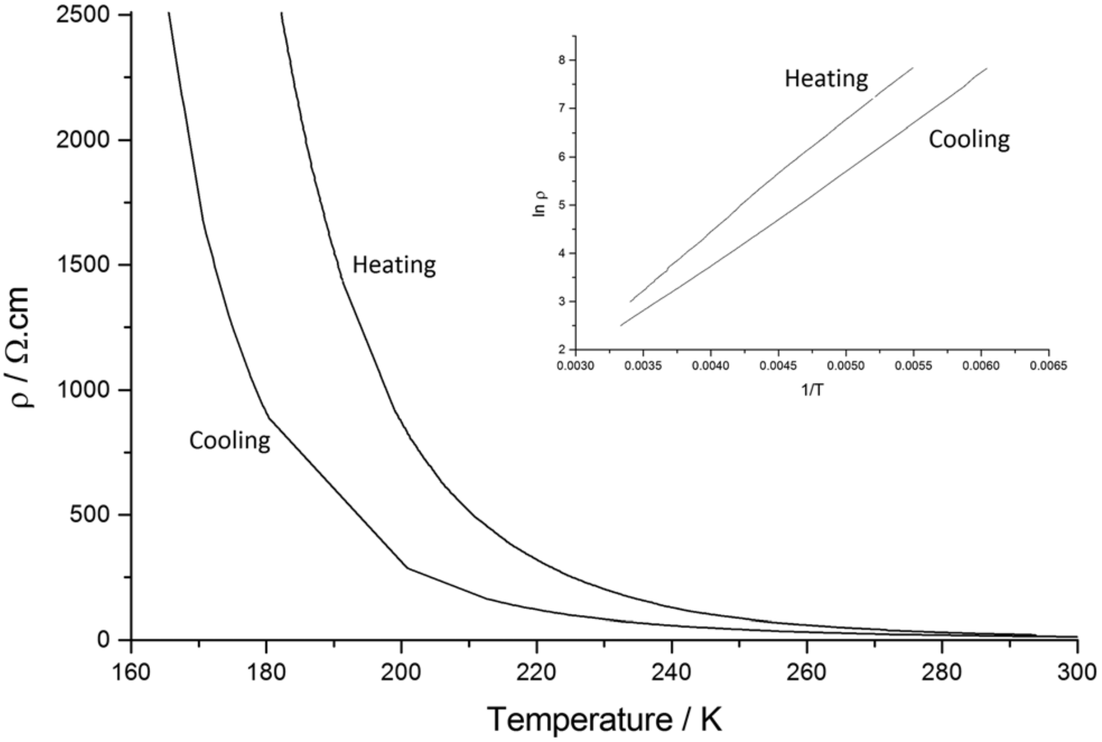

Graph 4.8. Temperature dependent resistivity for CTS 4.2. Inset: Logarithmic resistivity against 1/T for CTS 4.2.

	Cooling	Heating
ρ_{RT} / Ω.cm	15.015	
E_a / eV	0.164	0.202

Table 4.11. Room temperature resisitivty and activation energies for cooling and heating runs of CTS 4.2.

CTS 4.2 shows relatively low resistivity at room temperature (ρ_{RT} = 15.015 Ω.cm) and Arrhenius semiconducting behaviour is observed upon cooling from 300 K to 165 K where the resistivity reaches a maximum. Hysteretic behaviour is present on heating from 165 - 300 K resulting in an increase in activation energy is observed. (Table 4.11).

4.2 Bis(mandelato)borate

Mandelic acid is a chiral aromatic alpha hydroxy acid. It is capable of acting as a bidentate ligand through deprotonation at the two hydroxy groups. In keeping with the synthesis of chiral four-coordinate borate anions using two identical ligands with a stereogenic centre (Section 2.2), a possible six diastereoisomers are produced when using racemic mandelic acid and a possible two diastereoisomers when using chiral (*R*- or *S*+) mandelic acid.

The chiral $B(mandelate)_2^-$ anions have been studied quite extensively in terms of their chiral resolution and chiral co-crystallisation abilities. These properties can be attributed to the different shapes that are adopted, depending on whether the boron centre is in the *S* or *R* configuration. For instance, the B_S*RR* anion adopts a ‘V’ shape and the B_R*RR* anion adopts a planar ‘twist’ (Figure 4.22). The same holds true for the B_S*SS* (‘V’) and the B_R*SS* (‘twist’) anions. It is suggested that the ‘V’ shaped B_S anion has less packing modes available in terms of electrocrystallisation with radical cation salts when compared with the more planar ‘twisted’ B_R anion.

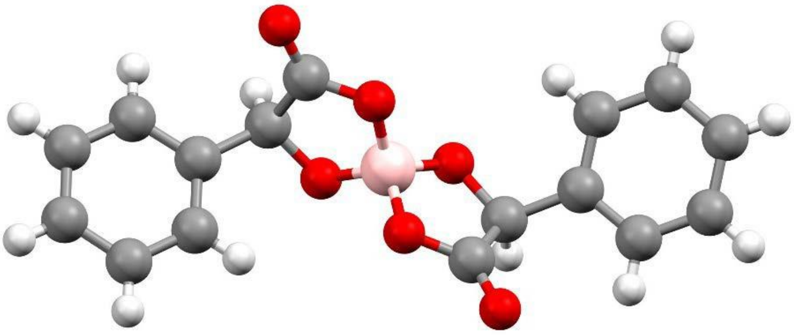

Figure 4.22. Representation of the planar ‘twisted’ $B(mandelate)_2$ anion of B_R*RR* stereochemistry.

4.2.1 β-(BEDT-TTF)$_2$B$_{R/S}$[(R/S)mandelate]$_2$

Electrocrystallisation of BEDT-TTF in the presence of the borate anion synthesised using racemic mandelic acid affords a charge transfer salt in which only two of the possible six diastereoisomers are included in the lattice; the B$_S$*RR* and B$_R$*SS* configurations. This is another example of diastereomeric induction within the electrocrystallisation environment. Structural, conducting and magnetic properties are discussed.

4.2.1.1 Electrocrystallisation Table

Donor	**Counterion**	**Electrolyte**	**Solvent**	**Current /μA**	**Crystal Growth**	**Observation**
ET	K$^+$	B*R/S*[(*R/S*)mandelato]$_2^-$	PhCl	0.2	YES	Large quantity of thin black plates collected from the electrode after 21 days.

Table 4.12. Electrocrystallisation table for the synthesis of CTS 4.3.

Chlorobenzene produced black/brown plates of CTS 4.3. Due to the extreme thinness of the crystals a sample was sent to the NCS (National Crystallographic Service) in Southampton for structural characterisation.

4.2.1.2 *Crystal Structure*

β-(BEDT-TTF)$_2$B$_{R/S}$[(*R*/*S*)mandelate]$_2$	
Formula	$C_{36}H_{28}O_6S_{16}B$
M_r/g mol^{-1}	1080.35
Temp / K	100
Radiation	Mo Kα
Wavelength	0.7105
Crystal System	Triclinic
Space group	P-*1*
a / Å	8.5373(11)
b / Å	11.7643(14)
c / Å	21.647(3)
α / °	93.708(7)
β / °	96.881(7)
γ / °	104.635(7)
V/Å^3	2078.2(5)
Z	2
ρ/g cm^{-1}	1.726
μ/cm^{-1}	0.0880
Absorption Applied	Yes
Abs. Type	Empirical
Abs. Range	0.562 – 1.000
Total Reflections	21083
Unique Reflections	7146
R$_1$ [all data]	0.1158
R$_1$ [$I > 2\sigma(I)$]	0.0750
wR [all data]	0.1572
Goodness of fit	0.841
Refinement Program	SHELX
Refinement Mode	F^2
Flack Parameter	n/a

Table 4.13. X-ray data for CTS 4.3.

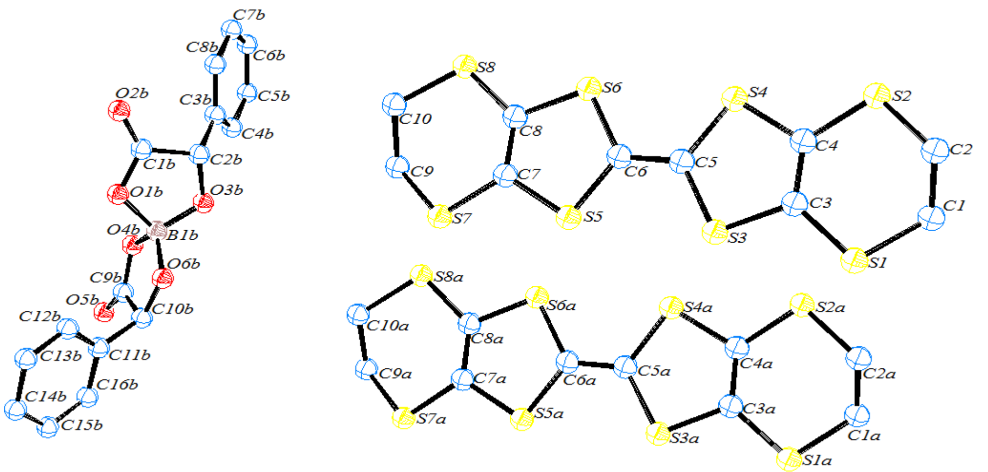

Figure 4.23. ORTEP diagram of the asymmetric unit of CTS 4.3. Displacement ellipsoids are drawn at the 50% probability level.

CTS 4.3 crystallises in the triclinic crystal system in the achiral space group P-1. The asymmetric unit contains two crystallographically independent BEDT-TTF molecules and one borate anion, Figure 4.23. The synthesis of the borate anion using racemic mandelic acid produces a possible six diastereoisomers, in a similar fashion to the B(malate)$_2^-$ synthesis discussed in Section 2.3.1. In CTS 4.3 however, only two diastereoisomers are present throughout the lattice, B_S*RR* and B_R*SS*. Each anion contains two mandelate ligands of the same chiral configuration. This is in contrast to the previously discussed racemic α-(BEDT-TTF)$_2$B$_{R/S}$[(*R/S*)malate]$_2$.(H$_2$O)$_{2.85}$salt where the two diastereoisomers present in the lattice are the racemic form of the anion and differ only in the configuration at the boron centre. The anions present in this salt differ by the configuration at the boron centre and by the chirality on the ligand, therefore each anion is chiral but the lattice overall is racemic. The four other anions; B_S*SS*, B_R*RR*, B_R*RS* and B_S*RS* are not present in the crystal lattice.

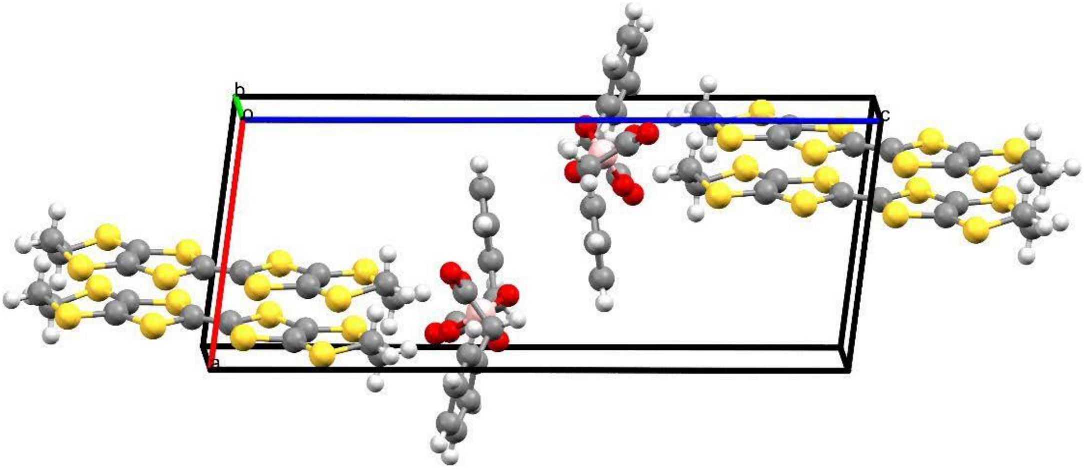

Figure 4.24. Unit cell of CTS 4.3 as viewed along the *b* axis.

The unit cell contains two asymmetric formula units and is shown in Figure 4.24. The donors from stacks in the *ab* plane with neighbouring stacks separated in the *c* direction by the anion layer. The B(mandelate)$_2^-$ anions stack in a double layer, with only one diastereomer present in each layer. Figure 4.25 below shows the layered structure viewed along the *a* axis. Short sulphur interactions below the sum of the vdW radii (3.6 Å) are shown in light blue lines. The anions are coloured according to the diastereoisomer, purple anions are the B_R*SS* configuration and the orange anions are the B$_S$*RR* configuration.

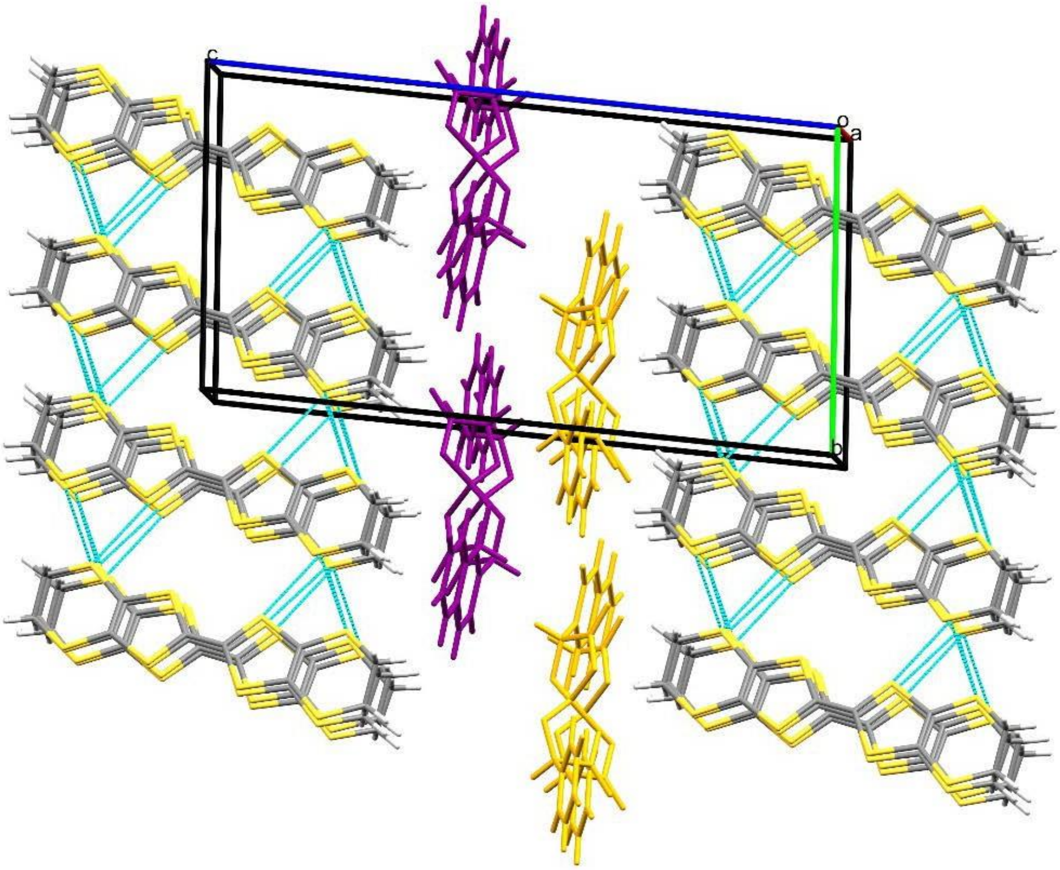

Figure 4.25. Layered structure of CTS 4.3. Viewed along the *a* axis. S...S contacts are shown in light blue lines.

The donors stack in the β phase with ordered rows propagating through the *ab* plane. Both 'in plane' and 'out of plane' side-to-side S...S contacts are observed. As seen in Figure 4.27 which shows the end on projection of the β-packing motif in the donor layers of CTS 4.3.

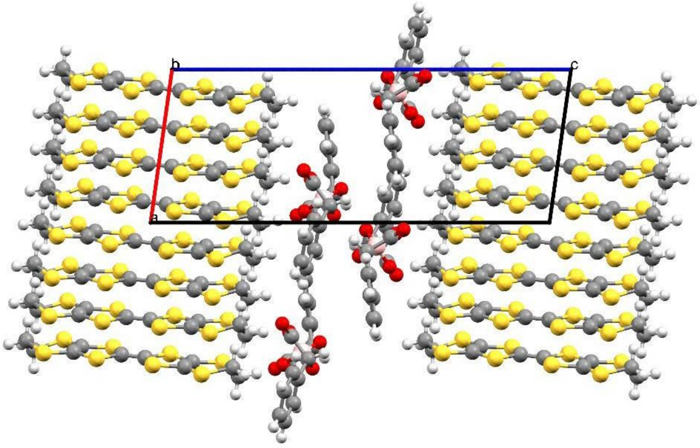

Figure 4.26. Packing arrangement of CTS 4.3. Viewed along the *b* axis.

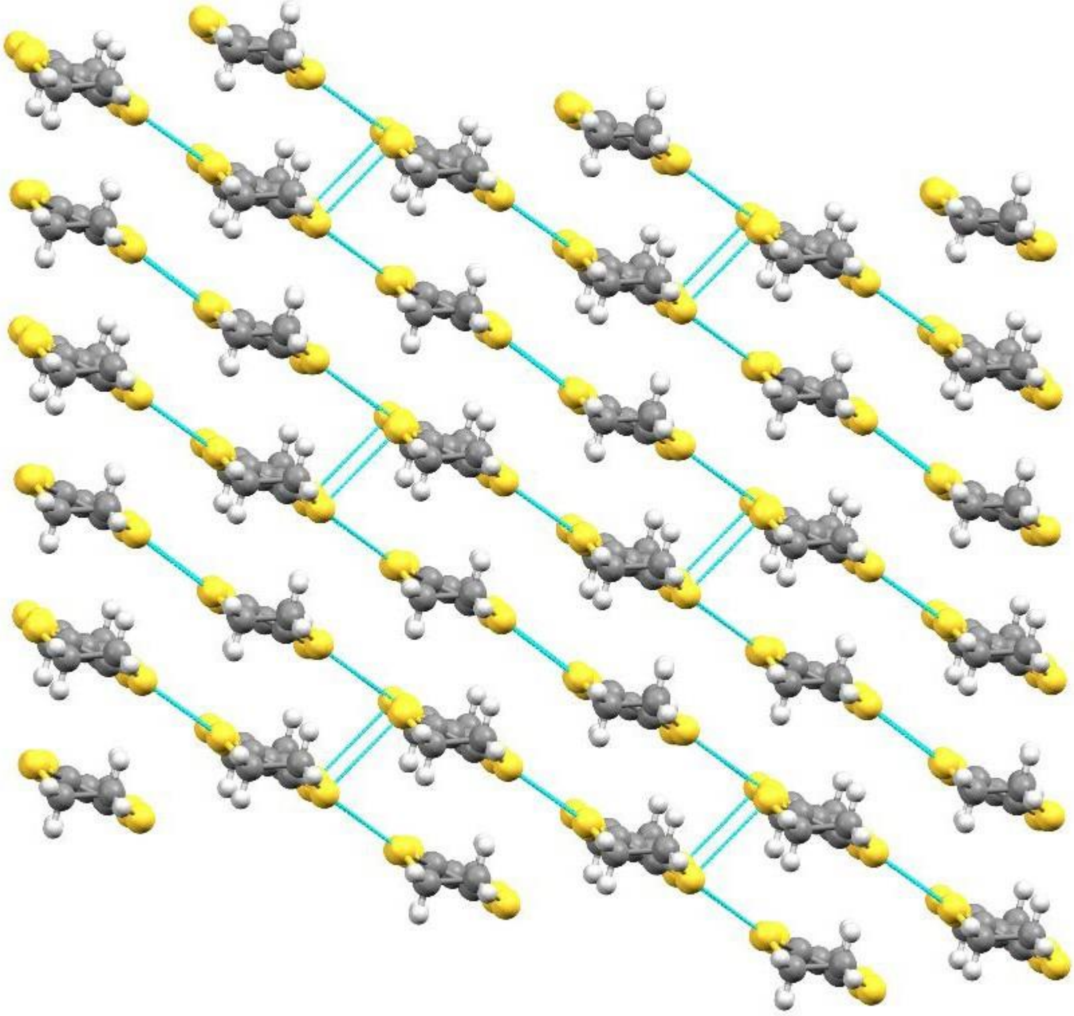

Figure 4.27. End on projection of donor stacking in CTS 4.3. Viewed along the *c* axis. S...S contacts are shown in light blue lines.

Figure 4.28 below shows donor A, pictured above in green. Short sulphur interactions below the sum of the vdW radii (3.6 Å) are shown in dotted red lines and contacts atoms are labelled in black. Contacts length and central TTF bond lengths in angstroms are shown in green. The donor makes a total of eight S...S contacts, two 'out of plane' side-to-side contacts and six 'in plane' side-to-side contacts. Both terminal ethylene groups are in the twisted eclipsed confirmation with all sp^3 carbons displaced equidistant from the TTF core. The side on profile view in Figure 4.29 shows that the donor is completely planar through the central TTF core. Charge estimation per Kepert *et al*.[2] procedure of averaging the TTF bond lengths calculate the donor to carry a charge of $^+$0.5.

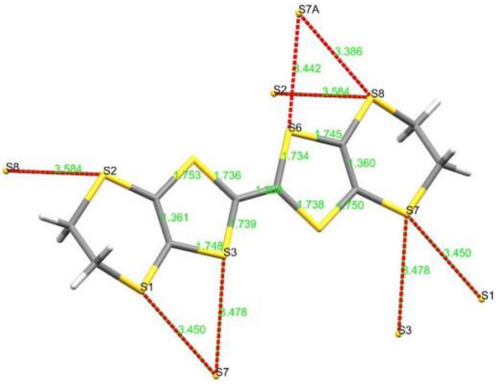

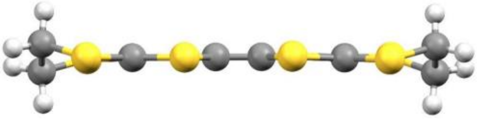

Figure 4.28 (left). CTS 4.3: Donor A with S...S contacts drawn in red and contact atoms labelled in black. Contact length and central TTF bond lengths are shown in green. Figure 4.29 (right). CTS 4.3: Side on profile view of donor A.

Figure 4.30 below shows donor B, pictured above in blue. Short sulphur interactions below the sum of the vdW radii (3.6Å) are shown in dotted red lines and contact atoms are labelled in black. Contacts length and central TTF bond lengths in angstroms are shown in green. The donors makes a total of six 'in plane' side-to-side contacts. The terminal ethylene groups are again in the twisted eclipsed confirmation and all the sp^3 carbons are displaced equidistant from the central axis of the molecule. Charge estimations calculate the donor to carry a charge of +0.5. Both these values are in good agreement with the overall formula β-(BEDT-

TTF)$_2$B$_{R/S}$[(*R/S*)man]$_2$, where B$_{R/S}$[(*R/S*)man] $^-$ is a monovalent anion and both BEDT-TTF molecules carry charges of $^+$0.5.

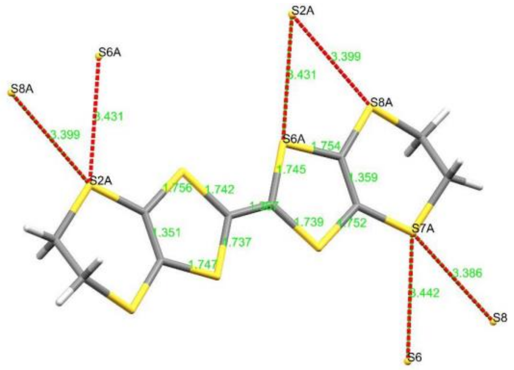

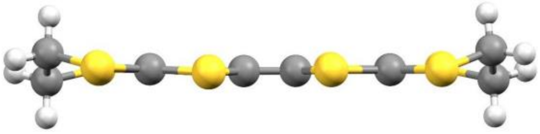

Figure 4.30 (left). CTS 4.3: Donor B with S...S contacts drawn in red and contact atoms labelled in black. Contact length and central TTF bond lengths are shown in green. Figure 4.31 (right). CTS 4.3: Side on profile view of donor B.

The double stack arrangement observed in the insulating layer is effectively the mirror image of itself, where only one diastereoisomer is present throughout a single row. A network of hydrogen bonding runs through each row but there are no intermolecular contacts between rows of anions. Each anion makes three hydrogen bonds with neighbouring B(mandelate)$_2$ $^-$ anions and there is hydrogen bonding between anions and donors. One carbonyl oxygen makes three hydrogen bonds, two with separate phenyl ring hydrogens of a neighbouring anion (O5B...H14B, 2.70(1) and O5B...H7B, 2.59(8) Å) and one with a donor ethylene hydrogen (O5B...H2A, 2.41(8) Å). One ring O atom makes a hydrogen bond with a phenyl ring hydrogen (O1B...H5B, 2.67(0) Å), the same ring O atom also makes a hydrogen bond with a donor ethylene hydrogen (O1B...H10C, 2.60(8) Å).

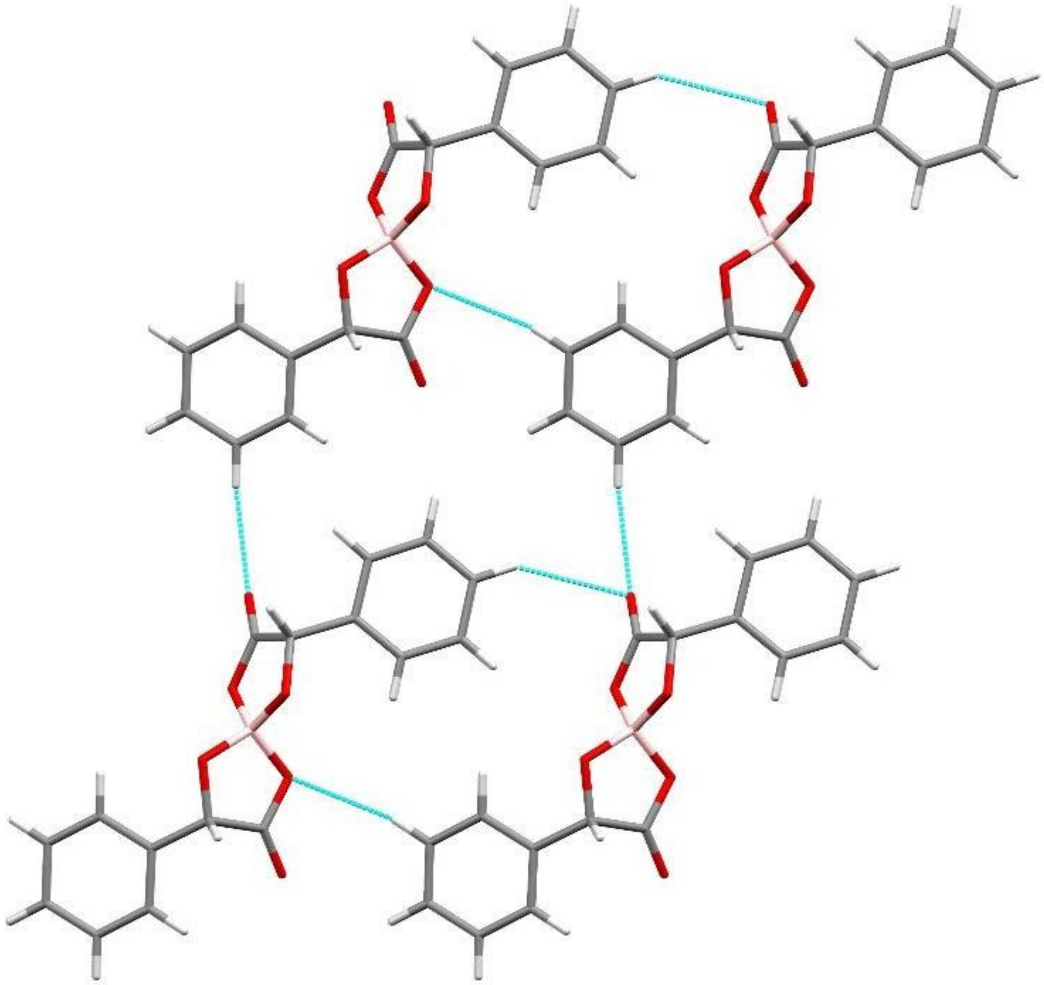

Figure 4.32. Hydrogen bonding interactions between B(mandelate)$_2^-$ anions in CTS 4.3.

4.2.1.3 S…S Contacts

Contact	***Atom***	***Atom***	***Length / Å***
1	S1	S7	3.450(2)
2	S3	S7	3.478(19)
3	S2	S8	3.584(17)
4	S6	S7A	3.442(18)
5	S8	S7A	3.386(18)
6	S2A	S6A	3.431(18)
7	S2A	S8A	3.399(19)

Table 4.14. Short sulphur interactions below the sum of the vdW radii (3.6 Å) in CTS 4.3.

Short sulphur interactions below the sum of the vdW radii (3.6 Å) are presented in Table 4.14 above. There are a total of seven S...S contacts. The shortest contact (S8...S7A, 3.386(18) Å) is between donor A and B.

4.2.1.4 C=C Bond Length, Charge Calculations and Raman

	A – Green	***B – Blue***
a / Å	1.368	1.367
b / Å	1.737	1.741
c / Å	1.749	1.752
d / Å	1.361	1.355
δ	0.757	0.771
Q	**0.697** (± 0.1)	**0.593** (± 0.1)

Table 4.15. Central C=C bond lengths for the BEDT-TTF molecules present in CTS 4.3.

The central C=C bond lengths of the two independent donors present in CTS 4.3 are very similar and suggestive that both BEDT-TTF molecules carry the same charge.

	A - Green	***B - Blue***
C=C Bond Length / Å	1.368(6)	1.367(6)

Table 4.16. BEDT-TTF charge estimations according to Kepert *et al.*[2] average TTF bond length calculations for CTS 4.3.

Charge estimation of the two independent BEDT-TTF molecules indicate that both donors carry equal charges of $^{+}$0.5, which is in good agreement with the values observed for central C=C bond lengths.

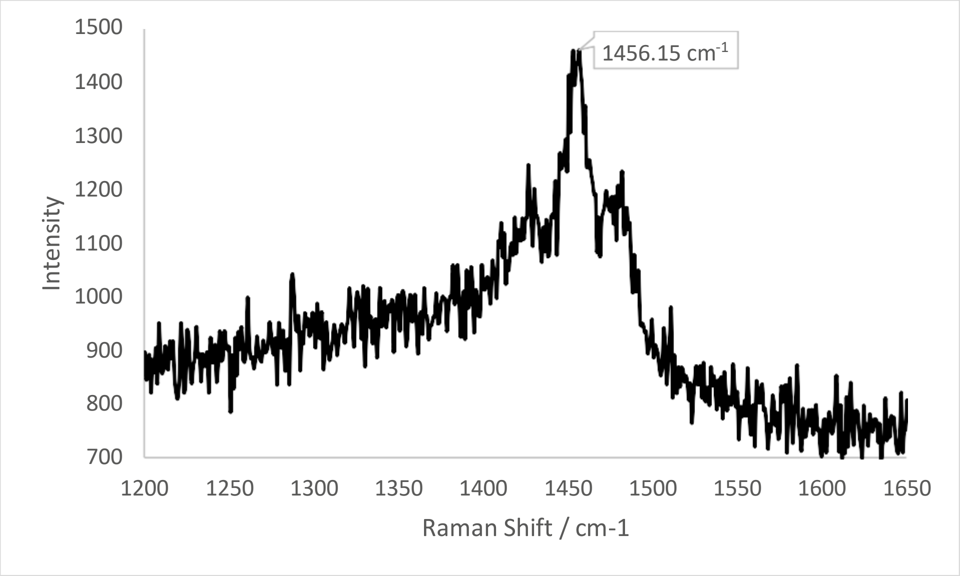

Graph 4.9. Relative intensity against Raman shift for one single crystal of CTS 4.3.

Room temperature Raman measurements were performed on one single crystal of CTS 4.3. The spectrum is noisy and there are peaks observed in the range 1420-1480 cm^{-1}. However, the data shows one high intensity peak at around 1450 cm^{-1} which suggests that all donors present in the salt carry the same charge. This is in good agreement with the charge estimation and C=C bond length values in Tables 4.15 and 4.16 above, indicating that both the BEDT-TTF molecules carry a charge of $^{+}$0.5

4.2.1.5 Magnetic Data

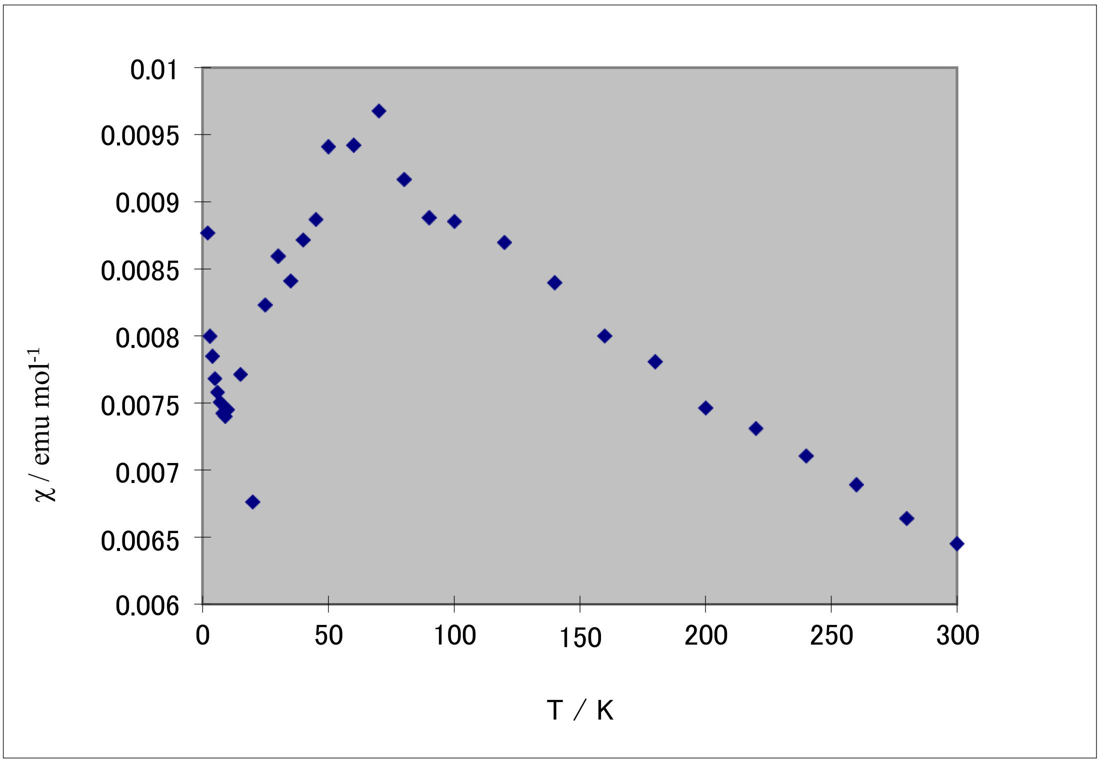

Graph 4.10. Temperature dependent magnetic susceptibility for CTS 4.3.

The magnetic data of CTS 4.3 shows an increase in magnetic susceptibility with decreasing temperature up to a maximum at 70 K, before decreasing rapidly until 20 K. The data has been fitted to the Curie-Weiss model by Prof. H. Akutsu of Osaka University.

4.2.1.6 Resistivity Data

Reproducible temperature dependent resistivity measurements were made on two single crystals of CTS 4.3. The material exhibits Arrhenius semi-conducting behaviour from 300 K down to 200 K (Graph 4.11) with a calculated activation energy of 0.044 eV. Below this temperature however the material does not show true exponential increase of resistivity with decreasing temperature, instead the resistivity begins to plateau from 200 K to 4 K. The logarithmic resistivity profile from 200 – 4 K is shown in Figure 4.12, the sharp increase at the start of the curve corresponds to the temperatures 200 – 70 K, the point at which the curve begins to flatten corresponds to temperatures 70 – 20 K and the plateau observed on the curve corresponds to temperatures 20 – 4 K. The regions described in the resistivity profile correlate with the magnetic susceptibility data and suggests a change in electronic structure as the material is cooled below 200 K. It is possible that the sharp drop in magnetic susceptibility from 70 – 20 K; the point at which the resistivity curve begins to flatten, is attributed to charge ordering within the salt. Below 20 K the magnetic data then seems to follow the Curie-Weiss law indicating a paramagnetic charge disproportionation within the conducting BEDT-TTF layer which can be described as the change from a (BEDT-TTF) $^{+0.5}$ ground state to a BEDT-TTF^{0}:BEDT-TTF^{+1} charge ordered state.

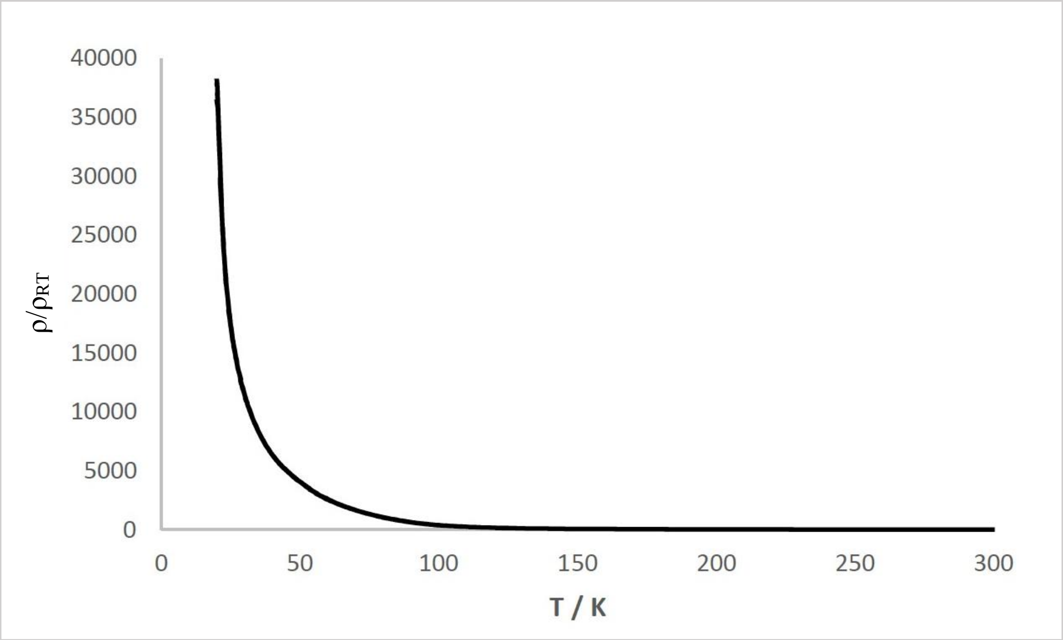

Graph 4.11. Temperature dependent resistivity for CTS 4.3

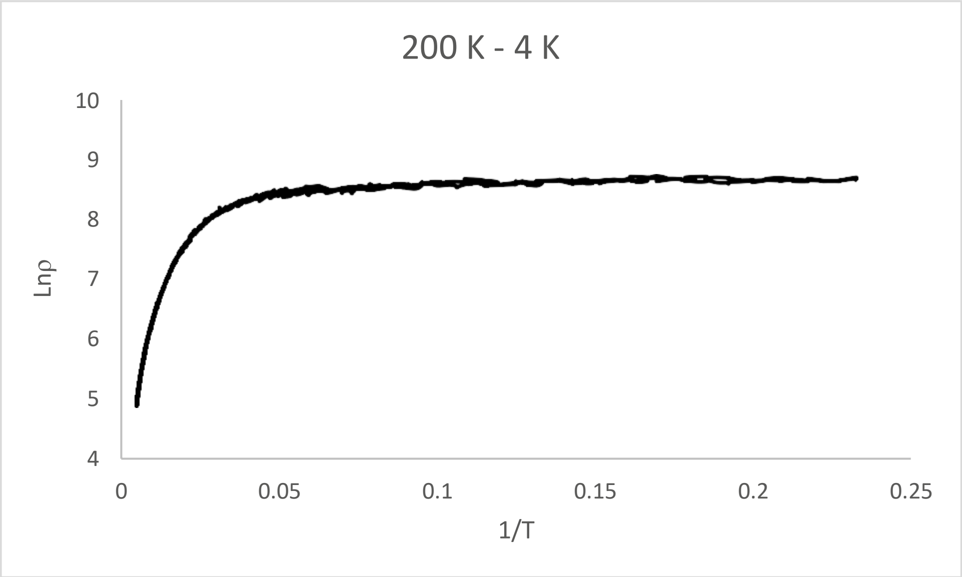

Graph 4.12. Full logarithmic resistivity profile for CTS 4.3

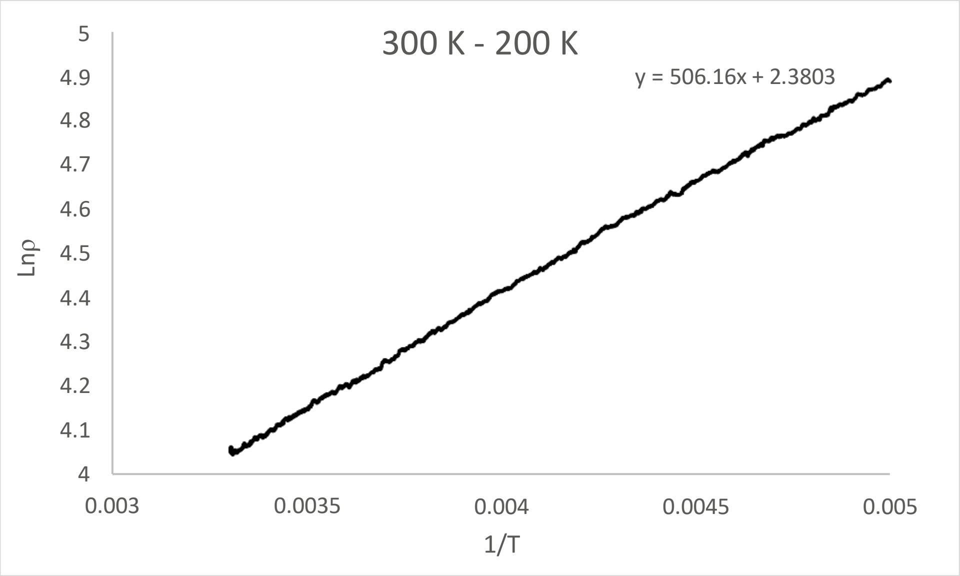

Graph 4.13. Logarithmic resistivity profile from 300 – 200 K for CTS 4.3, exhibiting Arrhenius temperature dependency.

4.2.2 Bis(S-mandelato)borate and BEDT-TTF

Electrocrystallisation of BEDT-TTF in the presence of the borate anion synthesised using *S*+ mandelic acid afforded a material adopting a polycrystalline helical morphology. The bent nature of the crystals has meant that X-ray diffraction measurements are impossible. However, Raman and magnetic measurements were performed, as were conducting measurements along the long axis of the helices.

4.2.1.1 Electrocrystallisation Table

Donor	**Counterion**	**Electrolyte**	**Solvent**	**Current /µA**	**Crystal Growth**	**Observation**
ET	K$^+$	B*R/S*[(*S*)mandelato]$_2^-$	PhCl	0.1	YES	Large quantity of tiny black amorphous crystals collected from electrode and H- cell. Too small for X-ray or physical characterisation.
ET	K$^+$	B*R/S*[(*S*)mandelato]$_2^-$	PhCl : EtOH 10 : 1	0.2	YES	Large quantity of macromolecular crystalline helices collected from electrode along with black rhombi.
ET	K$^+$	B*R/S*[(*S*)mandelato]$_2^-$	1,1,2-TCE	0.1	YES	Small quantity of black crystalline shards collected fom H-cell. Too small for X-ray mesaurements.

Table 4.17. Electrocrystallisation table for the synthesis of CTS 4.4.

Chlorobenzene and ethanol in a 10 : 1 ratio produced a large number of macromolecular crystalline helices. These were taken forward for further physical and structural characterisation. Attempts to grow crystals using other solvent combinations e.g. MeCN, DCM, PhBr proved unsuccessful.

4.2.2.2 Macromolecular Structure and Helical Morphology of Crystals

High resolution TEM images of the helices were taken to deduce the nature of the crystals. From the images below (Figures 4.33 and 4.44) it seems that the helices are made up of a large number of smaller bent single crystals. During electrocrystallisation, nucleation must have taken place around a chiral axis to produce polycrystalline macromolecular helices that are exclusively anti-clockwise (*L* or *S*) twists. This could be due to the presence of an excess of the chiral $B[(S+)man)_2]^-$ anion within the crystallisation environment.

Within the batch of helical crystals were a number of large single crystals that were identified as the $(BEDT\text{-}TTF)_3(HSO_4)_2$ phase. The crystals most likely formed due to trace amounts of sulphuric acid left over after acid washing of the electrodes. Further electrocrystallisation attempts with BEDT-TTF, chiral $B[(S+)man)_2]^-$ and a variety of different concentrations of sulphuric acid did not produce helical crystals or single crystals of BEDT-TTF:$B[(S+)man)_2]$, only the $(BEDT\text{-}TTF)_2(HSO_4)$ phase was observed. It can be concluded that the presence of trace amounts of sulphuric acid did not contribute to the formation of the chiral helices.

The synthesis of the $B[(S+)man)_2]$ anion produces two possible configurations, B_SSS and B_RSS. Due to both the chiral centre on the ligand and the chiral labile boron centre, the two diastereoisomers can be considered as different compounds as both adopt remarkably different shapes. The B_SSS anion adopts a 'V' shape and the B_RSS adopts a more planar 'twisted' shape (Figure 4.22). Wong *et al*. have stated that 'the twisted anion is favoured by just *ca*. 0.5 kcal mol^{-1} in MeOH over the 'V-shaped' anion, although it is exclusively preferred in the solid state for all salts studied to-date'. Therefore, a possible suggestion for this phenomenon is that preferential crystallisation of the twisted B_RSS anion with the radical cation BEDT-TTF occurred, while the 'V' shaped B_SSS anion remained in solution and directed the formation of the polycrystalline chiral helices.

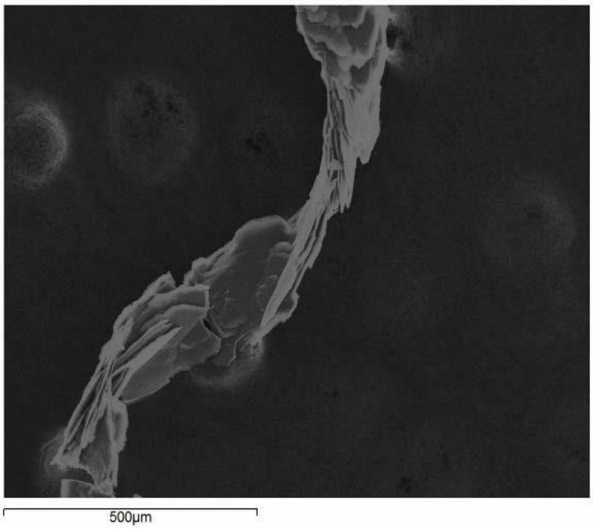

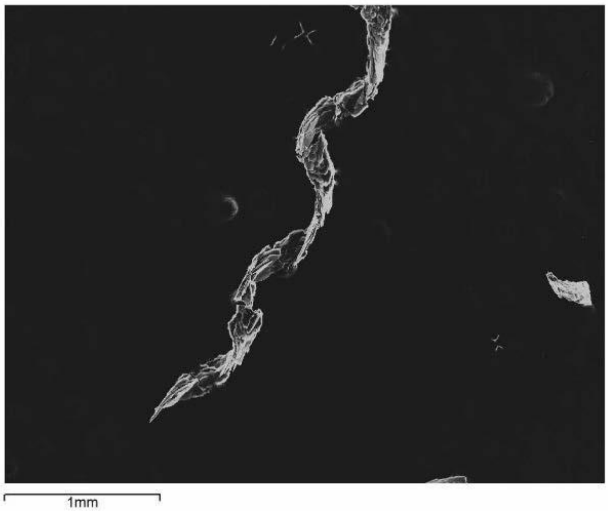

Figure 4.33. (Bottom) High resolution (1 mm) TEM images of the chiral anti-clockwise helices of CTS 4.4.

Figure 4.34. (Top) High resolution (500 µm) TEM image of a section of one helix of CTS 4.4.

4.2.2.3 Raman Data

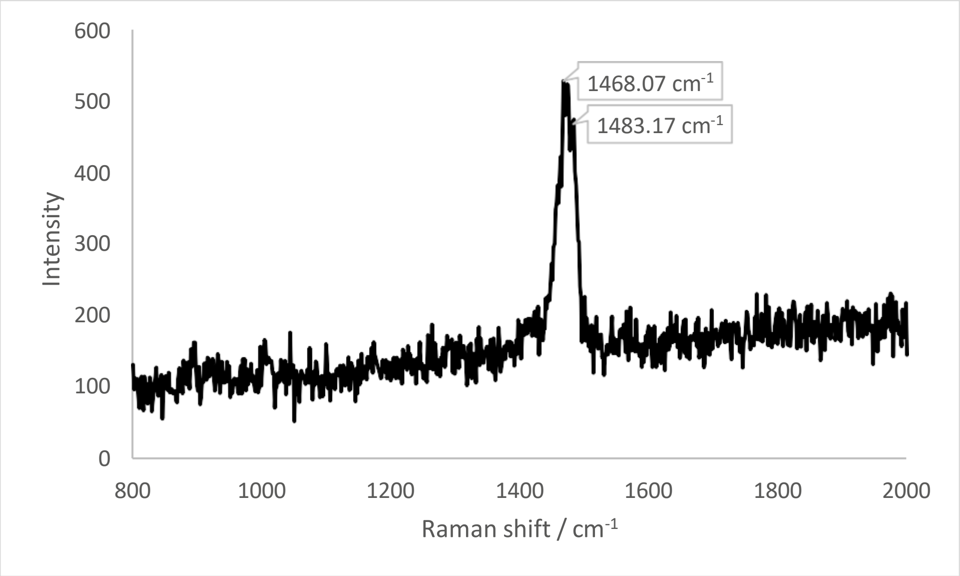

Graph 4.14. Relative intensity against Raman shift for one single crystal of CTS 4.4.

Reproducible room temperature Raman measurements were performed on several crystals of CTS 4.4. The spectrum above shows high intensity peaks at 1468 and 1483 cm^{-1} corresponding to the υ_4 and υ_3 stretching modes respectively. The relevant peaks are labelled in graph 4.14 above. The values fall within the range expected for a 2:1 BEDT-TTF radical cation salt. Therefore, it can be tentatively suggested that there are two BEDT-TTF$^{+0.5}$ molecules present in CTS 4.4, however in the absence of a crystal structure it is impossible to be certain.

4.2.2.4 *Magnetic Data*

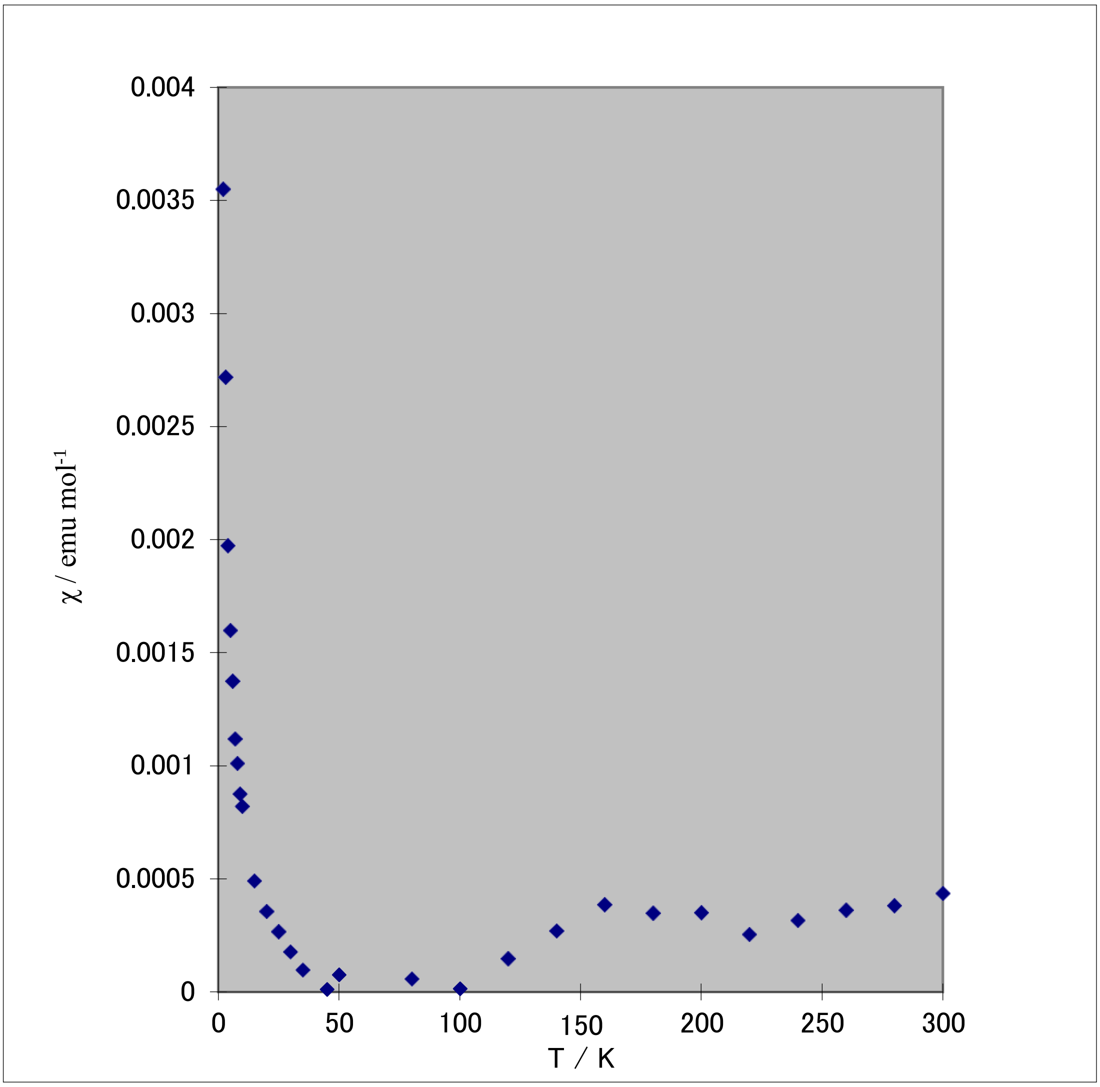

Graph 4.15. Temperature dependent magnetic susceptibility for CTS 4.4.

The magnetic susceptibility data indicates that a value of 3 x 10^{-4} is observed for the temperature independent susceptibility from 300 – 150 K at which point the susceptibility decreases with decreasing temperature and becomes zero at 100 K, suggesting a metal-insulator transition at 150 K. From 10-2 K the data can be fitted to the Curie-Weiss law with a curie constant of 0.011 emu K mol^{-1} and a Weiss constant of -0.87 K.

4.2.2.5 Resistivity Data

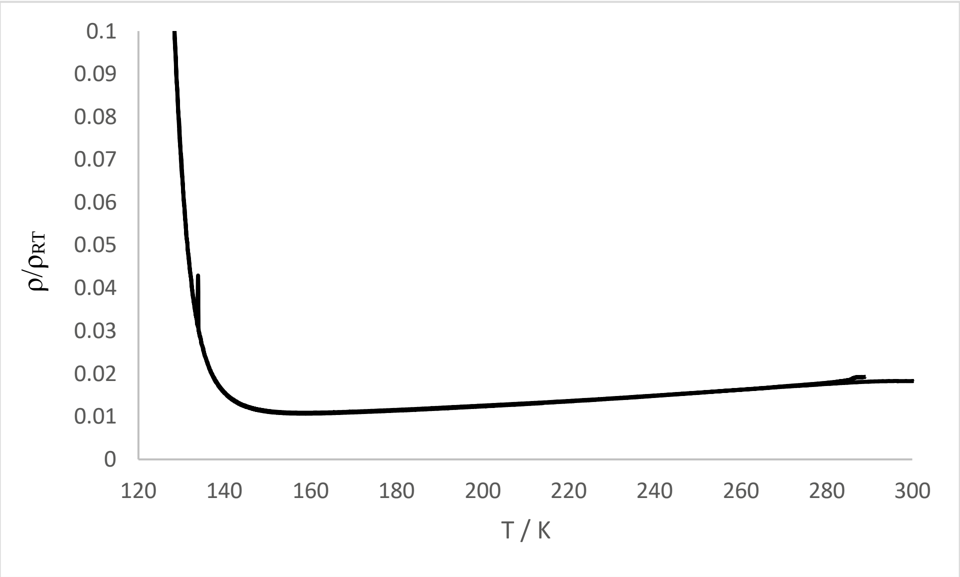

Graph 4.16. Temperature dependent resistivity for CTS 4.4.

Reproducible four-probe temperature dependent resistivity measurements were made on several crystals of CTS 4.4 along the long axis of the helix. The material exhibits metallic behaviour (ρ_{RT} = 0.0183 Ω.cm) from 300 - 150 K (ρ_{min} = 0.0109 Ω.cm) at which point a sharp up turn is observed indicating a metal-insulator transition. This is in good agreement with the magnetic susceptibility data.

4.3 Bis(glycolate)*borate*

Glycolic acid (hydroxyacetic acid) is able to act as a bidentate ligand through deprotonation at both hydroxyl groups to produce a four-coordinate chiral borate anion. The ligand itself is achiral however the molecular disymmetry at the boron centre produces enantiomers in which either the B_S or B_R configuration is observed. The relative lability of the boron centre in solution means that the anion is synthesised as a racemic mixture. This is in contrast to the previously discussed charge transfer salts containing borate anions, where the presence of a stereogenic centre on the ligand alongside the labile boron centre produced a number of diastereoisomers depending on whether the racemic or chiral ligand is used. The assignment of the configuration of the B(glycolate)$_2^-$ anion is therefore made simpler by the knowledge that there are only a possible two enantiomers, B_S(glycolate) $^-$ or B_R(glycolate) $^-$, both of which are present in the radical cation salt discussed in this section.

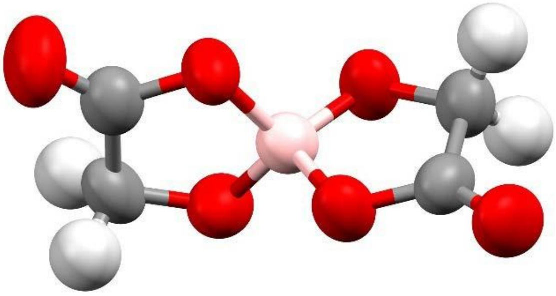

Figure 4.35. Representation of the chiral $B_{R/S}$(glycolate)$_2^-$ anion, thermal ellipsoids are drawn at the 50% probability level.

4.3.1 δ/δ'-(BEDT-TTF)$_2$[$B_{R/S}$(glycolate)$_2$]

Electrocrystallisation of BEDT-TTF in the presence of racemic $B_{R/S}$(glycolate)$_2^-$ produced large needle crystals suitable for structural, physical and magnetic measurements. Also contained in the same batch were crystals consisting of BEDT-TTF the B(glycolate)(OH)$_2$ anion and water, however structural determination could only produce a structure of R = 20%.

4.3.1.1 Electrocrystallisation Table

Donor	**Counterion**	**Electrolyte**	**Solvent**	**Current /μA**	**Crystal Growth**	**Observation**
ET	K^+	[B*R/S*(glycolate)$_2$]$^-$	$CHCl_3$	0.2	YES	Large quantity of black blocks and needles collected from the electrode after 1 month.

Table 4.18. Electrocrystallisation table for the synthesis of CTS 4.5.

After the first harvest of single crystals, the electrocrystallisation solution was filtered and added to a clean and dried H-cell along with 1 mg of BEDT-TTF. The third and second runs resulted in crystals of much higher quality than the first.

4.3.1.2 Crystal Structure

δ/δ'-(BEDT-TTF)$_2$[B$_{R/S}$(glycolate)$_2$]	
Formula	$C_{24}H_{20}O_6S_{16}B$
M_r/g mol^{-1}	928.19
Temp / K	297.3
Radiation	Mo Kα
Wavelength	0.7105
Crystal System	Monoclinic
Space group	P2/*c*
a / Å	33.7507(11)
b / Å	6.6736(3)
c / Å	15.7826(5)
α / °	90
β / °	98.485(7)
γ / °	90
V/Å^3	3515.9(2)
Z	4
ρ/g cm^{-1}	1.753
μ/cm^{-1}	10.237
Absorption Applied	Yes
Abs. Type	Multi-scan
Abs. Range	0.687-1.000
Total Reflections	32680
Unique Reflections	8062
R [all data]	0.0956
R_1 [$I > 2\sigma(I)$]	0.0700
wR [all data]	0.2324
Goodness of fit	1.063
Refinement Program	SHELX
Refinement Mode	Single
Flack Parameter	n/a

Table 4.19. X-ray data for CTS 4.5.

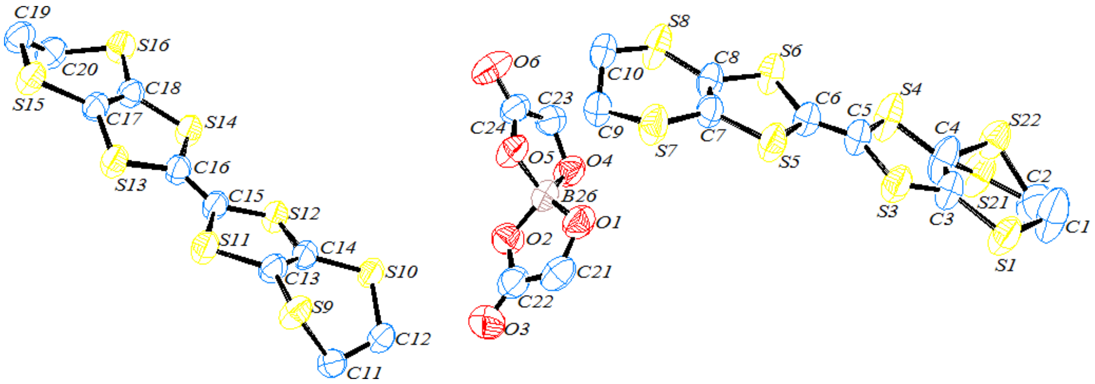

Figure 4.36. ORTEP diagram of the asymmetric unit of CTS 4.5. Displacement ellipsoids are drawn at the 50% probability level.

CTS 4.5 crystallises in the monoclinic crystal system in the centrosymmetric space group P2/*c*. The asymmetric unit contains two crystallographically independent BEDT-TTF molecules (A and B) and one borate anion. The unit cell contains four formula units and is shown below in Figure 4.37, viewed along the *b* direction. The bidentate glycolate ligand does not contain a chiral centre and therefore the racemic anion differs only in the configuration at the boron centre, either B_R(glycolate)$^-$ or B_S(glycolate)$^-$. The donors form stacks in the *bc* plane with neighbouring stacks separated in the *a* direction by the insulating layer. The anion layer is racemic throughout the stacks with rows of each enantiomer alternating along the *c* direction. The ORTEP diagram with displacement ellipsoids for the asymmetric unit is shown above in Figure 4.36. There is disorder on one sulphur of donor A, modelled as two partially occupied sites with a 0.51 and 0.49 occupancy respectively.

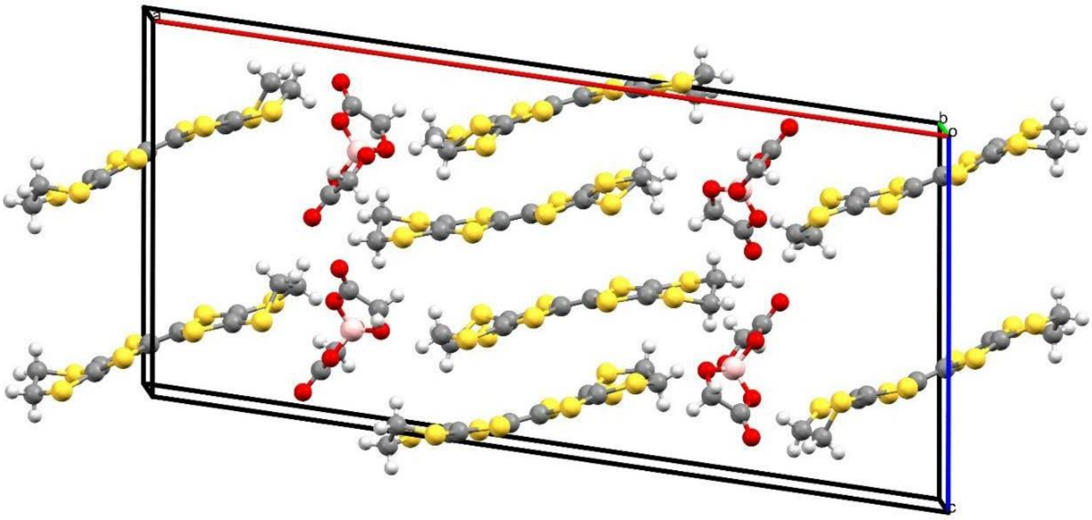

Figure 4.37. Unit cell of CTS 4.5. Viewed along the *b* axis.

The lattice packing viewed along the *c* axis is shown below in Figure 4.38. The donors adopt two crystallographically independent packing motifs throughout, with each arrangement consisting exclusively of only one of the independent donors. The two outer stacks (Figure 4.38), made up of only donor B are the conventional delta packing motif, with the donors stacked at about 90° on top of another about the central C=C bond. The central stack, containing only donor A can be termed the delta' motif, where the donors are stacked at two different angles on top of one another about the central C=C bond. The strange packing motif is caused by an anisotropy of the anionic layer.

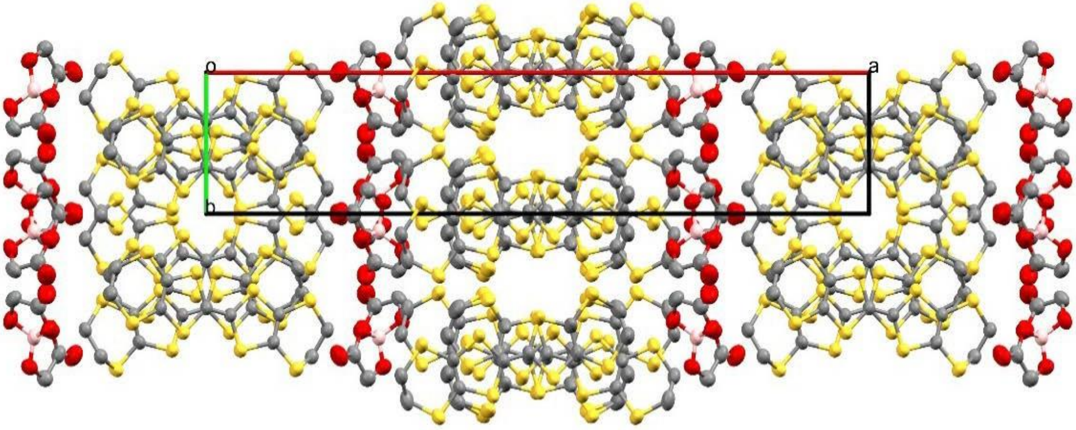

Figure 4.38. Expanded unit cell of CTS 4.5. Viewed along the *c* axis.

The lattice viewed along the *b* axis is shown below in Figure 4.39. Short sulphur interactions below the sum of the vdW radii (3.6 Å) are shown in light blue lines. The conventional delta packing results in both side-to-side and face-to-face contacts, with dimerization present throughout the stacks, creating a 2D conduction pathway. The delta' stacking results in only side-to-side S...S contacts being observed and a 1D conduction pathway.

The two donor stacks are shown separately overleaf (Figure 4.40[donor A, left] and [donor B, right]) with S...S contacts shown in light blue lines. Both figures are drawn viewing along the long axis of one row of BEDT-TTF molecules. The two arrangements differ only in the slip distances between double rows of donors. In the donor A stack there is no slip distance, producing donors that aren't dimerised and a lower number of S...S contacts. In the donor B stack there are shorter intermolecular contacts and dimerization throughout.

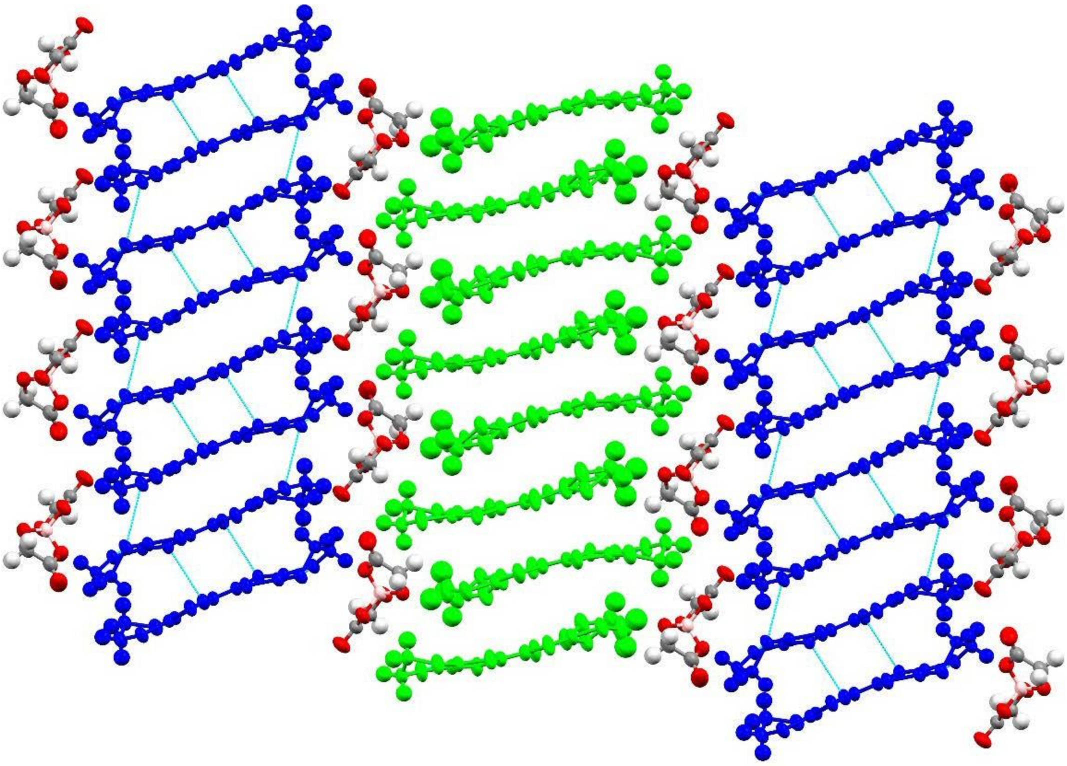

Figure 4.39. Lattice packing of CTS 4.5, viewed along the *b* axis. Face-to-face S...S contacts are shown in light blue lines. Crystallographically independent Donor A (green) and donor B (blue) stacks are shown.

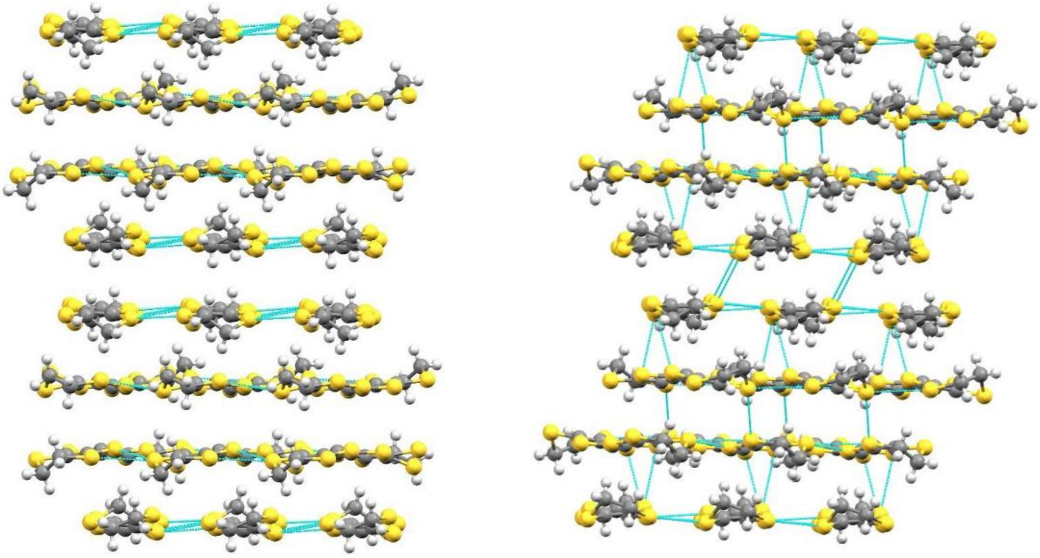

Figure 4.40 (left): Crystallographically independent donor A stack in CTS 4.5 and (right): crystallographically independent donor B stack in CTS 4.5. S...S contacts are shown in light blue lines.

Figure 4.41 shows donor A, pictured above in green. Short sulphur interactions below the sum of the vdW radii (3.6 Å) are shown in dotted red lines and contact atoms are labelled in black. Contact length and central TTF bond lengths in angstroms are shown in green. The donor makes a total of eight ‘in plane’ side-to-side S...S contacts. One end is in the half chair confirmation. It is difficult to ascertain which confirmation the opposite end is due to the disorder on S22, however it is apparent that each site produces either a half-chair or a boated confirmation. Charge estimation calculations are in agreement with a donor charge of $^{+}0.5$. The side on profile view in Figure 4.42 shows the donor to be relatively planar through the central TTF portion.

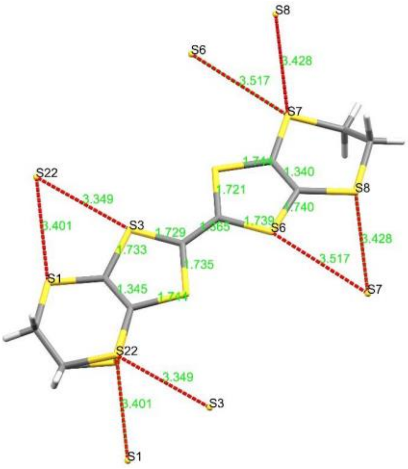

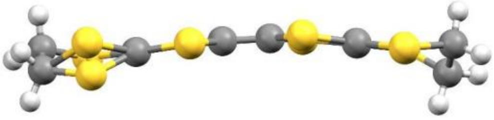

Figure 4.41 (left). CTS 4.5: Donor A with S...S contacts drawn in red and contact atoms labelled in black. Contact length and central TTF bond lengths are shown in green. Figure 4.42 (right). CTS 4.5: Side on profile view of donor A.

Figure 4.43 shows donor B, pictured above in blue. Short sulphur interactions are shown in dotted red lines and contact atoms are labelled in black. Contact length and central TTF bond lengths in angstroms are shown in green. The donor makes a total of ten S...S contacts. Four face-to-face contacts, two ‘out of plane’ side-to-side contacts and four ‘in plane’ side-to-side contacts. Contact length S12...S14 (3.53(9) Å) was omitted from the figure for clarity. One terminal ethylene group is in the half-chair confirmation and the other end is in the boat confirmation. The central TTF unit of the molecule is planar towards the end adopting the half-chair confirmation and the other is heavily bent towards the end adopting the boat confirmation, as can be seen from the side on profile view in Figure 4.44.

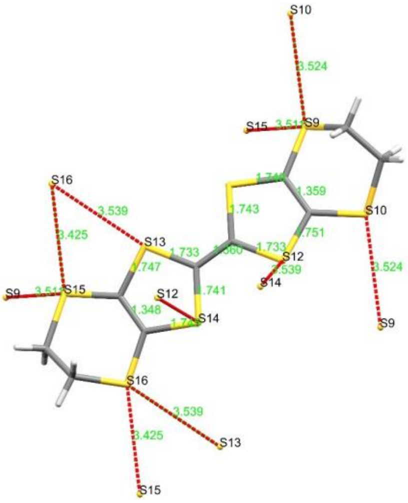

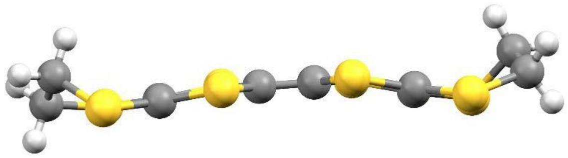

Figure 4.43 (left). CTS 4.5: Donor A with S...S contacts drawn in red and contact atoms labelled in black. Contact length and central TTF bond lengths are shown in green. Figure 4.44 (right). CTS 4.5: Side on profile view of donor A.

The anion layer is racemic and made up of alternating enantiopure rows of borate anions, labelled in black according to the stereochemistry at the boron centre. Interestingly, there is only one short contact below the sum of the vdW radii throughout the stacks. One methylene hydrogen makes a hydrogen bond with a ring O atom (O4...H21A, 2.751 Å). The insulating layer is stabilised mainly by short contacts between donor and anion. The contacts between BEDT-TTF methylene hydrogens and oxygens are shown below in Figure 4.46.

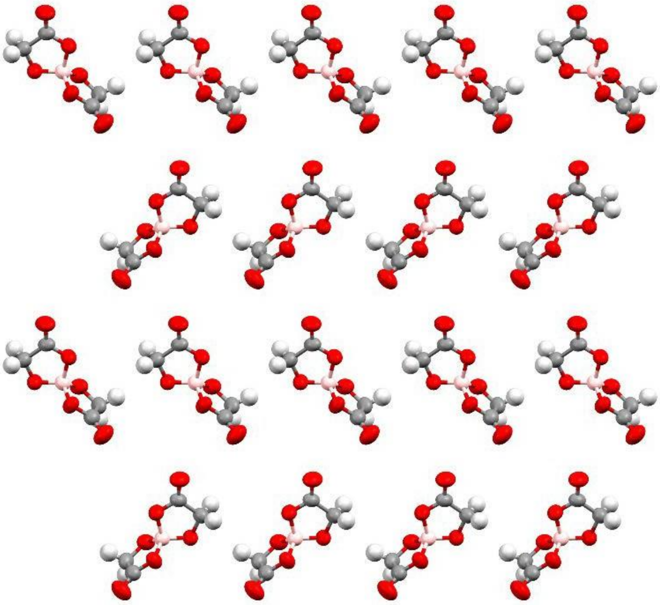

Figure 4.45 (above). Anionic $B_{R/S}(glycolate)_2^-$ layer in CTS 4.5. Viewed along the *c* axis.

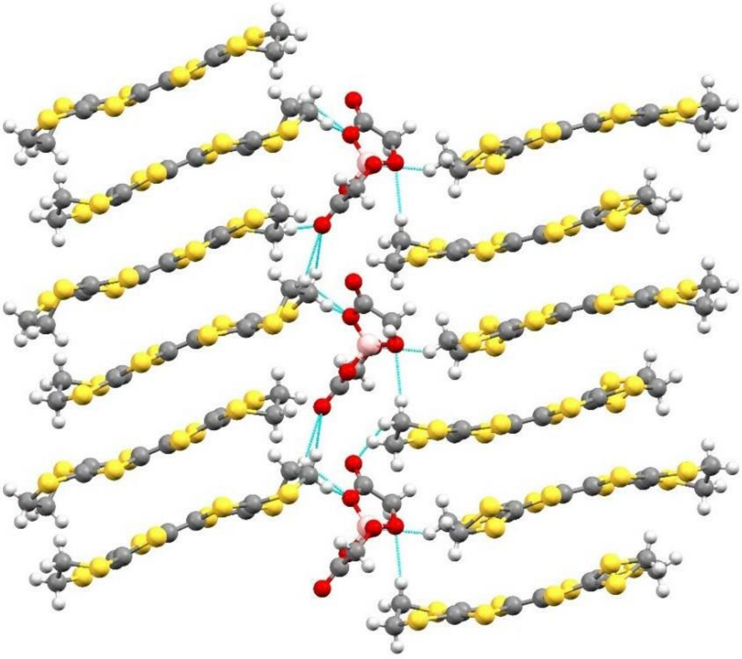

Figure 4.46. Hydrogen bonding interactions between $B_{R/S}(glycolate)_2^-$ anions and BEDT-TTF donor in CTS 4.5.

4.3.1.3 S…S Contacts

Contact	*Atom*	*Atom*	*Length / Å*
Donor A…Donor A			
1	S6	S7	3.517(11)
2	S8	S7	3.428(14)
3	S22	S1	3.401(14)
4	S22	S3	3.349(11)
Donor B...Donor B			
5	S10	S9	3.524(15)
6	S16	S13	3.539(13)
7	S16	S15	3.425(15)
8	S12	S14	3.539(18)
9	S9	S15	3.511(14)

Table 4.20. Short sulphur interactions below the sum of the vdW radii (3.6 Å) for CTS 4.5.

Short sulphur interactions for the two crystallographically independent donor layers are presented in Table 4.20 above. The two face-to-face contacts (S12...S14, 3.539(18) and S9...S15, 3.511(14) Å) are within the dimerised donor B stack.

4.3.1.4 C=C Bond Length, Charge Calculations and Raman

	A - Green	***B - Blue***
C=C Bond Length / Å	1.365(7)	1.360(8)

Table 4.21. BEDT-TTF central C=C bond lengths for independent donors present in CTS 4.5.

Central C=C bond lengths for the two independent donors are present above in Table 4.21. The two values suggest that the donors both carry similar charges.

	A – Green	***B – Blue***
a / Å	1.365	1.360
b / Å	1.731	1.738
c / Å	1.740	1.746
d / Å	1.343	1.354
δ	0.763	0.770
Q	**0.653** (± 0.1)	**0.601** (± 0.1)

Table 4.22. BEDT-TTF charge estimations via Kepert *et al.*[2] average TTF bond length calculations for CTS 4.5.

Charge estimations indicate that the two BEDT-TTF molecules both carry charges of $^{+}0.5$ which is in good agreement with the two central C=C bond lengths. However, as stated in the crystal structure discussion there are two crystallographically independent donor layers due to an anisotropy of the anionic layer, therefore it is possible that self-doping from the anionic layer might cause the donor B layer to carry a slightly lower charge than the donor A layer.

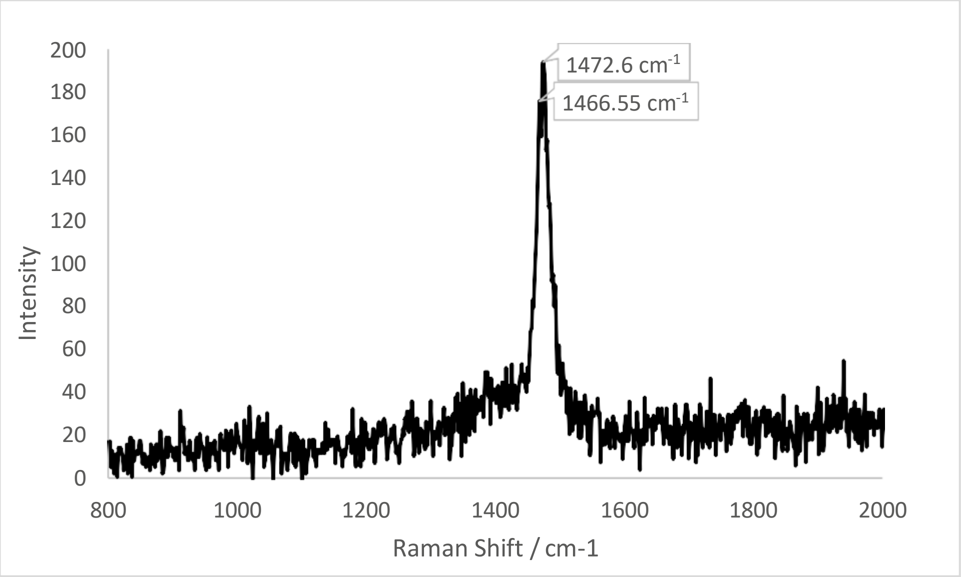

Graph 4.17. Relative intensity against Raman shift for a single crystal of CTS 4.5.

Reproducible room temperature Raman measurements were performed on several crystals of CTS 4.5. The two high intensity peaks are labelled in Graph 4.17 and indicate the presence of one type of donor cation. 1466 cm^{-1} is in the range expected for the υ_4 stretching frequency of a BEDT-$TTF^{+0.5}$ molecule. 1472 cm^{-1} is slightly lower than expected for the υ_3 stretching frequency of a BEDT-$TTF^{+0.5}$ molecule however, due to the possibility of charge doping between the anionic layer and the donor B layer it is likely that this value would be skewed slightly. Given the charge estimations and central C=C bond lengths presented above, the Raman data is in good agreement with the proposal that the unit cell of CTS 4.5 contains two BEDT-$TTF^{+0.5}$ molecules.

4.3.1.5 Magnetic Data

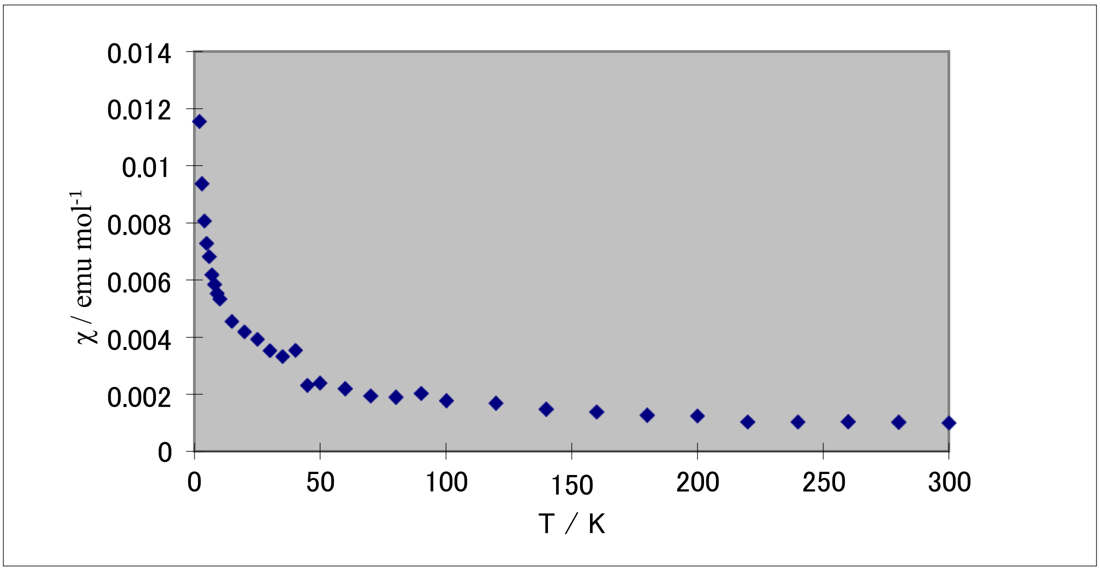

Graph 4.18. Temperature dependent magnetic susceptibility for CTS 4.5.

Magnetic susceptibility measurements were performed for CTS 4.5. The data does not show conventional behaviour expected for organic conductors and the small sample size (0.4mg) means that experimental error may be very high. However, one observes a sharp increase in susceptibility at 45 K, below which Prof. H. Akutsu of Osaka University has stated that the material then seems to follow the Curie-Weiss law down to 2K.

4.3.1.6 Resistivity Data

Reproducible four-probe resistivity measurements were made on several needle shaped crystals of CTS 4.5. The material is a semiconductor and exhibits a phase transition between 100 – 50 K. The resistivity profile from 300 – 20 K is shown in Graph 4.19 and the logarithmic resistivity against 1/T is shown in Graph 4.20. The phase transition is clear from the logarithmic curve. Between the temperatures 100 – 50 K the material is still a semiconductor but does not obey standard Arrhenius behaviour, showing a slight deviation from linear behaviour in the logarithmic resistivity against 1/T from 50-20K (Graph 4.22).

It is suggested that the phase transition to a more efficient semiconductor can be attributed to a slight change in crystal structure. Detailed above in the crystal structure discussion, CTS 4.5 contains two very similar, crystallographically independent donor layers due to anisotropy of the anionic $B_{R/S}(glycolate)_2^-$ layer. On decreasing temperature, the crystal lattice could shift from P2/*c* to P2 via loss of the glide symmetry to adopt a lower symmetry, lower energy state as both donor layers become crystallographically equal. A similar phase transition is observed in the κ- (BEDT-TTF)$_2$I$_3$ charge transfer salt[3]. The activation energies for the two regions of the logarithmic curve are calculated from Graph 4.21 and 4.22 below and presented in Table 4.23.

	$T_{300-100\ K}$	$T_{50-20\ K}$
E_a / eV	0.056	0.006

Table 4.23. Activation energies for the two temperature regions of the resistivity profile for CTS 4.5.

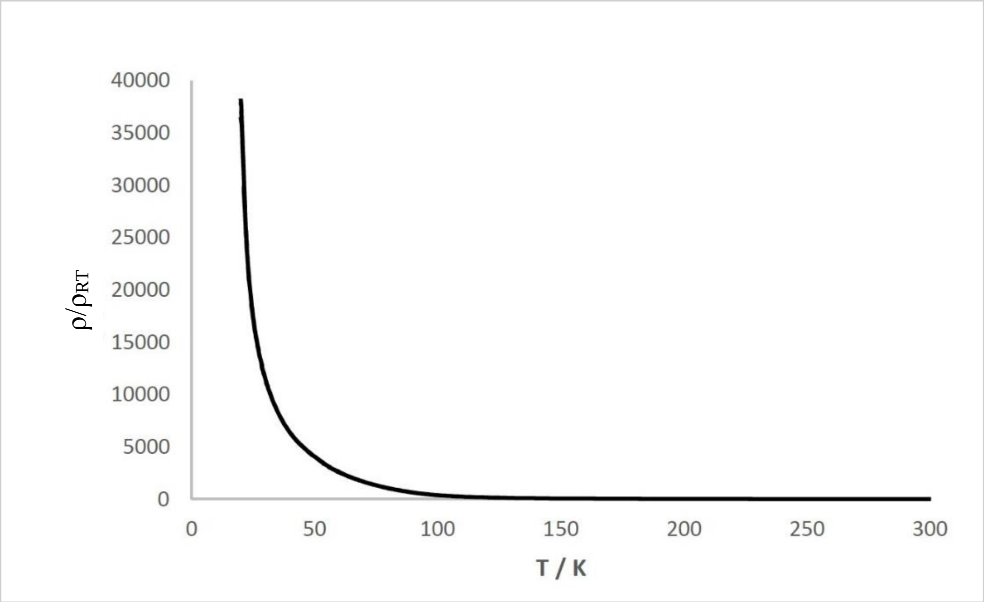

Graph 4.19. Temperature dependent resistivity for CTS 4.5.

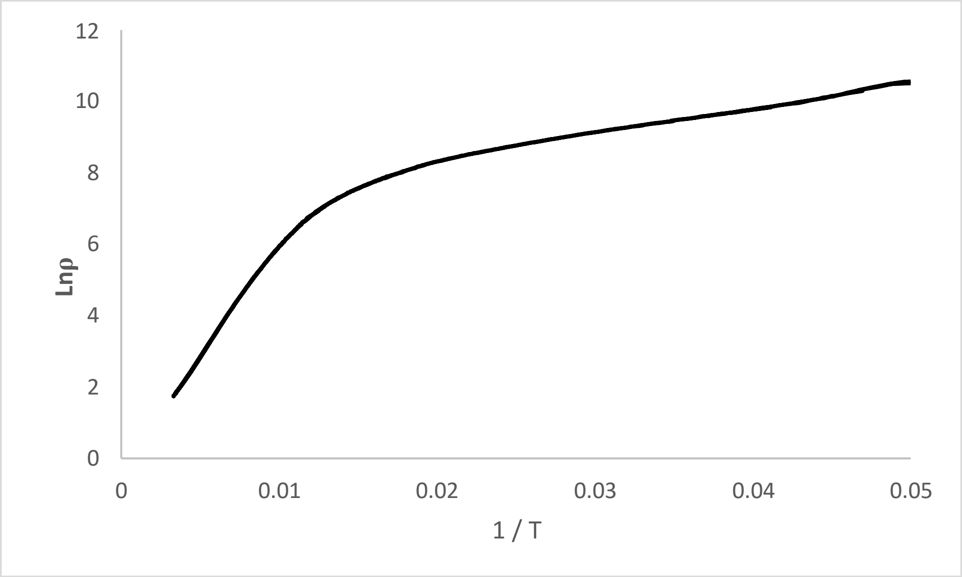

Graph 4.20. Logarithmic resistivity against 1/T for CTS 4.5.

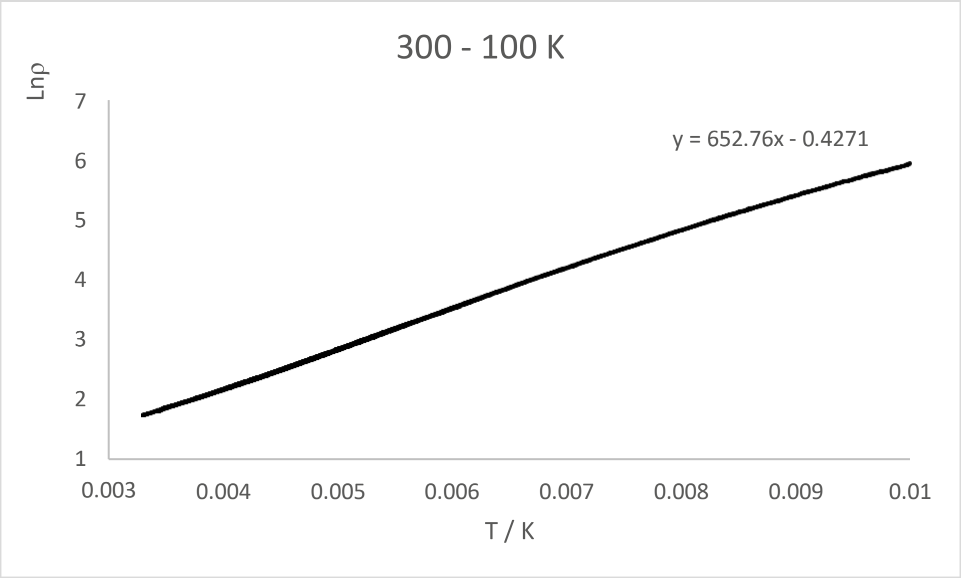

Graph 4.21. Logarithmic resistivity against 1/T for CTS 4.5 from 300 – 100 K for CTS 4.5.

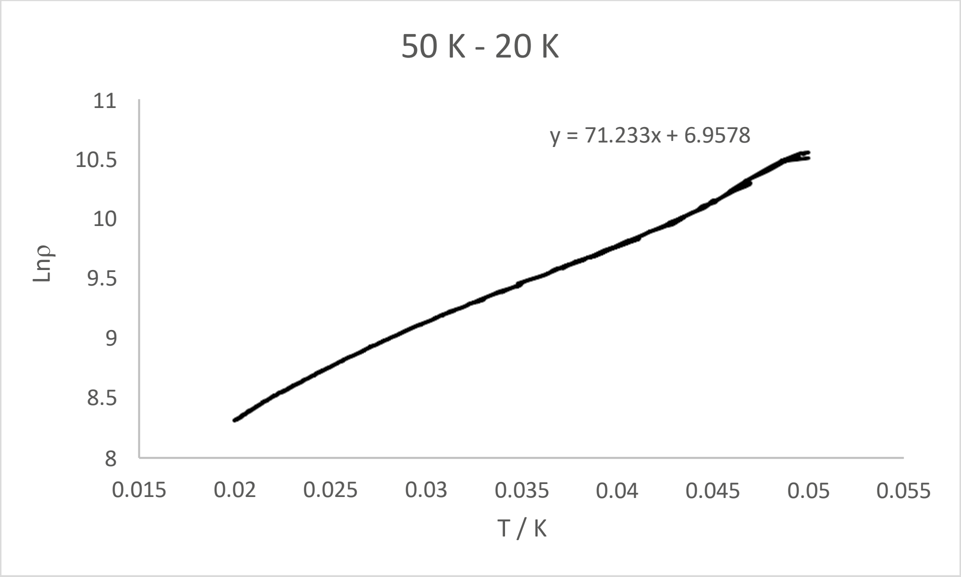

Graph 4.22. Logarithmic resistivity against 1/T for CTS 4.5 from 50 – 20 K for CTS 4.5.

4.4 Chapter Conclusions

The five salts discussed in this chapter are the first examples of BEDT-TTF charge transfer salts containing chiral and racemic four-coordinate borate anions. CTS 4.2 possesses a unique band structure for α-BEDT-TTF salts, due to the presence of the chiral and polar $B_S[(R)mal]_2^-$ anion, while the synthesis using the racemic mixture of the $B(malate)_2^-$ anion produced a salt exhibiting a semi-metallic to semiconductor transition due to band nesting at lower temperatures. These two salts also show the first examples of preferential diastereomeric induction within the electrocrystallisation environment.

Diastereomeric induction is also present in CTS 4.3 where only two of the possible six $B(mandelate)_2^-$ diastereomers were incorporated into the lattice, producing a semi-conductor that exhibits interesting magnetic behaviour due to the possibility of charge ordering at temperatures below 200 K. Electrocrystallisation of the chiral $B_{R/S}[(S)man]_2^-$ anion with BEDT-TTF produced metallic macromolecular helices exhibiting a metal-insulator transition at 150 K. The helices consist of many bent single crystals and shows the ability for chiral helices to form in the presence of $B_{R/S}[(S)man]_2^-$, perhaps by preferential induction of one diastereomer, while the other stays in solution and directs the formation of the chiral helix. Charge transfer salts displaying a macromolecular helical morphology have not been observed before.

Electrocrystallisation of racemic $B_{R/S}(glycolate)_2^-$ with BEDT-TTF has produced a semiconducting charge transfer salt which at room temperature includes two crystallographically independent donor layers due to anisotropy of the anionic stacks. A phase transition is observed between 100 – 50 K and it is suggested that this is accompanied by a change in crystal structure from the P2/*c* to P2 space groups.

The monovalent borate anions have tended towards the preferential formation of 2:1 radical cation salts with two crystallographically independent BEDT-TTF molecules. The exception is CTS 4.2 which chooses a charge ordered $^+1$ and 0 state for the two independent BEDT-TTF molecules, possibly driven by the chirality of the borate anion. In any case, all five of the borate charge transfer salts show exciting and novel properties that stem from the presence of chiral and diastereoisomeric anions within the electrocrystallisation environment. The salts have shown the wide variety of influences that chirality can have on the conducting properties of a material and also the effect of chirality on the nucleation and production of these crystalline materials.

4.5 References

1. J. R. Lopez, L. Martin, J. D. Wallis, H. Akutsu, Y. Nakazawa, J-i. Yamada, T. Kadoya, S. J. Coles and C. Wilson, *Dalton Trans.*, 2016, **45**, 9285.
2. P. Guionneau, C. J. Kepert, D. Chasseau, M. R. Truter and P. Day, *Synth. Met.*, 1997, **86**, 1973.
3. J. Wosnitza, X. Liu, D. Schweitzer, and H. J. Keller, *Phys. Rev.* B, 1994, **50**, 12747.

Chapter 5: Nine-coordinate Lanthanide Anion Charge Transfer Salts

The synthesis and characterisation of chiral lanthanide anions is a highly sought after area within inorganic synthetic chemistry as it offers routes to materials with a high number of applications e.g as chiral shift reagents for resolving NMR spectra of chiral Lewis bases[1] and as highly enantioselective catalysts and reagents[2]. The photo-physical properties of the lanthanide complexes also provide a means to easily study the behaviour of the complex by probing the metal centre[3]. Chiral oxazoline ligands have been used to coordinate to lanthanoid centres[4] and have proved successful in catalysing the polymerisation of isoprene[5].

The majority of literature concerning chiral lanthanides is focused on the coordination of atomically chiral ligands to the metal ion. However, there are a number of examples in which the coordination of three identical tridentate ligands to the lanthanide centre produces a chiral complex containing D_3 symmetry. The three propeller-like ligands form a complex in which there is a chiral twist through the central axis. The presence of very small amounts of thermal energy causes rapid racemisation of the labile 9-coordinate anions and therefore resolution prior to crystal engineering is very difficult. However, as previously stated, spontaneous resolution of some of these complexes in the past has been possible[6], showing the propensity of some chiral lanthanide anions to form enantiopure salts.

Previously, charge transfer salts of BEDT-TTF have been produced containing lanthanide complex anions, namely hexacoordinated thiocyanates or four-coordinate nitrates. A series of isostructural salts of the formula $(ET)_4Ln(NCS)_6.CH_2Cl_2$ (NCS = thiocyanate and Ln = Ho, Er, Yb and Y) showed semiconducting behaviour caused by the antiferromagnetic ordering of the ET π electrons below room temperature[7]. On the other hand, an $(ET)_2Dy(NO_3)_4$ salt undergoes a metal-insulator transition at around 200K with paramagnetic behaviour also observed through the strongly localised Dy^{3+} $4f^9$ electrons[8]. Tamura *et al.* have also reported the synthesis of metallic radical cation salts with $[Ln(NCS)_6]^{3-}$ and $[LnCl_4(H_2O)_6]^-$ using the radical cations BO and TTP[9].

In this chapter is discussed the synthesis of the first BEDT-TTF charge transfer salts containing chiral and racemic nine-coordinate lanthanide anions derived from the tridentate dpa and clo ligands respectively (dpa = dipicolinic acid, clo = chelidonic acid). The structural and physical properties of the salts are discussed in detail.

5.1 $[Ln(dpa)_3]^{3-}$ anion

The tris-chelate heterocyclic pyridine derivative, dipicolinic acid (2,6-pyridine dicarboxylic acid, or dpa) which has a pyridine ring with carboxylate groups at the 2 and 6 positions, forms stable nine-coordinate complexes with the majority of the lanthanide series[10]. Dipicolinic acid is an attractive molecule for crystal engineering of metal complexes due to its rigid and planar nature. The peripheral carboxylate oxygens and central nitrogen are potential donor atoms through which the tridentate ligand can coordinate, producing mononuclear lanthanide anions with a net formal charge of 3^-, the anion is pictured below in Figure 5.1.

Its coordination geometry produces a distorted tricapped trigonal prism polyhedron with the lanthanoid(III) ion at the centre and oxygens or nitrogens at each corner. Single crystal diffraction data has been reported for the full series of Lanthanide dpa sodium salts, and all the salts show paramagnetic behaviour. The crystal lattice can be described as layers of complex anions and layers of hydrated sodium cations.

The majority of the $Ln(dpa)_3$ complex anions present in the literature are synthesised as the sodium salts[11] however, in 2011 Hou *et al.* reported the synthesis of $(Hdipa)_3[Ln(dpa)_3]$ (where dipa = *N*-(1-methylethyl)-2-propanamine) for the full lanthanide series[12]. Much more recently the synthesis of Eu(III) and Tb(III) dpa salts including the 2- aminobenzothiazole (ABT) countercation have been synthesised and fully characterised[13].

The crystal structure exists as a hydrogen-bonded network of mononuclear $Ln(dpa)3^{3-}$ complex anions, ABT cations and solvate water molecules. Magnetic susceptibility measurements of the Tb(III) salt followed the Curie-Weiss law indicating paramagnetic behaviour until 50K where spin-orbit coupling and crystal field perturbation dominates and the effective moment begins to decrease. The Eu salt showed magnetic behaviour as expected for the $^7F_0$ ground state with U_{eff} decreasing with decreasing temperature.

Synthesis of the Eu(III) dpa salt containing either the Cs^{3+} or Co^{3+} counterion produced lattices in which a non-centrosymmetric space group and a centrosymmetric space group was observed respectively. However, definite assignment of the absolute configuration was not possible during refinement but the crystal was still optically active[14].

The synthesis of $[Ln(dpa)_3]^{3-}$ anions for inclusion into ionic lattices presents the opportunity to explore how a larger metal complex can affect the packing motif and consequently the conducting properties of a charge transfer salt. The carboxylate groups on the dpa ligand are well placed within the Ln coordination sphere to take part in non-covalent interactions during crystal engineering with BEDT-TTF. The interaction of magnetic lanthanide centres alongside conducting radical cations can also be explored. Discussed in this section are the first examples of conducting BEDT-TTF charge transfer salts in which the anion is a $Ln(dpa)_3$ complex.

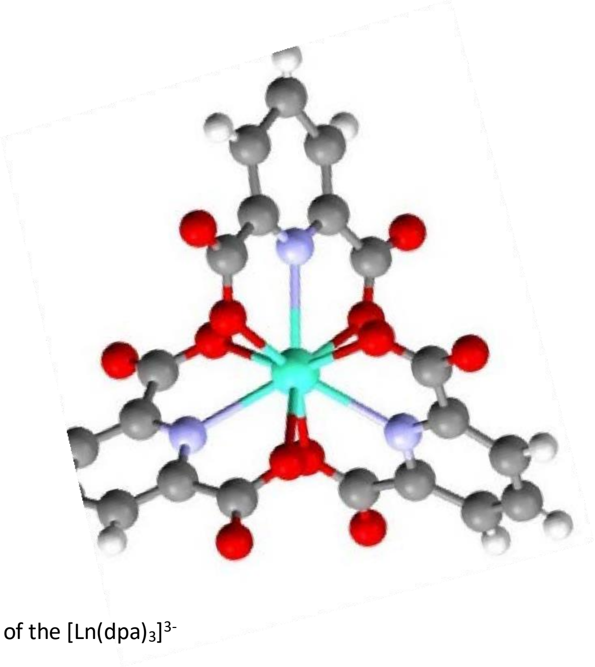

Figure 5.1. Representation of the $[Ln(dpa)_3]^{3-}$

5.1.1 α'''-(BEDT-TTF)$_{4.5}$[Ln(dpa)$_3$].(EtOH)$_2$.(H$_2$O)$_n$

Two crystals of the title compound have been produced, containing a lanthanum and a gadolinium centre respectively. Due to poor crystal quality of the gadolinium analogue only the lanthanum derivative is discussed in detail.

5.1.1.1 Electrocrystallisation Table

Donor	Counterion	Electrolyte	Solvent	Current /µA	Crystal Growth	Observation
ET	Na$^+$	[La(dpa)$_3$]$^{3-}$	PhCl:EtOH (20:1)	0.1 – Increased to 0.5 after 1 week.	Yes – Small quantity of clusters of black rectangles collected from electrode.	Crystal size sufficient for X-ray structure analysis and Raman measurements.
ET	Na$^+$	[La(dpa)$_3$]$^{3-}$	PhCl:EtOH (10:1)	0.1	Yes – Small quantity of black rectangles collected from electrode.	Crystals too thin for X-ray analysis.
ET	Na$^+$	[La(dpa)$_3$]$^{3-}$	PhCl:PhBr:EtOH (10:10:2)	0.1	Yes – Tiny amorphous black crystals collected from electrode.	Crystals too thin for X-ray analysis.

Table 5.1. Electrocrystallisation table for synthesis of CTS 5.1

It was not possible to produce crystals of CTS 5.1 to a sufficient size for charge transport measurements. The rectangular block single crystals formed clusters nucleating off one another and due to this it was impossible to cut off large enough single crystals to attach gold electrodes to. Substitution of the solvent for similar sized molecules i.e MeOH and MeCN to improve crystal quality and produce an isostructural family of salts containing different guest molecules proved unsuccessful. It was only possible to obtain a crystal structure of high R factor even after various solvents, concentrations and currents were explored. The isostructural Gadolinium salt, CTS 5.1a won't be discussed in detail as the crystal structure was of poor quality.

5.1.1.2 *Crystal Structure*

α'''-(BEDT-TTF)$_{4.5}$[Ln(dpa)$_3$].(EtOH)$_2$.(H$_2$O)$_n$		
Formula	$C_{81}H_{57}O_{12}N_3S_{48}La$	$C_{81}H_{57}O_{12}N_3S_{48}Gd$
M_r/g mol^{-1}	2924.14	2960.48
Temp / K	263	270
Radiation	Mo Kα	Mo Kα
Wavelength	0.71075	0.71075
Crystal System	Triclinic	Triclinic
Space group	P–*1*	P–*1*
a / Å	12.8104(15)	12.726(2)
b / Å	17.792(2)	17.862(3)
c / Å	21.182(2)	21.069(4)
α / °	96.108(7)	96.644(7)
β / °	93.647(7)	93.627(7)
γ / °	99.978(7)	99.530(7)
V/Å^3	4711.2(9)	4674.7(15)
Z	2	2
ρ/g cm^{-1}	2.074	1.784
μ/cm^{-1}	1.5833	1.5791
Absorption Applied	Yes	Yes
Abs. Type	Multi-scan	Multi-scan
Abs. Range	0.372-1.000	0.053 – 1.000
Total Reflections	45644	39855
Unique Reflections	21504	20928
R [all data]	0.2038	0.3022
R_1 [$I > 2\sigma(I)$]	0.1384	0.1917
wR [all data]	0.3546	0.5388
Goodness of fit	1.138	1.036
Refinement Program	SHELX	SHELX
Refinement Mode	F	F
Flack Parameter	n/a	n/a

Table 5.2. X-ray data for CTS 5.1

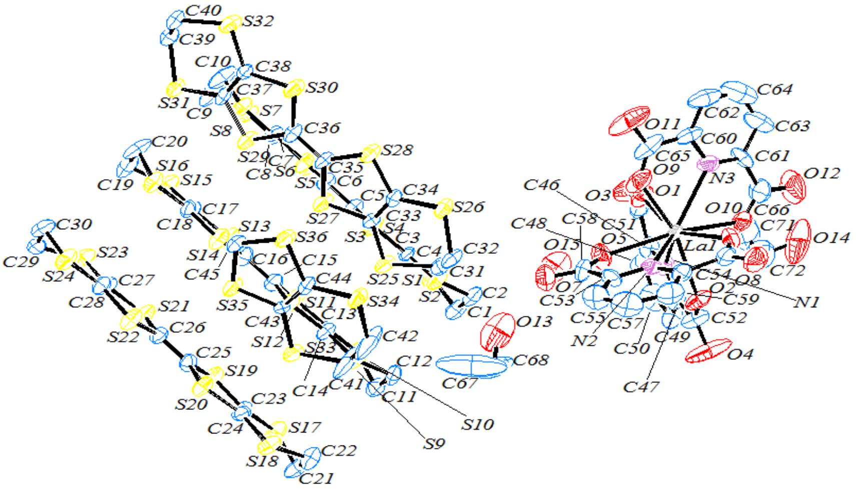

Figure 5.2. ORTEP diagram of asymmetric unit of CTS 5.1. Displacement ellipsoids are drawn at the 50% probability level. Hydrogens are omitted for clarity.

CTSS 5.1 and 5.1a crystallise in the centrosymmetric triclinic space group P-1. Figure 5.2 shows the ORTEP diagram and numbering scheme for the asymmetric unit of CTS 5.1 which consists of one anion, two guest ethanol molecules, one water and four and a half independent BEDT-TTF molecules (A-E). Donors A,B,C and E are twisted at both ends with each ethylene group displaced to the same degree as the other side of the molecule such that they eclipse one another when viewed down the long axis of the donor. Donor D is planar with no displacement of the ethylene groups from the central axis. The conducting layer forms stacks in the *b* direction with neighbouring stacks separated in the *c* direction by the insulating layer (Figure 5.3).

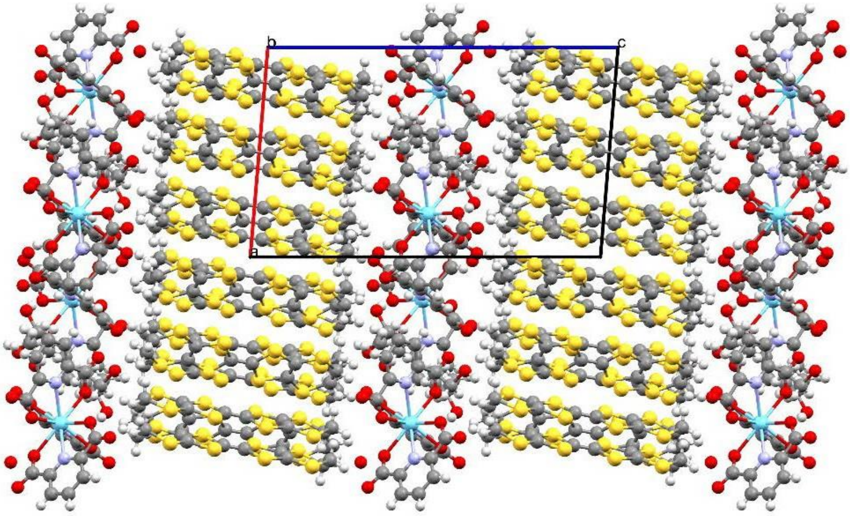

Figure 5.3. Lattice packing of CTS 5.1 viewed along the *b* axis.

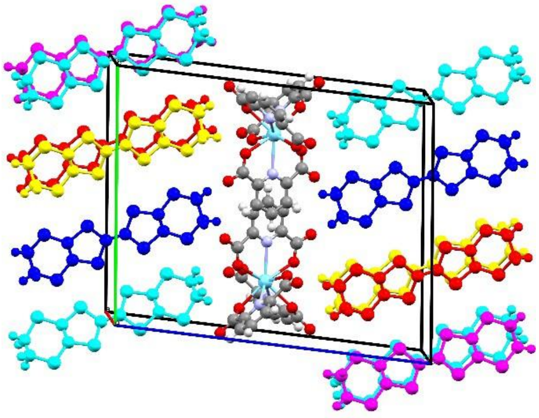

Figure 5.4. Unit cell of CTS 5.1

Figure 5.4 above shows the triclinic unit cell for the title compound. The donors form stacks along the *b* axis with each stack consisting of alternating columns of either donors B and D (column 1) or donors A, C and E (column 2) as viewed down the *a* axis (Figure 5.5), S...S contacts below the sum of vdW radii are shown in blue.

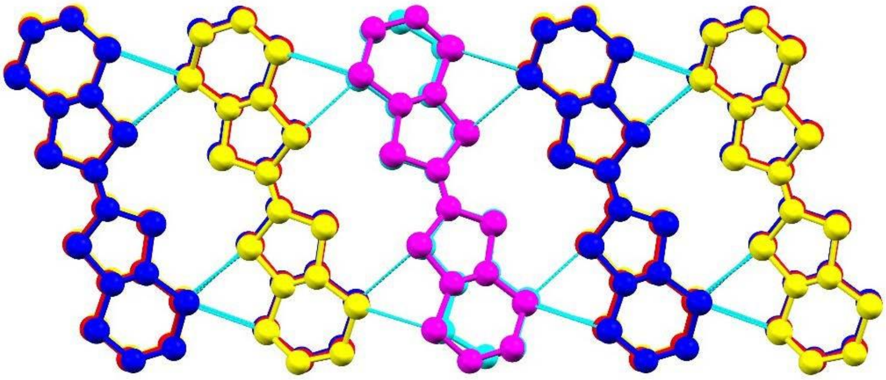

Figure 5.5. Single donor stack in CTS 5.1, viewed along the *a* axis. Donors are coloured according to symmetry equivalence and short sulphur interactions below the sum of the vdW radii (3.6 Å) are shown in blue lines. Hydrogens are omitted for clarity.

Figure 5.6 shows that column 1 stacks in a BDBBDB... fashion whereas column 2 is in a ACEA... arrangement. This arrangement is the alpha''' packing with donors forming a herringbone pattern where the dihedral stacks exist in a 2:1 ratio, meaning that column 1 is sandwiched either side by column 2. The donors alternate between charges of 1/3 and 2/3 through the *ab* plane with blocks of either 2/3 charge created by two neighbouring donor Cs (red) or 1/3 charge created by neighbouring face-to-face donor A in column 2. This is different to the previous alpha''' packing motifs where there the conducting layer is dominated by stripes of charge running through the ab plane. Donor D (cyan) is surrounded only by donors C and E of column 2. As can be seen from Figure 5.6 below, the network of S...S contacts formed creates an area of high electron density around the central column 1. There are no face-to-face intermolecular sulphur contacts observed which suggests that unlike previous charge transfer salts showing alpha packing motifs, the donors in this salt are not dimerised. In the following discussion, the terms 'out of plane' and 'in plane' will be used when referring to side-to-side sulphur interactions below the sum of vdW radii (3.6 Å). This is intended to differentiate between S...S contacts that are present either within the same plane of the central axis of the molecule in question (in plane) or S...S contacts that are present almost perpendicular to the central axis of the molecule in question (out of plane).

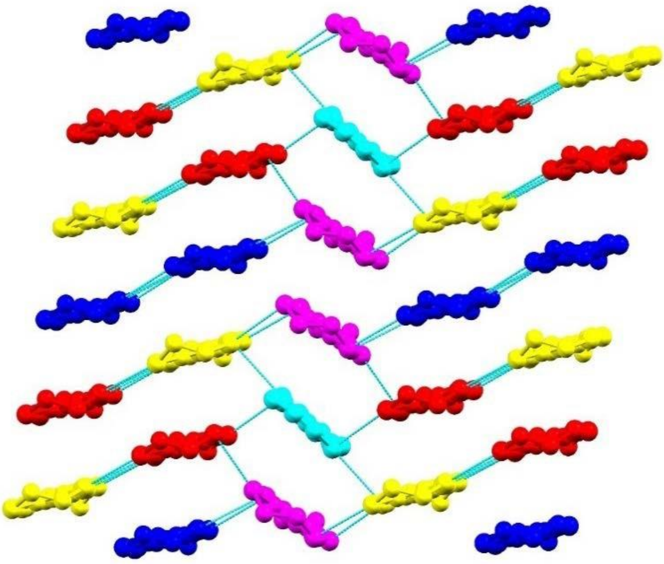

Figure 5.6. Donor packing of CTS 5.1, viewed along the *b* axis. S...S contacts are shown in blue lines. Hydrogens are omitted for clarity.

Figure 5.7 below pictures donor A shown above in dark blue. The central TTF bond lengths are shown in green and dotted red lines show the orientation and direction of S...S contacts below the sum of vdW radii (3.6 Å), lengths of the sulphur interactions are shown in green next to the red dotted lines. The donor makes six side-to-side short contacts with donors in adjacent stacks. Four of these contacts are between donor A and two are with donor B. The twisted eclipsed orientation of the ethylene groups is evident from the Figure 5.8 below. The central TTF portion of the molecule is planar however, there is a slight twist through the two six-membered rings due to the ethylene groups being displaced from the central ET axis by an unequal amount. It is of note that donor A has no ‘out of plane’ S...S contacts throughout the donor stacks. This creates a central channel running along the crystallographic *b* direction through which no sulphur interactions are observed.

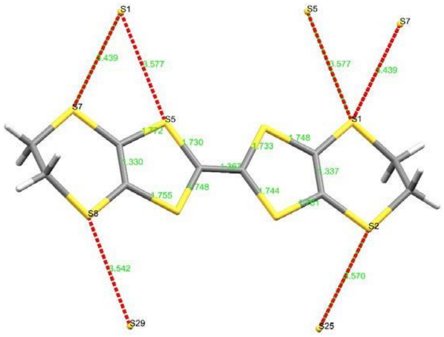

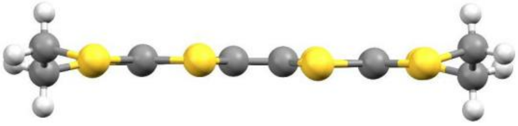

Figure 5.7. (left) CTS 5.1: Capped stick diagram of donor A. S...S contacts are shown in dotted red lines and contacts atoms are labelled in black. Contact length and central TTF bond lengths in angstroms are shown in green. Figure 5.8. (right) CTS 5.1: Side on profile view of donor A.

Figure 5.9 below shows donor B, pictured above in purple. Central TTF bond lengths are also shown in green. The donor makes five side-to-side S...S contacts below the sum of vdW radii and are shown in red dotted lines, the contact length is shown in green above the dotted lines. Due to the staggered alpha''' motif seen throughout the salt the donor makes contacts with only column 2 either above or below the plane of column 1. One contact is made with donor C and two contacts are made each with donor A and donor E. The central TTF portion of the donor remains planar while the twisted eclipsed ethylene groups (Figure 5.10) again create a slight twist in the two six-membered rings due to the unequal displacement from the central plane of the molecule.

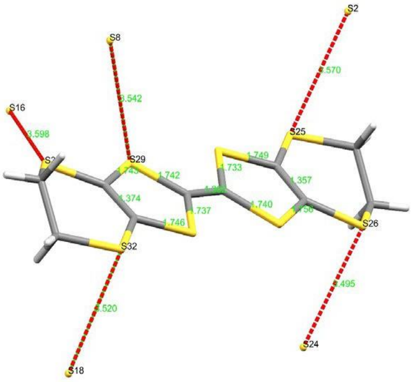

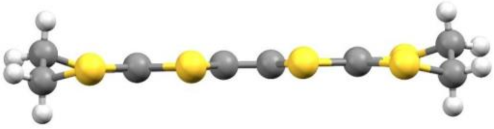

Figure 5.9. (left) CTS 5.1: Capped stick diagram of donor B. S...S contacts are shown in dotted red lines and contacts atoms are labelled in black. Contact length and central TTF bond lengths in angstroms are shown in green. Figure 5.10. (right) CTS 5.1: Side profile view of donor B.

Figure 5.11 below shows donor C pictured above in red. S...S contacts (red dotted lines), contacts length and central TTF bond lengths are shown in green. Donor C makes six sulphur interactions below the sum of vdW radii. One with the 'out of plane' donor B of column 1, one with 'in plane' donor D of column 1 and four with 'in plane' donor E of the same column (2). The ethylene groups hold a twisted eclipsed confirmation (Figure 5.12), however for donor C there is no unequal displacement, therefore the whole BEDT-TTF unit remains almost planar until the twist seen from the terminal ethylene groups.

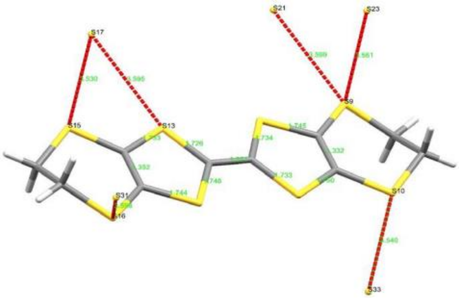

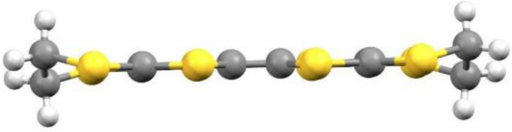

Figure 5.11. (left) CTS 5.1: Capped stick diagram of donor C. S...S contacts are shown in dotted red lines and contacts atoms are labelled in black. Contact length and central TTF bond lengths in angstroms are shown in green. Figure 5.12. (right) CTS 5.1: Side profile view of donor C.

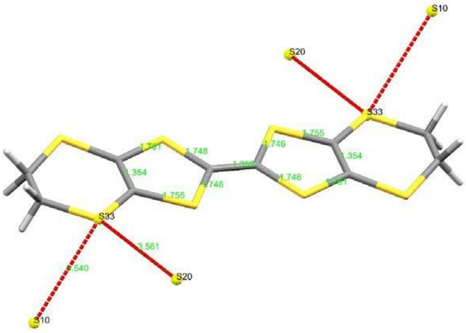

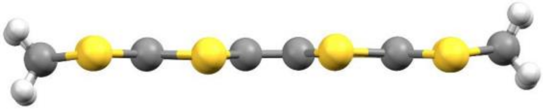

Figure 5.13. (left) CTS 5.1: Capped stick diagram of donor D. S...S contacts are shown in dotted red lines and contacts atoms are labelled in black. Contact length and central TTF bond lengths in angstroms are shown in green. Figure 5.14. (right) CTS 5.1 Side profile view of donor D.

Figure 5.13 above shows donor D. Pictured above in sky blue. S...S contacts are shown in red dotted lines with contact length shown above in green. Central TTF bond lengths are also shown in green. The central C=C bond lies on an inversion centre and therefore the donor is totally symmetrical about the central C=C bond and only half of the donor is present in the asymmetric unit. The half donor makes two ‘out of plane’ sulphur interactions below the sum of vdW radii, one with donor C and one with donor E. The donor is almost planar with no twist or boat confirmation observed (Figure 5.14). A very slight twist can be seen due to the peripheral sulphurs of the six-membered ring lying ever so slightly away from the plane of the molecule.

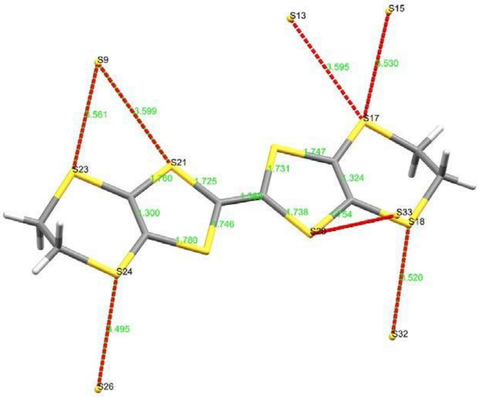

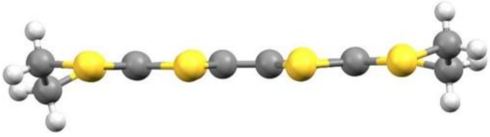

Figure 5.15. (left) CTS 5.1: Capped stick diagram of donor E. S...S contacts are shown in dotted red lines and contacts atoms are labelled in black. Contact length and central TTF bond lengths in angstroms are shown in green. Figure 5.16. (right) CTS 5.1: Side profile view of donor E.

Figure 5.15 above shows donor E, pictured above in yellow. Short sulphur interactions below the sum of the vdW radii (3.6 Å) are shown in dotted red lines, contact length and central TTF bond lengths are shown in green. The donor makes seven side-to-side S...S contacts. Four ‘in plane’ contacts are made with donor C of column 2, two ‘in plane’ contacts are made with donor B in column 1 and one ‘out of plane’ contacts is made with donor D of column 1. The donor has a twisted eclipsed confirmation at both terminal ethylene groups (Figure 5.16), with both groups displaced from the central axis of the molecule by an equal amount.

The $[Ln(dpa)_3]^{3-}$(Ln = Gd or La) anion is present as a racemic mixture throughout the salt. Each layer consists of equal quantities of both enantiomers. Figure 5.17 shows the space filling diagram of the orientation of the anion throughout the insulating layer as viewed down the *c* axis. The orange complexes correspond to the D enantiomer and the white complexes to the L. The guest and water molecules occupy the cavity left between the anions. The La-O bond length is between 2.511(1)-2.541(1) Å and La-N bond lengths are 2.664(1), 2.664(1) and 2.658(1) Å. La…La distance is 12.810(1) Å between anions of respective chirality.

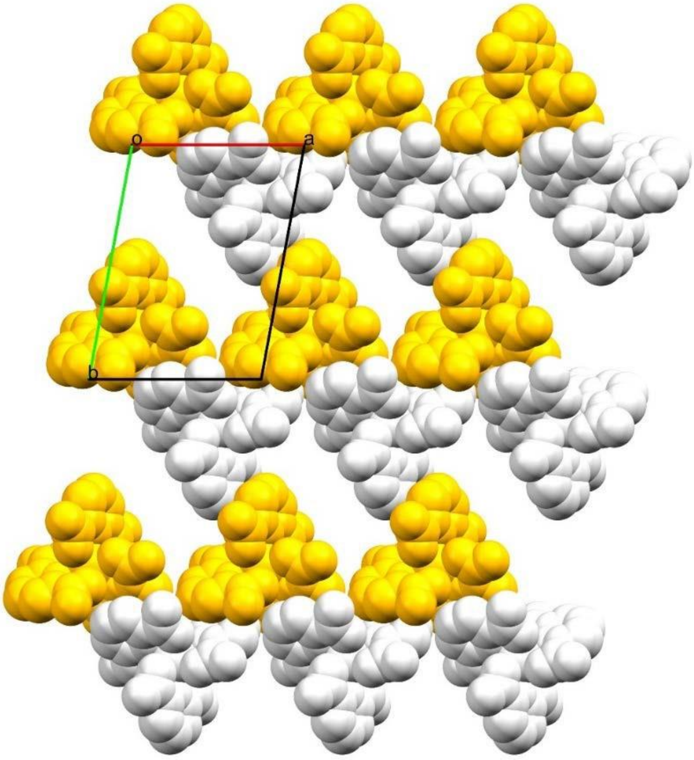

Figure 5.17. Spacefilling diagram of anion layer with guest solvent and water molecules removed. Viewed along the *c* axis. Anions are coloured according to the respective chirality. (Yellow = *D*, White = *L*).

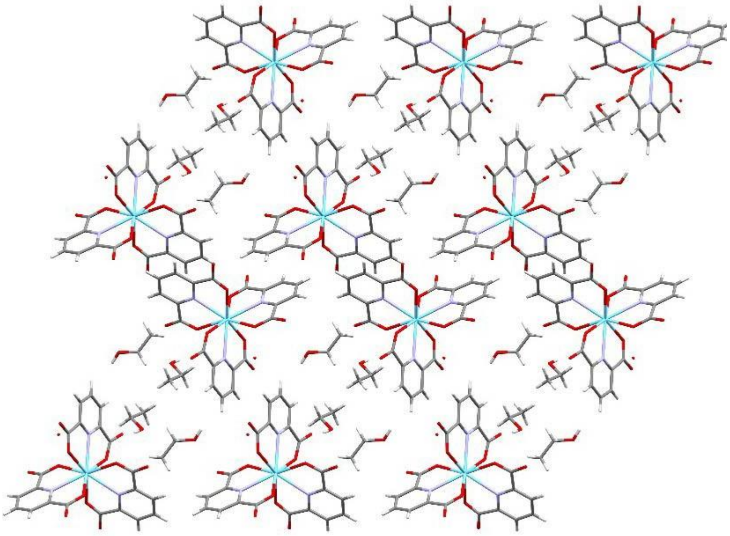

Figure 5.18. Capped stick diagram of the insulating layer including guest solvent and water molecules. Viewed along the *c* axis.

There is a large network of short contacts and hydrogen bonding between guest, water, anion and donor molecules, the majority of which are shown below in Figure 5.19. The two guests make three hydrogen bonds with donor A (O13...H2B, 2.622(1) Å), donor B (O13...H31A, 2.604(1) Å) and donor C (O14...H11B, 2.217(1) Å). The second ethanol also makes a hydrogen bond with a coordinated oxygen through the hydrogen on the alpha carbon (O10...H72B, 2.589(1) Å) while the first guest takes no part in hydrogen bonding with the anion molecule. The water molecule plays a role in stabilising both the insulating and conducting layers, it makes three hydrogen bonds, one with a ring hydrogen of a dipicalinato ligand (O15...H49, 2.617(1) Å) and two with neighbouring donor molecules A (O15...H2A, 2.547(1) Å) and E (O15...H22B, 2.648(1) Å). There are two inter-anion hydrogen bonds between coordinated oxygens and ring hydrogens (O6...H64, 2.513 and O9...H57, 2.626 Å). The two ligands that make inter-anion hydrogen bonds each make three short contacts with neighbouring donor molecules, while the third ligand makes a total of five hydrogen bonds with surrounding donor molecules. Interestingly donor D takes no part in hydrogen bonding throughout the lattice.

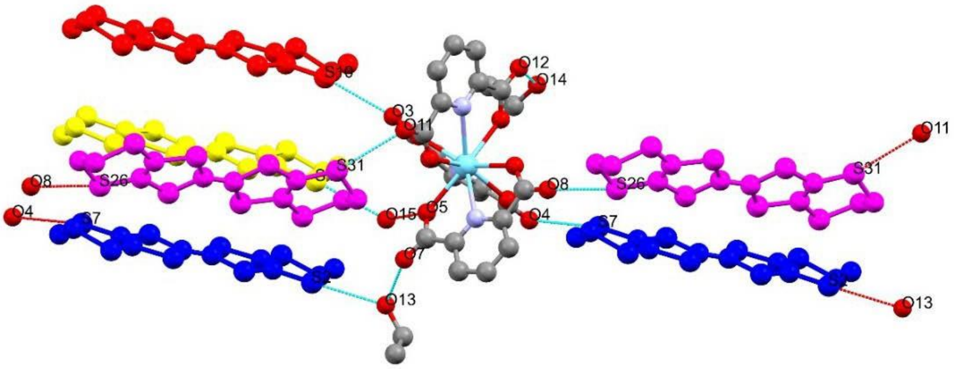

Figure 5.19. Short contacts (blue) between anion and donor. Contact atoms are labelled in black.

5.1.1.3 S…S Contacts

Contact	***Atom***	***Atom***	***Length / Å***
1	S1	S5	3.577(3)
2	S1	S7	3.439(3)
3	S2	S25	3.569(4)
4	S8	S29	3.542(3)
5	S9	S21	3.599(3)
6	S9	S23	3.561(4)
7	S13	S17	3.594(3)
8	S15	S17	3.529(4)
9	S16	S31	3.598(4)
10	S10	S33	3.539(4)
11	S18	S32	3.520(4)
12	S24	S26	3.494(3)
13	S20	S33	3.561(3)

Table 5.3. Short sulphur interactions below the sum of the vdW radii (3.6 Å) for CTS 5.1

Table 5.3 above shows the length, in angstroms, of short sulphur interactions below the sum of the vdW radii (3.6 Å) for the donors present in CTS 5.1. There are thirteen side-to-side contacts observed that range from 3.439(3) – 3.599(3) Å).

5.1.1.4 C=C Bond Length, Charge Calculations and Raman

	A - Blue	***B - Purple***	***C - Red***	***D – Sky Blue***	***E - Yellow***
C=C Bond Length / Å	1.367(15)	1.362(15)	1.371(16)	1.352(15)	1.368(16)

Table 5.4. Central ET C=C bond lengths for independent donors present in CTS 5.1

The central BEDT-TTF C=C bonds lengths suggest that donors A, B and E carry equal charges, the values of which are consistent with a BEDT-TTF charge of $^{+}2/3$. Central C=C bond lengths for donors C and E are consistent with donor charges of $^{+}1/3$.

	A – Dark Blue	***B - Purple***	***C - Red***	***D – Sky Blue***	***E – Yellow***
a / Å	1.367	1.362	1.371	1.352	1.368
b / Å	1.739	1.738	1.735	1.747	1.735
c / Å	1.759	1.749	1.736	1.758	1.760
d / Å	1.334	1.366	1.342	1.354	1.312
δ	0.797	0.759	0.758	0.799	0.815
Q	**0.399** (±0.1)	**0.683** (±0.1)	**0.690** (±0.1)	**0.384** (±0.1)	**0.265** (±0.1)

Table 5.5. Donor charge estimation using Kepert *et al.*[15] average TTF bond length calculation.

Estimated charge calculations for the independent donors are shown above. The values for donors A-D agree with the proposed $^{+}0.5$ valency of each inequivalent BEDT-TTF molecule. The calculation for donor E is slightly lower than expected.

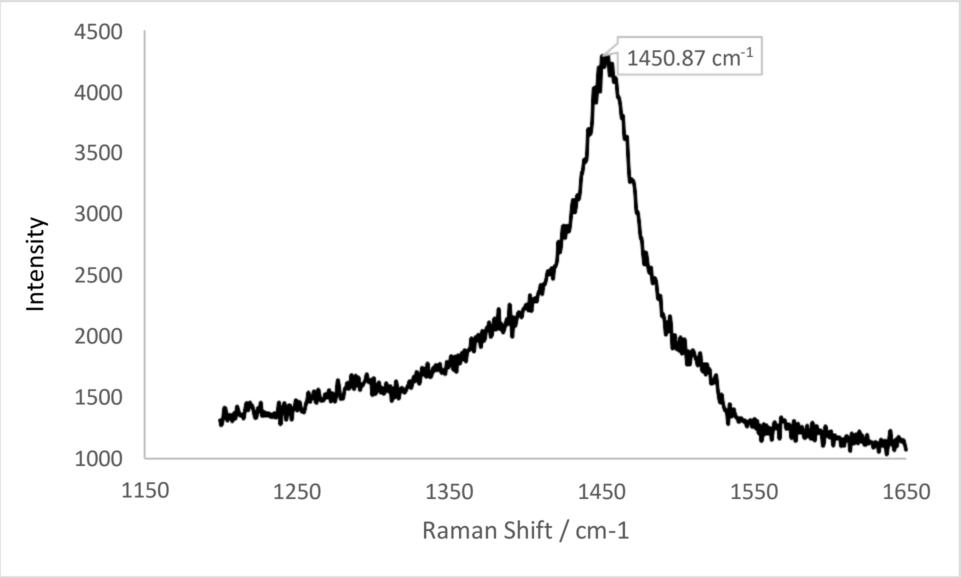

Graph 5.1. Relative intensity against Raman shifts of CTS 5.1

The experimental evidence for the symmetric C=C bond vibration frequencies for radical cation salts of 3:2 stoichiometry shows high intensity peaks in the Raman shift at 1460-1470 and 1480-1490 cm^{-1}, corresponding to the υ_4 and υ_3 stretching frequencies respectively for a donor cation of partial charge +2/3. There is no experimental evidence provided for the Raman shift from symmetric C=C bond vibration frequencies arising from the υ_4 and υ_3 stretching frequencies for radical cation salts of 3:1 stoichiometry, the values are taken from the extrapolated graph given by Wang *et al*. The values are approximately 1480-1490 and 1510-1520 cm^{-1} for the υ_4 and υ_3 modes respectively. Reproducible Raman scattering experiments were performed on several crystals of CTS 5.1. Due to the overlapping of vibration frequencies from the presence of two types of donor cations of different charge (+1/3 and +2/3), the Raman spectra that was recorded is noisy with four symmetric C=C bond modes present between 1460- 1520 cm^{-1} and consequently, only one broad peak at 1400 - 1500 cm^{-1} is observed.

5.1.2 α-(BEDT-TTF)$_4$-Λ-[Gd(dpa)$_3$].H$_3$O.H$_2$O

Through electrocrystallisation of racemic Gd(dpa)$_3$ with BEDT-TTF, a chiral charge transfer salt has been produced in which only one enantiomer of the Gd(dpa)$_3$$^{3-}$ anion is present throughout the crystal lattice. The chiral salt formed spontaneously from an achiral solvent and a racemic anion mixture in the presence of BEDT-TTF.

5.1.2.1 Electrocrystallisation Table

Donor	**Counterion**	**Electrolyte**	**Solvent**	**Current /µA**	**Crystal Growth**	**Observation**
ET	Na$^+$	[Gd(dpa)$_3$]$^{3-}$	PhBr	0.2	Yes – Large quantity of black plates collected from electrode.	Crystals were of high quality. Suitable for X-ray and physical measurements.
ET	Na$^+$	[Gd(dpa)$_3$]$^{3-}$	PhCl:EtOH 10:1	0.2	Yes – Large quantity of amorphous black crystals collected from electrode.	Crystals were of low integrity, diffraction data was poor and unreliable.
ET	Na$^+$	[Gd(dpa)$_3$]$^{3-}$	PhCl:PhBr	0.2	Yes – Small quantity of black plates collected from electrode.	Unit cell found however crystals were too thin for further data collection.

Table 5.6. Electrocrystallisation table for synthesis of CTS 5.2

It has been possible to produce a chiral crystal from spontaneous resolution of the $Na_3[Gd(dpa)_3]$ anion in the presence of BEDT-TTF and Bromobenzene, crystallising in the triclinic space group P 1. However, the Flack Parameter of 0.17612 (Table 5.7) indicates that there may just be a large excess of one enantiomer within the crystal structure. It is likely that some crystals within the batches contain the opposing enantiomer but more diffraction experiments are need to confirm this.

5.1.2.2 Crystal Structure

α-(BEDT-TTF)$_4$[Gd(dpa)$_3$.H$_3$O.H$_2$O	
Formula	$C_{61}H_{45}O_{14}S_{32}N_3Gd$
M_r/g mol^{-1}	2228.42
Temp / K	293
Radiation	Mo Kα
Wavelength	0.7107
Crystal System	Triclinic
Space group	P1
a / Å	10.3897(4)
b / Å	10.9484(4)
c / Å	20.4955(8)
α / °	83.663(3)
β / °	82.851(3)
γ / °	61.833(4)
V/Å^3	2035.75
Z	1
ρ/g cm^{-1}	1.818
μ/cm^{-1}	1.69804
Absorption Applied	Yes
Abs. Type	Analytical
Abs. Range	0.530-0.924
Total Reflections	19849
Unique Reflections	19808
R [all data]	0.0675
R_1 [$I > 2\sigma(I)$]	0.0655
wR [all data]	0.1652
Goodness of fit	1.016
Refinement Program	SHELX
Refinement Mode	F^2
Flack Parameter	0.17612

Table 5.7. X-ray data for CTS 5.2

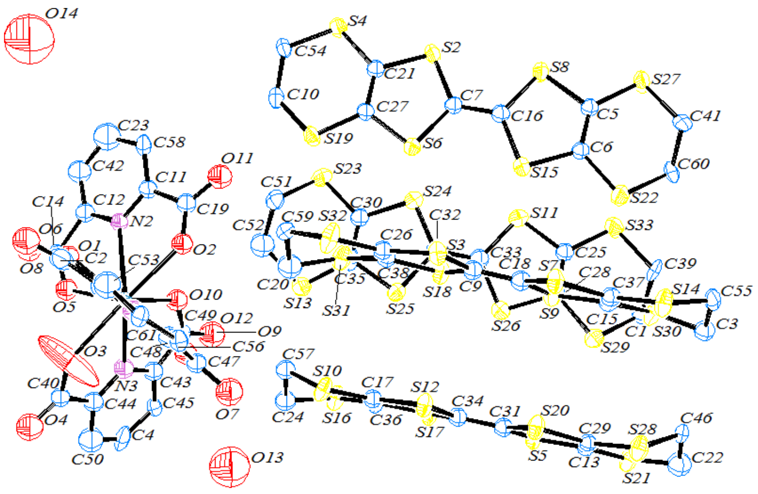

Figure 5.20. ORTEP diagram of asymmetric unit of CTS 5.2. Displacement ellipsoids are drawn at the 50% probability level. Hydrogens are omitted for clarity.

CTS 5.2 crystallises in the chiral, triclinic space group P1. Figure 5.20 shows the ORTEP diagram for the asymmetric unit of the Gadolinium salt with the atom numbering scheme. The asymmetric unit consists of one $[Gd(dpa)_3]^{3-}$ anion, one water molecule, one hydroxonium ion and four crystallographically independent donor molecules (A-D). The donors form stacks in the *a* direction with neighbouring stacks separated in the c direction by the insulating layer (Figure 5.22). The independent unit cell is shown below in Figure 5.21.

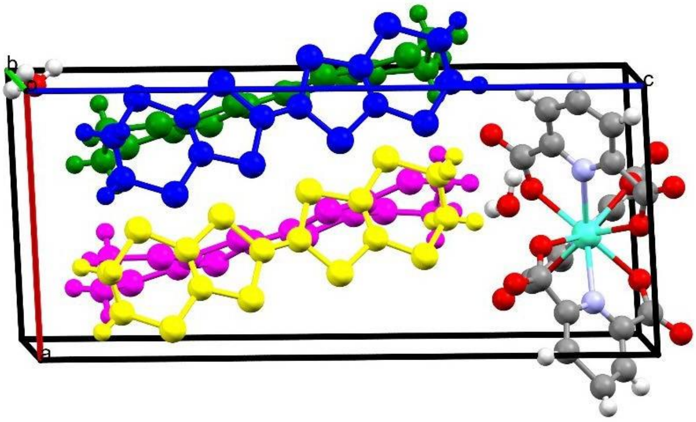

Figure 5.21. Unit cell of CTS 5.2. Donors are coloured according to symmetry.

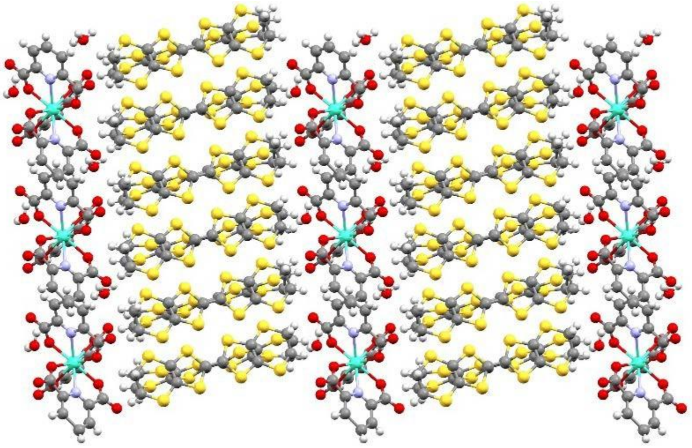

Figure 5.22. Lattice packing of CTS 5.2. Viewed along the *b* axis.

The ethylene groups on each donor are in the twist confirmation with each carbon displaced equidistant from the ET plane, such that when viewed down the long axis of the molecule the ethylene groups eclipse one another. The donors pack in the traditional alpha motif with stacks of donors at an orthogonal angle of ~86°. Donors A (green) and D (purple) make up one column and donors B (blue) and C (yellow) make up another. S...S contacts are shown in table 5.8, only side-to-side contacts are observed creating a 2D network flowing along the *a* and *c* directions. As can be seen from Figure 5.23 below donor D makes sulphur interactions only with donor B in the stack above and donor C in the stack below. There are no interstack contacts from donor D to donor B below and C above. This is a possible reason for the Arrhenius behaviour observed in the physical measurements, due to an incomplete network of S...S contacts. Donor A, shown in green, makes side-to-side interstack sulphur interactions with each neighbouring donor except donor D.

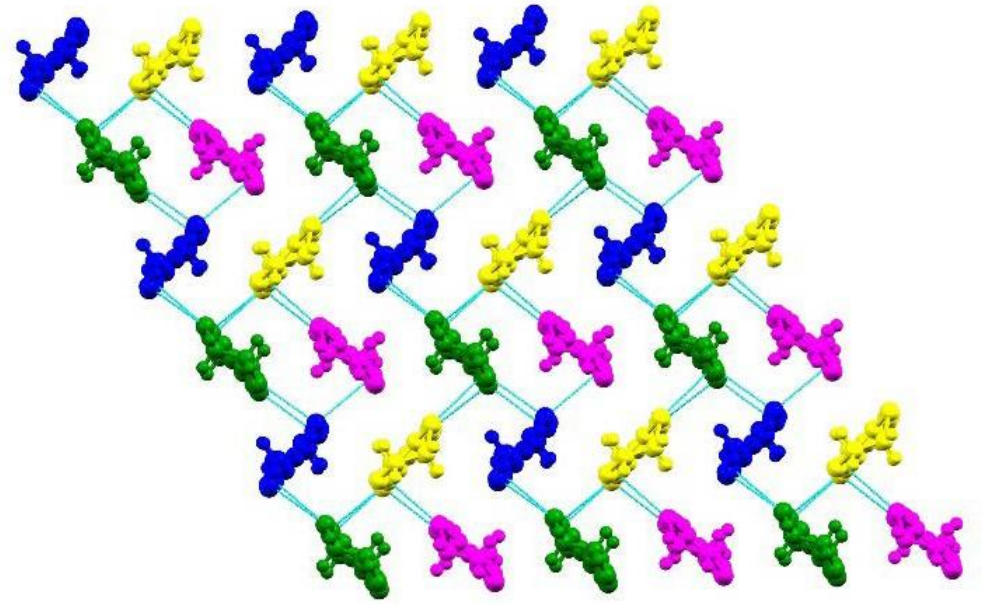

Figure 5.23. Donor stack in CTS 5.2 viewed along the *c* axis. S...S contacts below the sum of the vdW radii (3.6 Å) are shown in blue lines.

Figure 5.24 pictures donor A, shown above in green. Short sulphur interactions below the sum of the vdW radii are shown in dotted red lines, S...S contact length and TTF bond lengths are shown in green. The donor makes eight interstack S...S contacts with neighbouring donors, four 'in plane' contacts with donor C and four 'out of plane' contacts with donor D. The central TTF portion of the donor is planar and the peripheral ethylene groups are in the twisted eclipsed confirmation with both sides displaced from the central axis of the molecule by an equal amount. Donor A is calculated to hold a charge of $^{+}0.5$.

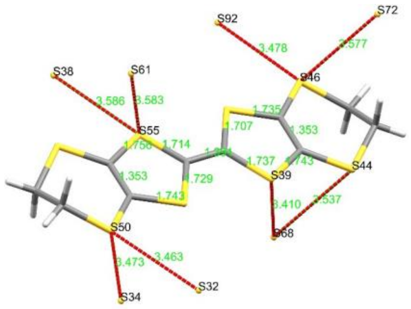

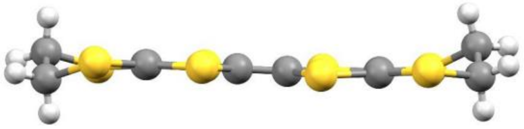

Figure 5.24 (left). CTS 5.2: Capped stick diagram of donor A. S...S contacts are shown in dotted red lines and contacts atoms are labelled in black. Contact length and central TTF bond lengths in angstroms are shown in green. Figure 5.25 (right). CTS 5.2: Side on profile view of donor A.

Figure 5.26 below pictures donor B, shown above in blue. Short sulphur interactions below the sum of vdW radii (3.6 Å) are shown in dotted red lines, contact length and central TTF bond lengths are shown in green, The donor makes six interstack side-to-side S...S contacts. Four of the contacts are ‘in plane’ with donor A and two are ‘out of plane’ contacts with donor D. The central TTF portion of the molecule is planar with the terminal ethylene groups in the twisted eclipsed confirmation. Donor B is calculated to hold a charge of $^{+}0.5$.

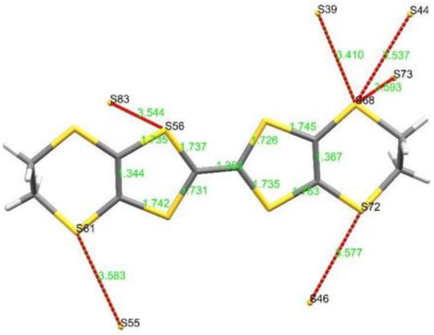

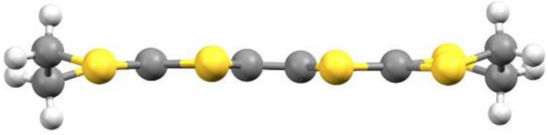

Figure 5.26 (left). CTS 5.2: Capped stick diagram of donor B. S...S contacts are shown in dotted red lines and contacts atoms are labelled in black. Contact length and central TTF bond lengths in angstroms are shown in green. Figure 5.27 (right). CTS 5.2: Side on profile view of donor B.

Figure 5.28 below pictures donor C, shown above in yellow. Short sulphur interactions below the sum of vdW radii (3.6 Å) are shown in dotted red lines, contact length and central TTF bond lengths are shown in green. The donor makes five interstack side-to-side short contacts with neighbouring donors. Four ‘out of plane’ contacts with donor A and one ‘in plane’ contact with donor D. The TTF portion of the molecule is planar with the terminal ethylene groups in the twisted eclipsed confirmation however the methylene groups are displaced by different degrees from the central axis of the BEDT-TTF molecule. Donor C is calculated to hold a charge of $^{+}0.5$.

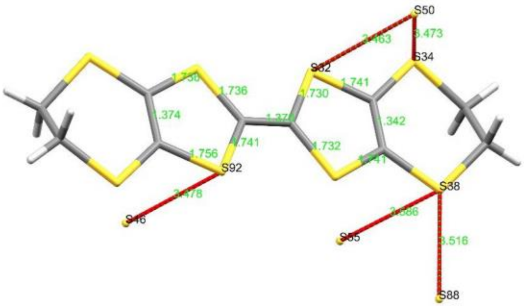

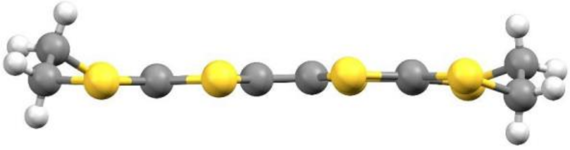

Figure 5.28 (left). CTS 5.2: Capped stick diagram of donor C. S...S contacts are shown in dotted red lines and contacts atoms are labelled in black. Contact length and central TTF bond lengths in angstroms are shown in green. Figure 5.29 (right). CTS 5.2: Side on profile view of donor C.

Figure 5.30 below pictures donor D, shown above in purple. Short sulphur interactions below the sum of vdW radii (3.6 Å) are shown in dotted red line, contact length and central TTF bond lengths are shown in green. The donor makes a total of three interstack side-to-side S...S contacts with neighbouring donors. Two 'in plane' contacts with donor B and one 'out of plane' contacts with donor C. The donor is slightly bent with the terminal ethylene groups again in the twisted eclipsed confirmation with each methylene group displaced by an unequal degree with respect to the central axis of the BEDT-TTF molecule. Donor D is calculated to hold a partial charge of $^{+}$0.5.

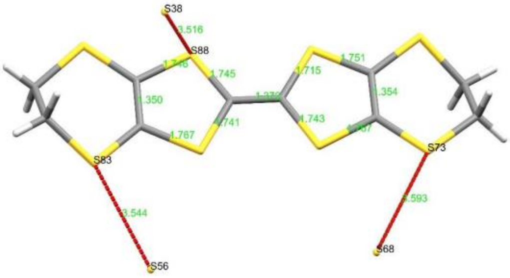

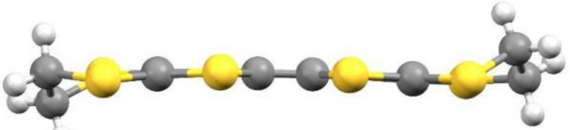

Figure 5.30 (left). CTS 5.2: Capped stick diagram of donor D. S...S contacts are shown in dotted red lines and contacts atoms are labelled in black. Contact length and central TTF bond lengths in angstroms are shown in green. Figure 5.31 (right). CTS 5.2: Side on profile view of donor D.

The gadolinium anion is coordinated by three tridentate dipicolinato ligands with Gd-O bond lengths of 2.401(1)-2.436(1) Å and Gd-N bond lengths of 2.504(1), 2.536(1) and 2.549(1) Å. Each ligand has one Gd-O bond significantly shorter (~0.03 Å) than the other, creating a slight twist through the plane of each dipicolinato moiety. The anion packing motif as viewed along the *c* axis is shown in Figure 5.32. The anion packs in enantiopure stacks, with exclusively the L enantiomer present throughout the lattice. The longest Gd-N bond length and consequently the ligand that is furthest from the coordination sphere can be seen in Figure 5.33 as the propeller that cuts across the ab plane (point to top right). This positions the complexes such that two cavities are formed between the anions and are filled by two guest molecules. The Gd…Gd distances between anions are 10.390 Å in the *a* direction and 10.948 Å in the *b* direction.

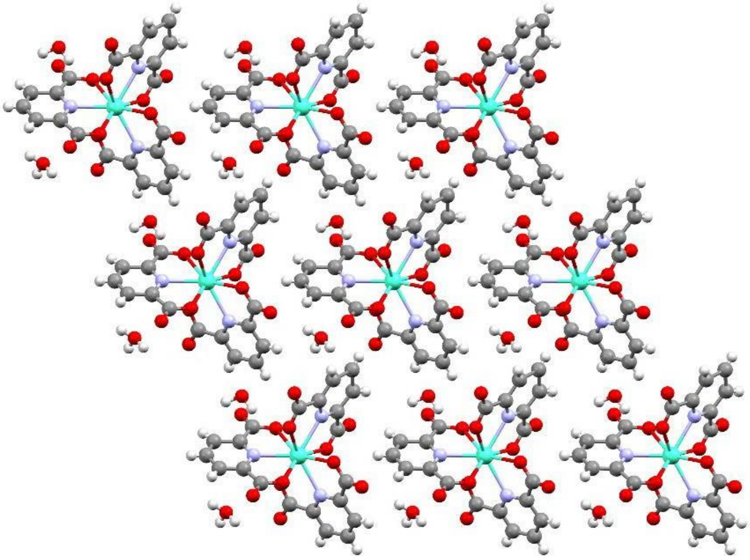

Figure 5.32. Insulating layer of CTS 5.2, including guest water and hydronium molecules. Viewed along the *c* axis.

There are a total of 19 short contacts below the sum of vdW radii between ligated oxygens and peripheral hydrogens on the surrounding donor molecules. This creates a network of hydrogen bonding running through the channel between the insulating and conducting layers. Two uncoordinated carboxylate oxygens also make a hydrogen bond with a ring hydrogen on the neighbouring anion (O48...H1051, 2.333(1) and O47...H1081, 2.479(1) Å). The two water molecules make hydrogen bonds with neighbouring donor molecules, one water with donor D (O106...H1031, 2.374(1) Å) and donor B (O106...H882, 2.618(1) Å) and the second water makes a hydrogen bond with donor B (O112...H932, 2.473 Å). Ligand three plays the largest role in stabilising the packing motif of the conducting layer as it makes a total of eight short contacts with neighbouring donor molecules, six of these between uncoordinated carboxylate oxygens and the four independent donors. The ring hydrogens of this ligand are also the atoms which take part in the inter-anion non-covalent interactions.

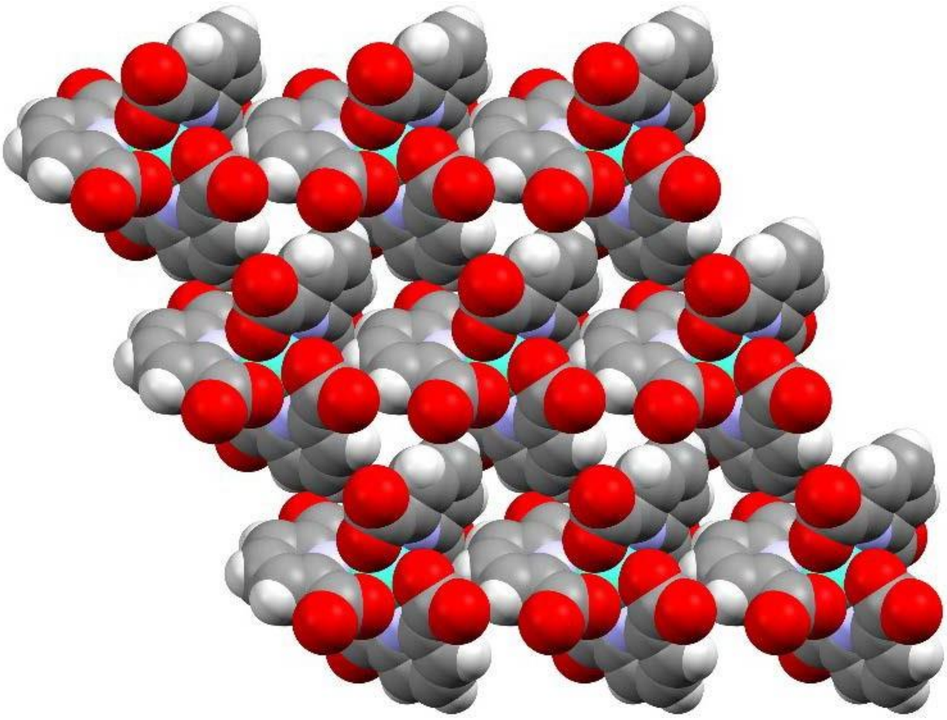

Figure 5.33. Spacefilling diagram of the chiral anionic layer in CTS 5.2. Viewed along the *c* axis. Guest molecules have been removed for clarity.

5.1.2.3 S…S Contacts

Contact	***Atom***	***Atom***	***Length / Å***
1	S2	S10	3.576(3)
2	S32	S17	3.482(4)
3	S12	S18	3.415(4)
4	S12	S20	3.536(4)
5	S9	S25	3.508(5)
6	S16	S26	3.546(3)
7	S12	S28	3.5876)
8	S3	S29	3.583(4)
9	S10	S6	3.478(5)
10	S32	S7	3.472(3)
11	S29	S9	3.593(6)

Table 5.8. Short sulphur interactions below the sum of the vdW radii (3.6 Å) for CTS 5.2

Table 5.8 above shows the length, in angstroms, of short sulphur interactions below the sum of the vdW radii (3.6 Å) for the donors present in CTS 5.2. There are eleven side-to-side S...S contacts observed that range from 3.415(4) – 3.593(6) Å).

5.1.2.4 C=C Bond Length, Charge Calculations and Raman

	A - Green	***B - Blue***	***C - Yellow***	***D - Purple***
C=C Bond Length / Å	1.357(3)	1.352(2)	1.352(3)	1.354(7)

Table 5.9. Central C=C bond lengths for independent donors present in CTS 5.2.

BEDT-TTF central C=C bond lengths suggest that all donors carry the same charge. The values are consistent with a donor charge of BEDT-TTF$^{+0.5}$.

	A – Green	***B – Blue***	***C - Yellow***	***D – Purple***
a / Å	1.357	1.352	1.352	1.355
b / Å	1.734	1.738	1.741	1.741
c / Å	1.747	1.749	1.747	1.757
d / Å	1.336	1.345	1.341	1.335
δ	0.788	0.790	0.795	0.808
Q	**0.466** (±0.1)	**0.451** (±0.1)	**0.414** (±0.1)	**0.317** (±0.1)

Table 5.10. Donor charge estimation for CTS 5.2 using Kepert *et al*. average TTF bond length calculation.

The donor charge estimations are in good agreement with the central C=C bond lengths in Table 5.10 above. The calculation for donor D is slightly lower than expected but taking into account the asymmetric unit of (BEDT-TTF)$_4$[Gd(dpa)$_3$].H$_3$O.H$_2$O it is likely that all four BEDT-TTF molecules carry a charge of $^+$0.5.

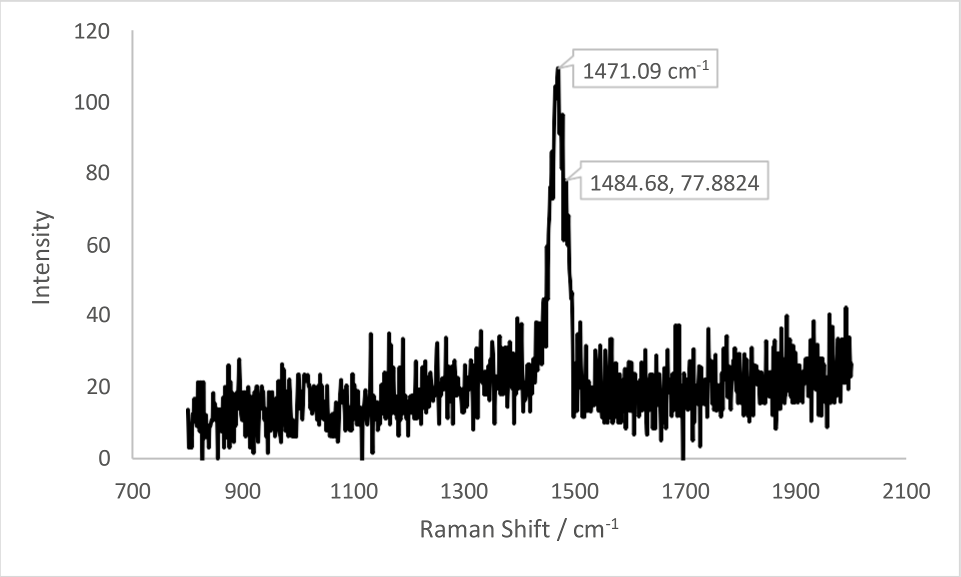

Graph 5.2. Relative intensity against Raman shift for a single crystal of CTS 5.2.

Reproducible room temperature Raman measurements were made on several single crystals of CTS 5.2. The single sharp peak indicates that only one type of BEDT-TTF cation is present. The stretching frequencies expected for BEDT-TTF$^{+0.5}$ are between 1457 – 1471 cm^{-1} and 1488 – 1498 cm^{-1} for the υ_4 (highest intensity) and υ_3 respectively. Although the spectrum is noisy, high intensity peaks between the ranges expected for BEDT-TTF$^{+0.5}$ are observed. The high and mid intensity peaks are labelled, corresponding to the υ_4 and υ_3 totally symmetrical C=C stretching modes.

5.1.2.5 Magnetic Data

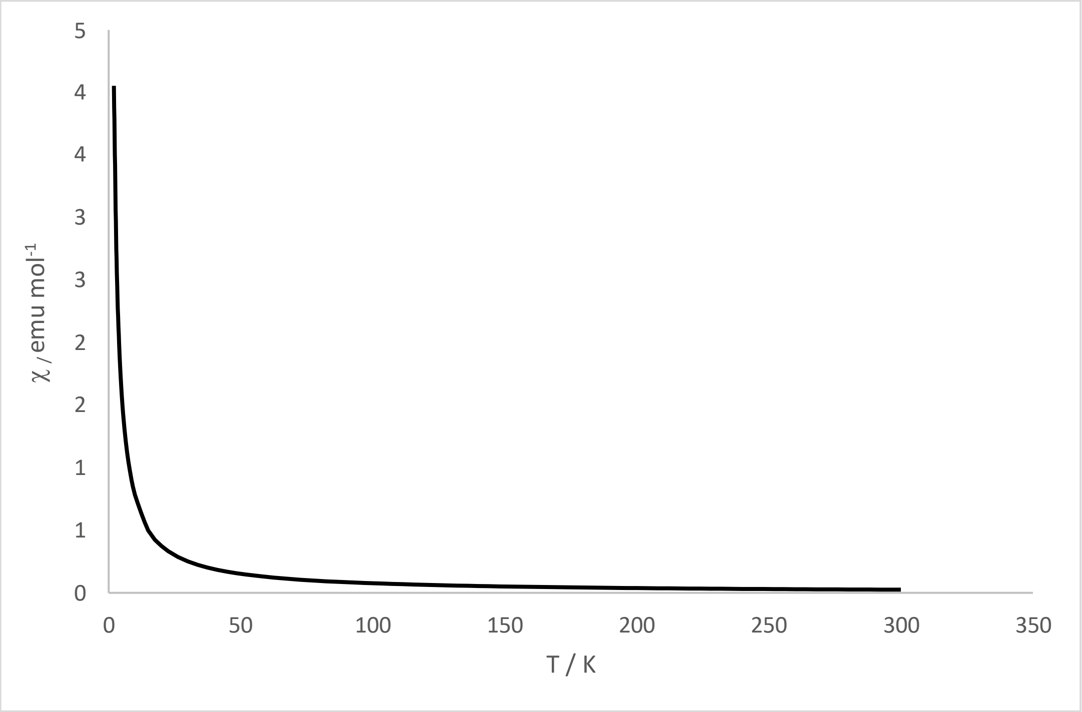

Graph 5.3. Temperature dependent magnetic susceptibility for CTS 5.2.

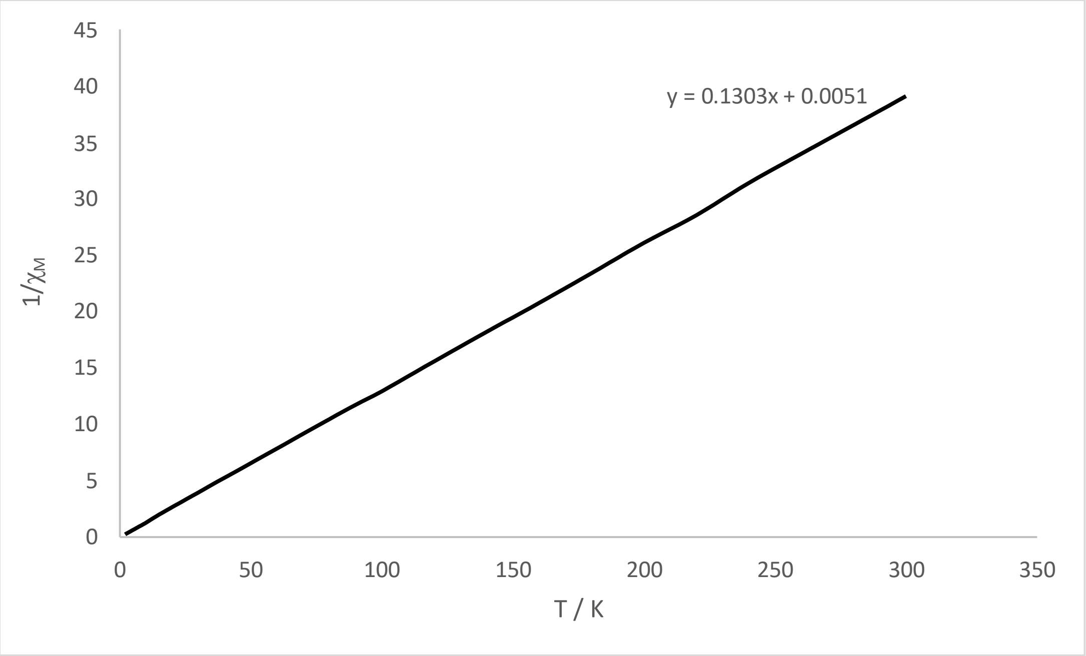

Graph 5.4. Reciprocal magnetic susceptibility against temperature for CTS 5.2.

The magnetic susceptibility data for CTS 5.2 has been fitted to the Curie-Weiss law for a simple paramagnet by Prof. H. Akutsu of Osaka University (Graph 5.3). Plotting the molar magnetic susceptibility, χ_M against temperature shows a sharp rise in magnetisation at 20 K. A plot of $1/\chi_M$ vs. Temperature (Graph 5.4) gives a straight line from which the Curie constant, 7.675 emu K mol^{-1} typical for Gd^{3+} ions (S =7/2) and Weiss constant, +0.0051 K can be calculated. A positive Weiss constant usually indicates that short-range ferromagnetic ordering is present however such a small value could be due to experimental error and hence can’t be considered evidence of short-range magnetic coupling. The strong paramagnetic signal produced by the seven unpaired electrons associated with the gadolinium centre means that detection of the magnetic behaviour present in the organic conducting layer is not possible.

5.1.2.6 Resistivity Data

Sample A

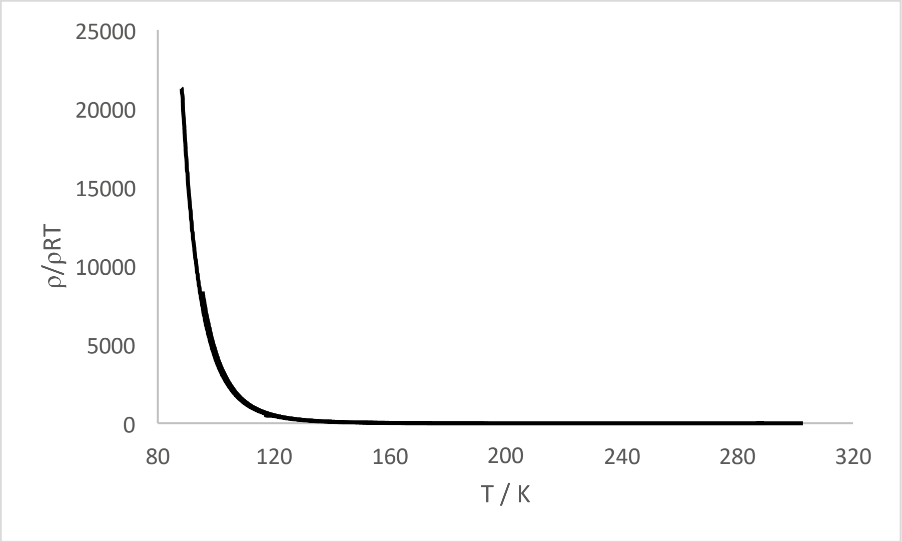

Graph 5.5. Temperature dependent resistivity for CTS 5.2 sample A.

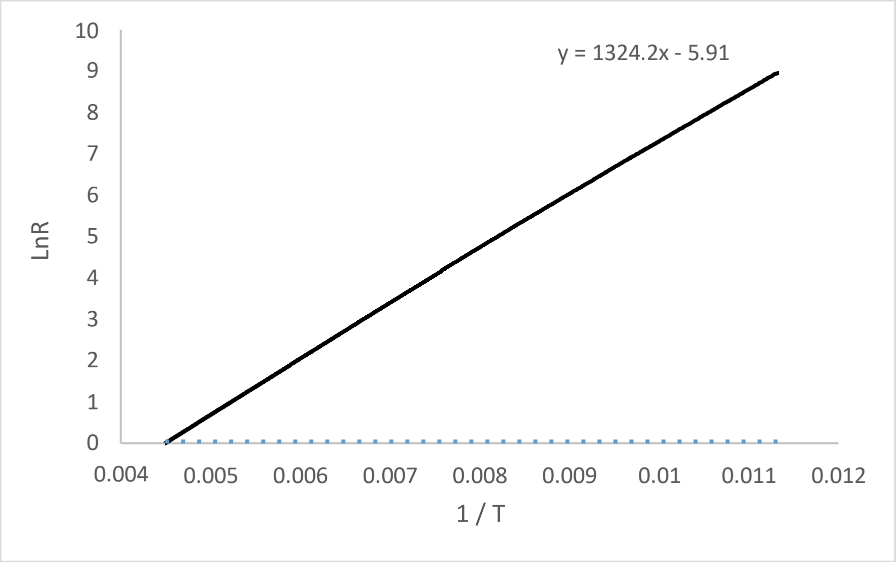

Graph 5.6. Logarithmic resistivity against reciprocal temperature for CTS 5.2 sample A.

Sample B

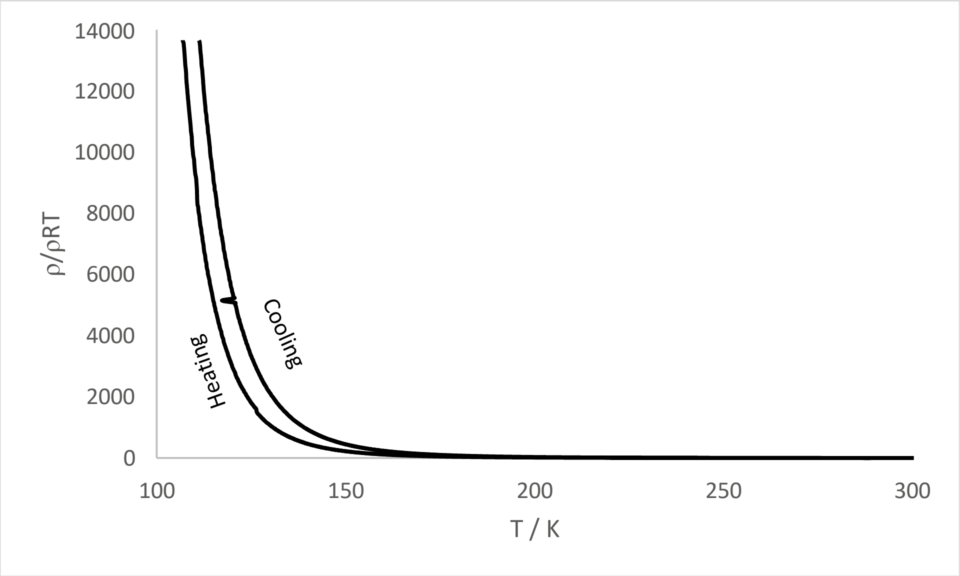

Graph 5.7. Temperature dependent resistivity of CTS 5.2 sample B.

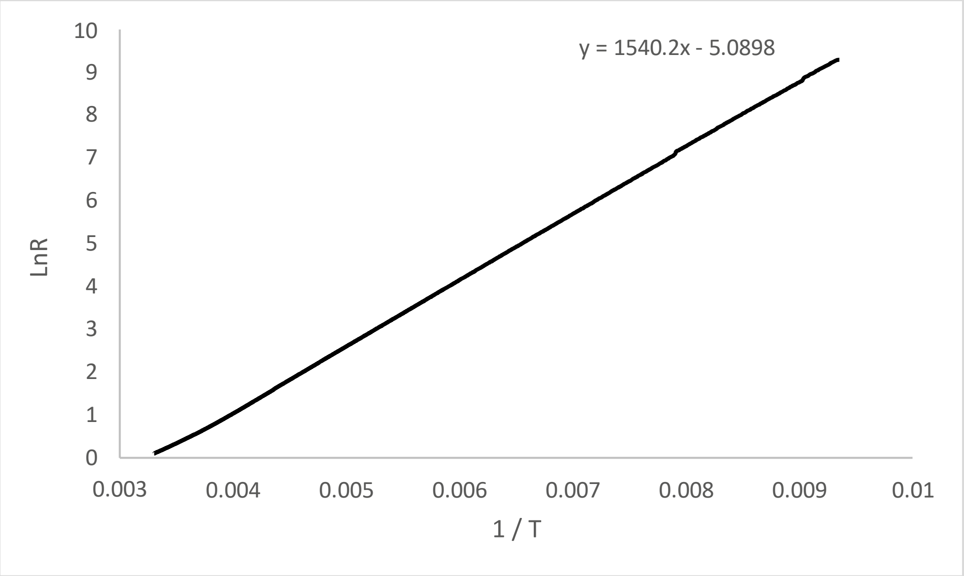

Graph 5.8. Logarithmic resistivity against reciprocal temperature for CTS 5.2 sample B.

Sample C

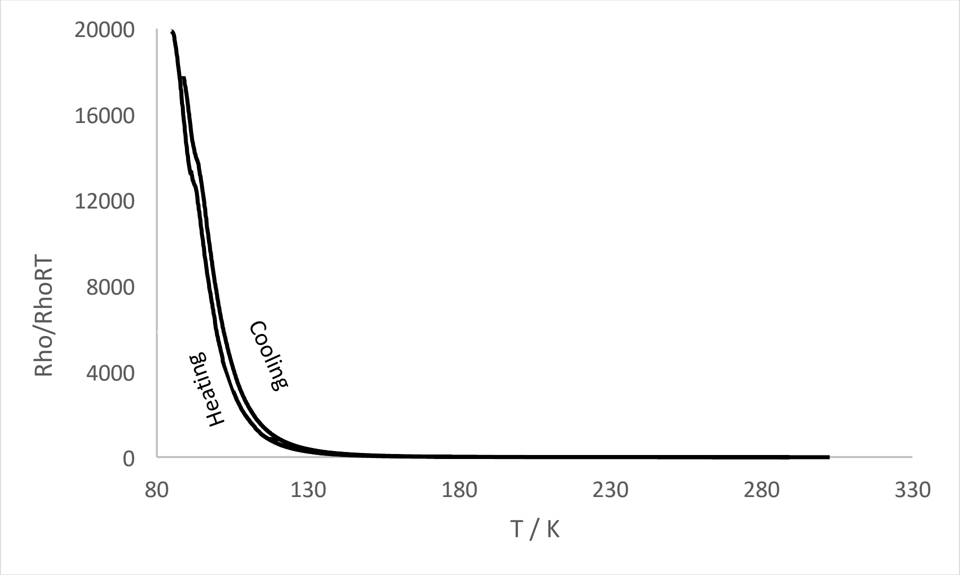

Graph 5.9. Temperature dependent resistivity for CTS 5.2 sample C.

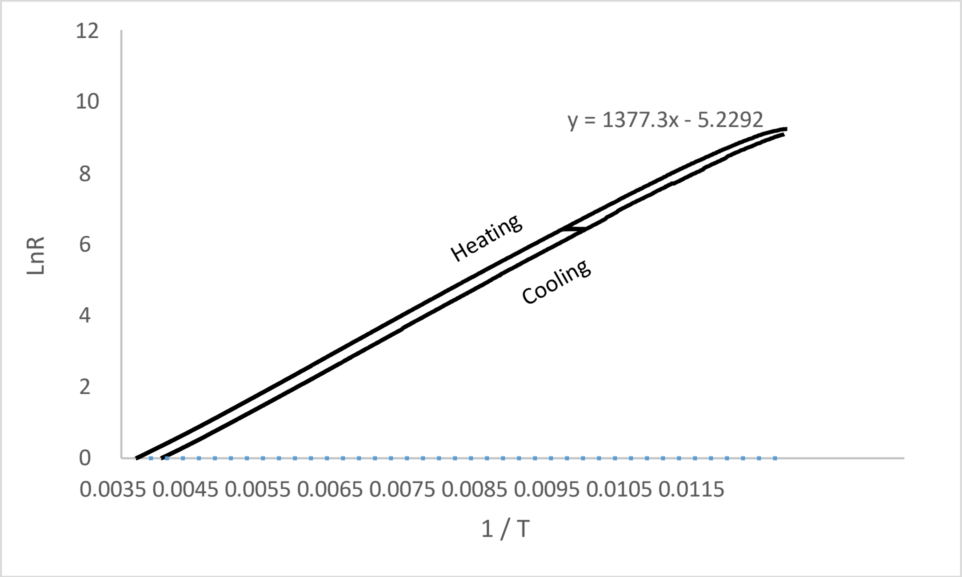

Graph 5.10. Logarithmic resistivity against reciprocal temperature for CTS 5.2 sample C.

	A	B	C
$\boldsymbol{E_a}$	0.114 eV	0.133 eV	0.119 eV
$\boldsymbol{\rho RT / \Omega cm}$	0.253	1.258	0.561

Table 5.11. Activation energy and room temperature resistivity for three single crystals (A, B and C) of CTS 5.2.

Four probe resistivity measurements were performed on three single crystals of CTS 5.2. The material exhibits semiconducting behaviour with a low room temperature resistivity. There is a small hysteresis seen in samples A and B, however the increase in activation energy between cooling and heating runs is negligible and this behaviour is likely to occur due to structural defects occurring within the crystal during the initial cooling to low temperature.

The values of activation energies for samples A and C are similar however, sample B has an activation energy much larger. This could be due to experimental error but in this case, it is possible that sample B is either the opposing enantiomer or a racemic phase.

5.2 [Ln(clo)$_3$]$^{3-}$ Anion

Chelidonic acid (4-oxo-4*H*-pyran-2,6-dicarboxylic acid) and its coordination chemistry has been investigated previously and the ligand shows a remarkable number of coordination modes[16] . When used as a tridentate ligand to produce nine-coordinate lanthanoids the two carboxylate groups and ring oxygen provide the donor atoms[17].

After chelation the phenol oxygen provides more scope for non-covalent interactions throughout crystal engineering with BEDT-TTF than the previously discussed dpa ligand. It also increases the coordination sphere of the anion which results in a completely different packing arrangement from the dpa derived charge transfer salts. Discussed in this section is one charge transfer salt of the mononuclear [Tb(clo)$_3$]$^{3-}$ anion and BEDT-TTF. The crystal structure provides the first evidence of a nine-coordinate lanthanide(III) chelidonate complex through single crystal X-ray diffraction measurements. It is also the first example of a metallic and paramagnetic BEDT-TTF charge transfer salt containing the [Tb(clo)$_3$]$^{3-}$ anion.

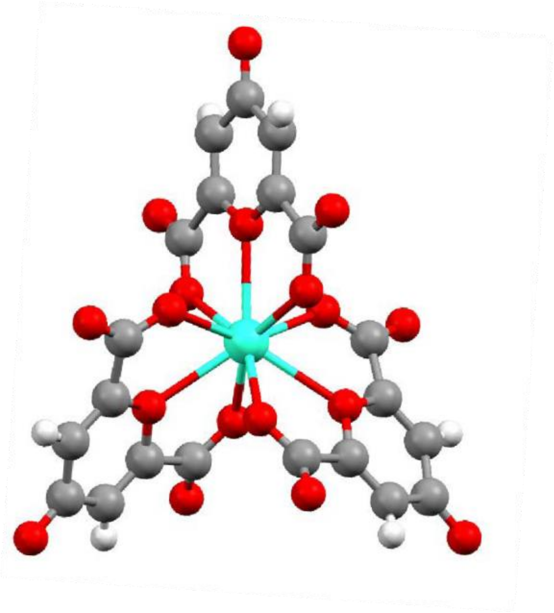

Figure 5.34. Representation of the [Tb(clo)$_3$]$^{3-}$ anion.

5.2.1 (BEDT-TTF)$_5$[Tb(clo)$_3$]

Electrocrystallisation of BEDT-TTF in the presence of Na$_3$[Tb(clo)$_3$] afforded a charge transfer salt of the title compound. Structural and physical experimental data is presented below.

5.2.1.1 Electrocrystallisation Table

Donor	**Counterion**	**Electrolyte**	**Solvent**	**Current /μA**	**Crystal Growth**	**Observation**
ET	Na$^+$	[Tb(clo)$_3$]$^{3-}$	PhCl: EtOH	0.1 – Increased to 0.5 after 1 week.	Yes – Large quantity of black hexagonal crystals collected from electrode after 4 weeks.	Crystals were of high quality, enough for X-ray structure determination and physical measurements.
ET	Na$^+$	[Tb(clo)$_3$]$^{3-}$	THF	0.2	Yes – small quantity of black hexagonal crystals collected from electrode after six weeks	Crystals were of lower quality than above such that only a matching unit cell was obtained.

Table 5.12. Electrocrystallisation table for synthesis of CTS 5.3.

Both tetrahydrofuran and chlorobenzene as electrocrystallisation solvent produced hexagonal crystals of high quality. X-ray diffraction measurements using the crystals from the chlorobenzene batch produced a structural model of lower R factor and the slightly thicker nature of the crystals meant that this batch was taken forward for charge transport and magnetic measurements. The reproducible Raman measurements and X-ray diffraction experiments from the THF batch were in agreement with the crystals grown from chlorobenzene, indicating that both batches contained the same phase.

5.2.1.2 *Crystal Structure*

α-(BEDT-TTF)$_5$[Tb(clo)$_3$]	
Formula	$C_{70}H_{46}O_{18}S_{40}Tb$
M_r/g mol^{-1}	1314.15
Temp / K	150
Radiation	Mo Kα
Wavelength	0.71073
Crystal System	Monoclinic
Space group	I2/*c*
a / Å	21.0088(5)
b / Å	11.0487(3)
c / Å	41.2486(9)
α / °	90
β / °	94.4034(19)
γ / °	90
V/Å^3	9546.36
Z	4
ρ/g cm^{-1}	1.82888
μ/cm^{-1}	1.680648
Absorption Applied	Yes
Abs. Type	Analytical
Abs. Range	0.712-0.908
Total Reflections	21000
Unique Reflections	9805
R [all data]	0.0701
R_1 [$I > 2\sigma(I)$]	0.06401
wR [all data]	0.1801
Goodness of fit	1.000
Refinement Program	SHELX
Refinement Mode	F^2
Flack Parameter	n/a

Table 5.13. X-ray data for CTS 5.3.

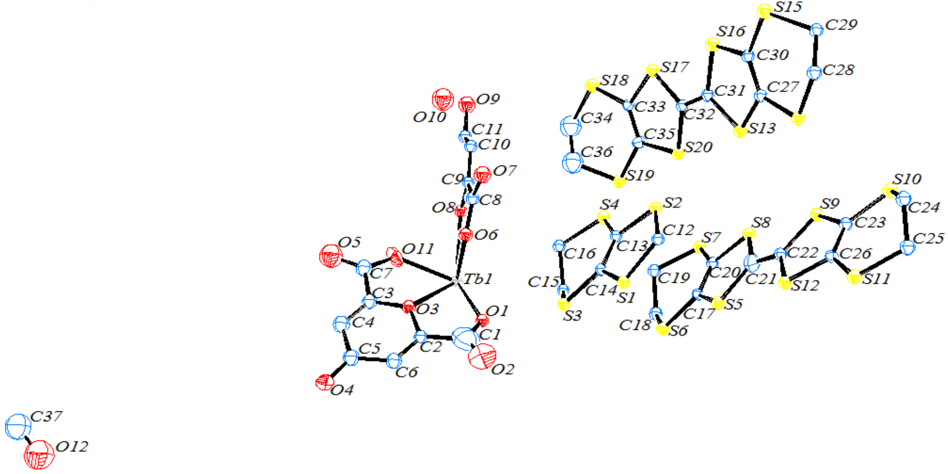

Figure 5.35. ORTEP diagram of the asymmetric unit of CTS 5.3. Thermal ellipsoids are drawn at the 50% probability level.

CTS 5.3 crystallises in the monoclinic crystal system in the space group I 2/*c*. The asymmetric unit consists of half a $[Tb(clo)_3]^{3-}$ anion, two and a half crystallographically independent donor molecules (A-C), one water molecule and an ethanol molecule. The ethanol is disordered with two possible confirmations within the unit cell. The hydroxyl groups are modelled over two partially occupied sites each of 0.5 occupancy. The donors stack in the ab plane with neighbouring stacks separated in the c direction by the insulating layer. The independent unit cell as viewed along the *b* axis is shown in Figure 5.36. Figure 5.37 is shown the layered structure of the lattice as viewed down the crystallographic *a* axis. The chiral anion is present as a racemic mixture within the lattice.

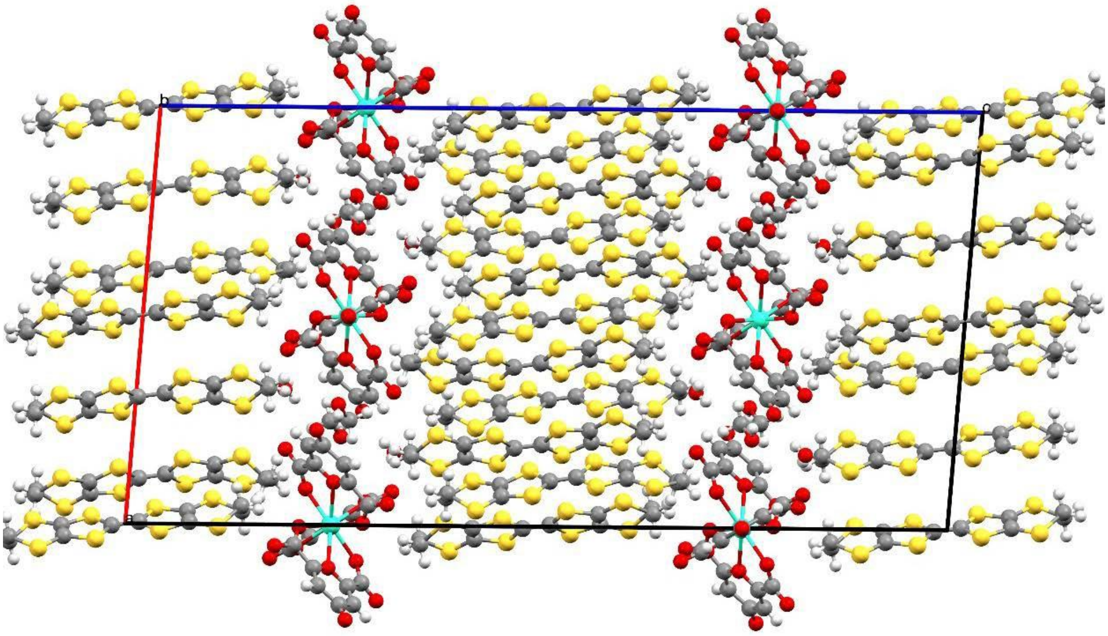

Figure 5.36. Independent unit cell of CTS 5.3.

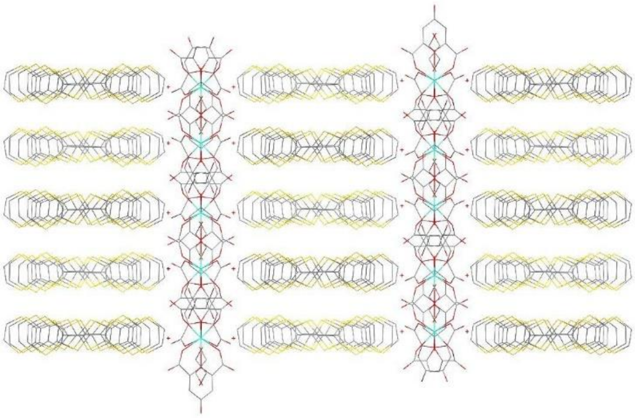

Figure 5.37. Lattice packing of CTS 5.3 viewed along the *a* axis.

The conducting layer packs in the alpha motif with a dihedral angle of ~100°. The donors form staggered columns along the a axis of CABAC:CABAC, (':' denotes the slip between staggered groups of five). Figure 5.38 below shows one layer of donor and anion, note the staggered effect caused by the non-planar arrangement of donor C creating blocks of five donors (CABAC) each flanked by an anion of differing chirality on either side. The anions also alternate between enantiomers throughout the insulating layer making each anion layer racemic and each is centred between the cationic donors ABA (black). Along the *c* direction each consecutive donor layer is rotated by an angle of ~180°, such that when one donor layer is viewed 'face on' the next is positioned 'side on' with respect to the viewer (Figure 5.38). The $^{+}1$ donors are shown in black, the neutral donors are shown in yellow, the L enantiomer of the anion is shown in purple and the D enantiomer orange.

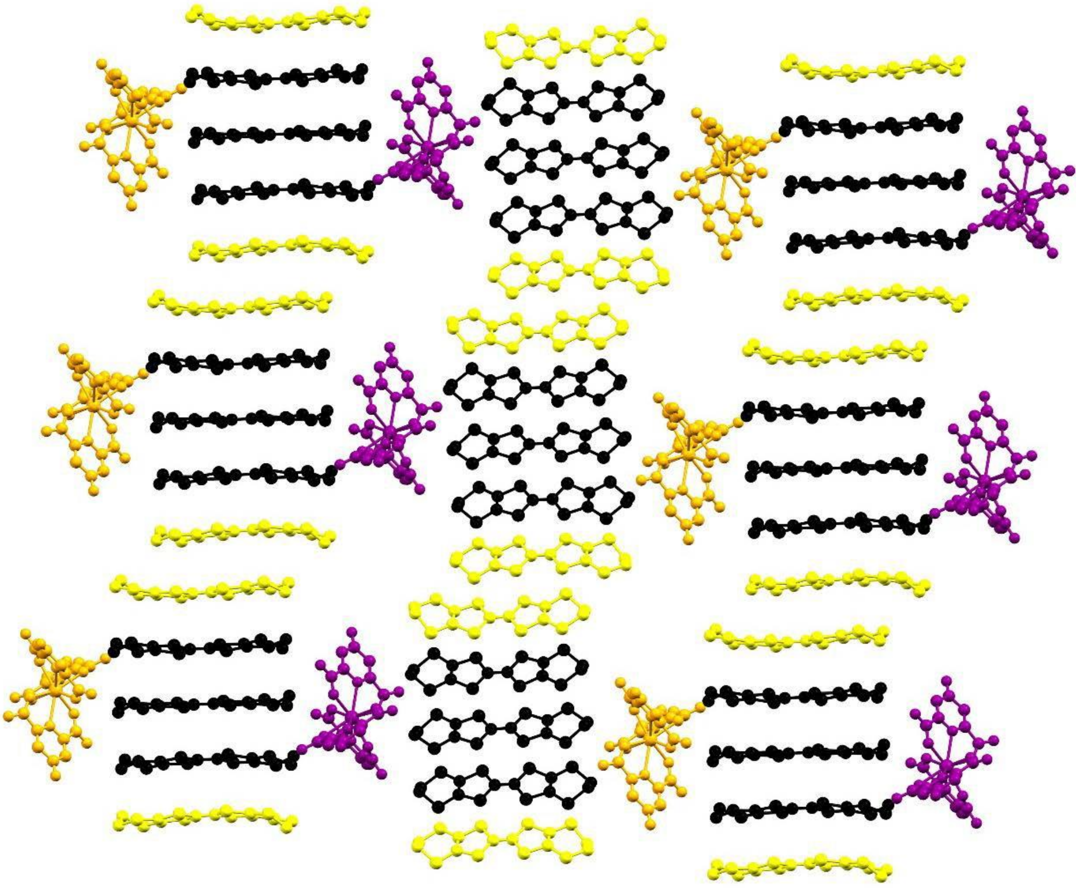

Figure 5.38. CTS 5.3: Displays rotation of neighbouring donor stacks and alternating chirality of $[Tb(clo)_3]^{3-}$ anions. The cationic and neutral donors are coloured black and yellow respectively.

Along the *b* axis each column of donors is shifted with respect to the next such that the neutral donor C pair is sandwiched either side by the two cationic donors which are stacked in an ABA fashion, producing blocks of neutral charge within the conducting plane (Figure 5.39). Consequently the charge throughout each column is $^{+}1$,$^{+}1$,$^{+}1$,0,0, $^{+}1$,$^{+}1$,$^{+}1$,0,0 at least at 150 K. Donor A forms $^{+}1$ charged stripes along the *b* axis throughout the conducting layer with neighbouring stripes alternating between blocks of neutral charge (donor C) and $^{+}1$ (donor B). Side to side S...S contacts below the sum of vdW radii (3.6 Å) are shown in blue with hanging contacts removed for clarity. There is a continuous network of sulphur interactions running along the crystallographic *ab* plane with no face-to-face contacts observed.

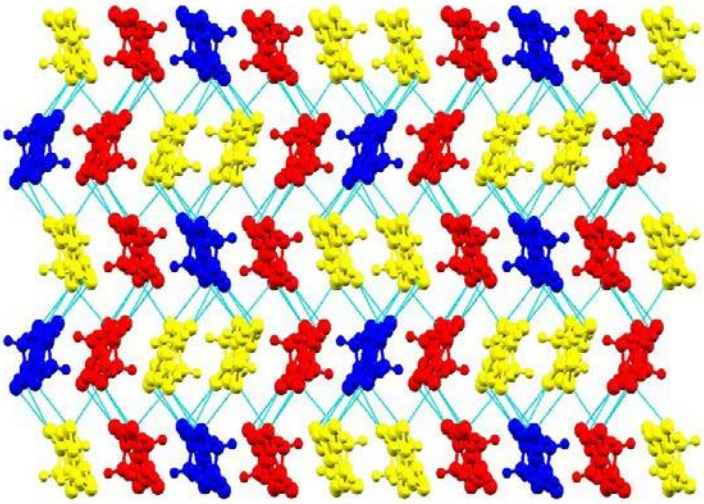

Figure 5.39. Donor packing arrangement of CTS 5.3 viewed along the *c* axis. S...S contacts below the sum of the vdW radii (3.6 Å) are shown in blue lines.

Figure 5.40 below pictures donor A, shown above in red. The dotted red lines show the short sulphur interactions below the sum of vdW radii (3.6 Å). The lengths of S...S contacts and central TTF bond lengths are also shown in green. The donor makes a total of six side-to-side S...S contacts with donors C and A in neighbouring stacks. Three 'in plane' and three 'out of plane' contacts are observed and due to the CABAC stacking of the BEDT-TTF molecules there are no contacts with donor B. The donor is in the twisted eclipsed confirmation with one methylene group displaced to a larger degree from the central axis of the molecule. The molecule is also slightly bent with the end groups tending towards donor C and away from the central donor B. Donor A is calculated to carry a charge of $^{+}1$ at 150 K.

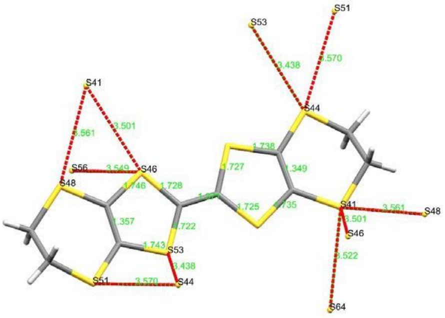

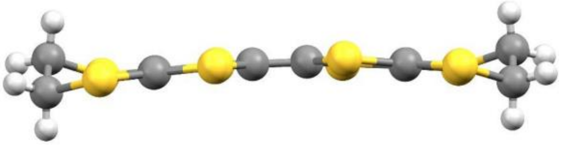

Figure 5.40 (left). CTS 5.3: Capped stick diagram of donor A. Short sulphur interactions below the sum of the vdW radii (3.6 Å) are shown in red dotted lines and contacts atoms are labelled in black. Contact length and central TTF bond lengths in angstroms are shown in green. Figure 5.41 (right). CTS 5.3: Side profile view of donor A.

Figure 5.42 below pictures donor B, shown above in blue. S...S contacts below the sum of vdW radii (3.6 Å) are shown in dotted red lines, the contact length and central TTF bond lengths are shown in green. The donor lies on an inversion centre and is totally symmetrical about the central C=C bond, it makes a total of seven side-to-side ‘out of plane’ S...S contacts per half donor, all with donor C. The donor is in the twisted eclipsed confirmation with both methylene groups displaced to the same degree from the central axis of the molecule. The central TTF portion of the molecule is completely planar until the peripheral ethylene groups. Donor B is calculated to carry a charge of $^{+}1$ at 150 K.

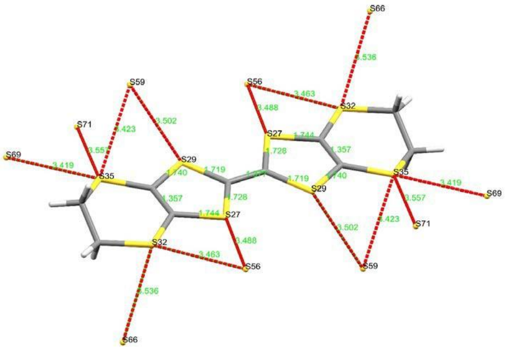

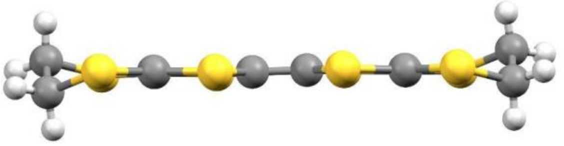

Figure 5.42 (left). CTS 5.3: Capped stick diagram of donor B. Short sulphur interactions below the sum of the vdW radii (3.6 Å) are shown in red dotted lines and contacts atoms are labelled in black. Contact length and central TTF bond lengths in angstroms are shown in green. Figure 5.43 (right). CTS 5.3: Side profile view of donor B.

Figure 5.44 below pictures donor C, shown above in yellow. Short sulphur interactions below the sum of vdW radii (3.6Å) are shown in dotted red lines, contact length and central TTF bond lengths are shown in green. The donor makes a total of nine side-to-side S...S contacts with donors A and B in neighbouring stacks. Two contacts are made with donor A above the plane of the molecule and seven are made with donor B below the plane of the molecule. The donor holds the twist confirmation at one end and the boat confirmation at the other and is heavily bent towards the boated end. This orientation of the donor causes the staggered effect seen throughout each donor column in Figure 5.39. Intermolecular contact distances also suggest that donor A and C are almost dimerised with shorter contacts observed between these two donors within each block than between donors A and B. Therefore, the planar orientation of donor B which is present in the middle of each block of five donors serves to separate the almost dimerised donors within each block. Donor C is calculated to carry a neutral charge at 150 K.

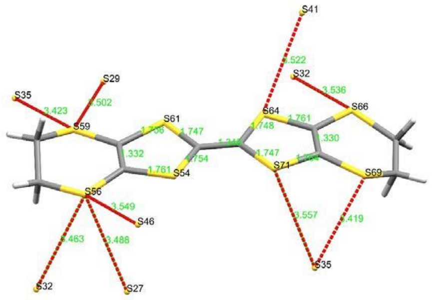

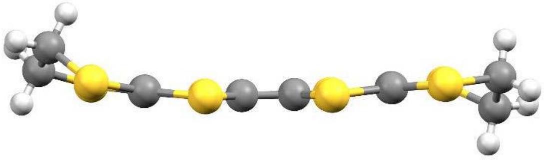

Figure 5.44 (left). CTS 5.3: Capped stick diagram of donor C. Short sulphur interactions below the sum of the vdW radii (3.6 Å) are shown in red dotted lines and contacts atoms are labelled in black. Contact length and central TTF bond lengths in angstroms are shown in green. Figure 5.45 (right). CTS 5.3: Side profile view of donor C.

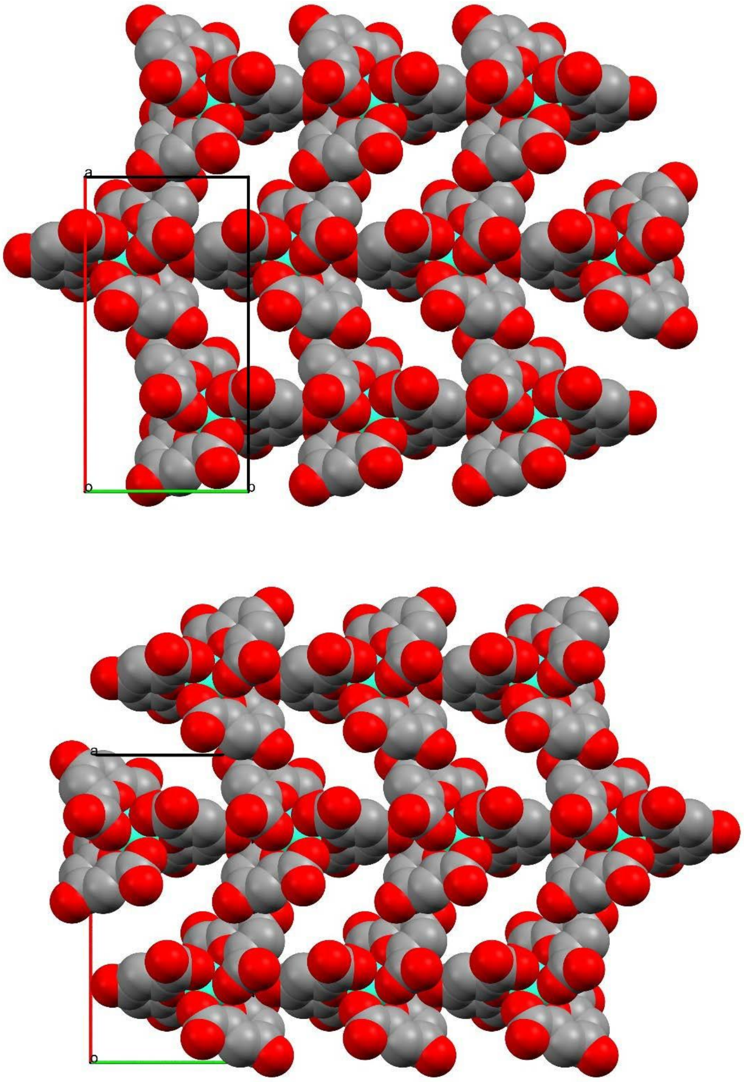

Figure 5.46. Displays two separate insulating layers alternating along the *c* axis in CTS 5.3.

Shown above in Figure 5.46 are two separate anion layers alternating along the crystallographic *c* axis. The anions pack in racemic stacks alternating between enantiomers along the crystallographic *b* axis, therefore enantiopure rows propagate through the *a* direction. Also present in the insulating layer is a water molecule and a disordered guest ethanol molecule which are hydrogen bonded throughout.

Figure 5.47 below shows the crystal packing arrangement as viewed along the *c* axis with molecules and complexes coloured to their symmetry equivalence. It is clear to see that each anion is centred around the charged BEDT-TTF molecules with the central Tb atom of each complex directly in the centre of donor B and almost no overlap with the neutral donor C.

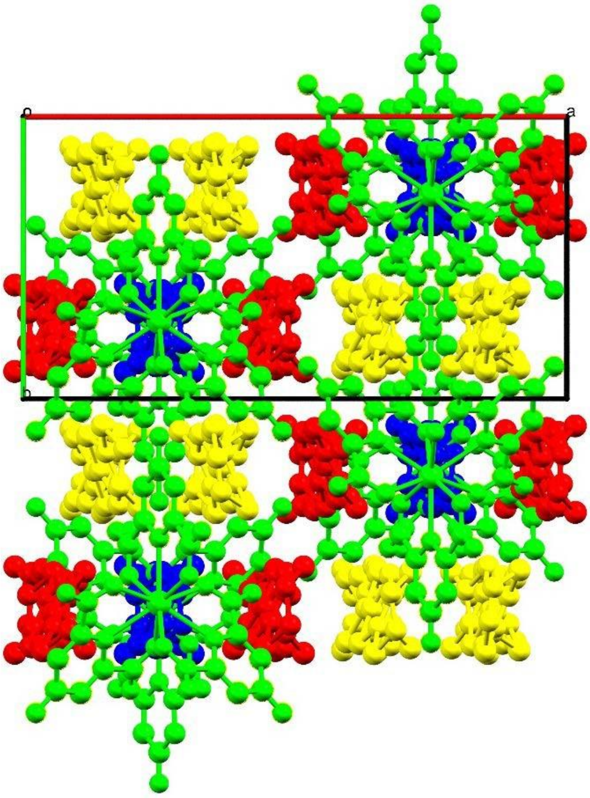

Figure 5.47. Lattice packing viewed along the *c* axis. Donors are coloured according to symmetry equivalence and anions are coloured green. Hydrogens are omitted for clarity.

Tb-O bond lengths are 2.567 – 2.589 Å. Due to the Tb centre lying directly on a 2-fold symmetry axis, only half of the complex is present in the asymmetric unit and one and a half of the chelidonate ligands are generated by symmetry to produce the complete anion in the crystal structure. The ligand with the longest Tb-O bond length (2.589 Å) and consequently has the carboxylate oxygens positioned further outside of the coordination sphere and both oxygens make a hydrogen bond with neighbouring donor A (O6...H14, 2.505 and O7...H14, 2.525 Å). O7 also makes a hydrogen bond with the guest water (O7...H19, 2.136 Å), shown below in Figure 5.48. There is likely to be a network of hydrogen bonding throughout the insulating layer between anion and guest molecules.

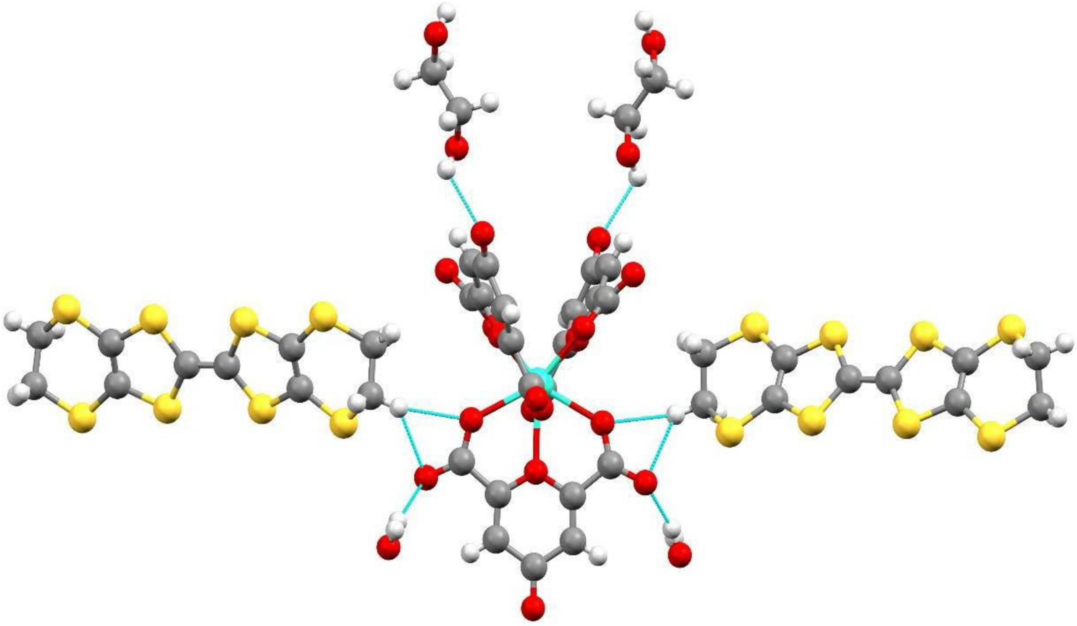

Figure 5.48. Geometry of hydrogen bonding interactions between anion and donors.

The phenol oxygen of ligand one and two makes a hydrogen bond with a methylene hydrogen of donor A (O19...H491, 2.583(1) Å) and methylene hydrogen of donor C in the same stack (O19...H672, 2.652 Å). One uncoordinated carboxylate oxygen makes a hydrogen bond with a methylene hydrogen of donor C (O15...H571, 2.647(1) Å) while the other makes a hydrogen bond with three ethylene hydrogens of neighbouring donor A (O9...H431, 2.577 and H432, 2.529 and H422, 2.573 Å). The uncoordinated carboxylate oxygen on ligand three makes two hydrogen bonds with donor A and B respectively (O21...H581, 2.476(1) and H502, 2.547(1) Å) while the coordinated oxygen makes a hydrogen bond with the same atom (O2...H502, 2.502). The short contacts produce a ring-like network around ligand three of each Tb complex. No short contacts are observed between anion and donor B. Figure 5.49 below shows some of the hydrogen bonding network present between donor and anion.

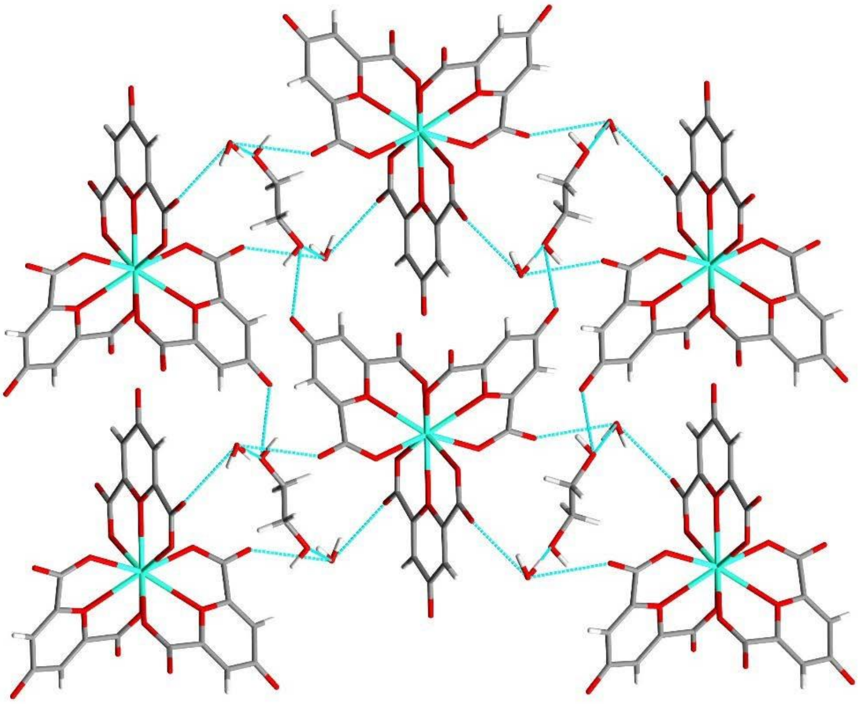

Figure 5.49. Possible hydrogen bonding interactions between anion, water and disordered guest EtOH molecule in CTS 5.3.

5.2.1.3 S…S Contacts

Contact	*Atom*	*Atom*	*Length / Å*
1	S3	S18	3.493(11)
2	S2	S15	3.513(13)
3	S4	S15	3.380(12)
4	S4	S19	3.386(14)
5	S4	S20	3.519(13)
6	S1	S14	3.455(12)
7	S3	S14	3.423(12)
8	S6	S9	3.441(11)
9	S6	S10	3.515(9)
10	S11	S7	3.572(12)
11	S12	S7	3.423(11)
12	S6	S17	3.490(13)
13	S6	S18	3.593(11)
14	S9	S14	3.496(12)

Table 5.14. Short sulphur interactions below the sum of the vdW radii (3.6 Å) in CTS 5.3.

Table 5.14 above shows the length, in angstroms, of short sulphur interactions below the sum of the vdW radii (3.6 Å) for the donors present in CTS 5.3. There are thirteen side-to-side contacts observed that range from 3.419(1) – 3.570(1) Å).

5.2.1.4 C=C Bond Length, Charge Calculations and Raman

	A - Red	***B - Blue***	***C - Yellow***
C=C Bond Length / Å	1.377(3)	1.370(6)	1.347(8)

Table 5.15. Central BEDT-TTF C=C bond lengths for donors present in CTS 5.3.

Central BEDT-TTF C=C bond lengths suggest that donors A and B carry equal charges of $^+1$, while donor C is neutral.

	A - Red	***B - Blue***	***C – Yellow***
a / Å	1.371	1.377	1.348
b / Å	1.726	1.724	1.749
c / Å	1.741	1.742	1.761
d / Å	1.353	1.357	1.331
δ	0.743	0.732	0.831
Q	**0.802** (± 0.1)	**0.884** (± 0.1)	**0.145** (± 0.1)

Table 5.16. BEDT-TTF Charge estimations for independent donors present in CTS 5.3.

Charge estimations are in good agreement with the central C=C bond lengths, indicating that there is a charge localisation between donors A and B while donor C is neutral. This satisfies the formula of $(BEDT\text{-}TTF)_5[Tb(clo)_3].EtOH.H_2O$ consisting of two molecules of donor A and C and one molecule of donor B, producing a net charge of $^+3$ which satisfies the trivalency of the $[Tb(clo)_3]^{3-}$ anion.

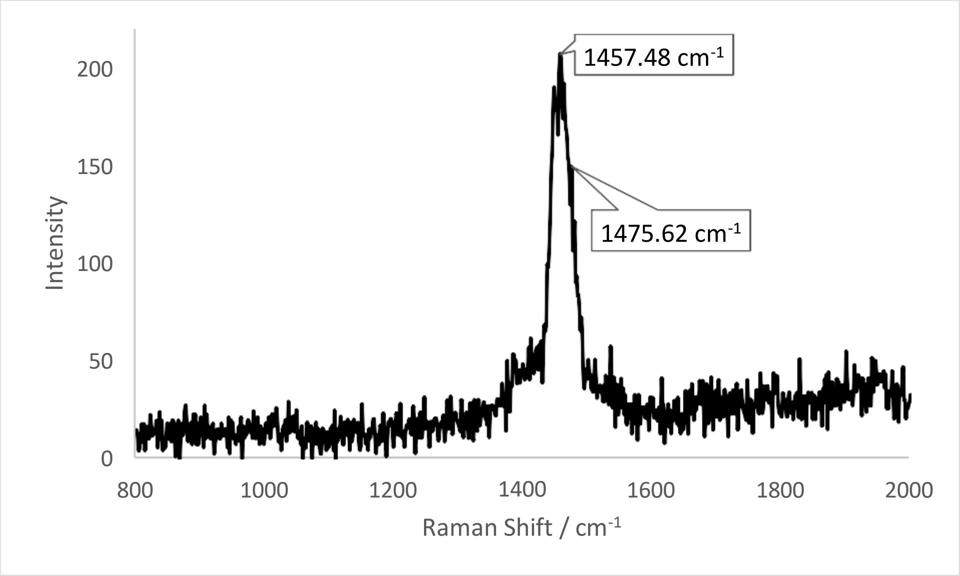

Graph 5.11. Relative intensity against Raman shift for a single crystal of CTS 5.3.

Reproducible room temperature Raman measurements were made on several single crystals of CTS 5.3. The data is in contrast to the proposed charge localisation suggested by the central C=C bond lengths and the charge estimations, as the single sharp peak in the Raman spectra indicates that all three donors carry equal charges. It is of note that the X-ray data was collected at low temperature so it is possible that at room temperature the salt selects an equally charge distributed state. Assuming this is the case, to satisfy the charge of the $Tb(clo)_3^{3-}$ anion each donor must carry a charge of $^{+}2/3$. The stretching frequencies reported for 3:2 BEDT-TTF radical cation salts range from 1460 - 1468 cm^{-1} and 1476 – 1487 cm^{-1} for the υ_4 and υ_3 modes respectively. The high and mid intensity peaks are labelled corresponding to the υ_4 and υ_3 modes, these are in good agreement with the proposal of an equal charge distribution within CTS 5.3 at room temperature where each donor carries a charge of $^{+}2/3$

5.2.1.5 Resistivity Data

Reproducible temperature dependent resistivity measurements were made on two single crystals of CTS 5.3. Both samples showed metallic behaviour from 300 K down to 170-180 K where a sharp upturn is observed indicating a transition to an insulating state at low temperatures. Room temperature resistivities are within the expected range for metallic conductors, shown below in Table 5.17.

CTS 5.3	***Sample A***	***Sample B***
ρRT / Ohm.mm	0.590	0.082
ρ_{min} / K	178	183

Table 5.17. Room temperature resistivity and resistivity minimum for two samples of CTS 5.3.

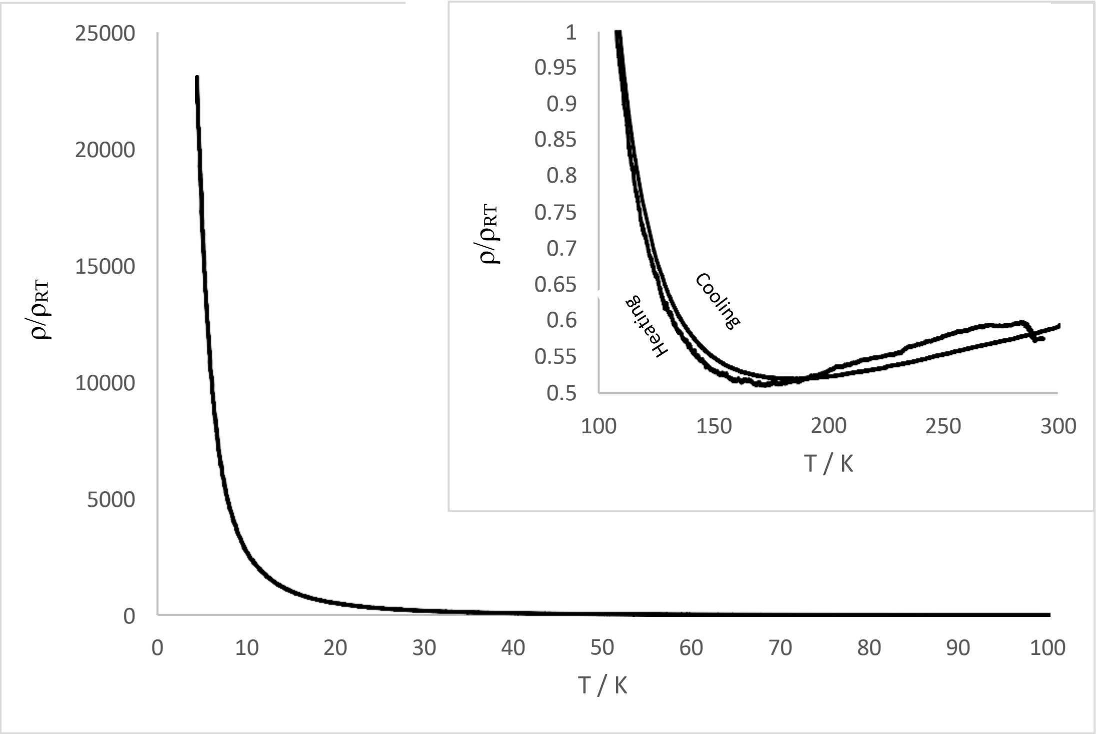

Graph 5.12. Temperature dependent resistivity profile for CTS 5.3 sample A. (Inset): Temperature dependent resistivity from 300 – 100 K for CTS 5.3 sample A.

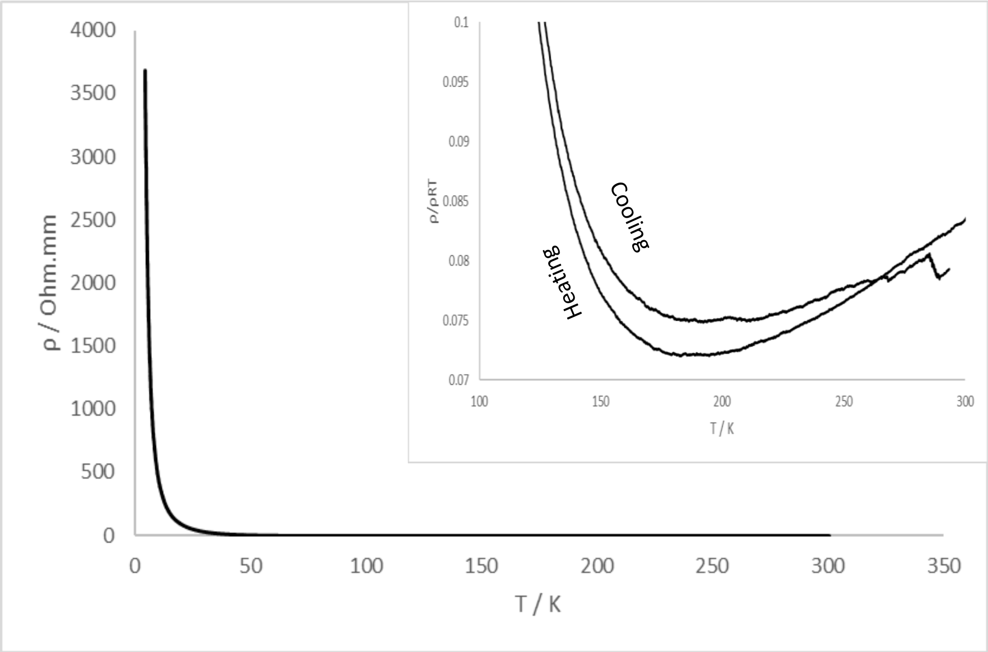

Graph 5.13. Temperature dependent resistivity profile for CTS 5.3 sample B. (Inset): Temperature dependent resistivity from 300 – 100 K for CTS 5.3 sample B.

5.3 Chapter Conclusions

Reported in this chapter are the first examples of racemic and chiral charge transfer salts containing lanthanide anions. An isostructural pair of racemic charge transfer salts containing the racemic [Ln(dpa)$_3$]$^{3-}$ anion (Ln = La, Gd) produces alpha''' packing arrangement of the donor molecules. However crystal quality meant that full physical characterisation was not possible.

Spontaneous resolution of the racemic [Gd(dpa)$_3$]$^{3-}$ anion in the presence of BEDT-TTF and bromobenzene has produced a chiral, paramagnetic, semi-conducting charge transfer salt crystallising in the non-centrosymmetric triclinic space group P 1. This result is compelling as it proves not only the propensity for the [Ln(dpa)$_3$]$^{3-}$ anion to form chiral materials in the solid state but also the observation of three properties within the same lattice – chirality, paramagnetism and semi-conductivity. This material is therefore a promising candidate to take forward in the investigation of chiral conducting materials.

The third material discussed in this chapter is the first evidence of a tris-lanthanum chelidonate anion via X-ray diffraction measurements. It is also the first metallic charge transfer salt containing a racemic lanthanide anion. The BEDT-TTF molecules adopt the common alpha packing motif and choose a fractional ground state at room temperature where the three independent donors carry a charge of $^{+}2/3$ – leading to metallic properties. As temperature is decreased to around 170 K the BEDT-TTF molecules then adopt a $^{+}1$, 0, $^{+}1$ charge ordered state. Localisation of the conducting electrons produces insulating properties below this temperature.

5.4 References

1. G. M. Whitesides and D. W. Lewis, *J. Am. Chem. Soc.* 1970, **92**, 6979; G. M. Whitesides and D. W. Lewis, *J. Am. Chem. Soc.* 1971, **93**, 5914.
2. L. Pu, *Chem. Rev.* 1998, **98**, 2405.
3. S. Faulkner, S. J. A. Pope and B. P. Burton-Pye, *Appl. Spectr. Rev.*, 2005, **40**, 1.
4. S. D. Bennett, B. A. Core, M. P. Blake, S. J. A. Pope, P. Mountford and B. D. Ward, *Dalton Trans.*, 2014, **43**, 5871.
5. W. J. Evans, D. G. Giarikos and N. T. Allen, *Macromolecules*, 2003, **36(12)**, 4256.
6. A. Lennartson and M. Håkansson, *CrystEngComm*, 2009, **11**, 1979.
7. M. Tamura, F. Matsuzaki, Y. Nishio, K. Kajita, T. Kitazawa. H. Mori and S. Tanaka, *Synth. Met.*, 1999, **102**, 16.
8. Y. N. Shvachko, D. V. Starichenko, A. V. Korolyov and N. D. Kushch, *Synth. Met.*, 2008, **158**, 315.
9. S. Ueki, T, Nogami, T. Ishida and M. Tamura, *Mol. Cryst. Liq. Cryst.*, 2006, **455**, 129.
10. J. Albertsson, *Acta Chem. Scand.*, 1972, **26**, 1005.
11. C. Reinhard and H. U. Gudel, *Inorg. Chem.*, 2002, **41**, 1048.
12. K-L. Hou, F-Y. Bai, Y-H. Xing, Y-Z. Cao, D-M. Wei and S-Y. Niu, *J. Inorg. Organomet. Polym.*, 2011, **21**, 213.
13. N. Hojnik, M. Kristl, G. Ferk, A. Golobic, M. Turel, Z. Jaglicic and M. Drofenik, *J. Coord. Chem.*, 2016, **69(9)**, 1484.
14. P. A. Brayshaw, J-C. G. Buenzli, P. Froidevaux, J. M. Harrowfield, Y. Kim and A. N. Sobolev,

Inorg. Chem,**.** 1995, **34**, 2068.

15. P. Guionneau, C. J. Kepert, D. Chasseau, M. R. Truter and P. Day, *Synth. Met*., 1997, **86**, 1973.
16. A. Belén Lago, R. Carballo, N. Fernàndez-Hermida and E. M. Vázquez-López *CrystEngComm*, 2011, **13**, 941.
17. C.-M. Liu, J. Xiong, D.-Q. Zhang, B.-W. Wang and D.-B. Zhu, *RSC Adv*., 2015, **5**, 104854.

Chapter 6: Racemic Metal Trisoxalate Charge Transfer Salts

The synthesis of β’’-$(BEDT\text{-}TTF)_4[(H_3O)Fe(C_2O_4)_3]$.benzonitrile and the subsequent observation of both paramagnetism and superconductivity in this material prompted a huge amount of research centred around the combination of magnetism and conductivity in the same lattice. In the last 20 years a large family of isostructural salts have been prepared by changing either the guest solvent or the metal centre (Fe, Cr, Ga and Ru)[1-5].

Small changes in formula within this family has produced a variety of different structural phases including ferromagnetic metals, antiferromagnetic semiconductors and a proton-conducting metal. Despite extensive research on this family of tris(oxalate)metallate salts and until very recently, only the above superconducting phase was known. A new ambient pressure superconductor was reported recently within this research group containing a novel superlattice β’’-$(BEDT\text{-}TTF)_2[(H_2O)(NH_4)_2Rh(C_2O_4)_3]$.18-crown-6[6].

Reported in this chapter are the next two isostructural salts in this series of new ambient pressure superconductors. Produced by substituting the metal centre for Cr and Ir. The Ir salt produced crystals that were too thin for bulk and single crystal physical measurements, however a structure of low R factor was obtained confirming that it is isostructural to the above Rh salt. The Cr analogue produced large needle crystals that were of high quality. Such that full physical characterisation was possible and Shubnikov-de Haas oscillations in the resistivity under applied magnetic field was observed.

6.1 β”-$(BEDT\text{-}TTF)_2[(H_2O)(NH_4)_2M(C_2O_4)_3]$.18-crown-6 (M = Cr or Ir)

Two isostructural salts of the title compound were produced through electrocrystallisation experiments using either chromium or iridium tris(oxalate), BEDT-TTF and crown ether. Previously an isostructural salt containing $[Rh(C_2O_4)_3]^{3-}$ has been reported, showing ambient pressure superconductivity and a superlattice containing $[Rh(C_2O_4)_3]^{3-}$, BEDT-TTF and 18-crown-6[5]. The chromium analogue showed ambient pressure superconductivity akin to the previously reported Rhodium salt[7]. The iridium crystals however, were too small for resistivity and magnetoresistance measurements.

6.1.1 Electrocrystallisation Table

Donor	Counterion	Electrolyte	Solvent	Current /µA	Crystal Growth	Observation
ET	NH_3^+	$[Cr(C_2O_4)_3]^{3-}$	TCB : PhCOMe : EtOH 10 : 10 : 1	1.0	Yes	Large quantity of thick black needles were collected from the electrode after 21 days.
ET	NH_3^+	$[Cr(C_2O_4)_3]^{3-}$	TCB : PhCOMe : EtOH 9 : 9 : 2	1.0	Yes	Large quantity of thin black needles were collected from the electrode after 21 days.
ET	NH_3^+	$[Ir(C_2O_4)_3]^{3-}$	TCB : PhCOMe : EtOH 10 : 10 : 1	1.0	Yes	Small quantity of thin brown needles were collected from the electrode after 28 days.

Table 6.1. Electrocrystallisation table for CTS 6.1 and 6.2.

The concentration of crown ether within the electrocrystallisation environment is thought to be integral to the formation of high quality crystals. Different concentrations of 18-c-6 were used when attempting to grow samples of CTS 6.1 (Cr) and 6.2 (Ir), it was found that 250 mg of crown ether along with 20 ml of the solvent mixture shown in table 6.1 above produce crystals of highest integrity (TCB = 1,2,4-trichlorobenzene and PhCOMe = acetophenone).

6.1.2 Crystal Structure

β''-(BEDT-TTF)$_2$[(H$_2$O)(NH$_4$)$_2$M(C$_2$O$_4$)$_3$].18-crown-6		
Formula	$C_{38}H_{50}O_{19}S_{16}N_2Cr$	$C_{38}H_{50}O_{19}S_{16}N_2Ir$
M_r/g mol^{-1}	1403.77	1544.0
Temp / K	110	110
Radiation	Mo Kα	Mo Kα
Wavelength	0.7107	0.7107
Crystal System	Triclinic	Triclinic
Space group	P-*1*	P-*1*
a / Å	10.2565(6)	10.3115(3)
b / Å	11.1039(7)	11.1855(4)
c / Å	27.3786(15)	27.1250(7)
α / °	86.474(6)	86.213(6)
β / °	82.734(6)	82.827(6)
γ / °	64.165(5)	64.215(5)
V/Å^3	2783.8(3)	2794.78(18)
Z	2	2
ρ/g cm^{-1}	1.675	1.835
μ/cm^{-1}	8.774	30.646
Absorption Applied	Yes	Yes
Abs. Type	Multi-scan	Multi-scan
Abs. Range	0.752 – 1.000	1.000-1.000
Total Reflections	26682	26988
Unique Reflections	12672	12712
R [all data]	0.0971	0.0634
R_1 [$I > 2\sigma(I)$]	0.0718	0.0465
wR [all data]	0.1951	0.1089
Goodness of fit	1.104	1.056
Refinement Program	SHELX	SHELX
Refinement Mode	F	F
Flack Parameter	n/a	n/a

Table 6.2. X-ray data for CTS 6.1 and 6.1.

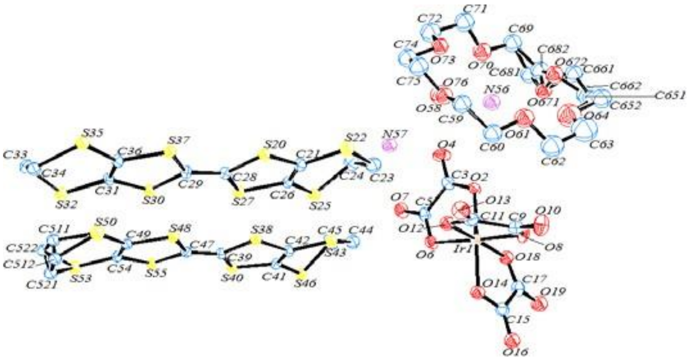

Figure 6.1. ORTEP diagram of the asymmetric unit of CTS 6.2. Displacement ellipsoids are drawn at the 50% probability level. Hydrogens are omitted for clarity.

CTS 6.1 and 6.2 are isostructural and crystallise in the triclinic space group P-*1*. The asymmetric unit consists of two crystallographically independent BEDT-TTF molecules, two NH_4^+, one H_2O, one $M(C_2O_4)_3^{3-}$ and one 18-crown-6 molecule. The two donors A(green) and B (blue) are both calculated to carry a charge of $^{+}0.5$ and stack in the β'' motif through the *ab* plane with neighbouring stacks separated in the *c* direction by the insulating layer. The independent unit cell as viewed along the crystallographic *b* axis is shown below in Figure 6.2. The chiral anion is present as a racemic mixture throughout the lattice with the crystal structure built up of successive layers of β"-BEDT-TTF (layer A), Λ-$(NH_4)M(C_2O_4)_3$ (layer B), $(H_2O)(NH_4)$18-crown-6 (layer C), and Δ-$(NH_4)M(C_2O_4)_3$ (layer D) giving an ABCDABCDA… pattern along the crystallographic *c* axis. Of the two structures, the iridium phase (CTS 6.2) refined to a lower R factor, therefore unless stated in the figure captions all figures are rendered from the iridium structure.

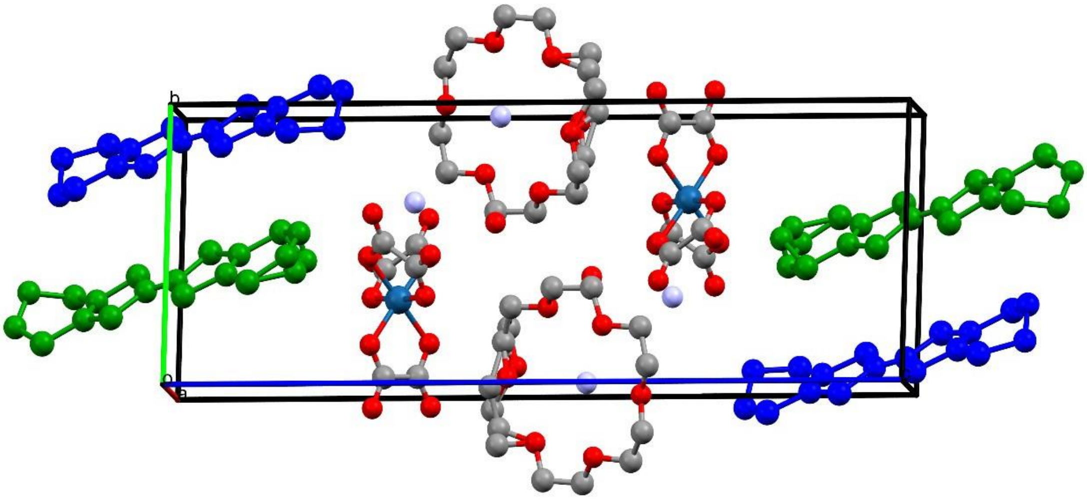

Figure 6.2. Unit cell of CTS 6.2 viewed along the crystallographic *b* axis. Donors are coloured according to symmetry equivalence.

The layered structure of CTS 6.1 and 6.2 is shown in Figure 6.3. There is static disorder present in one ethylene group of donor A and two methylene carbons and an ether oxygen on the crown ether molecule. These are all modelled as two partially occupied sites with occupancy competitively refined. The BEDT-TTF molecules pack in the β'' motif (Figure 6.4) with the characteristic network of short S...S contacts below the sum of the van der waals radii (<3.6 Å), all of which are side-to-side between donor molecules, the contact lengths are shown below in Table 6.3. The reader is directed overleaf to Figure 6.4 which shows the β'' packing motif with S...S contacts shown in light blue lines.

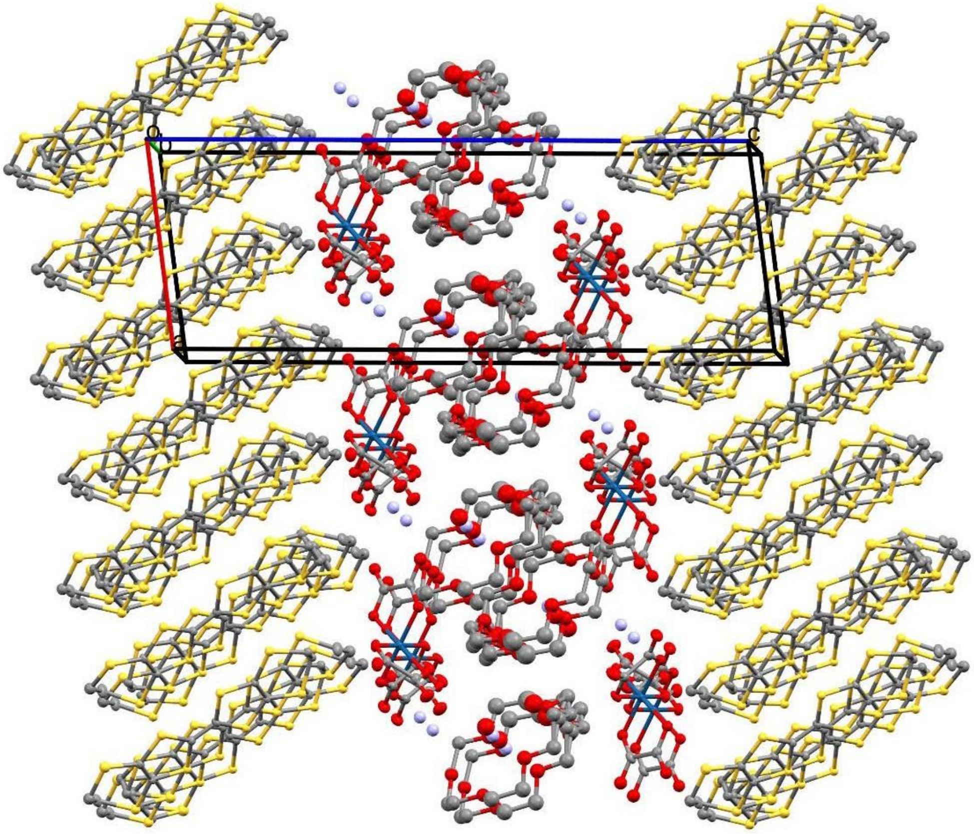

Figure 6.3. Layered structure of CTS 6.2. Of note is the width of the insulating layer.

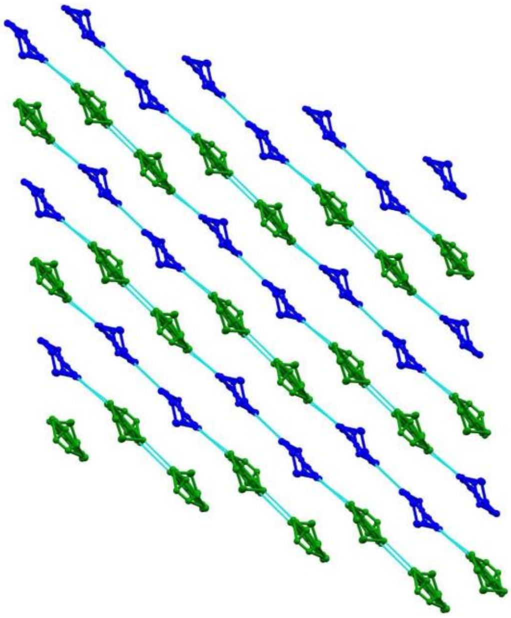

Figure 6.4. Beta'' packing motif of donors in CTS 6.2. Short sulphur interactions are shown in light blue lines. Hanging contacts are removed and hydrogens omitted for clarity.

The insulating layer forms stacks in the *ab* plane in a BCD arrangement as described above, with a layer of 18-crown-6 molecules sandwiched either side by the anion stacks. The anion layer contains $M(C_2O_4)_3^{3-}$ and NH_4^+ adopting the familiar hexagonal packing found in the paramagnetic superconducting series β”-(BEDT-TTF)$_4$[(A)M(C_2O_4)$_3$].Guest. Each layer contains only a single enantiomer of $M(C_2O_4)_3^{3-}$ with the adjacent layer containing exclusively the opposite enantiomer. In contrast to previous β’’ salts there is a layer of 18-crown-6 molecules sandwiched between the two anion layers. This produces an insulating layer of considerable width when compared to other β’’ superconductors. The crown ether molecules protrude into the hexagonal cavity of the anion layer on only one side and this side alternates between crown ethers as they stack through the *a* direction (Figure 6.5). Figure 6.6 shows the crown ether molecules occupying the hexagonal cavity formed by the packing arrangement of the trisoxalate anions.

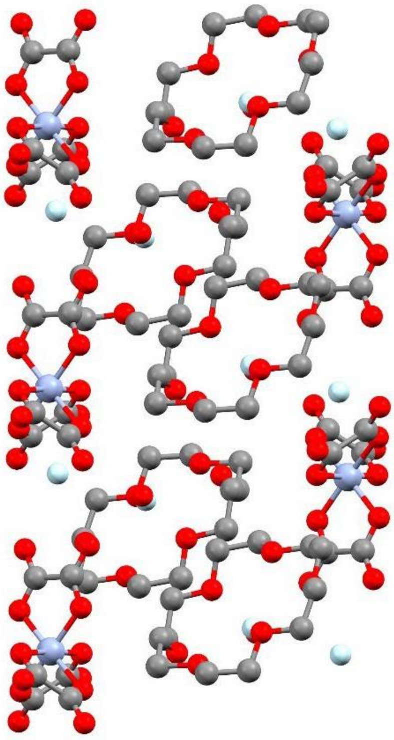

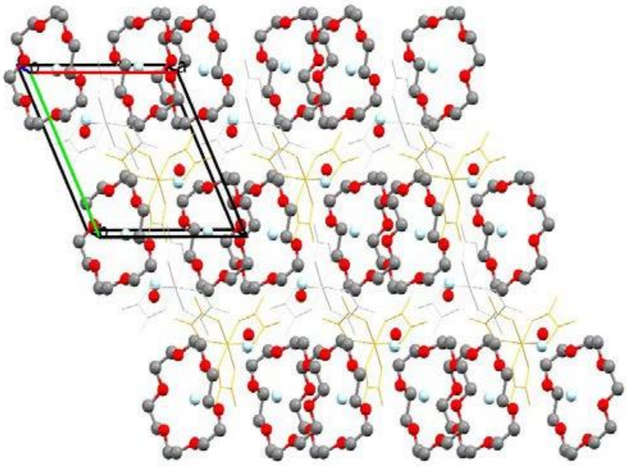

Figure 6.5 (Left). Insulating layer of CTS 6.2 viewed along the *b* axis. Crown ether molecules are sandwiched either side by trisoxalate and ammonium molecules.

Figure 6.6 (Right). Insulating layer of CTS 6.2. Crown ether molecules occupy the hexagonal cavity left by the packing arrangement of the trisoxalate molecules.

Figure 6.7 below pictures donor A, shown above in green. Short sulphur interactions below the sum of vdW radii (3.6 Å) are shown in dotted red lines, contacts length and central TTF bond lengths are shown in green. The donor makes a total of eight ‘in plane’ side-to-side S...S contacts with neighbouring BEDT-TTF molecules. The central TTF portion of the donor is planar while one end is in the boat confirmation and the disordered ethylene group on the opposite end is in the sofa confirmation. Donor A is calculated to carry a charge of $^{+}$0.5.

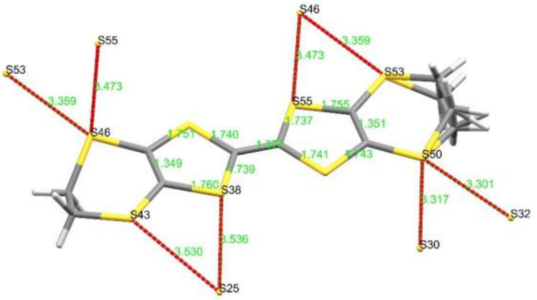

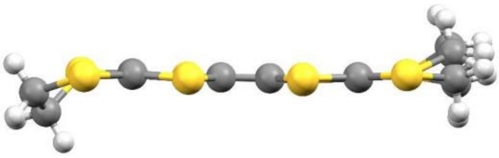

Figure 6.7 (left). CTS 6.2: Donor A with S...S contacts drawn in red and contact atoms labelled in black. Contact length and central TTF bond lengths are shown in green. Figure 6.8 (right). CTS 6.2: Side on profile view of donor A.

Figure 6.9 below shows donor B, pictured above in blue. Short sulphur interactions below the sum of vdW radii (< 3.6 Å) are shown in dotted red lines, contacts length and central TTF bond lengths are shown in green. The donor makes a total of six ‘in plane’ side-to-side S...S contacts with neighbouring BEDT-TTF molecules. The terminal ethylene group on one side of the donor is in the sofa confirmation while the other is in the twist confirmation. Donor B is calculated to have a charge of +0.5.

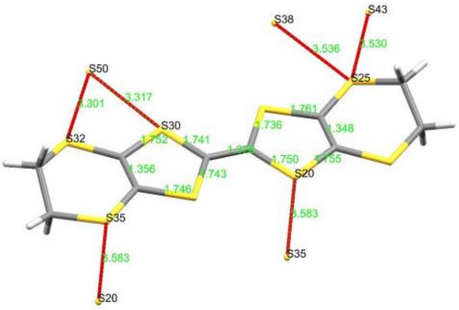

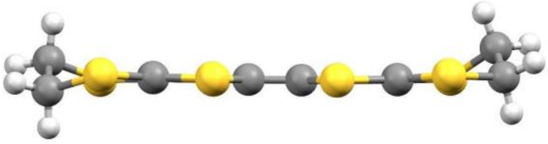

Figure 6.9 (left). CTS 6.2: Donor B with S...S contacts drawn in red and contact atoms labelled in black. Contact length and central TTF bond lengths are shown in green. Figure 6.10 (right). CTS 6.2: Side on profile view of donor B.

The hexagonal cavities have side-to-side distances and hexagonal sides slightly smaller than the distance observed for both the previously published isostructural Rh salt and also the β''-(BEDT-TTF)$_2$[(H$_3$O)Fe(C$_2$O$_4$)$_3$].halobezene series.

Each ether oxygen makes a short contact with the NH_4^+ molecule in the crown ether layer, placing the cation in the centre of the ring (Figure 6.11). Three O-H contacts (O61...HH56A, 2.014(1), O67...H56D, 2.027(1) and O73...H56C, 2.087(1) Å) and three O-N contacts (O58...N56, 2.896(1), O64...N56, 2.848(1) and O73...N56, 2.876(1) Å). The fourth hydrogen on the ammonium cation makes a short contact with a carboxylate oxygen in the anion layer (O4...H56B, 1.955(1) Å).

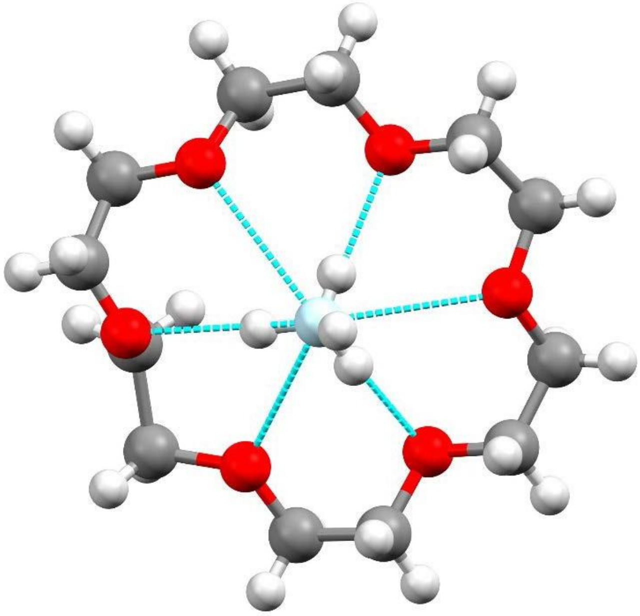

Figure 6.11. Light blue dotted lines show ether oxygen and ammonium short contacts in CTS 6.2.

Each uncoordinated carboxylate oxygen on the anion makes a short contact with the NH_4^+ molecule present in the anion layer (Figure 6.12). The Nitrogen atom making only one contact in Figure 6.12 below is the ammonium cation that is present in the crown ether layer. Three O-N contacts (O10...N57, 3.025(1), O19...N57, 3.047(1) and O4...N57, 2.922(1) Å) and three O-H contacts (O16...H57C, 2.065(1), O13...H57A, 2.215(1) and O7...H57D, 2.173(1) Å) are observed.

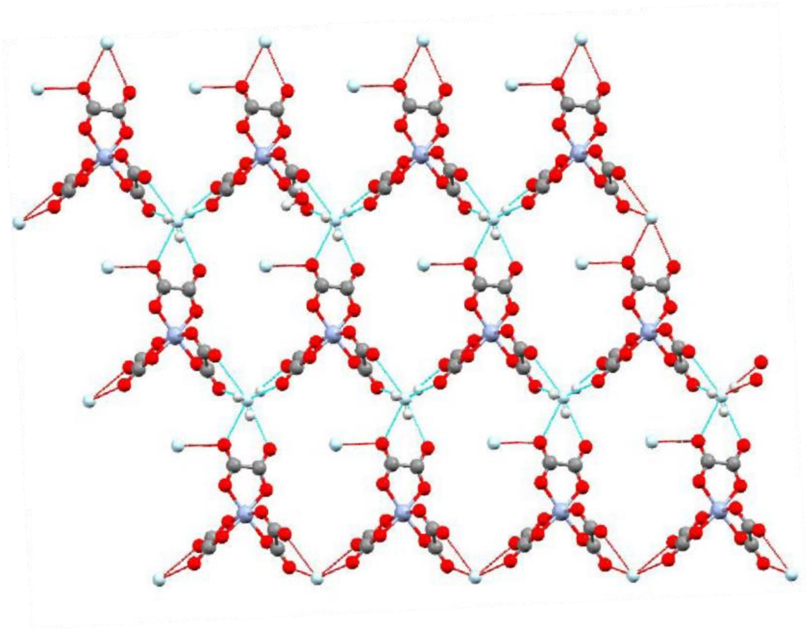

Figure 6.12. Short contacts between ammonium cations and uncoordinated carboxylate oxygens in CTS 6.2. Completed contacts are shown in light blue lines, hanging contacts are shown in red lines.

6.1.3 S…S Contacts

			Cr	***Ir***
Contact	***Atom***	***Atom***	***Length / Å***	***Length / Å***
1	S20	S35	3.540(2)	3.583(2)
2	S25	S38	3.550(3)	3.536(3)
3	S25	S43	3.521(4)	3.530(4)
4	S30	S50	3.284(3)	3.317(3)
5	S32	S50	3.246(3)	3.301(2)
6	S46	S53	3.333(3)	3.359(2)
7	S46	S55	3.453(2)	3.473(2)

Table 6.3. Short sulphur interactions present in CTS 6.1 and 6.2.

Table 6.3 above shows the length, in angstroms, of short sulphur interactions below the sum of the vdW radii (3.6 Å) for the two independent donors present in CTS 6.1 and 6.2. There are seven side-to-side contacts observed for each salt respectively that range from 3.246 – 3.550 Å (CTS 6.1) and 3.301 – 3.583 Å (CTS 6.2). Due to the difference in size of the metal centres the S...S contacts are slightly shorter in the chromium salt.

6.1.4 C=C Bond Length and Charge Calculations

	Cr		***Ir***	
	A - Green	***B - Blue***	***A - Green***	***B - Blue***
C=C Bond Length / Å	1.370(7)	1.375(7)	1.374(6)	1.379(7)

Table 6.4. Central BEDT-TTF C=C bond lengths in CTS 6.1 and 6.2.

Central BEDT-TTF C=C bond lengths are shown above in table 6.4. The donors in each salt have similar bond lengths indicating that both independent BEDT-TTF molecules carry the same charge. The bond lengths are consistent with BEDT-TTF$^{+0.5}$ cations.

	Cr		***Ir***	
	A - Green	***B - Blue***	***A - Green***	***B - Blue***
a / Å	1.370	1.370	1.374	1.378
b / Å	1.740	1.744	1.739	1.743
c / Å	1.757	1.756	1.752	1.754
d / Å	1.349	1.346	1.350	1.352
δ	0.778	0.784	0.767	0.767
Q	**0.541** (±0.1)	**0.496** (±0.1)	**0.623** (±0.1)	**0.623** (±0.1)

Table 6.5. Charge estimations according to Kepert *et al.*[8] average TTF bond length calculations for CTS 6.1 and 6.2.

BEDT-TTF charge estimations suggest that the two independent donors in each salt carry a charge of $^{+}$0.5. This is in agreement with the central C=C bond lengths displayed above and also the stoichiometry of the salts. A cumulative charge of $^{+}$1 in the donor layer along with the presence of two monovalent ammonium cations satisfies the trivalency of the $M(C_2O_4)_3^{3-}$ anion.

6.1.5 Charge Transport, Magnetotransport and Magnetic Properties of CTS 6.1

Due to the extreme thinness of CTS 6.2 crystals, only CTS 6.1 was taken forward for bulk magnetic and single crystal physical characterisation. Initial four probe temperature dependent resistivity measurements indicated that the material was metallic down to 5 K. Magnetic and magnetotransport measurements were performed by Professor Hiroki Akutsu and Shusako Imajo of Osaka University on several single crystals of CTS 6.1. The material was of high quality and the superconducting critical parameters were defined along with the observation of Shubnikov de-haas oscillations[7].

6.1.6 Magnetic Data

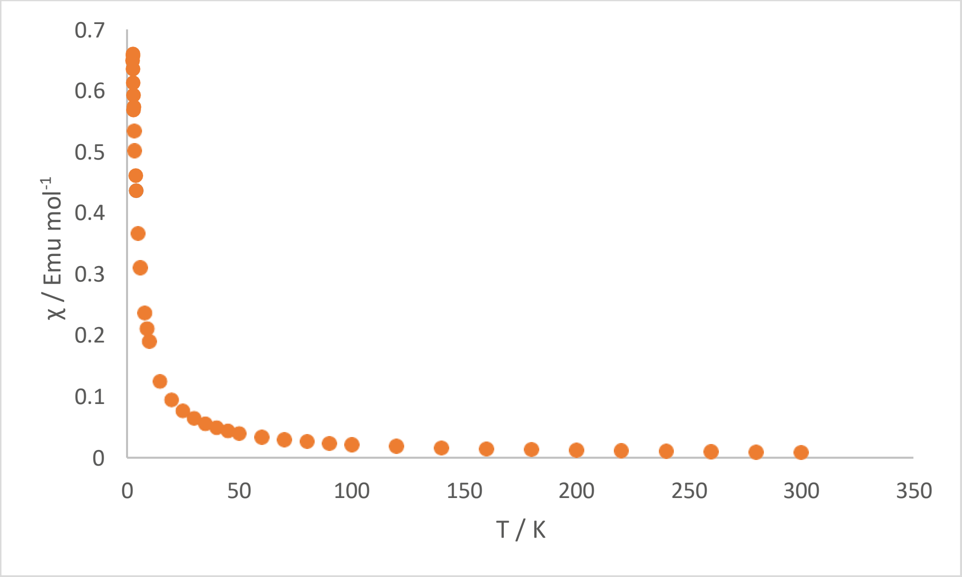

Graph 6.1. Temperature dependent magnetic susceptibility of CTS 6.1.

Initial magnetic susceptibility measurements at a constant applied field of 0.1T on randomly orientated polycrystalline sample of CTS 6.1 can be fitted by the Curie-Weiss law of a paramagnet from 2-300 K, where a Curie constant of 1.895 emu K mol^{-1} typical for Cr^{3+} ion (S = 3/2) and Weiss constant of 0.17 K (5-300 K) is observed. The small negative value for the Weiss constant indicates that there is no cooperative interaction between neighbouring Cr ions.

Further magnetic susceptibility measurements at a constant applied field of 2G (Graph 6.2 overleaf) produced a graph in which the paramagnetic contribution of the metal centres was suppressed and the onset of a Meissner signal was observed from the conducting phase, indicating the transition from a metallic to a diamagnetic superconducting state. The initial T_C from the MT curve below was estimated to be between 2.5 – 2.6 K.

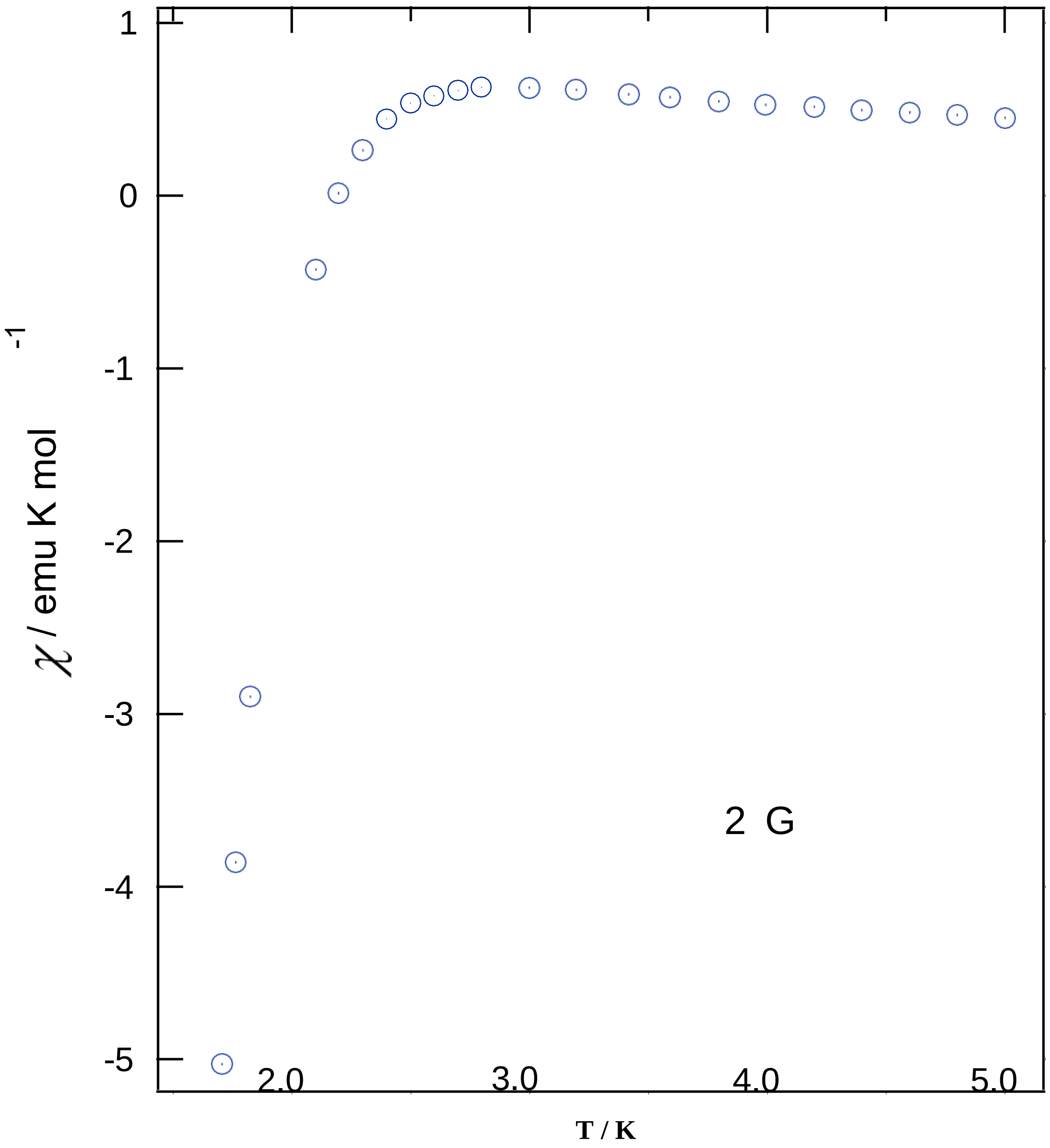

Graph 6.2. Temperature dependent magnetic susceptibility of CTS 6.2 at a constant applied field of 2G. A strong Meissner signal is observed at around 2.5 K indicating the shift to a diamagnetic superconducting state.

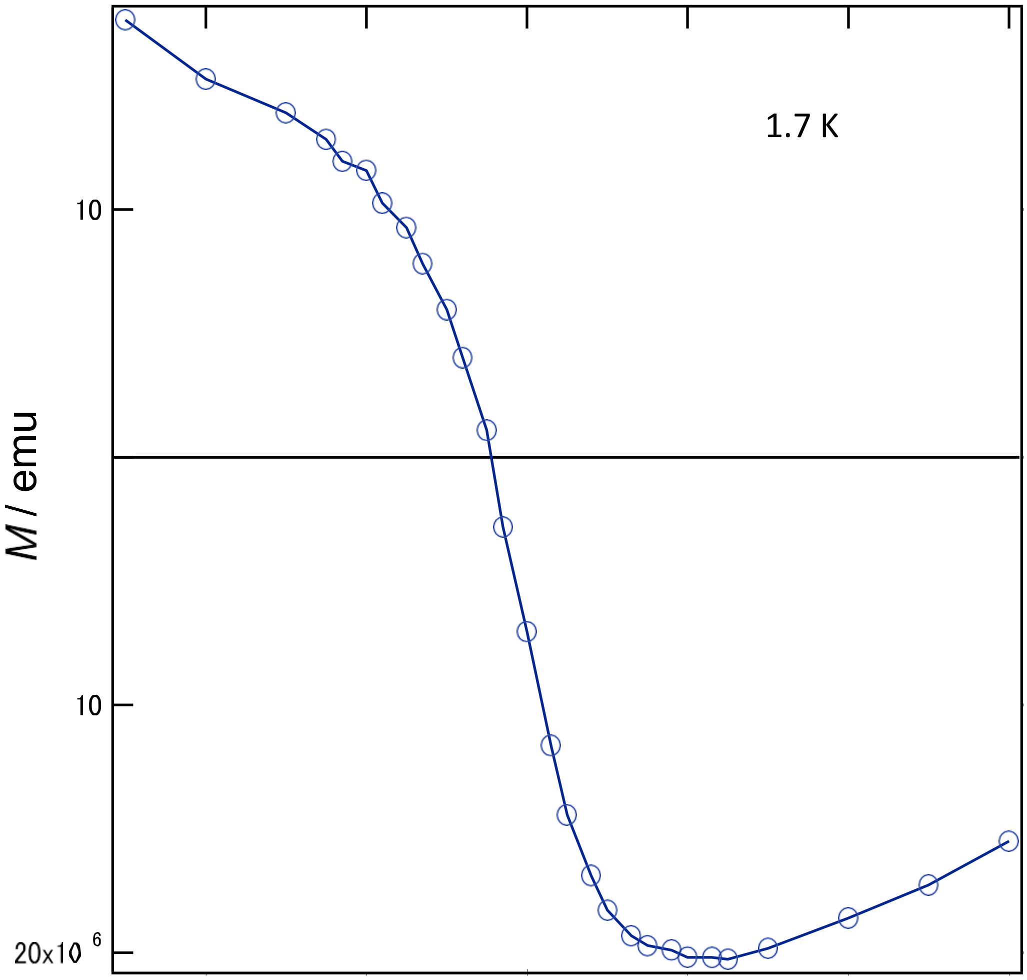

Graph 6.3. Magnetic field dependency of the magnetic susceptibility at 1.7 K

Magnetic field dependency of the magnetic susceptibility at 1.7 K of CTS 6.1 produced a curve indicative of a superconducting material.

6.1.7 Resistivity Data

Temperature dependent electrical resistivity measurements were performed on single crystals of CTS 6.1 down to 1 K using the four probe method. The resistance decreases upon cooling with a downturn at 4.2 K indicating the onset of superconductivity (Graph 6.4). The broad transition to T_{zero} at 1.8 K suggests a possible Kosterlitz-Thouless transition. At temperatures just above the superconducting transition there is no hump observed as can be seen in other examples of the beta'' BEDT-TTF tris(oxalate)metallate family where resistivity begins to increase below a minimum at a temperature typically in the range 30-150 K.

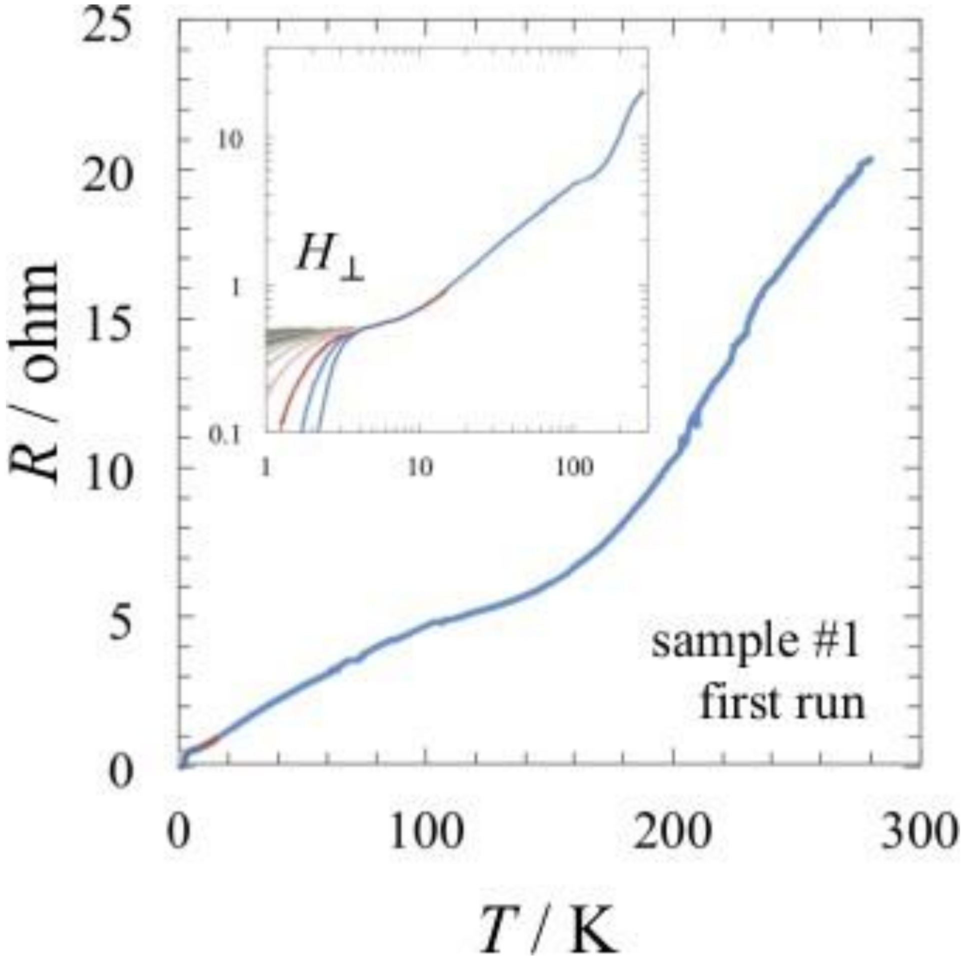

Graph 6.4. Temperature dependent resistivity profile from 300 – 0 K for CTS 6.1. (Inset) Magnetic field dependence of the superconducting transition perpendicular to the conducting plane.

The application of a magnetic field perpendicular or parallel to the conducting plane surpresses the superconducting transition (Graph 6.5). The magnetic field dependence of the superconducting critical temperature perpendicular to the conducting plane gives an upper critical field $\mu_0 H_{c2\perp} > 1.5$ T (Graph 6.5). The magnetic field dependence of the superconducting critical temperature parallel to the conducting plane gives an upper critical field $\mu_0 H_{c2//} > 8$ T (Graph 6.6), which is over the calculated Pauli-Clogston limit for this material[9]. Ginzburg-Landau coherence lengths are $\xi// \sim 160$ Å and $\xi\perp \sim 25$ Å. Graphs 6.6 and 6.7 below shows the relationship of the applied magnetic field (parallel and perpendicular) versus the superconducting T_C. The superconducting T_C is suppressed easier in the perpendicular application of the magnetic field.

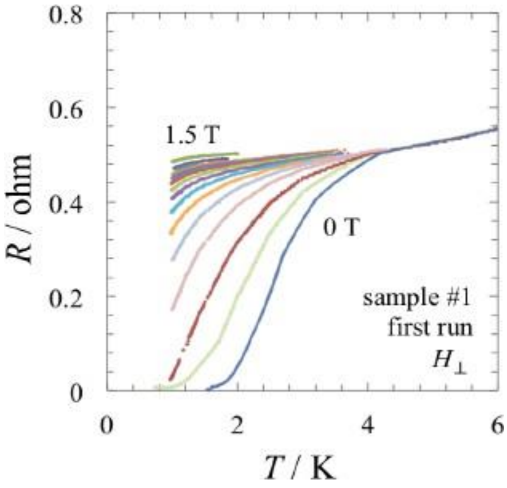

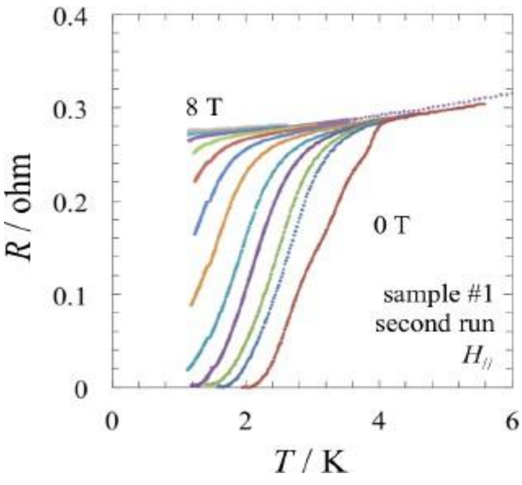

Graph 6.5. Magnetic field dependence of the superconducting critical temperature perpendicular to the conducting plane.

Graph 6.6. Magnetic field dependence of the superconducting critical temperature parallel to the conducting plane.

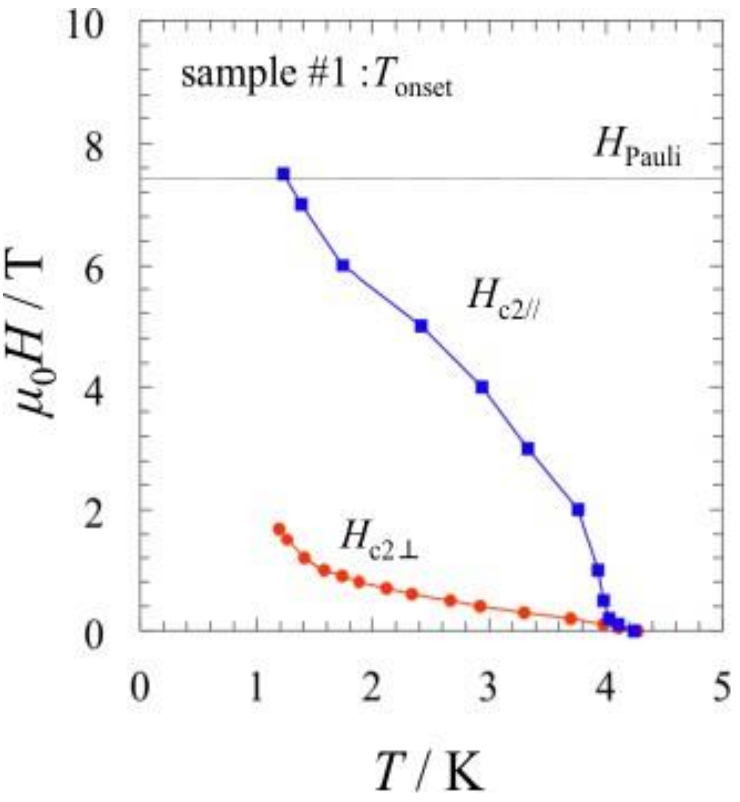

Graph 6.7. Magnetic field dependence of the superconducting critical temperature (T_{onset}) both perpendicular and parallel to the conduction plane.

Shubnikov-de Haas (SDH) oscillations, related to the quantum hall effect, are oscillations of the resistivity parallel to the current flow in the edge states of a 2D electron gas (2DEG) in an applied magnetic field. Applying a magnetic field to a 2DEG causes the electrons in the bulk regions to perform circular motions. At the border regions (i.e. in this case, the edge of the crystal) the electrons cannot perform full circular motions because they are scattered back from the interface. The scattering events give the electrons a higher energy and the magnetic field forces the scattered electrons to move in a forward direction so that the current flows without resistivity in the edge channels. This is seen experimentally as a deviation or regular oscillation away from the mean resistivity due to electron scattering.

The magnetic field dependence of the resistivity for CTS 6.1 shows strong Shubnikov-de Haas oscillations and Fermi liquid behaviour ~H^2. The magnetic field was applied perpendicular to the conducting plane. The fourier transform of the Shubnikov-de Haas oscillations show a small Fermi surface *F* ~ 2331.1 ± 1.2 T and light effective mass *m*/m* ~ 1.4 (Graph 6.9).

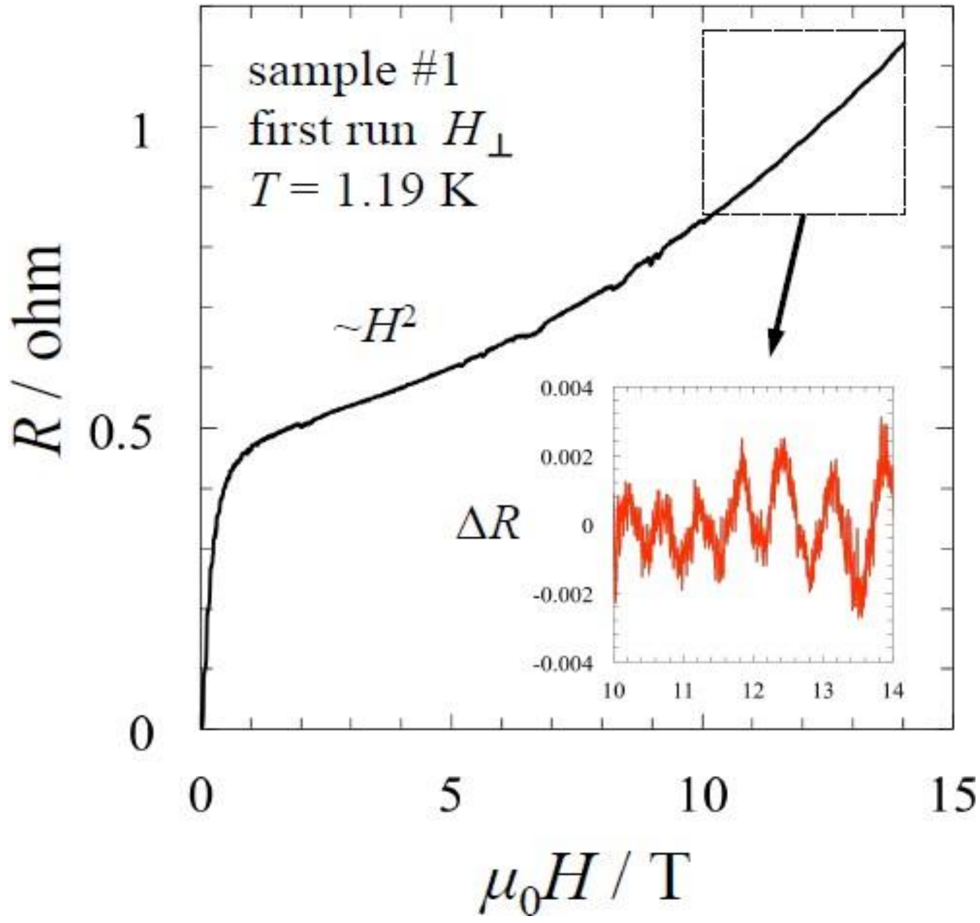

Graph 6.8. SDH oscillations in CTS 6.1 when magnetic field is applied perpendicular to the conducting plane.

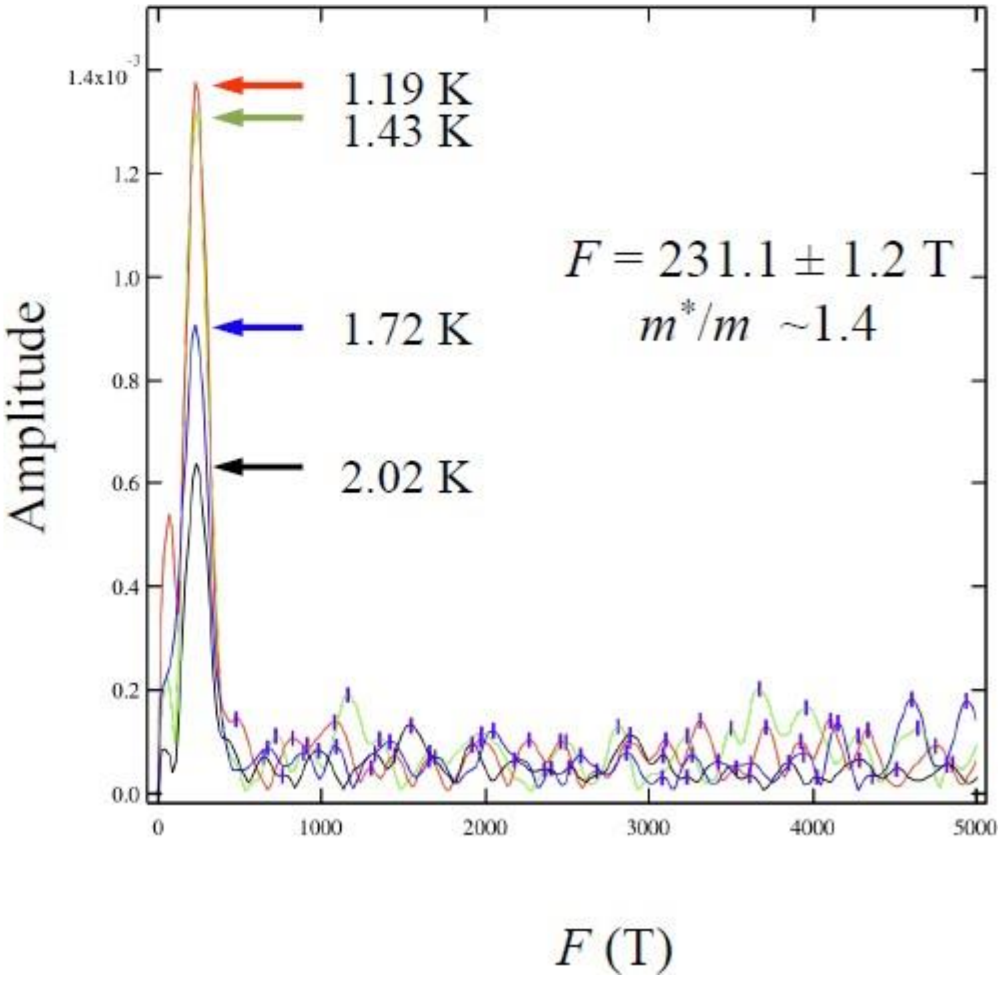

Graph 6.9. Fourier transform of the SDH oscillations. Fermi surface and effective mass are given inset.

6.2. Definitions

6.2.1 Pauli-Clogston Limit

The Pauli-clogston limit is the amount of applied magnetic field which should break the Cooper pair of electrons and destroy BCS superconductivity, i.e. it's critical upper field H_{C2}[9].

6.2.2 Ginzburg-Landau Coherence Length

The Ginzburg-Landau coherence length is the distance in the material that the number of superconducting electrons per unit volume are disturbed by an applied electric or magnetic field.

For $T > T_c$ (normal phase),

$$\xi = \sqrt{\frac{\hbar^2}{2m|\alpha|}}$$

Whilst in the superconducting state it is more relevant, for $T < T_c$,

$$\xi = \sqrt{\frac{\hbar^2}{4m|\alpha|}}$$

Where Ђ^2 is the reduced Plank constant, α is a constant, and m is the mass of a Cooper pair, which is equal to twice the electron mass.

6.3 Chapter Conclusions and Future Work

In conclusion, the Cr superconductor has a multi-layered packing arrangement of BEDT-TTF, $Cr(C_2O_4)_3$ and 18-crown-6. This is the 2D superconductor with the widest gap between conducting layers, where only a single donor packing motif is observed (β''). The strong 2D nature of this system strongly suggests that the superconducting transition is a Kosterlitz-Thouless transition. This Cr salt has a higher T_C (4.2 K) when compared with the isostructural Rh salt (2.7 K). Crystals of the Ir analogue were too thin for physical characterisation, however the X-ray crystal structure proved that the salt is isostructural to the Cr and Rh derivatives.

Isostructural derivatives of this phase of superconductor could be synthesised by replacing the metal centre with Al, Co, Fe, Ga, Ru to allow a systematic study of the effect the metal centre has upon the conducting properties. Better quality crystals of the isostructural iridium analogue should also be synthesised for charge transport and magnetotransport investigations.

6.4 References

1. A. W. Graham, M. Kurmoo and P. Day, *J. Chem. Soc. Chem. Commun*., 1995, 2061.
2. L. Martin, S. S. Turner, P. Day, F. E. Mabbs and E. J. L. McInnes, *Chem. Commun.*, 1997, 1367.
3. H. Akutsu, A. Akutsu-Sato, S. S. Turner, P. Day, D. A. Tocher, M. R. Probert, J. A. K. Howard, D. Le Pevelen, A.-K. Klehe, J. Singleton and V. Laukhin, *Synth. Met*., 2003, **137**, 1239.
4. T. G. Prokhorova, L. V. Zorina, S. V. Simonov, V. N. Zverev, E. Canadell, R. P. Shibaeva and E. B. Yagubskii, *CrystEngComm*, 2013, **15**, 7048.
5. L. Martin, A. L. Morritt, J. R. Lopez, H. Akutsu, Y. Nakazawa, S. Imajo and Y. Ihara, *Inorg. Chem.*, 2017, **56(2)**, 717.
6. L. Martin, A. L. Morritt, J. R. Lopez, H. Akutsu, Y. Nakazawa and S. Imajo, *Inorg. Chem.*, 2017, **56(22)**, 14045.
7. P. Guionneau, C. J. Kepert, D. Chasseau, M. R. Truter and P. Day, *Synth. Met*., 1997, **86**, 1973.
8. A. M. Clogston, *Phys. Rev. Lett*., 1962, **9**, 266.

Chapter 7: Final Conclusions and Future Work

7.1 Chiral and Racemic Donor Molecules

New charge-transfer salts have been synthesised and characterised from two new donor molecules: BHM-EDT-TTF and BHM-BEDT-TTF.

BHM-EDT-TTF has produced a family of 1:1 salts with tetrahedral and octahedral anions of the form BHM-EDT-TTF.X (X = BF_4, ClO_4 and PF_6). *S*,*S*-BHM-EDT-TTF.X and *R*,*R*-BHM-EDT-TTF.X salts are isostructural while the disordered *meso*-BHM-EDT-TTF.X forms an almost isostructural lattice. The room temperature resistivities and activation energies are similar for all enantiopure salts from perchlorate, tetrafluoroborate and hexafluorophosphate salts but slightly different for the rac/meso forms. The resistivities of some of the chiral radical-cation salts are lower than might have been expected for TTF or EDT-TTF $(\text{donor})_2^{2+}$ dimers having inter-dimer S…S contacts >3.7 Å to the nearest neighbouring dimer. Further work is already being performed with BHM-EDT-TTF in the Martin and Wallis research groups and this donor is proving to be fruitful at forming radical-cation salts with a variety of anions owing, in part, to the flexibility and the hydrogen-bonding ability of the 2-hydroxypropylthio side-chains. A variety of BHM-EDT-TTF donor packing motifs with the anions I_3^-, I_8^-, $Fe_2(\text{oxalate})_5^{4-}$, TCNQ-$F_4$, bromide and chloride anions have now been reported. The racemic donor BHM-BEDT-TTF forms a semiconducting hydrated 2:1 salt in the presence of a solvent and chloride ions. The crystals are twined with a possible minor confirmation of the donors. It is clear however that the interactions between hydroxyl groups and the insulating layer is key to producing the packing motif od the donor. The two independent donors are in a charge ordered +1 and 0 ground state, leading to semiconducting behaviour. This donor has also produced an insulating 1:1 salt with TCNQ which has an interesting packing arrangement in that the donors are segregated into stacks consisting of only a single enantiomer in the mode *SS:SS:RR:RR:SS:SS.*

Both of these donor molecules have proved that the hydrogen-bonding ability of their side-chains makes them excellent for growth of charge-transfer salts. Future work could be directed towards their use with more complex chiral anions, especially the tris(oxalate)metallate anions that have proven excellent counter-anions with BEDT-TTF. The synthesis of these chiral conductors could be promising candidates to allow the investigation of the electrical magnetochiral anisotropy effect.

7.2 Racemic Spiroborate Anion BEDT-TTF Salts

New charge-transfer salts have been synthesised and characterised from BEDT-TTF with the three anions $B(\text{malate})_2$, $B(\text{mandelate})_2$, and $B(\text{glycolate})_2$. These salts are the first examples of BEDT-TTF charge transfer salts containing chiral and racemic four-coordinate borate anions.

α-(BEDT-TTF)$_2$[B$_s$(R-malate)$_2$] possesses a unique band structure for an α-BEDT-TTF salt, which is owing to the chiral and polar B(malate)$_2$ anion, while the synthesis using the racemic mixture of the B(malate)$_2$ anion produced α-(BEDT-TTF)$_2$B*R/S*[(*R/S*)malate]$_2$.(H$_2$O)$_{2.85}$ which exhibits a semi-metallic to semiconductor transition due to band nesting at lower temperatures. These two salts also show the first examples of preferential diastereomeric induction within the electrocrystallisation environment.

Diastereomeric inductions is also present in β-(BEDT-TTF)$_2$B*R/S*[(*R/S*)-mandelate]$_2$ where only two of the possible six B(mandelate)$_2$ diastereomers are incorporated into the lattice, producing a semi-conductor that exhibits interesting magnetic behaviour due to the possibility of charge ordering at temperatures below 200 K. Electrocrystallisation of the chiral B*R/S*[(*S*)-mandelate]$_2$ anion with BEDT-TTF produced metallic macromolecular helices exhibiting metal-insulator transition at 150 K. The helices consist of many bent single crystal and shows the ability for chiral helices to form in the presence of B*R/S*[(*S*)-mandelate]$_2$, perhaps by preferential induction of one diastereomer, while the other stays in solution and directs the formation of the chiral helix. Charge-transfer salts displaying a macromolecular helical morphology have not been observed before.

Electrocrystallisation of racemic B*R/S*(glycolato)$_2$ with BEDT-TTF has produced a semiconducting charge-transfer salt, δ/δ'-(BEDT-TTF)$_2$[BR/S(glycolate)$_2$], which at room temperature includes two crystallographically independent donor layers due to anisotropy of the anionic stacks. A phase transition is observed between 100 – 50 K and it is suggested that this is accompanied by a change in crystal structure from the $P2/c$ to $P2$ space groups.

The monovalent borate anions have tended towards the preferential formation of 2:1 radical cation salts with two crystallographically independent BEDT-TTF molecules. All five of the spiroborate charge-transfer salts show novel structures that stem from the presence of chiral and diastereomeric anions within the electrocrystallisation environment. The salts have shown the effect of chirality on the nucleation and production of these crystalline materials.

7.3 Racemic Nine-coordinate Lanthanide Anion BEDT-TTF Salts

New charge-transfer salts have been synthesised and characterised from BEDT-TTF with La(dipicolinato)$_3$, Gd(dipicolinato)$_3$, and Tb(chelidonato)$_3$. These are the very first examples of charge-transfer salts containing racemic and chiral lanthanide anions. An isostructural pair of racemic charge transfer salts containing the racemic [Ln(dipicolinato)$_3$]$^{3-}$ anion (Ln = La, Gd) produces salts α'''-(BEDT-TTF)$_{4.5}$[Ln(dpa)$_3$].(EtOH)$_2$.(H$_2$O)$_n$, though unfortunately crystal quality meant that full physical property characterisation was not possible.

Spontaneous resolution of the racemic [Gd(dipicolinato)$_3$]$^{3-}$ anion in the presence of BEDT-TTF and bromobenzene has produced a chiral, paramagnetic, semi-conducting charge transfer salt crystallising in the non-centrosymmetric triclinic space group *P*1 - α-(BEDT-TTF)$_4$-Λ-[Gd(dpa)$_3$].H$_3$O.H$_2$O. This result is compelling as it proves not only the propensity for the [Ln(dipicolinato)$_3$]$^{3-}$ anion to form chiral materials in the solid state but also the observation of three properties within the same lattice – chirality, paramagnetism and semi-conductivity – with the further potential of including luminescence. This materials is therefore a promising candidate to take forward in the investigation of chiral conducting materials.

The new salt α-(BEDT-TTF)$_5$[Tb(clo)$_3$].EtOH.H$_2$O is the first structural evidence of a tris(chelidonato)lanthanide anion *via* X-ray diffraction measurements. It is also the first metallic charge transfer salt containing a racemic lanthanide anion. The BEDT-TTF molecules adopt the common alpha packing motif and has a fractional ground state at room temperature where the three independent donors have a charge of +2/3, leading to metallic properties. As temperature is decreased to around 170 K the BEDT-TTF molecules then adopt a +1, 0, +1 charge ordered state. Localisation of the conduction electrons produces insulating properties below this temperature.

Future work on these salts would start with producing isostructural salts but changing the metal centre to other lanthanides, There is the potential for interesting new families of salts with a variety of high magnetic moments and potentially luminescent properites. Of interest would be changing the metal centre or solvent in the metal-insulator α-(BEDT-

TTF)$_5$[Tb(clo)$_3$].EtOH.H_2O salt to see if chemical pressure can produce a salt which is metallic down to low temperatures and maybe observer superconductivity. Future work should involve resistivity measurements of the Tb salt under hydrostatic pressure.

7.4 Racemic Tris(oxalate)metallate Anion BEDT-TTF Salts

A new molecular superconductor, β”-(BEDT-TTF)$_2$[(H_2O)(NH_4)$_2$Cr(C_2O_4)$_3$].18-crown-6, has been synthesised. This is the 2D superconductor with the widest gap between conducting layers where only a single donor packing motif is present (β”). Superconducting critical temperatures at ambient pressure observed by electrical transport and magnetic measurements are 4.0-4.9 and 2.5 K, respectively. The strong 2D nature of this system strongly suggests that the superconducting transition is a Kosterlitz-Thouless transition. This Cr salt has a higher T_C (4.2 K) when compared with the previously published isostructural Rh salt (2.7 K). The results of the Rh salt are very different from those of the Cr salt. Zero resistivity for the Cr salt is clearly observed below 1.8 K and the Meissner signal is relatively large, although the transition is broader than those of normal superconducting salts and T_{cT} and T_{cM} differ greatly. It is somewhat strange because both Cr and Rh salts are isomorphous and the difference is very small. Crystals of the Ir analogue were too thin for physical characterisation, however the X-ray crystal structure proved that the salt is isostructural to the Cr and Rh derivatives. In future work, better quality crystals of the isostructural iridium analogue from both racemic and chiral tris(oxalate)iridate should be synthesised for charge transport and magnetotransport investigations. In further work, isostructural derivatives of this superconducting phase could be synthesised by replacing the metal centre with Al, Co, Fe, Ga, Ru to allow a systematic study of the effect the metal centre has upon the superconducting properties, as well as combinations of metal centres to produce ferro- or anti-ferromagnetic analogues of what is only the 2nd BEDT-TTF phase to show superconductivity with the tris(oxalate)metallate anion.